Doctorate Dissertation

博士論文

In-beam gamma-ray spectroscopy of ^{78}Ni

(^{78}Ni のインビームガンマ線核分光)

A Dissertation Submitted for Degree of Doctor of Philosophy

July 2018

平成30年7月博士（理学）申請

Department of Physics, Graduate School of Science,

The University of Tokyo

東京大学大学院理学系研究科物理学専攻

Ryo Taniuchi

谷内 稜

Abstract

Our understanding of the atomic nucleus is largely built on the information collected on nuclei at and close to the valley of nuclear stability. More than a half century has passed since the magic numbers of nuclei were correctly described theoretically: when the number of either protons or neutrons is equal to 2, 8, 20, 28, 50, 82 or 126, nuclei, which exhibit a local maximum of stability, were found to have closed shells by introducing spin-orbit interactions. However, after the construction of accelerators to produce Radioactive Ion Beams created the opportunity to study nuclei very far from stability in an energy domain from rest to a few GeV/nucleon, magic numbers turned out not to be universal. This phenomenon of disappearance of known shell closures and appearance of new ones, which is called shell evolution, influences our understanding of the nuclear interaction.

^{78}Ni, which has 28 protons ($Z = 28$) and 50 neutrons ($N = 50$), 14 additional neutrons to the last stable nickel isotope ^{64}Ni, is one of the most intriguing isotopes in the chart of nuclei. It is the most neutron-rich, exotic "doubly magic" nucleus that can be produced at present state-of-the-art facilities. So far, no spectroscopic information for ^{78}Ni has been obtained. In this work, excited states of ^{78}Ni have been investigated at the radioactive isotope beam factory, RIBF, by measuring their de-excitation γ rays after one- and two-proton knock-out reactions from ^{79}Cu and ^{80}Zn beams. To achieve a high γ-ray yield, the detection system comprised of a 10 cm-thick liquid hydrogen target with a recoil proton tracking system, MINOS, and a surrounding NaI(Tl) based γ-ray detection array, DALI2. Eventually, 310 and 222 events with at least one detected γ ray with more than 300 keV with the $(p,2p)$ and the $(p,3p)$ reactions, respectively, were obtained.

The structural information of ^{78}Ni is discussed with the obtained γ-ray transitions for each reaction channel. The most intensive γ-ray peak in the $(p,2p)$ channel at 2600(33) keV, with a significance level of 7.6σ, was assigned as the transition to the ground state from the first excited state with the spin and parity as $J^\pi = 2_1^+$. The other γ-ray transitions at lower energies in the $(p,2p)$ channel were placed on top of the 2_1^+ state in the level scheme, while a distinct transition at 2900(43) keV observed in the $(p,3p)$ reaction channel was considered as independent γ-ray transition feeding to the ground state directly without going through the 2_1^+ state. The observation of this high-lying state, which was tentatively assigned as a 2_2^+ state, was considered as an emergence of shape coexistence, driven by the collapsing shell gaps in the nuclei caused by the weakening spin-orbit interactions.

Further physical interpretation of the experimentally deduced level scheme was done by comparison with state-of-the-art theoretical predictions: Large-scale shell model, beyond mean-field, and *ab initio* calculations. Only shell model calculations with a large neutron model space reproduced the shape coexistence character in ^{78}Ni. The shell model calculations predicted both one-particle one-hole ($1p$-$1h$), which is assumed as the excited 2_1^+ state favored in the $(p,2p)$ channel, and many-particle many-hole excitation states, which is consistent with the 2_2^+ state manifested in the $(p,3p)$ channel. In addition, both levels were predicted at around 2-3 MeV. Furthermore, according to the shell model predictions in more exotic isotopes and isotones, the proton and neutron shell gaps at $Z = 28$ and $N = 50$ quench quickly beyond ^{78}Ni.

In addition to the γ-ray analysis, the cross sections to the excited states and the ground state were deduced experimentally and compared with reaction theory based on a DWIA formalism. Compared to the other neighboring nuclei, particularly small inclusive cross sections of ^{79}Cu$(p,2p)^{78}$Ni and ^{80}Zn$(p,3p)^{78}$Ni were observed. This was explained by the largest fraction of the final states of the proton removal reactions going to higher lying states above the neu-

tron separation energy, immediately evaporating neutrons. This assumption was supported by the reaction theory, whose exclusive cross sections to the excited states of ^{78}Ni were in good agreement with the experiment, including the observation of no direct feeding to the 2^+_1 state. In summary, the spectroscopic study of ^{78}Ni was performed for the first time, and at least two excited 2^+ states and other higher lying states were found. This casts a question about the nature of the shell closure in ^{78}Ni and the possible shape coexistence. Though the doubly magic nature was confirmed to be persistent, at the same time, the shell gap is anticipated to vanish beyond ^{78}Ni.

Table of Contents

List of Figures

List of Tables

Chapter 1

Introduction

The atomic nucleus is one of the most intriguing physical objects as a finite quantum many-body system consisting of two types of fermions: protons and neutrons. The system is organized by an interplay between the repulsive Coulomb force and the nuclear force, which is a short-range strong interaction confining the system within a few femtometers. After the discovery of such a dense system by Coulomb elastic scattering more than a century ago [1], numerous works have been performed to explain various phenomena in the nuclear system, such as deformation, shell closure, and particle emission. Since it has a surface, it can be deformed to gain binding energy, and sometimes exhibits several shapes coexisting simultaneously. Besides, it is also known to have a shell structure, similar to an atomic electron system, which was theoretically explained successesfully in 1949 by M. Goeppert-Mayer [2] and O. Haxel, J. Jensen, and H. Suess [3]. However, further experimental studies of the very unstable nuclei far from the stability line revealed the structure is rather transient. To understand the emerging characteristics in such exotic nuclei, one of the most symbolic nuclei locating far from the stability line, ^{78}Ni, was investigated in this work.

In this introductory chapter, general understanding of the atomic nucleus (section 1.1), experimental findings (section 1.2) and theoretical approaches (section 1.3) toward ^{78}Ni, and the strategy of this work (section 1.4) are explained in the respective sections.

1.1 Nucleus as a finite quantum many-body system

1.1.1 Magic numbers

The magic number is a universal concept in a finite quantum many-body system consisting of any kind of fermions within a certain attractive potential; in case the number of the fermions in the system equal to the magic number, the system is locally more stabilized than others. This tendency to stabilize the system has been conceived from empirical observations and is now understood as “shell closure”. In such conditions, the quantized orbitals are occupied by the fermions from low-energy states by satisfying the Pauli exclusion principle. Since the locations of the discretized levels are determined uniquely by the properties of the potential in the system, the shell structure, which is regarded as a set orbitals within similar energy, is also different for each system.

A prominent case of magic numbers is provided by the shell structure of atomic electrons, which are bound by a central Coulomb force. By taking into account the surrounding electrons weakening the Coulomb potential, which is known as a shielding effect, the degenerated orbitals with the principal quantum number are rearranged. As a result, when the number of elec-

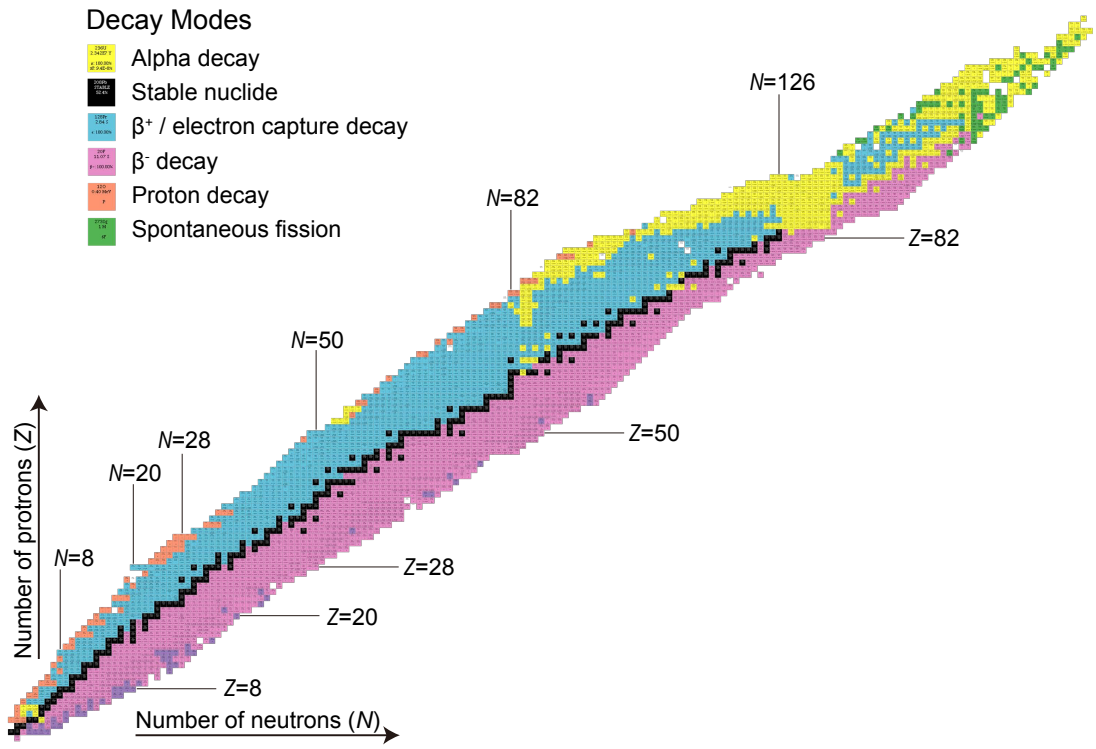

Fig. 1.1: The chart of nuclides. The main decay modes are represented by colors. The stable isotopes are drawn in black. The magic numbers of protons and neutrons are indicated. Data were taken from [6].

trons becomes equal to 2, 10, 18, 36, 54, or 86, the respective valence shell of electrons is filled and establishes a shell closure. Elements having the same atomic numbers (=electron numbers) as these magic numbers are known as noble gases, which are chemically stable against forming molecules by chemical bonds.

A similar phenomenon was found in a mass distribution of metal cluster ions, such as $(\mathrm{Na})_n$, $(\mathrm{Cu})_n$, $(\mathrm{Ag})_n$, and $(\mathrm{Au})_n$ [4, 5]. By counting the abundance of the masses, shell-closing magic numbers were found. The experimental consequence triggered theoretical discussions; the attracting potential in the cluster was understood as not a three-dimensional harmonic oscillator but rather a three-dimensional square well potential. In this way, experimental studies on the magic numbers can have an important impact to improve understanding of the interactions in such quantum many-body systems.

Hereafter, magic numbers observed in atomic nuclear systems are discussed as a finite quantum many-body system consisting of protons and neutrons.

1.1.2 Shell closure and its evolution of atomic nuclei

The atomic nuclei have a wide variety of isotopes (isotones), which are defined as nuclei having different numbers of protons (neutrons), but same numbers of neutrons (protons). Isotopes are often illustrated by a two-dimensional Segrè chart with numbers of protons (Z) and neutrons (N) as Fig. 1.1. In the figure, stable isotopes are indicated with black squares, while other unstable nuclei are colored by their main particle-decay modes, α, β^-, β^+, electron capture,

proton, and spontaneous-fission decays. It was noticed at an early stage that some isotopes and isotones are stabilized or possessing longer lifetimes at particular combinations of protons and/or neutrons. From the available data at that time, the numbers, 2, 8, 20, 50, 82, and 126 were pointed out as magic [7], while they were unable to be reproduced by the predicted shell structure from simple mean-field potentials. The single-particle shell structure in a three-dimensional harmonic oscillator potential, shown in Fig. 1.2, results in the shell closures at the numbers of 2, 8, 20, 40, 70, and 112, which are not the same as the proposed magic numbers. Even utilizing more realistic Woods-Saxson type potential, based on the assumptions that the nucleons are in a certain saturation density and interacting with a short-range correlation, the magic numbers could not be reproduced. This disagreement was finally solved by M. Goeppert-Mayer [2], and O. Haxel, J. Jensen, and H. Suess [3] independently in 1949. They introduced a spin-orbit interaction in the Woods-Saxon type potential as illustrated in the right column of Fig. 1.2.

The proposed model had explained many phenomena well, such as mass systematics, β decay half-lives, and related nuclear structures, in the vicinity of the stability line, however, after the innovation of the technique with accelerators to produce unstable nuclei away from the stability line, the magic numbers turned out not to be universal but rather highly dependent on their locations in the Segrè chart. The ground state of the neutron-rich beryllium isotope, ^{11}Be ($Z = 4, N = 7$), has been experimentally indicated as having a spin and parity of $J^\pi = \frac{1}{2}^+$, which differs from $J^\pi = \frac{1}{2}^-$, assumed by the naive picture of the single-particle shell model, filling the seven neutrons from the lower states in Fig. 1.2 [8]. This was interpreted empirically as the energy level of the $2s_{1/2}$ orbit was lowering down to the one of the $1p_{1/2}$ orbit with varying nucleon number [9].

The rearrangement of the single-particle orbits has been found to occur in a wider area of the Segrè chart. The measurement of masses of unstable sodium isotopes ($Z = 11$), ^{31,32}Na ($N = 20, 21$), revealed an anomaly from the theoretical predictions at that time [10]. The breakdown of the $N = 20$ magic number of sodium isotopes was confirmed by several works around this region: radii from laser spectroscopy [11], β-delayed γ-ray spectroscopy [12, 13], and Coulomb excitation [14]. These observations had cast a question about the nature of the shell closure and its conventional magic number away from stability, and triggered searches for the driving mechanisms in such unstable nuclei.

More recently, the disappearance of further traditional magic numbers and the emergence of new magic numbers have been confirmed in extremely neutron-rich unstable nuclei. The collapse of the $N = 8$ gap was noticed with measurements of the mass [10] and the matter radius [15] of ^{11}Li followed by measurements of the partial cross sections, momentum distributions, and excited states of ^{11}Li and ^{12}Be [16–18]. Similarly, the traditional magic number at $N = 28$, which was originally reproduced by inclusion of the spin-orbit force, was also discovered to be eroded below the doubly magic ^{48}Ca by measurements of the excited states of ^{40}Si [19], ^{44}S [20], and ^{42}Si [21, 22], and the two-proton removal cross section measurement with two-state mixing analysis of ^{40}Mg [23]. On the other hand, appearances of new magic numbers in neutron-rich isotopes are also intriguing. A new magic number of $N = 16$ was reported by reconstructing the unbound excited 2^+ state of ^{24}O [24]. Besides, measurements of neutron-rich calcium isotopes ($Z = 20$) have been actively studied as ^{52}Ca ($N = 32$) [25, 26] and ^{54}Ca ($N = 34$) [27, 28], which had been concluded that both numbers are representing good shell closures by their excitation energies and mass measurements. It is natural to conceive this phenomenon caused by the same reason as the disappearance of the traditional magic numbers by rearrangement of the single-particle states. These phenomena, which are called shell evolution, have been actively studied by both experimentally and theoretically to understand

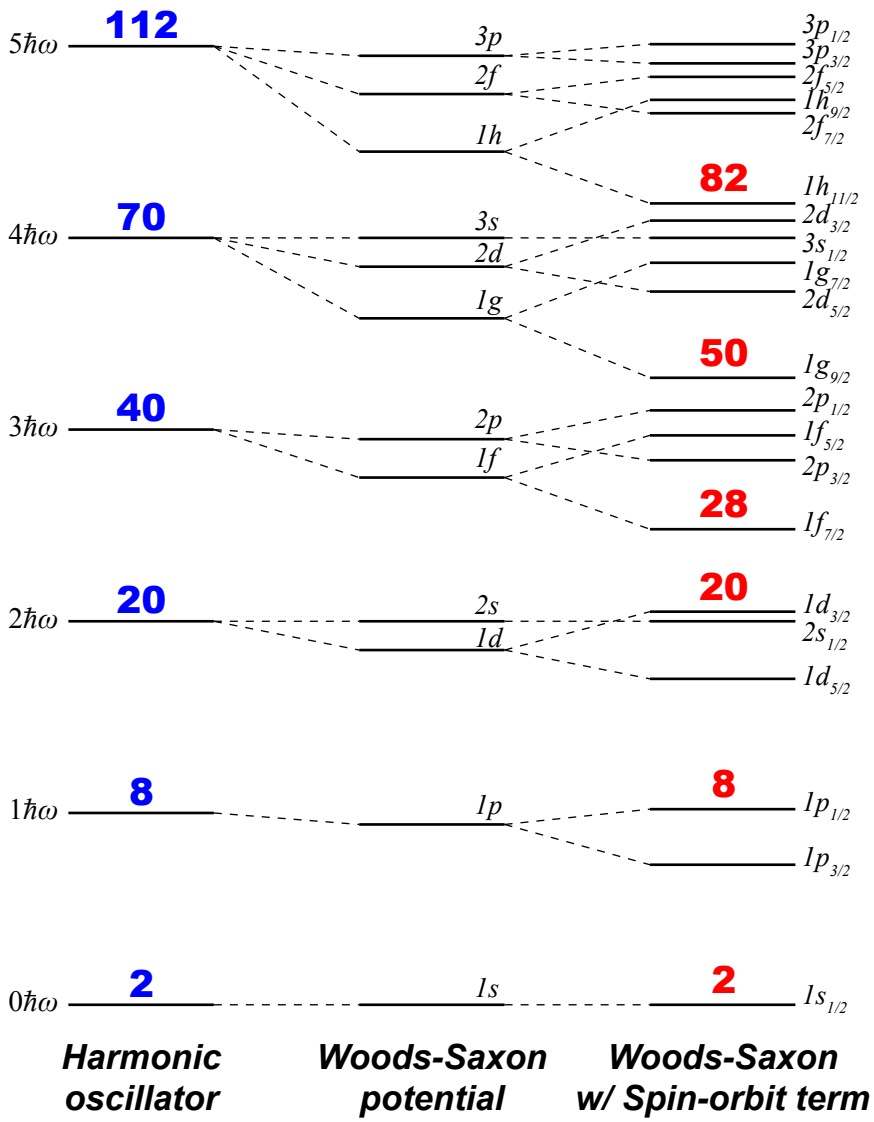

Fig. 1.2: Single-particle states in nuclei. The orderings of the single-particle states from a simple harmonic oscillator to Woods-Saxson potential, and finally including a spin-orbit term are shown.

their origin. More detailed descriptions can be found in some review articles as [29, 30].

1.1.3 Nuclear deformation and shape coexistence

As the nuclear system consists of a finite number of fermions, the surface of nuclei exhibits various characters. While the original shell model [2, 3] explained the properties of closed shell nuclei, most of open-shell nuclei have the flexibility for deformation owing to the gain of energy by breaking the spherical symmetry. Since the nuclei have a saturation property, in other words the volume of nuclei is rather constant, axially symmetric quadrupole deformation, which is categorized into two types, oblate (two long axes and one short axis) and prolate (one long axis and two short axes), occurs in most open-shell nuclear systems. For such cases, the single-particle energies in the shell model description shift accordingly with the realistic Woods-Saxon potential. In this way, open-shell nuclear systems can gain energy by deforma-

tion. Furthermore, a certain nucleus can have several local minima in the degree of deformations; it has orthogonal states with two or more different shapes. It was firstly proposed in the publication [31], and was termed shape coexistence [32,33]. Note that such shape coexistence is also predicted for ^{78}Ni in recent large scale shell model calculation [34].

1.1.4 Theoretical descriptions of nuclear system

Here, principles of the theoretical approaches are described. The Schrödinger equation for the wave function of an A-body system, ψ, taking only two-body forces into account, is described as:

$$H\psi = \left[\sum_{i=1}^{A} T_i + \sum_{i<j}^{A} W(i,j) \right] \psi = E\psi. \tag{1.1}$$

Here, kinetic energy and two-body nucleon-nucleon interaction are defined as $T_i = -\frac{\hbar^2}{2m}\nabla_i^2$ and $W(i,j)$, respectively. Since it is difficult to solve the many-body equations in general, an approximation of a single-particle in a spherical mean-field potential is commonly adopted to depict the nuclear structure. Assume the Hamiltonian can be separated into two parts: independent particles in a single-particle potential, H_0, and remaining residual interaction, H_{res}, as:

$$H = H_0 + H_{res}. \tag{1.2}$$

Here, each term is defined as:

$$H_0 = \sum_{i=1}^{A} T_i + V_i(\mathbf{r}_i), \tag{1.3}$$

$$H_{res} = \sum_{i<j}^{A} W(i,j) - \sum_{i=1}^{A} V_i(\mathbf{r}_i). \tag{1.4}$$

By applying an adequate potential, $V_i(\mathbf{r}_i)$, to minimize the contribution from H_{res}, the residual interaction can be neglected. Note that the spin-orbit coupling term, described as $V_s(\mathbf{r}_i)\mathbf{l}_i \cdot \mathbf{s}_i$, claimed by M. Goeppert-Mayer [2] and O. Haxel, J. Jensen, and H. Suess [3], can also be contained in the term of $V_i(\mathbf{r}_i)$. Here, $\mathbf{l}_i$ and $\mathbf{s}_i$ are the orbital and spin angular momenta, respectively.

While closed shell nuclei in the neighborhood of the stability line can be described by a simple model with H_0 and a spin-orbit interaction by utilizing a Woods-Saxson potential as the nucleon density can be considered as almost uniform, the contributions of the residual interaction is known to be important for open-shell nuclei. To address the missing term in the Hamiltonian, several theoretical approaches have been developed. The *ab initio* formalism is the most straight forward way, in which nucleons are treated as a many body problem interacting with each other. The nucleon-nucleon (NN) interactions were originally derived phenomenologically from free nucleon-nucleon scattering experiments, such as Argonne v_{18} [35], CD-Bonn [36], and chiral effective field theory (EFT) [37–39], which is based on low-energy quantum chromodynamics (QCD). Within its energy region, the main contributions of the strong interaction are the pion exchange and the short-range nucleon contact interaction. Furthermore, the importance of the three-nucleon forces, $3NF$, has been shown by a recent study of neutron-rich isotopes [40]. As the calculation requires huge computing power because of

its degrees of freedom, several formalisms to deal medium-mass nuclei were developed, such as many-body perturbation theory (MBPT) [41], coupled-cluster (CC) [42, 43], or in-medium similarity renormalization group (IM-SRG) [44–46]. These calculations succeeded in reproducing the mass and excitation energies of neutron-rich calcium isotopes ($Z = 20$). Currently, the calculations of neutron-rich nickel isotopes ($N = 28$) mark the new frontier [46, 47].

While *ab initio* calculations are still under development, two main alternative methods, the large-scale shell model [29, 48–53] and the mean-field formalism [54–57], have succeeded in reproducing the nuclear properties. The concept of the large-scale shell model calculation is to assume the nucleus as consisting of a spherical mean-field core H_0 and nucleons in valence space H_{res}. The valence nucleons in a given model space located outside of the core are governed by effective NN interactions obtained by fitting parameters with phenomenological data, namely two-body matrix elements (TBME). TBME can be decomposed into central, spin-orbit, and tensor terms to examine each component separately. Recently, the importance of the tensor term was recongnized in the nuclei with large neutron-to-proton ratio, N/Z, working as reducing the spin-orbit splitting of orbitals [50–52]. Nowadays, the term shifting the effective single-particle energies (ESPEs) are expected to be a key to explain the shell evolution. Besides the tensor force, $3NF$ are also recognized to be crucial to explain neutron-richi nuclei, such as unbound oxygen isotopes heavier than ^{24}O [53].

Self-consistent mean-field formalisms, which utilize effective energy density functionals, are also employed to describe the nuclear structure among the entire nuclear chart. The mean-field formalism is constituted by tuning the parameters of the density-dependent nucleon-nucleon interactions to recreate the empirical nuclear properties. For non-relativistic calculations, Gogny and Skyrme interactions are commonly used [54, 55]. Likewise, relativistic mean-field (RMF) calculations are based on an effective Lagrangian with the electromagnetic field and exchanging mesons among nucleons [56, 57]. Introduction of the tensor forces in mean-field frameworks are also attempted in addition to modifications of spin-orbit splittings.

1.2 Experimental approaches towards the most neutron-rich doubly magic nucleus, ^{78}Ni

^{78}Ni, which has 50 neutrons and 28 protons, is one of the most intriguing isotopes since it has been expected to be the most neutron-rich/exotic doubly magic nucleus ($N/Z \approx 1.79$) with a bound ground state. By investigating the characteristics of such an extreme case, our understanding of the nuclear structure is expected to vastly expand. Other candidates of uninvestigated bound doubly magic nuclei are ^{100}Sn and ^{70}Ca. The former one is the $N = Z$ isotope of tin, which was indirectly concluded as a doubly closed shell by the observation of a large transition probability of β^+ decay [58]. However, no final measurement has been performed yet. The latter one is a more exotic candidate since it has not been concluded whether it is bound. The heaviest calcium isotope observed at present is ^{60}Ca [59]. Therefore, ^{78}Ni is presently the only candidate for a new bound neutron-rich doubly magic nucleus. Until now, numerous attempts to acquire the information of the nuclei have been conducted to prove or disprove the nature of closure of both $N = 50$ and $Z = 28$ shells after the first production of ^{78}Ni with three counts at GSI in 1995 [60]. However, no absolute conclusion of the doubly shell closure had been obtained until this work. In the following sections, several experimental approaches in the vicinity of ^{78}Ni to investigate the characteristics of shell closures in nuclei are outlined.

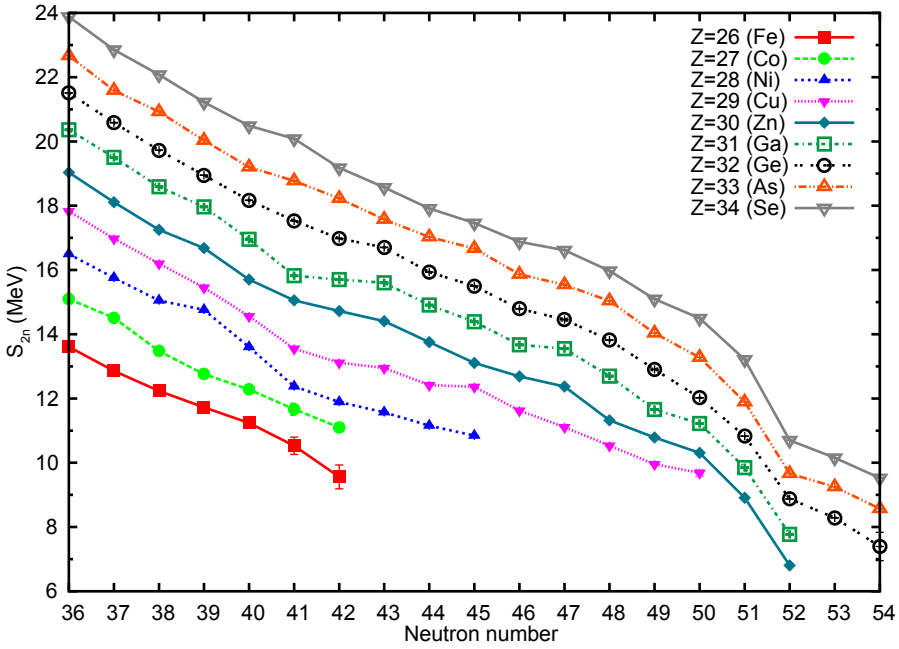

Fig. 1.3: Evolution of two-neutron separation energy. S_{2n} values along the isotopic chains from $Z = 26$ to 34 are drawn. Values are taken from Refs. [61, 62].

1.2.1 Mass systematics

The nuclear mass is a direct observation to quantify the binding energy, which has a direct relationship with the shell closure. The relationships among the mass, $M(N,Z)$, the mass excess, ME(N,Z), and the binding energy, $B(N,Z)$, are described below with the masses of neutron (m_n = 939.5654133(58) MeV), proton (m_p = 938.2720813(58) MeV), electron (m_e = 0.5109989461(31) MeV), and the atomic mass constant (u = 931.4940054(57) MeV), which is one twelfth of the mass of ^{12}C atom [63]:

$$\mathrm{ME}(N,Z) = M(N,Z) - (N+Z)u, \tag{1.5}$$

$$B(N,Z) = Nm_n + Z(m_p + m_e) - M(N,Z). \tag{1.6}$$

The systematic charts of the two-neutron (two-proton) separation energy $S_{2n}(S_{2p})$, defined below, are often used to illustrate the shell gap in the isotopic (isotonic) chains.

$$S_{2n} = -\mathrm{ME}(N,Z) + \mathrm{ME}(N-2,Z) + 2\mathrm{ME}(n) = B(N,Z) - B(N-2,Z), \tag{1.7}$$

$$S_{2p} = -\mathrm{ME}(N,Z) + \mathrm{ME}(N,Z-2) + 2\mathrm{ME}(^1\mathrm{H}) = B(N,Z) - B(N,Z-2) + 2B(^1\mathrm{H}). \tag{1.8}$$

Figure 1.3 displays the S_{2n} values around ^{78}Ni. Here, respective values are taken from Refs. [6, 62]. Because the particle separation energy is connected with its binding energy, shell gaps are indicated as the change of the steepness of the lines. The figure confirms the existence of the shell gap at $N = 50$ down to zinc ($Z = 30$) isotopes, while no data exist beyond $N = 50$ for lighter isotopes including nickel ($Z = 28$). The same discussion can be done for the proton shell gap at $Z = 28$ with S_{2p} trends. To prove the shell closures of $N = 50$ and $Z = 28$ for ^{78}Ni, mass measurements of $^{76-80}$Ni, ^{77}Fe, and ^{76}Cr are necessary, but cannot be achieved at present.

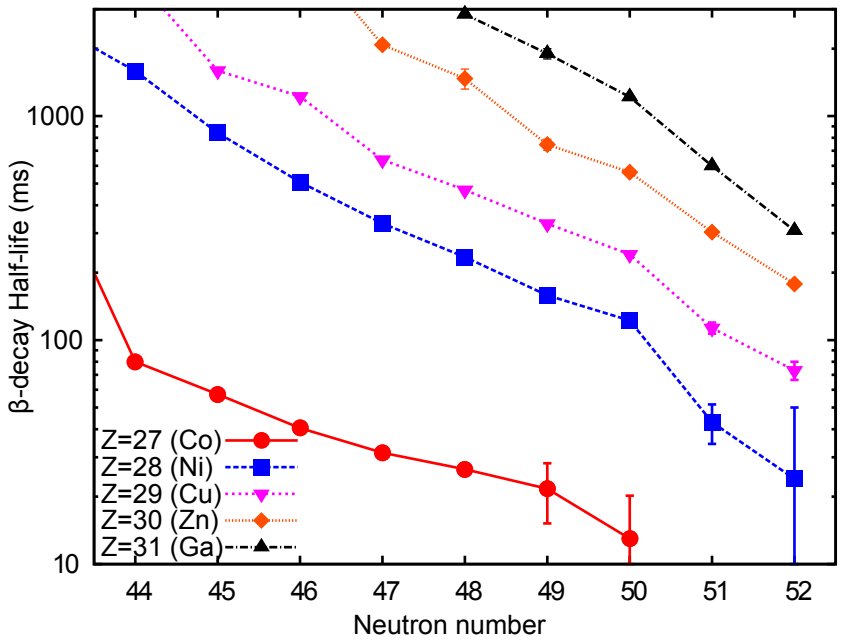

Fig. 1.4: Evolution of β-decay lifetimes. Measured half-lives of nuclei around ^{78}Ni are shown. Data are taken from Refs. [6, 64].

1.2.2 β-decay half-lives

The trend of mass differences of unstable nuclei can be obtained by a systematic study of the β-decay half-lives, $\tau_{1/2}$. The β-decay and the relationship between the released energy, Q_β, and the mass difference between the initial and final nuclei are described as below:

$$(N,Z) \rightarrow (N-1,Z+1) + \beta(e^-) + \overline{\nu}_e, \tag{1.9}$$

$$Q_\beta/c^2 = M(N,Z) - M(N-1,Z+1) - m_e - m_{\overline{\nu}_e}. \tag{1.10}$$

As known as Sargent's rule [65, 66], the fifth-power of Q_β is approximately proportional to the half-life. Thus, the systematic trend of the half-lives $\tau_{1/2}$ can be treated similarly to the trend of the neutron separation energy, especially for the nuclei apart from the stability line.

The first lifetime measurement of ^{78}Ni was performed at NSCL in 2005, which observed only about ten β-decay events. This was insufficient to conclude on the shell closure [67]. Subsequently, another measurement with high statistics was performed at RIBF in 2014 [64] for which the results are shown in Fig. 1.4. The systematic charts display sudden jumps above both $N = 50$ and $Z = 28$, which gives a consistent picture of the persistency of the magicity of ^{78}Ni. However, the observation itself could not conclude the shell closure nature of ^{78}Ni as the β-decay lifetime is highly dependent with the matrix element between the ground state of the mother nucleus and the final state of the daughter nucleus. In other words, it is not only the property of the mother nuclei itself, but rather dependent on the relationship with the daughter nuclei. Therefore, several theoretical calculations which reproduce the β-decay lifetimes in the vicinity of ^{78}Ni were required to be compared with the result. As a consequence, ^{78}Ni was claimed as doubly magic, as these measured lifetimes are in agreement with calculations which predict the double shell closure of ^{78}Ni. Since it is an indirect measurement, direct clues from further experimental studies are desired.

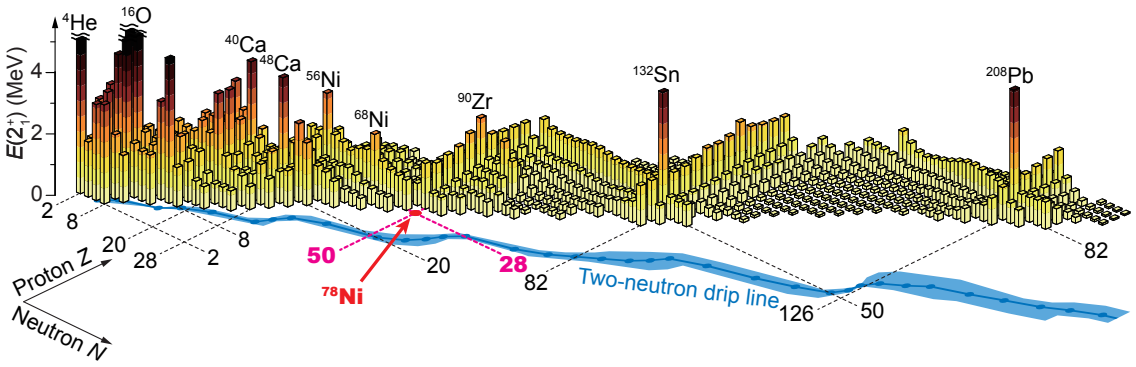

Fig. 1.5: Systematic chart of the first 2^+ energies for even-even nuclei. The excitation energy is a measure for shell closures in nuclei. Because the excitation energies of ^{4}He, ^{14}C, and ^{14,16}O are extremely high, their lengths are trimmed. 2^+ excitation energies of the doubly magic nuclei are more than twice the energy of neighboring semi magic nuclei. Values are taken from Refs. [6,68–86]. The theoretically estimated neutron-dripline and its associated errors [87] are also drawn with a blue line and blue hatched area. This figure is also included in the submitted paper of this work [88].

1.2.3 Systematics of the excited 2_1^+ states

The excitation energy trend of the first 2^+ states in even-even nuclei shows signatures of shell closures. These states are mainly obtained by γ-ray spectroscopic experiments. Figure 1.5 shows a systematic chart of the 2_1^+ excitation energies for even-even nuclei across the nuclear chart. When the number(s) of protons or/and neutrons equals to a magic number, more energy is required to excite the nucleus than in the vicinity because of its large shell gap(s). As seen in Fig. 1.5, the excitation energies along the magic numbers are higher than others. Particularly, the doubly magic nuclei located at crossing points of lines representing the magic numbers exhibit extremely high excitation energy. Note that the sudden rise in of the excitation energy of ^{68}Ni and ^{90}Zr are understood as rather local phenomena and not because of the $N = 40$ (^{68}Ni) and $Z = 40$ (^{90}Zr) harmonic oscillator shell gap [89,90].

In the case of ^{78}Ni, the conclusion has not been obtained yet. While the trend of the excitation energy along the nickel isotopic chain is decreasing towards $N = 50$, a Coulomb excitation experiment at ISOLDE of neutron rich zinc isotopes ^{76,78,80}Zn, suggested the persistence of the shell closure of ^{78}Ni [91]. Within this thesis, excited states of ^{78}Ni, particularly the first excited 2^+ state, were measured for the first time.

1.2.4 The ratio of the energies: R_{42}

Information on the deformation, or the collectivity, can be obtained from the ratio of the energies of the 2^+ state and the 4^+ state, $R_{42} = E_4^+/E_2^+$. There are mainly two types of collective quadrupole nuclear excitations competing in the nuclear system, rotations and vibrations. When the nucleus is deformed, the rotational excitation is preferred. For the case of a rigid rotor, the excitation energies for spin I are described as:

$$E_{\mathrm{rot}}(I) = \frac{\hbar^2}{2\mathfrak{I}} I(I+1), \tag{1.11}$$

where $\mathfrak{I}$ is the effective moment of inertia of the nucleus [92,93]. The rotational excitation band is constituted from a deformed band head. When the ground state of a even-even nucleus is deformed, which is an equivalent condition as the spherical shell closure not being established,

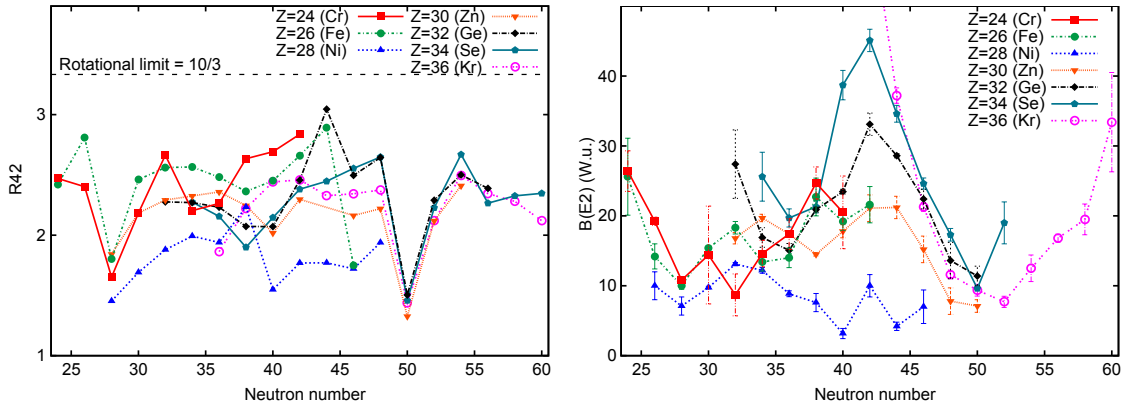

Fig. 1.6: Systematic trends of $R_{42} = E_4^+ / E_2^+$ and the transition probability $B(E2; 2^+ \rightarrow 0^+)$ in the vicinity of ^{78}Ni. The left figure shows the systematic trend along the isotopic chains of the R_{42} value from $Z = 24$ to $Z = 36$ within the range of $N = 24$ to 60. Sudden decreases, indicating the shell closures, can be seen at $N = 28$ and $N = 50$. Similar systematic graphs for $B(E2; 2^+ \rightarrow 0^+)$ are shown in the right figure. While parabolic shapes with local minima around $N = 28$ and $N = 50$ can be seen above $Z = 30$, constantly low values for $Z = 28$ can be seen because of the proton shell closure. Valuese are taken from Refs. [6, 80].

the rotational band will be observed with the R_{42} value approaching asymptotically to

$$R_{42} = \frac{4}{3} \approx 3.33. \tag{1.12}$$

A nucleus with spherical ground state but with degree of freedom of quadrupole deformation is considered to form vibrational excitations as:

$$E_{\mathrm{vib}}(I) = \frac{\hbar\omega}{2} I. \tag{1.13}$$

Thus, the ratio of 2^+ to 4^+ energy become $R_{42} \approx 2$. Conversely, a nucleus with closed shells favors single-particle excitations, which requires enough energy to overcome the shell gap for the first excited state. Generally, in case of doubly magic nuclei, the R_{42} value becomes lower than 2, such as: ^{16}O ($R_{4/2} = 1.50$), ^{40}Ca (1.35), ^{48}Ca (1.18), ^{56}Ni (1.46), and ^{208}Pb (1.06). Therefore, low values of $R_{4/2}$ are interpreted as a manifestation of magicity.

The isotopic trends of R_{42} values approaching in the vicinity of ^{78}Ni are illustrated in the left of Fig. 1.6. It shows the $N = 50$ shell closure down to $Z = 30$ nuclei, while no observation has been achieved for ^{78}Ni. Most recently, the measured R_{42} value of ^{80}Zn was reported in agreement with a $N = 50$ shell closure [82].

1.2.5 Systematics of the transition probabilities: $B(E2 : 2_1^+ \rightarrow 0_{gs}^+)$

The transition probability from the 2_1^+ to the ground state, $B(E2; 2^+ \rightarrow 0^+)$, is also known as an indicator for the collectivity of the ground state. By definition the transition probability is inverse proportional to the lifetime of the initial state, which is detailed in several references as [80, 94, 95]. Experimentally, they are determined by the measurement of the lifetime of the excited states, or the population cross section induced by Coulomb excitation. The values of the transition probability, $B(E2)$, are often scaled by Weisskopf estimates [96], which are the probability for a pure single-particle transition. The scaled transition probability is a non-dimensional value, but is always noted with Weisskopf units (W.u.). If the measured transition

probability is as low as 1 W.u., the transition is interpreted as a single-particle, which concludes the shell closure nature. On the other hand, when the value is much larger than 1 W.u., a collective excitation is inferred.

The obtained values in the neighborhood of ^{78}Ni are illustrated at the right panel of Fig. 1.6. These values are the adopted values with compilation work of Ref. [80]. In this figure, parabolic shapes with local minima around $N = 28$ and $N = 50$ can be seen above $Z = 30$. Besides that, along the $Z = 28$ chain the interpretations of measured $B(E2)$ values have been discussed extensively. In previous studies [89,97], a sudden increase of the $B(E2)$ value of ^{70}Ni after ^{68}Ni was observed. The fact had cast a question of the persistency of the $Z = 28$ gap and trigged several works along the nickel isotopic chains. Further studies on ^{72,74}Ni were performed with several experimental techniques, as inelastic proton scattering to obtain the deformation length [98], a Coulomb excitation experiment [99], and a direct lifetime measurement [100]. And finally, these results concluded no quenching of the $Z = 28$ gap toward $N = 50$, though so far no proper explanation about the sudden rise of the $B(E2)$ value of ^{70}Ni has been presented. A more recent systematic study of the $B(E2)$ values in the vicinity of ^{78}Ni as ^{72,74}Ni and ^{76,80}Zn with a direct proton inelastic scattering, (p, p') reaction, indicated the conservation of the both shell gaps, $Z = 28$ and $N = 50$ [101]. The transition probabilities of more neutron-rich nickel isotopes, as ^{76,78}Ni, are desired to be measured.

1.2.6 Other approaches

Other experimental attempts to comprehend the shell closure nature of ^{78}Ni have also been reported. Evidence of shape coexistence in ^{80}Ge was obtained by its internal conversion electron spectroscopy [102]. In that work, an intruder 0_2^+ state was measured, and suggested a possibility of a low-lying 0_2^+ state at around 2.5 MeV even in the doubly magic ^{78}Ni. A similar conclusion was obtained by collinear laser spectroscopy on ^{79}Zn at ISOLDE [103]. A long-lived $1/2^+$ isomer was confirmed by the isomer shift method. With support of theoretical calculations, the hypothesis of the shape coexistence nature in the region of ^{78}Ni is reinforced.

During the same experimental campaign of this work, excited states of ^{79}Cu, which has one more proton to ^{78}Ni, were also obtained [104, 105]. Several high energetic transitions were observed, and are interpreted as the signature of the persistence of the shell closure in both proton and neutron shells.

Up to now, there are still arguments remaining about the doubly magic nature of ^{78}Ni, and there is a possibility of competition between two features, shape coexistence and shell closure. Further studies of both ground and excited states of ^{78}Ni are desired. In the next section, the current discussions with theoretical frameworks about the nuclear structure in the vicinity of ^{78}Ni are described.

1.3 Theoretical studies towards ^{78}Ni

1.3.1 Tensor term

The nuclear structure of ^{78}Ni has been studied actively by numerous theoretical approaches, such as large scale shell model calculations, beyond mean-field calculations, and *ab initio* calculations. In the recent studies for neutron-rich isotopes, the importance of the tensor term in the residual monopole interaction has been recognized to rearrange the effective single particle states [50–52]. Figure 1.7 **a)** shows a schematic picture of the tensor force between a proton and a neutron in respective orbitals. This interaction works as reducing the spin-orbit splitting of

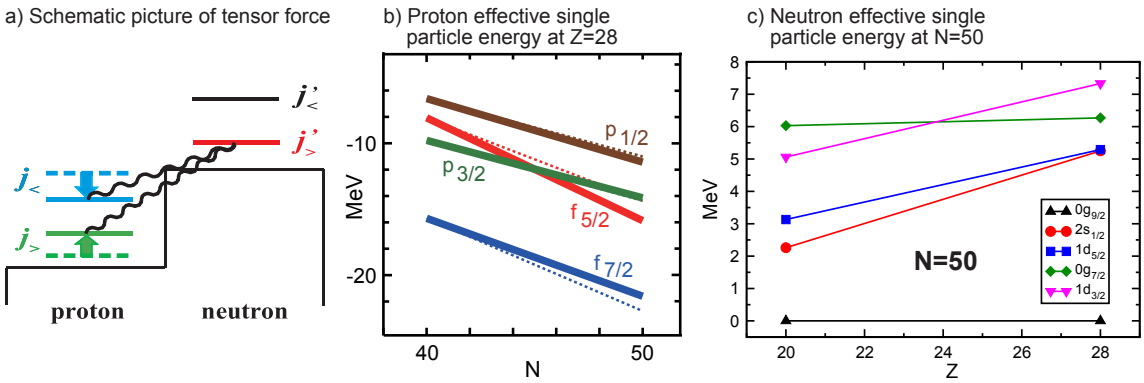

Fig. 1.7: Conceptual picture of the tensor interaction. **a)** Schematic picture of the tensor force between a proton and a neutron in respective orbitals. $j_<$ and $j_>$ represent orbitals with spin-orbit splitting, that is $j_<(j_>) = l + 1/2(-1/2)$. This interaction works as reducing the spin-orbit splitting of the proton (neutron) shell associated with adding neutrons (protons) in the $j_>^{(\prime)}$ orbital. **b)** Evolution of effective single particle energies of proton orbitals for the $Z = 28$ isotopic chain from $N = 40$ to 50. **c)** Evolution of effective single particle energies of neutron orbitals for the $N = 50$ isotonic chain from $Z = 20$ to 28. Respective figures are taken from Refs. [50], [51], and [34].

the proton (neutron) shell in accordance with adding neutrons (protons) in the $j_>^{(\prime)}$ orbital. In the case of nickel istopes, the spin-orbit splitting of proton orbitals forming the $Z = 28$ shell gap between $f_{7/2}$ ($= j_<$) and $f_{5/2}$ ($= j_>$), is reduced by adding neutrons into the $g_{9/2}(j'_>)$ orbital. Figure 1.7 **b)** illustrates the evolution of effective single particle energies (ESPEs) of proton shells along the isotopic chain of nickel isotopes [51]. Here, the ESPEs of $f_{5/2}$ and $p_{3/2}$ orbitals are crossing at around $N = 45$, which reproduces the results of several measurements of ^{79}Cu isotopes [106–109]. Above the crossing point toward $N = 50$, the $Z = 28$ gap, created by $f_{7/2}$ and $f_{5/2}$ orbitals, is predicted to be reduced by filling neutrons in $g_{9/2}$. A similar calculation for the $N = 50$ gap along the $N = 50$ isotopic chain is also shown in Fig. 1.7 **c)** [34]. Though the $N = 50$ gap at ^{78}Ni between $g_{9/2}$ and $s_{1/2}$ (or $d_{5/2}$) orbitals is large as 5 MeV, it is expected to diminish in lighter isotopes. The hypothesis above is not only within the shell model frameworks, but also discussed with mean-field calculations [110].

1.3.2 Large-scale shell model calculation

Large-scale shell model calculations were employed for the excited states of nickel isotopes by several empirical interactions and model spaces. There are mainly two groups actively developing the calculations to recreate the nuclear structure in the neutron-rich mid-mass isotopes: Large-scale shell model (LSSM) calculations by the Strasbourg group [34, 111, 112] and Monte Carlo shell model (MCSM) calculations by the Tokyo group [113–115]. The former has multiple calculations for the nickel region with different model spaces. The LNPS interaction with pf shell for protons, and $f_{5/2}$, $p_{3/2,1/2}$, $g_{9/2}$ and $d_{5/2}$ orbitals for the neutrons succeeded in reproducing the excited states of $Z = 24$ to $Z = 28$ isotopes up to $N = 46$ [111]. It also proposes the weakening of the $N = 50$ gap below $Z = 28$ isotones. In fact, this assumption was reinforced by a good agreement with the measurement of low-lying 2_1^+ and 4_1^+ states in neutron-rich ^{66}Cr and ^{70,72}Fe, which locate in the midst of $N = 40$ and $N = 50$ neutron numbers [116, 117]. Based on this interaction, a new calculation with larger model space, that is pf and sdg shells for protons and neutrons, respectively, with a ^{60}Ca core, named as PFSDG-U, was performed [34, 118].

It predicts quenching of the $N = 50$ shell gap below ^{78}Ni, while ^{78}Ni itself remains doubly magic. However, due to the onset of a diminishing of the shell gap, excited states with deformed shape are also predicted. Here, the 2^+ excitation energy in the ground-state spherical band is estimated at 3.2 MeV, while the states in the deformed band, $0^+_{deformed}$ and $2^+_{deformed}$, are at 2.7 and 2.9 MeV. That is, in other words, the emergence of shape coexistence in ^{78}Ni.

The latter calculation by the Tokyo group, MCSM, has the ability to integrate a larger model space in the calculation. A MCSM calculation with A3DA-m interaction, which utilizes pf, $g_{9/2}$, and $d_{5/2}$ model spaces for both protons and neutrons, was developed for understanding the shape coexistence phenomena in ^{68,70}Ni [114, 115]. This calculation expects ground and excited states as spherical shell closure with the energy $E(2^+) = 2.9$ MeV. No shape coexistence phenomena were predicted for ^{78}Ni. Very recently, a new calculation was developed based on the same interaction as A3DA-m but with an expanded model space, full $pfsdg$ shells for both proton- and neutron-valence spaces [119]. Especially because of the widen neutron-valence space as LSSM calculation, it predicts a result similar to the recent LSSM calculation: Shape coexistence in ^{78}Ni. Here, a ground state band with $E(2^+_{spherical}) = 2.6$ MeV and deformed band with $E(0^+_{deformed} = 2.6$ MeV and $E(2^+_{deformed}) = 2.9$ MeV were deduced. The detailed discussion is found in chapter 6.

1.3.3 Mean-field calculation

Beyond mean-field based calculations with the Hartree-Fock-Bogolyubov formalism with the Gogny force are also applied to the ^{78}Ni case [120, 121]. In these calculations, two models, the quasi-particle random-phase approximation (QRPA) formalism and the five-dimension collective Hamiltonian (5DCH) for configuration mixing, are applied. While the QRPA assumes a spherical ground state with possible single-particle or vibrational excited states, 5DCH calculates the axially symmetric deformed states constructing a rotational band. The former has the advantage for the prediction of the excited states of nuclei with shell closure, and expects the first 2^+ of ^{78}Ni just above 3.0 MeV. The latter, in contrast, calculates the first 2^+ at around 1.6 MeV because of the different hypothesis.

1.3.4 First-principles calculation

A first-principles (*ab initio*) calculation of coupled-cluster (CC) formalism has been performed for the excited states of ^{78}Ni [47]. It expects a spherical ground and excited state with $E(2^+) = 2.5$ MeV. Though it cannot predict the deformed states as the shell models did, the agreement of the energy of the spherical excited 2^+ state with the two shell model calculations mentioned above demonstrates the progress of the *ab initio* formalism. Besides the CC formalism, the in-medium similarity renormalization group (IM-SRG) formalism was also applied to ^{78}Ni [44–46, 122]. While the CC calculates the excitation energies of closed core nuclei, this formalism has an advantage to predict the masses of ground and excited states of open-shell nuclei. Recent calculations for open-shell calcium and lighter nickel isotopes reproduced the experimental results well [44–46]. The one-neutron separation energy S_n was predicted in this calculation resulting at $S_n \simeq 4.5$ MeV, which is consistent with the AME (Atomic Mass Evaluation) 2016 [61] ($S_n = 5.16(78)$ MeV). However, it has still difficulties to predict the excited states in closed-shell nuclei limited by the size of the harmonic oscillator model spaces to treat NN interactions satisfactorily. Futhermore, the inclusion of $3N$ forces is recognized as an important key. Thus, the excited 2^+ energy in the closed-shell nuclei, the 2^+ energy of ^{78}Ni is expected at 3.3 MeV.

Further discussions comparing the energy between the measured result and the theoretical calculations are written in chapter 5.

1.4 Strategy of the experiment

There are several methods to investigate the shell closures of ^{78}Ni. Mass measurements gives direct information on the ground state properties. However, it is necessary to measure the masses of nuclei located two-neutron/proton further from ^{78}Ni to see the systematic trend of two-neutron/proton separation energy; i.e., measurements of ^{80}Ni and ^{76}Fe are required. No current radioactive-ion beam (RIB) facility can provide sufficient intensity of these exotic isotopes. Alternatively, β-decay half-life measurements in the vicinity of ^{78}Ni were performed previously [64, 67]. In the later work of 2014, the doubly magic character of ^{78}Ni was inferred with an estimation that the β-decay half-life is mainly determined by the mass difference between the mother and daughter nucleus, Q_β. However, since the β-decay occurrs across the shell-gaps, the nuclear structure around ^{78}Ni may cause some effect on these half-lives. Thus, more conclusive measurements are desired.

γ-ray spectroscopy is one of the most powerful tools to investigate the shell evolution and is often used as a first indicator. The energy levels of the first excited 2^+ and 4^+ states are important to understand the structure of nuclei. There are several ways to measure the de-excitation γ rays at a RIB facility: β-delayed γ-ray emission, isomer spectroscopy, and in-beam γ-ray spectroscopy. The measurement of β-delayed γ-ray emission is one of the most common tools to measure the excited states as the measurement can be performed with a stopped beam, which is experimentally easier than in-beam γ-ray spectroscopy. In the case of ^{78}Ni, the β-decay from ^{78}Co is needed. The experimental setup can be similar to the previous β-decay experiments [64, 67]. Produced RIB of ^{78}Co will be stopped at a prepared decay station, and the γ rays emitted after the β-decay can be measured by a γ-ray spectrometer. However, the expected count rate of the nuclei is very low to perform the β-γ spectroscopy. Furthermore, it is generally known that the β-decay from nuclei far from the stability line tend to emit neutrons immediately after the β-decay due to the low neutron separation energy values, S_n, and its high Q_β value. Experimentally, the elimination of such contaminant events from neutron-emission decay is difficult. Isomer spectroscopy is also a common strategy to measure the de-excitation γ rays with RIBs. However, in this case the nucleus is necessary to have an isomeric excited state, which is not the case for ^{78}Ni. Thus, this method is not applicable.

In this work, in-beam γ-ray spectroscopy of ^{78}Ni was performed to investigate its excited states in a two-step reaction. After the production of the secondary RIBs by following reactions of a ^{238}U primary beam and a primary target (^{9}Be), another nuclear reaction takes place at the secondary reaction target. This method has strong advantages as: A relatively thick target can be utilized to increase the luminosity and obtained events can be filtered by identifying the incoming beam and the outgoing residuals of the secondary target. At the same time, prompt γ rays emitted from the populated excited states of the residual nucleus are measured by a γ-ray spectrometer placed in close vicinity of the secondary target. The same method was utilized for spectroscopic experiments in the vicinity of ^{78}Ni; such as ^{66}Cr, ^{72}Fe [116, 117], and ^{79}Cu [104, 105].

Since the uncertainty of the reaction position in thick targets degrades the accuracy of the Doppler reconstruction of the γ-ray energy, the secondary target needs to be carefully chosen to obtain sufficient statistics while keeping enough resolution. In order to maximize the luminosity per unit of energy loss, targets with low atomic number, especially hydrogen, are ideal.

However, liquid hydrogen has a low density, resulting in a thick target, which degrades the energy resolution by the uncertainty of the reaction position. In this work, to achieve both high luminosity and energy resolution of the detected γ rays from very rare events, a newly developed detector system consisting of a Time Projection Chamber (TPC), which tracks the recoil protons after the knockout reaction to determine the reaction position in a thick target, and thick liquid hydrogen target, MINOS [123, 124], was employed for the first time. It was installed at the standard focal plane for secondary reactions of the RIBF at RIKEN, Japan. At the same time, the γ rays emitted from the reaction residues were detected by a γ-ray spectrosctrometer consisting of an array of NaI(Tl) scintillators, DALI2 [125, 126]. This detector was aimed to maximize the detection efficiency by covering the almost 4π solid angle. The measurement was performed for 6 days with the maximum primary beam intensity of the RIBF at that time, ^{238}U with 7.5×10^{10} particles per second, to obtain sufficient statistics. The detailed description of the experiment and the detector setup are explained in chapter 3.

1.5 Thesis objectives

This thesis reports the first spectroscopic study of the excited states of ^{78}Ni, populated via proton knockout reactions. Energies of the following de-excitation γ rays were measured to determine the levels of the states. This thesis consists as follows: In chapter 2, the principle of the experiment and strategy of this work are described. In chapter 3, the experimental devices and the measurement information are explained. The calibrations for detectors, the performed particle identification, and the measured reaction cross sections are described in chapter 4. The obtained spectra of γ rays and the related analysis are shown in chapter 5. As a result, the most intensive γ-ray transition was assigned as the one feeding the ground state from the first excited state of ^{78}Ni, which was assigned a spin-parity $J^\pi = 2^+_1$. The theoretical predictions are compared with this experimental consequence to obtain the physics interpretations in chapter 6. At the end, the entire work is summarized with the conclusion and the future outlook in chapter 7.

For this experimental work, I have contributed for experimental preparations, measurements, development of the analysis codes, data analysis, and physics discussions to abstract the characteristics of the ^{78}Ni. While the experimental preparations and the measurements were performed within a collaboration named SEASTAR (Shell Evolution And Search for Two-plus energies At RIBF), most of the apparatuses, that are the beam line detectors to identify the incoming and outgoing particles, the γ-ray spectrometer, and the related electrical circuits including the data acquisition system, were managed under my responsibilities. During the data taking, I have committed to the tuning of the particle spectrometers to optimize the production of beams, and subsequently, I have dedicated for the tuning of the detectors, the circuit, the trigger, and the data acquisition systems. Discussions and negotiations with the staffs for the accelerator and the particle spectrometer as a person in charge of the experiment were also my responsibility.

The data analysis was separately performed by the responsible persons of the individual reaction channels. I have constantly improved the analysis and simulation codes and shared the information with others. I have also contributed to the development and improvement of the analysis code to reconstruct the proton tracks to obtain the vertices, even though the hardware of the secondary target system with the vertex reconstruction system, MINOS [123, 124], which will be explained later in chapter 3, was prepared by the colleagues from CEA Saclay, France, who developed and brought the system for the experiment. Finally, I obtained the γ-ray spectra

of ^{78}Ni after the $(p,2p)$ and the $(p,3p)$ reaction channels by myself. Statistical treatments were performed to build the level scheme of the excited states.

The discussions of the characteristics of the ground and excited states of ^{78}Ni were conducted with my initiatives with several theoretical physicists. Especially, communication with physicists of the shell model calculations and of the reaction calculation was the most important to obtain the theoretical result of the exclusive cross sections to the ground and excited states. Therefore, I worked as liaison between them by communicating frequently even with face-to-face for several time.

Finally, the overall results and discussions of the excited states of ^{78}Ni are detailed in this thesis. These results have been summarized in one regular article paper, submitted to a journal [88].

Chapter 2

Experimental Principles

In this chapter, the principles and concepts of the experiment are described. Firstly, the procedure of the production of radioactive-ion beams and the method of particle identification are introduced in section 2.1. Then, the method of in-beam γ-ray spectroscopy is discussed in section 2.2.

2.1 Radioactive-ion beams

2.1.1 Beam production with in-flight fission

As the concept of the experimental strategy was briefly introduced in section 1.4, the excited states of ^{78}Ni were produced by a two-step fragmentation process. One of the most important aspects of this experimental work is the production of radioactive-ion beams (RIB). The RI-beam factory (RIBF), operated by the RIKEN Nishina Center and the Center of Nuclear Study of the University of Tokyo [127], is currently the only facility in the world, which generates unstable nuclei far from the stability line with sufficient intensity to perform spectroscopy on ^{78}Ni.

Figure 2.1 depicts the schematic layout of the accelerator complex and the following particle spectrometers. A ^{238}U primary beam with an intensity of 7.5×10^{11} particles per second was accelerated by the superconducting injector RILAC2 and four coupled cyclotrons, named RRC, FRC, IRC, and SRC, to an energy of 345 MeV/u and impinged on a 3-mm-thick beryllium production target, which induced in-flight fission in the relativistic moving frame. The production target was located at the first focal plane, F0, of the following in-flight fragment separator, BigRIPS [128, 129]. BigRIPS consisted of two stages; the first stage from F0 to F2, optimized the beam purification to reduce the count rate from the contaminant events, and the second stage from F3 to F7, utilized for the particle identification (PID) of the secondary beam [130–132]. For the first stage, $B\rho - \Delta E - B\rho$ selection was applied with optimized magnetic rigidity $B\rho$ and energy loss ΔE with an 8-mm thick aluminum degrader installed at the F1 focal plane. The magnetic rigidity $B\rho$ is a physical quantity defined by the applied magnetic field B and the radius of the trajectory ρ, and is proportional to the momentum of the particle as deduced in the equation as explained later Eq. (2.2). For the purification stage, two dipole magnets were installed at both sides of the degrader material. By putting dedicated physical slits after each magnet, a certain momentum of the particles can be selected. In addition to the momentum selection, the energy loss ΔE in the degrader material was essential for the purification. Because the energy loss of ions in material is proportional to the square of the atomic number, Z^2, described in Eq. (2.7), the degrader was employed for discriminating particles with same momentum $B\rho$ but different atomic numbers. After the purification stage, the atomic number Z and the mass-

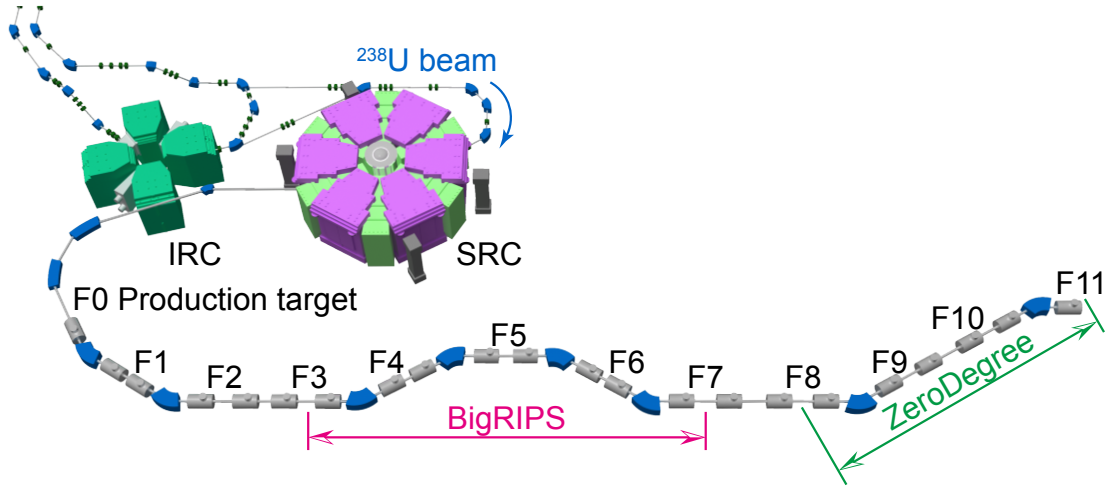

Fig. 2.1: Schematic layout of the BigRIPS and ZeroDegree spectrometers. The final two cyclotron stages, IRC, and SRC, of the RIBF along with the BigRIPS and ZeroDegree fragment separators are shown. This figure is also included in the submitted paper of this work [88].

to-charge ratio A/Q of these particles were identified by means of the $B\rho-\Delta E-$TOF method, detailed in the following section, with an additional 2-mm thick aluminum degrader at F5.

Following the PID process in BigRIPS, the particles were transported to the dedicated reaction target system, MINOS [123, 124], located at F8, for which details are explained in section 3.2.1. Then, following the secondary reaction, the reaction residues from the secondary target were identified by the ZeroDegree spectrometer from F8 to F11, which utilized the same method as the PID process of BigRIPS.

2.1.2 Particle identification with $B\rho-\Delta E-$TOF method

Both of the BigRIPS and ZeroDegree spectrometer distinguished the particles by means of the $B\rho-\Delta E-$TOF method, which are also detailed in Ref. [130]. The physics constants, c, e, m_u, and m_e represent the speed of light, the elementary charge, the atomic mass unit, and the mass of the electron, respectively[a)].

Focal planes There are twelve focal planes from F0 to F11, as shown in Fig. 2.1, along the beam line after the primaly target. The first stage of BigRIPS from F0 to F2 was used as purification step by the $B\rho-\Delta E-B\rho$ selection. Then, the particles were identified event-by-event along the second stage from F3 to F7 by the $B\rho-\Delta E-$TOF method. Here, the focal planes at F0, F2, F3, and F7 were set as fully achromatic foci, while the ones at F1 and F5 were set as momentum dispersive foci to filter according to the magnetic rigidity. The same $B\rho-\Delta E-$TOF method was applied to the ZeroDegree spectrometer with the achromatic foci at F8 and F11, and the momentum dispersive foci at F9 and F10.

Velocity The velocity $\beta(=v/c)$ was obtained by the interval of the timings, called as Time-of-Flight (TOF), between two plastic scintillator detectors located at the entrance and the exit of

[a)] $c = 2.998\times10^{8}$ m/s, $e = 1.602\times10^{-19}$ C, $m_u c^2 = 931.5$ MeV, $m_e c^2 = 0.5110$ MeV

each spectrometer as following:

$$\beta = \frac{L}{c} \cdot \frac{1}{\mathrm{TOF}}. \tag{2.1}$$

Here, L is the flight path length between the detectors. The length between F3 and F7, L_{37}, was 46.566 m, while the one between F8 and F11, L_{811}, was 36.48 m.

Momentum The momentum $p = \gamma m v$, where γ is defined as $\gamma \equiv \frac{1}{\sqrt{1-\beta^2}}$, was deduced from the equation of rotation. The equation of the relativistic motion can be written as:

$$\begin{aligned} \gamma m \frac{v^2}{\rho} &= Qv B, \\ B\rho = \frac{\gamma m v}{Q} &= \frac{\beta \gamma c m_u}{e} \cdot \frac{A}{Z}. \end{aligned} \tag{2.2}$$

The radius, the charge, the mass, and the magnetic field are defined as ρ, $Q \equiv Ze$[b)] , $m \equiv Am_u$ and B, respectively. Here, A and Z are the relative atomic mass and the atomic number. By employing the ion-optical transfer matrix elements from the position and angle information at each focal plane by the PPAC chambers [133], which are explained later in section 3.1.2, the reconstruction of the trajectories and the $B\rho$ values, which enable deducing the A/Z values, are obtained. As an example, the transfer matrix for F3 to F5 foci with 1$^{\mathrm{st}}$ order approximation can be written as:

$$\begin{pmatrix} x_5 \\ a_5 \\ \delta_{35} \end{pmatrix} = \begin{pmatrix} (x|x) & (x|a) & (x|\delta) \\ (a|x) & (a|a) & (a|\delta) \\ 0 & 0 & 1 \end{pmatrix} \begin{pmatrix} x_3 \\ a_3 \\ \delta_{35} \end{pmatrix} \tag{2.3}$$

In this equation, x_3, x_5, a_3 and a_5 are X-position at F3, X-position at F5, X-angle at F3 and X-angle at F5. The δ_{35} represents the fractional $B\rho$ deviation from the central value $B\rho_0$ as:

$$\delta_{35} = \frac{B\rho - B\rho_0}{B\rho_0} = \frac{\Delta(B\rho)}{B\rho_0} = \frac{\Delta p}{p_0} \tag{2.4}$$

In an simplified case, the elements of the transfer matrix between F3 achromatic focus to F5 dispersive focus with 31.7 mm/% momentum dispersion, which was 24.8 mm/% for ZeroDegree, can be described as:

$$\begin{pmatrix} x_5 \\ a_5 \\ \delta_{35} \end{pmatrix} = \begin{pmatrix} 1 & 0 & 31.7 \\ 0 & 1 & 0 \\ 0 & 0 & 1 \end{pmatrix} \begin{pmatrix} x_3 \\ a_3 \\ \delta_{35} \end{pmatrix} \tag{2.5}$$

In this analysis, the matrix elements, which have been obtained by previous measurements, were used. The Eq. (2.3) is solved as:

$$\begin{pmatrix} a_3 \\ \delta_{35} \end{pmatrix} = \begin{pmatrix} (x|a) & (x|\delta) \\ (a|a) & (a|\delta) \end{pmatrix}^{-1} \cdot \left[\begin{pmatrix} x_5 \\ a_5 \end{pmatrix} - \begin{pmatrix} (x|x) \\ (a|x) \end{pmatrix} \times x_3 \right] \tag{2.6}$$

This equation concludes that the $B\rho$ value for each particle can be deduced at first order by only three parameters, X-position for both foci and X-angle for one focus. To obtain more accurate $B\rho$ and A/Q for ZeroDegree spectrometer second order optical corrections were also applied.

[b)] The kinetic energy of the beam of this experiment was around 200MeV/u which was high enough to assume most of the nuclei were stripped fully, *i.e.*, $Q = Ze$.

Atomic number Energy deposition in the ionization chamber MUSIC was utilized to deduce the atomic number Z. The mean energy loss per distance of the kinetic energy, $-\frac{dE}{dx}$, of a nucleus with atomic number Z in the material, or gas in the MUSIC, with the mean electron number density and the mean excitation potential n and I[c)] in Bethe-Bloch formula is shown as:

$$-\frac{dE}{dx} = \frac{4\pi}{m_e c^2} \cdot \frac{Z^2}{\beta^2} \cdot \left(\frac{e^2}{4\pi\varepsilon_0}\right)^2 \cdot n \left[\ln\left(\frac{2m_e c^2\beta^2}{I\left(1-\beta^2\right)}\right) - \beta^2\right]. \tag{2.7}$$

Assuming the change of velocity is small, $|\Delta\beta| \ll \beta$, in the gas chamber of the MUSIC detector, Eq. (2.7) is simplified to:

$$|\Delta E| \propto \left(\frac{Z}{\beta}\right)^2. \tag{2.8}$$

The atomic number of the nucleus Z passing through the spectrometer was deduced by Eq. (2.1) and Eq. (2.8).

In summary, by measuring three values TOF, $B\rho$, and $|\Delta E|$ particle by particle, the velocity β, the atomic number Z, atomic mass A, and neutron number $N = A - Z$ were identified.

2.2 In-beam γ-ray spectroscopy

2.2.1 Technique

Spectroscopy of de-excitation γ rays is the most common way to determine the energy of the nuclear excited states. To populate the excited states, there are several strategies, such as nuclear reactions, Coulomb excitation, and β-decay. Because the targeted nucleus, ^{78}Ni, is located far from stability, in-beam γ-ray spectroscopy following two-step fragmentation (nuclear reaction) in inverse kinematics is most efficient [126].

As described in the previous section, a primary beam (^{238}U in this case) reacts on a production ^{9}Be target, which induces in-flight fission. After the collection and the purification of the fission products, the secondary reaction to populate the excited states of the nuclei of interest occurs at the secondary target. The type of the secondary reaction will be chosen according to the requirement and the incident kinetic energy of the nuclei. Nucleon-knockout/removal, nucleon-transfer, and charge-exchange reactions have a selectivity of the proton or neutron state of the nuclei, which can be determined by the choice of the reaction. Especially the nucleon-knockout reaction is favored over others with higher beam energy region compared to the Coulomb barrier (order of a few MeV). To reach the most neutron-rich nuclei, proton-knockout reactions at a fast-beam facility are very powerful. The fragmentation reaction, which is a multi-nucleon removal reaction, can also be employed to reach neutron-rich or neutron-deficient region, but the γ-ray spectrum can be complicated with more populated states than "pure" reactions because of the number of the possible configurations are determined by the number of the participating nucleons.

2.2.2 Doppler broadening

In-beam γ-ray spectroscopy has the advantage of the efficient population to the excited states of the unstable nuclei. However, the de-excitation γ rays are emitted from the moving frame,

[c)] When the mean atomic number in the material/gas is z, mean electrun number density n is written as $n = N_A \cdot z \cdot n_{\text{material}}$ with the Avogadro number N_A and the number density of the material n_{material}.

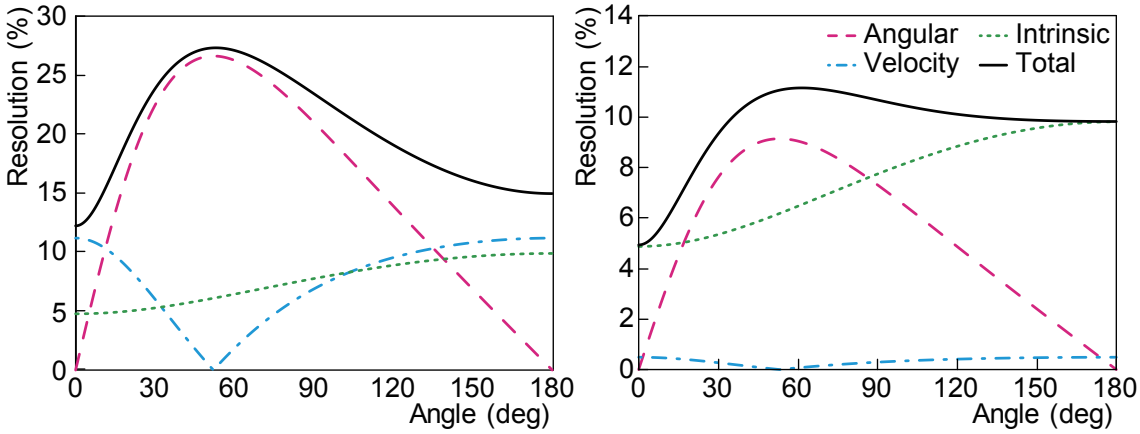

Fig. 2.2: Elements of the uncertainty of energy resolution with azimuthal angles for γ-ray spectroscopy. Two figures are depicted to compare the resolutions without and with the vertex reconstruction apparatus. In these cases, the projectile particle and the reaction target are respectively selected to ^{79}Cu with a velocity of $\beta = 0.6$, and a 10-cm thick liquid hydrogen target. While the case in the left figure has no information of the vertex position, the right case uses a vertex reconstruction system. A 1-MeV γ-ray in the rest frame is assumed to be emitted immediately after the reaction. The intrinsic energy resolution of the γ-ray spectrometer is set to 6.5% at 1 MeV with a square-root dependence explained in the text. The magenta dashed line is the component of the angular resolution described in Eq. (2.11). The blue dashed-dotted line is the uncertainty of the velocity β due to the finite target thickness (Eq. (2.12)). The green dotted line corresponds to the intrinsic energy resolution of the γ-ray spectrometer itself. The black line represents the combined value.

thus, a Doppler shift of the emitted γ-ray is unavoidable. With an energy of E_{γ_0} at the center of mass, the γ-ray energy in the lab frame, E_γ, is described as:

$$\frac{E_\gamma}{E_{\gamma_0}} = \frac{\sqrt{1-\beta^2}}{1-\beta\cos\theta_\gamma}. \tag{2.9}$$

Here, β is the velocity of the nucleus (center of mass), and θ_γ is the angle between the γ-ray and the particle. To eliminate the effect, the γ-ray detector should have good angular resolution with position sensitivity or a high granularity.

The effective energy resolution is determined by the Doppler broadening in addition to the intrinsic resolution of the γ-ray spectrometer. Sources of the resolution consist of three parts as intrinsic resolution $\delta_{\text{intr.}}$, the Doppler broadening caused by the angular uncertainty δ_θ, and the uncertainty of the velocity of the nuclei in a target with a certain thickness δ_β, formulated as:

$$\delta^2_{\text{tot.}} = \left(\frac{\Delta E_{\gamma_0}}{E_{\gamma_0}}\right)^2 = \delta^2_\theta + \delta^2_\beta + \delta^2_{\text{intr.}}. \tag{2.10}$$

δ_θ and δ_β can be obtained by calculating the differentials of Eq. (2.10) with the uncertainties, $\Delta\theta_\gamma$ and $\Delta\beta$,

$$\delta_\theta = \frac{\beta\sin\theta_\gamma\Delta\theta_\gamma}{1-\beta\cos\theta_\gamma}, \tag{2.11}$$

$$\delta_\beta = \frac{(\beta-\cos\theta_\gamma)\Delta\beta}{(1-\beta^2)(1-\beta\cos\theta_\gamma)}. \tag{2.12}$$

The intrinsic error is in a first order possible to be assumed to follow the Poisson distribution, which formulated as:

$$\delta_{\text{intr.}} \propto \frac{1}{\sqrt{E_\gamma}}. \tag{2.13}$$

Two realistic cases, with an 8-mm thick Be target and thick liquid hydrogen target with 5-mm vertex resolution, are calculated according to Eq. (2.10) as shown in Fig. 2.2. In these cases, the projectile particle is selected to ^{79}Cu with a velocity $\beta = 0.6$ and a 1-MeV γ-ray in the rest frame will be emitted after the reaction. The intrinsic energy resolution and angular resolution of the γ-ray spectrometer are obtained from the typical values of the NaI(Tl) scintillator array used in this work, DALI2, which will be described in section 3.2.3. See the caption in Fig. 2.2 for a detailed description of the charts.

2.2.3 Target selection

A secondary target was used to populate the excited states of the nuclei of interest for in-beam γ-ray spectroscopy experiments. As discussed in Eq. (2.10), the thickness of the secondary target degrades the effective energy resolution because of the uncertainty of the velocity and the angle of the emitted γ rays, while the population probability is proportional to the number of the target atoms per area, which is proportional to the thickness. Therefore it was necessary to optimize the thickness of the secondary target to gain as much luminosity as possible, and at the same time, it was important to select the thickness not to degrade the energy resolution of the γ-ray spectrometer.

The atomic number Z of the material of the target was also needed to be considered. The Z value should be low in the sense of the atomic background, which is caused by the X-rays when the ionized target atoms recombine [126], and also in the sense of energy deposit per unit length followed by the Bethe-Bloch formula, described in Eq. (2.7). If the deposited energy is as large as the amount of the kinetic energy of the particle, not only the energy resolution becomes worse as Eq. (2.12), but also charge state contaminants can cause low transmission and low efficiency of the particle identification (see section 3.1 also).

To balance all requirements discussed above, solid targets with low Z material, such as Be, C, or CH_2 targets, are commonly selected because gaseous or liquified hydrogen have low density and requires thicker target for a certain luminosity. Note that the energy loss between the solid material with lowest atomic number, Be ($Z = 4$), and hydrogen ($Z = 1$) are a factor of 4 per energy loss. As the production of the excited states of ^{78}Ni is almost at or even above the limit of the current RIB facility with normal solid target, a secondary target system with a 10-cm thick liquid hydrogen target and vertex reconstruction system from the recoil protons, MINOS [123,124], was newly developed. In the next section, the concept of the detector system and the experimental campaign are introduced.

2.2.4 Overview of the experiment: SEASTAR

As discussed in the previous section, the reaction luminosity and the energy resolution, degraded by the β uncertainty, δ_β, are competing with each other. To overcome the weak point of in-beam gamma-ray spectroscopy, a new secondary target system, MINOS, which is a thick liquid hydrogen target combined with a vertex reconstruction apparatus, was proposed and employed the first time for experiments at the Radioactive Isotope Beam Factory [127], Japan. Thanks to the high energy of the secondary beam around 200 MeV/u, thick secondary targets can be employed to gain luminosity. The relatively high efficient γ-ray spectrometer, DALI2,

which consist of $\sim$ 200 NaI(Tl) scintillator detectors, was used to detect the de-excitation γ rays. Prior to the introduction of MINOS, thick targets have caused limited energy resolution. MINOS uses a 10-cm thick liquid hydrogen target system with a vertex reconstruction system, which compensates the degression of the energy resolution caused by uncertainties of the angle of γ-ray emission and the velocity of the nucleus at the emission. A new experiment with the combination of DALI2 and MINOS at RIBF to measure the energies of the excited states of neutron-rich nuclei systematically, was proposed and named SEASTAR, "Shell Evolution And Search for Two-plus energies At RIBF". The measurement of the $E(2^+)$ of ^{78}Ni was performed during the first experimental campaign. At the same time, it was the first time to utilize the MINOS for a physics experiment.

Chapter 3

Experimental Devices

The equipment used for the experiment is described in this chapter. Detectors used for particle identification in the BigRIPS and Zerodegree spectrometers are described in section 3.1. The detectors located at the secondary reaction target, MINOS and DALI2, are described in section 3.2. During the experiment, a common trigger with event-by-event data acquisition system (DAQ) was employed. In section 3.3, the electrical circuits from the front end to the DAQ are introduced. The data analysis framework is explained in section 3.4. The summary of the data acquisition runs for the DALI2 γ-ray calibration and the physics experiments are listed in section 3.5.

3.1 Beam-line detectors

To achieve the particle identification based on the $B\rho-\Delta E-$TOF method on an event-by-event basis as explained in section 2.1.2, plastic (section 3.1.1), PPAC (section 3.1.2), and MUSIC (section 3.1.3) detectors were installed along the BigRIPS and ZeroDegree beamlines. The details about these detectors are described in this section.

3.1.1 Plastic scintillator

Four plastic scintillation counters [129] were installed at F3, F7, F8, and F11 to obtain the Time-of-Flight (TOF) of the particles. The surface area of each scintillator was 120 mm height times 100 mm width. Their thicknesses were 0.2 mm for F3, F7, and F11 and 1.0 mm for F8[a)]. Two photomultiplier tubes (PMTs) were attached on the left and right side of each scintillator. The high voltage setting of each PMT was set between 1700-2000 V by adjusting each signal height to a few hundred mV. To recover the deterioration of the timing resolution, caused by the walk-effect, or slew-effect in other words, on the leading edge discriminator for low amplitude signals of the PMTs, the charge values of the signals were recorded in addition to the timing of the pulse of the discriminator. The timing of the passage of the particle through each plastic scintillator, T_{ave}, is defined by the average of the timings of both left and right PMTs' signal.

$$T_{ave} = \frac{T_L + T_R}{2}. \tag{3.1}$$

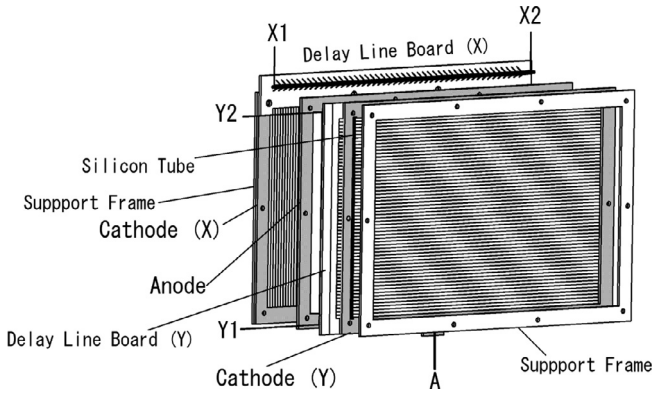

Fig. 3.1: Schematic view of the 240 × 150 mm PPAC detector. The figure is taken from [133].

3.1.2 PPAC

Several position-sensitive Parallel Plate Avalanche Counters (PPACs) were used in the experiment to deteremine the x, y positions and the angles a, b at four achromatic foci, F3, F7, F8, and F11, and two dispersive foci, F5 and F9. A schematic view of a PPAC detector is shown in Fig. 3.1, which is taken from Ref [133]. In order to cover a wide area of the dispersive foci, PPACs with 240 × 150 mm acceptance area were used. There are four cathode outputs, named X1, X2, Y1, and Y2 which are connected to the delay lines to determine the position by constant-fraction-discriminators (CFD) and multi-hit time-to-digital converters (TDCs) by the equation below:

$$X = \alpha \times (T_{X1} - T_{X2}) + X_{\mathrm{off}}, \tag{3.2}$$

where the α (mm/ns) is the position coefficient, which is determined by the delay lines, and X_{off} is the position offset, which was calibrated with an alpha source prior to the experiment. No anode output was used.

At each focal plane, two sets of double PPAC detector were used. In one double PPAC, two PPACs, A and B, from upstream of the beamline were packed in one box to improve detection efficiencies. Two double PPACs were placed in a certain distance in the camber of the focal plane to determine the X and Y angles A and B. To reconstruct the momenta of the particles, the X-position and X-angle (A) are necessary for each focal plane, while Y-position and Y-angle (B) are not used for the higher order optical corrections. In this work, to obtain highest efficiencies, only X and A information were used. If at least one of both upstream and downstream PPAC of the focal plane was above the threshold of their discriminators, the event was accepted.

3.1.3 MUSIC

In order to obtain the atomic number Z of nuclei passing through the BigRIPS and ZeroDegree spectrometers, their energy loss was measured by a multi-sampling ionization chamber (MUSIC) [128, 134] located at the end of each spectrometer, F7 and F11. The ionization chamber was filled by P10 gas with a mixture ratio of Ar:CH_4=90:10. As shown in Fig. 3.2, the detector consisted of 24 stacked parallel plate ionization chambers with alternately located cathodes and anodes. The bias voltage was set to 500 V, and applied to all anode electrodes. The signals

[a] In principle, thinner plastic is better to avoid energy loss of the partice, but from the requirement from other practical issue, 1.0 mm was used for F8.

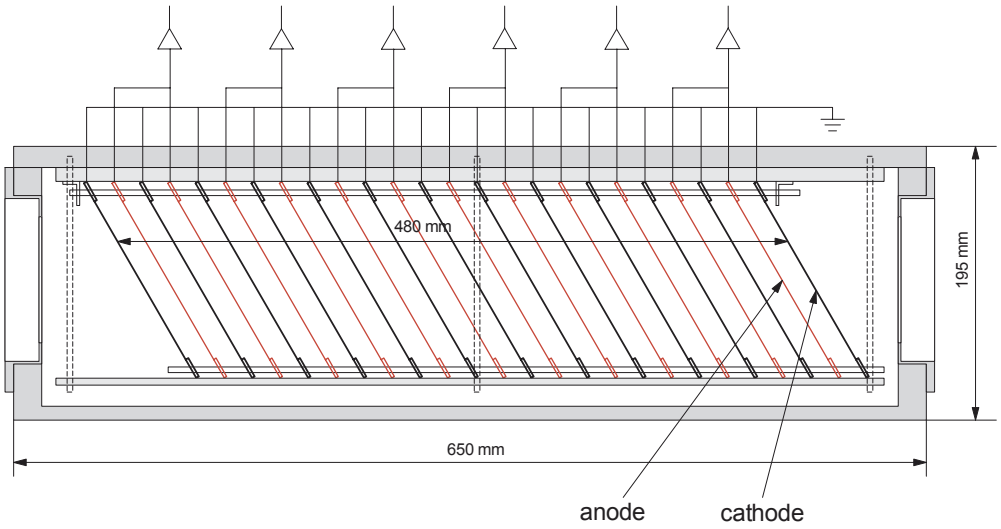

Fig. 3.2: View of the MUSIC detector. The figure is taken from Ref. [134].

from six preamplifiers attached for each two anode electrodes were amplified by six shaping amplifiers and the pulse height were recorded. The geometric average of them was taken as the ΔE in the analysis:

$$\Delta E = \alpha \times \left(\prod_{i=0}^{N} (ADC_i - c_i) \right)^{\frac{1}{N}}. \tag{3.3}$$

Here, N, α, and c_i are the number of the channels with a certain threshold determined in the analysis code, calibration coefficient, and the offsets of the ADC values, ADC_i. Because the typical drift time of the electron was several 100 ns, the shaping time was set to 1-2 μs, which can cause some pile-up events for high rate beam experiment from around 100 kHz. In this experiment, the beam rate was less than 10 kHz. Therefore, there were less than 1% of pile-up events.

3.2 Detectors for the secondary reactions: MINOS and DALI2

The secondary beams selected by BigRIPS were guided into ZeroDegree, and the secondary reaction took place at the first achromatic focal plane F8. The MINOS system [123, 124], which consisted of a 102(1) mm thick liquid hydrogen target and a Time Projection Chamber (TPC), was set at the focal plane as a secondary target with an ability to reconstruct the reaction vertices with a resolution of 2 mm(σ). Figure 3.3 is a schematic chart of the vertex reconstruction with the MINOS system [123, 124]. For detailed descriptions of the apparatus, see the caption of the figure and the reference papers. Around the MINOS system, DALI2 [125, 126], an array composed of 186 NaI(Tl) detectors covering polar angles from 12° to 96° degrees, was placed to detect de-excitation γ rays. Details of each device are described in the following sections.

3.2.1 Liquid hydrogen secondary target MINOS

Several factors should be considered in the selection of the thickness and material of the secondary target: Reaction luminosity, energy loss of the beam, and energy resolution of the γ-ray detector. Since the reaction rate of populating the excited states ^{78}Ni was expected to be small,

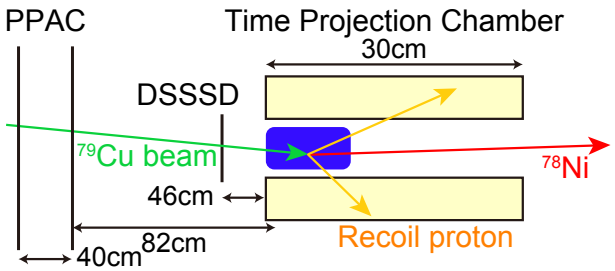

Fig. 3.3: Schematic picture of vertex reconstruction with MINOS. A 10 cm-thick liquid hydrogen secondary target located in the MINOS TPC chamber was connected to the cryostat module installed backward of the detector system (not drawn) [123, 124]. The green and red arrows show the secondary beam from BigRIPS, in this case ^{79}Cu, and the reaction residue heading to the ZeroDegree spectrometer, respectively. After the $(p,2p)$, $(p,3p)$, or other fragmentation reactions, protons recoiling from the target penetrate into the TPC, shown as yellow arrows in the figure. Then, the protons ionize the gas in the TPC chamber along their tracks. An electric field $\vec{E}$ in the chamber was applied to collect the drifting electrons with a certain drift velocity. At the end of the TPC chamber is a micromegas detector (not drawn) to amplify the electrons to produce signal outputs. Following the amplification process, the electrical signals were read with segmented electrodes to determine the position projected on the detector plane. To allow for vertex reconstruction with only one reconstructed track, a DSSSD, installed at the upstream of the target, and the PPACs at the F8 focal plane were also used. The scheme of the vertex reconstruction is described in the text.

thick target was favored to achieve a high reaction luminosity. See section 2.2.3 for the discussions of the selection of the target material. In this experiment, a 102(1) mm thick liquid hydrogen target was used, where the beam energy at the exit of the target is expected to be around 185 MeV/u with 250 MeV/u beam at the entrance. A TPC was installed to reconstruct the vertex position, which improved the energy resolution of the γ-ray spectrometer. This technique is explained in the next section.

3.2.2 Vertex reconstruction system: Time Projection Chamber, DSSSD, and PPAC

In Fig. 3.3, the vertex reconstruction scheme is illustrated. When the proton knockout reaction occurs in the liquid hydrogen target, recoil proton and knockout proton(s) penetrate into the TPC. Electrons, which are generated by ionization of the gas in the TPC along the tracks of the protons, drift due to the applied electric field in the chamber. At the end of the chamber, the free electrons are amplified and collected by the meshed electron multiplier and segmented anode electrodes, micromegas [123, 124]. The obtained signal for each pad of electrode is recorded by the GET based flash ADC. From the timing and charge information, the trajectory of each proton is reconstructed. When two or more tracks of the protons are recognized by TPC analysis, the vertex position of the reaction is determined by the closest point of these tracks.

In case only one proton track is reconstructed, the trajectory of the incoming beam is used. To acquire the track of the beam, a double-sided silicon strip detector (DSSSD), located at the entrance of the liquid hydrogen chamber, and the PPAC detectors, installed at F8 focal plane, were utilized (see also Fig. 3.3). Because the DSSSD was located closer to the target, the position information of the DSSSD was used with the average positon of PPAC detectors.

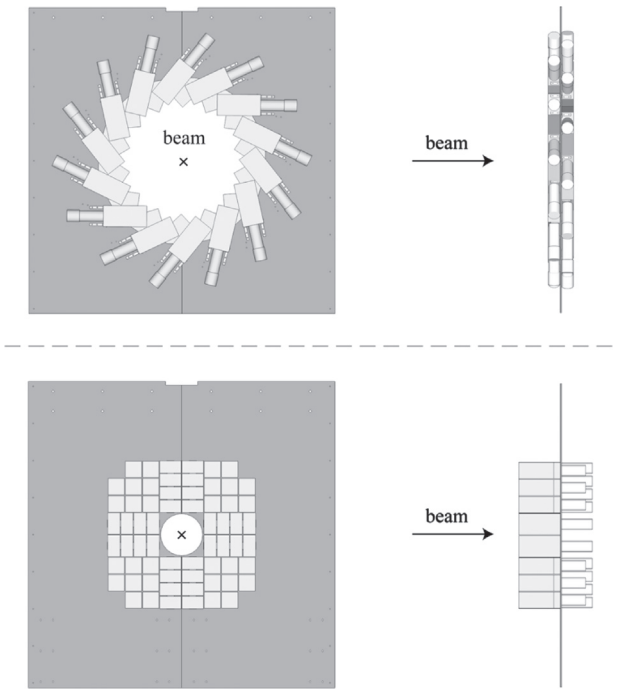

Fig. 3.4: Layout of the DALI2 layers. The upper figure shows the configuration of the DALI2 layers upstream, which surrounds the target chamber and the TPC. The configuration of the most downstream layer is called "wall configuration" which consists of crystals packed closely to get high efficiency for the Doppler boosted γ rays for forward angles, as shown at the bottom of the figure. These figures are taken from Ref. [125].

3.2.3 γ-ray detection and the Doppler correction with DALI2

The DALI2 γ-ray detector array [125] was surrounding the TPC chamber of the MINOS system. The array was composed of three types of the NaI(Tl) scintillators: 66 scintillators with $40 \times 80 \times 160$ mm^3 manufactured by Scionix, 88 scintillators with $45 \times 80 \times 160$ mm^3 manufactured by Saint-Gobain, and 32 scintillators with $60 \times 60 \times 120$ mm^3 manufactured by Bicron (Saint-Gobain now). The former two types of crystals were coupled with 38$-$mmΦ Hamamatsu R580 photomultipliers, and the latter one was coupled with 50$-$mmΦ Hamamatsu R1306 photomultipliers. Each crystal was covered by 1-mm thick aluminum housing. The detector array consisted of 11 detector layers located within the limited space between the cryostat duct of the MINOS target system and the superconducting quadrupole magnet (STQ17) of the ZeroDegree spectrometer. Figure 3.4 shows the configurations of the layers. As for forward angle detectors γ-ray energies were due to the Doppler boost, the most downstream detectors were aligned parallel to the beam direction consisting of a layer with a "wall" configuration. The other 10 layers surrounded the target chamber and the TPC with a circular formation.

Before the experiment, high voltage settings for the photomultipliers were adjusted to make the dynamic range up to 10 MeV (in the lab frame). Because the ADC can accept input signals up to 8 V, the signal heights after the shaping amplifier, with coarse gain set to 32 and shaping time of 3 μs, were adjusted to roughly 1 V with a ^{60}Co standard source by oscilloscope by eye. The explanations of the electronic circuits are written in the following section.

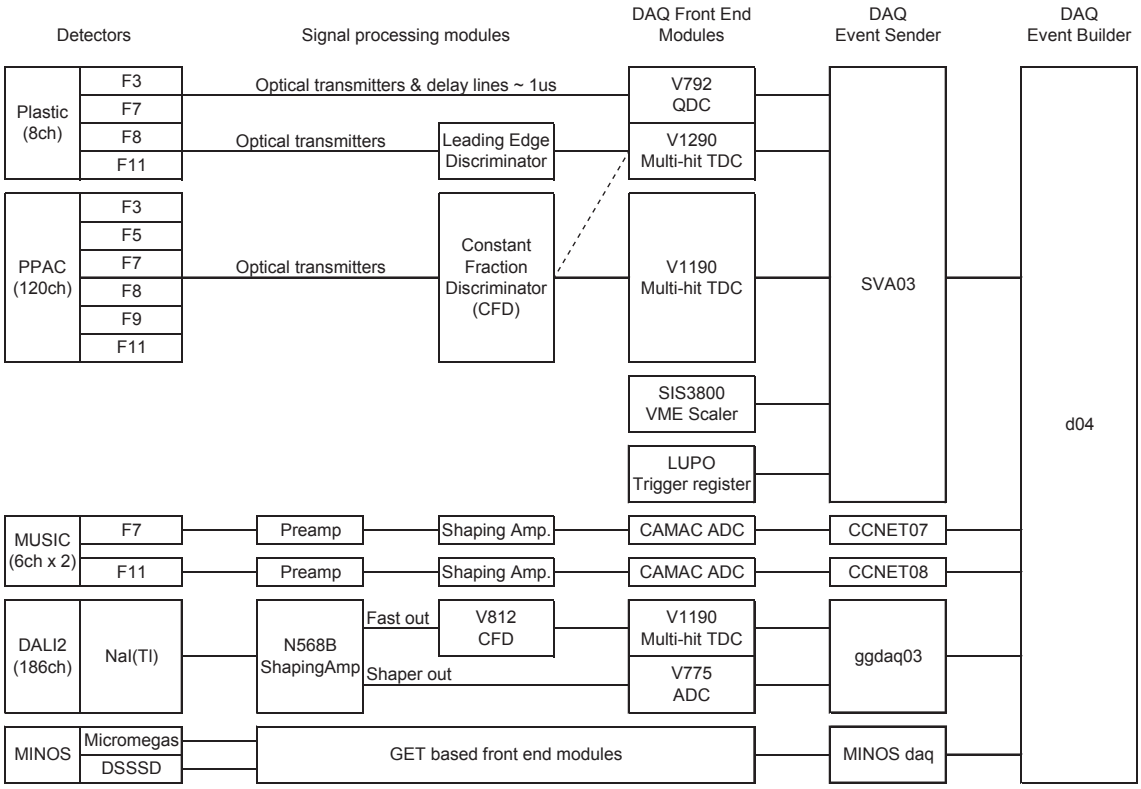

Fig. 3.5: Chart of the signal processing circuits and data acquisition modules. The detectors and the data acquisition modules which were used during the data runs are shown. See text for the detailed explanations.

3.3 Peripheral equipments

In this section, peripheral electrical circuits: Data acquisition system (section 3.3.1), trigger circuit (section 3.3.2), and scaler (section 3.3.3) are explained.

3.3.1 Detectors and data acquisition system

Figure 3.5 displays the scheme of the signal processing circuits and data acquisition modules. The RIBF standard data acquisition system, RIBFDAQ [131, 132], was used. Signals from the detectors were converted into the digital values by several analog-to-digital converters (ADCs) and merged with five DAQ fragments named as SVA03, CCNET07, CCNET08, ggdaq03, and MINOS daq, event-by-event sharing a common trigger for all frangments. SVA03 was the VME-based controller module assigned for the beam-line detectors, except MUSIC, trigger informations, and VME scaler. It was placed at the counting room to enable users monitoring and modifying the analog signals with radioactive beams. CCNET07 and CCNET08 were the CAMAC-based controller modules specified for the MUSIC detectors at F7 (BigRIPS) and F11 (ZeroDegree), respectively. ggdaq03 was the VME-based controller module assigned for the DALI2 γ-ray detector. MINOS-daq was the newly implemented DAQ module at this experiment, designed for the data acquisition of the MINOS-TPC and the double-sided silicon strip detector (DSSSD). All the data were sent to and stored in the event-building server, d04, via ethernet.

Plastic detector There were in total eight channels from the four plastic detectors with two PMTs on the left and the right sides, placed at F3, F7, F8, and F11. The analog signals were converted into the amplitudes of the light and transmitted with optical fibers to the counting room [133, 135]. Then, the signals were splitted into two circuits: Charge sensitive analog-to-digital converters (QDCs) and leading-edge discriminators followed by multi-hit time-to-digital converters (TDCs). Because the timing resolution of the plastic detectors was important for the particle identification, the CAEN's V1290 module, which has typically 35 ps intrinsic resolution, was used.

PPAC All of the analog signals were transmitted to the counting room with optical fibers [133, 135]. The timing of the signal was determined by the constant fraction discriminators (CFDs). As each PPAC module had five outputs (X1, X2, Y1, Y2, Anode), there were $4 \times 6 \times 5 = 120$ channels in total to be acquired. The typical rise-time of the PPAC signal was not as fast as the plastic scintillator. Therefore, other than the remaining channels of the V1290, which was used for the plastic detector, CAEN's V1190, a high-density (128 channels) multi-hit TDC module was used. Amplitude signals were not recorded.

MUSIC Each MUSIC chamber had six electrodes to readout. These signals were amplified by pre-amps and shaping amplifiers channel-by-channel and read by an ADC in CAMAC with the CCNET controllers [132] placed at F7 and F11.

DALI2 DALI2 consisted of 186 NaI(Tl) scintillator modules and photomultiplier tubes followed by NIM based shaping amplifier modules, N568B [125]. The fast outputs from the amplifiers were transmitted to the VME based CFD module, V812. Because the gamma-trigger, which created at least one output among the CFDs, was used in a coincidence gate with the beam-trigger, it was important to reduce the background events by optimizing the threshold energy of the NaI(Tl) scintillators. During the experiment, the threshold energy was set around 150 keV in the laboratory frame. The amplitude of the shaped outputs from the amplifiers were converted by V785 ADC with the dynamic range set to around 10 MeV in the lab-frame, which corresponds to 5 MeV in the rest-frame of the nuclei for the most forward detectors. To reduce the data size transmitted to the event builder, the channels, with their signals under the set threshold of the CFD, were recognized as pedestal events and discarded by the threshold of ADC. ggdaq03 was also used in a stand-alone mode to make γ-ray energy calibrations with standard sources. The trigger source was selected with FPGA based trigger selecting VME module, called LUPO (Logic Unit for Programmable Operation) DAQ master, and the events were stored and analyzed by the local computers placed next to the DALI2 detector [132].

MINOS and DSSSD The pulse-shapes obtained by the micromegas electrodes of the MINOS TPC and that of the DSSSD were digitized by GET modules (general electronics for TPC) [123, 124]. Because the drift time of the electron from the far end of the TPC to the micromegas electrode was expected to be not more than 10 μs, 512 points of the pulse-shape were reconstructed with a sampling rate of 50 MHz. By setting the threshold of the signal height for each channel, the pulse-shapes with a certain charge deposit were recorded in the temporal memory of MINOS-daq. This process was executed channel-by-channel at the time of the arrival of the signal, independently to the main DAQ system. Only when the trigger, which is discussed in detail in the next section, invokes the MINOS-daq, the pulse-shapes recorded within a specified range of time-window are sent to the event builder server [131].

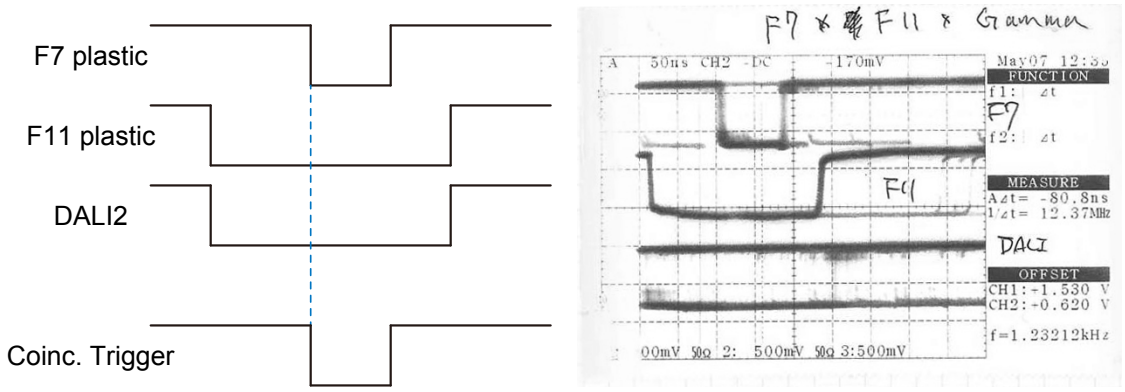

Fig. 3.6: Timing alignment of the trigger sources. As the timing of coincidence trigger was determined with reference to the F7 plastic timing as the scheme shown in the left figure. Delays were adjusted to make the trigger sources of F11 plastic and DALI2 (Gamma) arrive earlier than the F7 plastic signal. The right figure is a screenshot of the oscilloscope to check the timings. The procedure for adjusting the timings is described in the text.

3.3.2 Trigger

As discussed in section 3.3.1, the DAQ worked on an event-by-event basis with a common trigger. Triggers were organized by a FPGA based dedicated module, GTO (General Trigger Operator), with common dead-time for all the DAQ fragments [132]. The module could pick-up several trigger fragments with an OR gate and accepted the next trigger only when all the End of Busy (EOB) signals from each DAQ fragment had arrived.

The trigger consisted during the physics run of two trigger fragments, one was the main trigger, F7 × F11 × γ, and the other was the beam trigger, DSF7 (Down-scaled F7). The former one was created with a NIM-based coincidence module of Technoland Corporation by requiring triple-coincidence. To align the timings of F11 plastic and DALI2 (γ) with reference to the timing of the PMT on the left side of the F7 plastic, the timing of the coincidence was determined by the F7 signal by arranging the delays of each signal illustrated in the chart, Fig. 3.6. Firstly, the delay of DALI2 was adjusted relative to the F7 timing by putting a thick material, in this case the MINOS target, to generate sufficient amount of prompt γ rays to visualize the signal in the oscilloscope. Then, the target was emptied to guide the beam to the end of the beam line, F11, to align with the timings of the F11 trigger source. The screenshot of the oscilloscope during the time adjustment is shown in the right panel of Fig. 3.6. The latter trigger fragment, DSF7, which was essential for the cross section measurements, was created by a down-scaling module of Fuji Diamond International Co., Ltd. The down-scale factor was set from 20 (until run 242) to 40 (from run 243) to reduce the dead-time of the DAQ during the experiment. Trigger fragments of F7 × F11 and 1 kHz clock signal were also prepared for some purposes such as maintenance or tuning during the beam time.

Several trigger fragments were used during the experiment, depending on the purpose. To identify each event with trigger sources, the condition of the trigger fragments was recorded as a binary number by a dedicated input register, “coincidence register”. Table 3.1 shows the list and the registered number of each trigger fragment bit. For the case of two or more trigger fragments are produced simultaneously, respective bits are recorded, which can be regarded as summed number of them. In the table, examples of the DSF7 trigger and F7 × F11 × γ cases are described also.

Tab. 3.1: Trigger fragments and the configuration of the coincidence register. Each trigger fragment was registered as a binary number by a dedicated input register, "coincidence register" to mark the event with trigger sources.

Trigger name	Registered number
Accepted trigger	1 (2^0)
F7 × F11 × γ	2 (2^1)
Down-scaled F7	4 (2^2)
F7 × F11	8 (2^3)
Triggered by DSF7	5, 13 or 15
Triggered by F7 × F11 × γ	11 or 15

3.3.3 Scaler

The VME based 32-channel 32-bit scaler (counter) SIS38000 was installed at SVA03 DAQ. Table 3.2 shows the assignment of the connections of the inputs. An 1 kHz clock pulse was inserted as a reference of time to calculate the count rates of other channels. The numbers of the scaler values were cleared at every beginning of the data runs, and the DAQ system read the values automatically with a certain interval to monitor the detectors on-line. At the end of the run, the final counts were recorded. The last two rows of Tab. 3.2 show the summed counts and the averaged count rates during the runs for ^{78}Ni physics measurement, from run 211 to run 355 (see section 3.5.1 for the run summary).

3.4 Data analysis framework

Data were taken by the RIBFDAQ system as written in section 3.3.1. All the digital converted data were accumulated and stored event-by-event in the event building server with a specified data format called RIDF (RIBF data format). This RIBFDAQ and RIDF system also allowed the on-line analysis to check and monitor the beam status and the detectors. The data accumulation rate was roughly 10 GB/hour with a 500 Hz trigger rate. Because the RIDF files were raw data files, which included lots of header information and data from the unused detectors, it was not convenient to analyze data directly from RIDF format. As the ROOT [136] framework is commonly used for the nuclear and particle experimentalists for the data analysis, the decoder named ANAROOT [137], which converted and calibrated the raw signal to the physics values to the ROOT tree, was used. LISE++ [138] was used to simulate the particle trajectory along the beamline. Also the Monte Carlo simulation toolkit, GEANT4 [139–141] was used in the analysis to simulate the response function of the DALI2 γ-ray detector. See details in chapter 4 for the analysis descriptions.

3.5 Summary of data sets

3.5.1 Beam experiments

[i] ^{79}Cu was centered in BigRIPS and ZeroDegree.
[ii] Filled target run with ^{79}Cu centered in BigRIPS and ^{79}Cu centered in ZeroDegree.
[iii] From run 234, the energy threshold of DALI2 changed from 100 mV (~200 keV) to 75 mV (~150 keV).

Tab. 3.2: Configurations and summed counts of the 32 channel SIS3800 VME scaler module installed at SVA03. Values are summed from run 211 to run 355.

Channel	Description	Total counts	Rate (Hz)
0	Ungated trigger	2.075E+08	459.6
1	Gated trigger	1.884E+08	417.3
2	F3 Plastic Left	4.967E+09	11000.9
3	F3 Plastic Right	4.631E+09	10256.2
4	F7 Plastic Left	2.680E+09	5935.1
5	F7 Plastic Right	2.734E+09	6054.7
6	F8 Plastic Left	2.671E+09	5914.7
7	F8 Plastic Right	2.664E+09	5899.1
8	F11 Plastic Left	2.425E+08	537.0
9	F11 Plastic Right	2.436E+08	539.4
10	F3 Plastic	3.834E+09	8491.7
11	F7 Plastic	2.676E+09	5925.6
12	F8 Plastic	2.660E+09	5891.4
13	F11 Plastic	2.404E+08	532.4
14	Down-scaled F7 Plastic	8.530E+07	188.9
15	F7 × F11	2.420E+08	535.9
16	Gamma	1.654E+10	36639.4
17	F7 × F11 × Gamma	1.259E+08	278.8
23	SVA03 End of Busy	1.884E+08	417.3
24	MINOS End of Busy	1.884E+08	417.3
25	DALI End of Busy	1.884E+08	417.3
26	CCNET07 End of Busy	1.884E+08	417.3
27	CCNET08 End of Busy	1.884E+08	417.3
30	Gated trigger	1.884E+08	417.3
31	1 kHz Clock	4.515E+08	1000.0

Tab. 3.3: Summary of the physics runs. During the data taking, the trigger conditions were changed. The fractions written in the brackets represents the set down-scale factors for the beam trigger gated by F7 plastic detector.

Run number	Start time	End time	Trigger	Purpose of the run(s)
147	May 7 11:31	May 7 11:40	F7(1/1)	Empty target run[i)]
148	May 7 12:06	May 7 12:25	F7(1/1)	Filled target run [i)]
149	May 7 12:32	May 7 13:41	F7(1/1)	Production estimation[ii)]
201	May 7 13:45	May 7 14:32	Physics + F7(1/20)	Production estimation[ii)]
210-242	May 7 17:48	May 8 22:31	Physics + F7(1/20)	Data taking[iii)]
243-355	May 8 22:31	May 13 9:04	Physics + F7(1/40)	Data taking

Tab. 3.4: List of the configurations of the magnets and slits. See the explanations in the text.

Run number	147	148	149-222	224-246[iii)]	247-355
F1 slits (mm)	-46.0, +64.2	-46.0, +64.2	-46.0, +64.2	-46.0, +64.2	-40.0, +64.2
F2 slits (mm)	±4.0	±4.0	±4.0	±4.0	±4.0
F5 slits (mm)	-120.0, +75.0	-120.0, +75.0	-120.0, +75.0	-120.0, +75.0	-120.0, +65.0
F7 slits (mm)	±70.0	±70.0	±70.0	±70.0	±70.0
$B\rho_{01}$ (Tm)	7.8920	7.8920	7.8920	7.8920	7.8920
$B\rho_{12,23}$ (Tm)	7.0362	7.0362	7.0362	7.0362	7.0362
$B\rho_{34,45}$ (Tm)	7.0543	7.0543	7.0543	7.0543	7.0543
$B\rho_{56,67}$ (Tm)	6.7992	6.7992	6.7992	6.7992	6.7992
$B\rho_{78}$ (Tm)	6.7306	6.7306	6.7306	6.7306	6.7306
$B\rho_{89}$ (Tm)	6.4500	5.4336	5.5213	5.6020	5.6020
$B\rho_{910,1011}$(Tm)	6.4347	5.4232	5.5111	5.5914	5.5914

Tab. 3.5: List of the standard γ-ray sources. 3 standard γ-ray sources were used. The intensities written in the table are the dated at May 1, 2014.

Source	Intensity (Bq)	Half-life	γ-ray energy (keV)
^{60}Co	5.1×10^4	5.27 y	1173.2, 1332.5
^{88}Y	1.1×10^5	106.6 d	898.04, 1836.1
^{137}Cs	7.5×10^3	30.08 y	661.66

The measurement was performed from May 7th to 13th, 2014, for 6 days, following experiments targeting the excited states of ^{66}Cr and ^{70,72}Fe. Table 3.3 summarizes the descriptions of every physics runs. During the data taking, the trigger conditions were changed. In the beginning, the data acquisition was aiming at deducing the transmission of the spectrometers with and without the liquid hydrogen target and estimating the production rates. To avoid any bias caused by trigger conditions, the beam trigger, which was F7 plastic without any down scaling, was used. After beam and detector tuning, from run 210 the data taking was performed with a physics trigger (F7 × F11 × γ) and down-scaled F7 beam trigger (DSF7), which was used for the inclusive cross section measurement. The fractions written in the brackets represent the set down-scale factors for the beam trigger gated by F7 plastic detector. From run 243, the down-scale factor was changed from 1/20 to 1/40 to reduce the trigger rate and the dead time of the DAQ. Table 3.4 provides the list of the configurations of each slit width and each magnetic rigidity $B\rho$ settings during the measurement. During run 223, the magnetic settings were shifted. Therefore, the data were not used for the analysis. Because of the count rate of ^{78}Ni was too small to optimize the magnetic fields along the ZeroDegree spectrometer, the center of ^{78}Ni was fine-tuned after the run 224 according to the accumulated statistics until run 222. From run 224, ^{78}Ni was almost centered in the ZeroDegree spectrometer. From run 247, the slits at the dispersive foci, F1 and F5, were narrowed to reduce the trigger rate from the contaminants in the secondary beam. The change increased contaminants mixed in the beam, which caused an increased trigger rate at F7. Therefore, to reduce the background events from the beam trigger, the down-scale factor was changed as described above.

Tab. 3.6: Summary of the γ-ray calibration runs for DALI2.

Run number	Start time	End time	γ-ray source	Physics runs
33, 35, 38	May 7 8:27	May 7 10:24	^{60}Co, ^{88}Y, ^{137}Cs	run 210-222
41	May 8 14:05	May 8 14:30	^{88}Y	run 224-246
43, 44	May 9 14:09	May 9 14:58	^{60}Co, ^{88}Y	run 247-270
46, 47	May 10 14:09	May 10 14:51	^{60}Co, ^{88}Y	run 271-300
50, 51	May 11 14:01	May 11 14:46	^{60}Co, ^{88}Y	run 301-324
54, 55	May 12 14:09	May 12 14:53	^{60}Co, ^{88}Y	run 325-346
57, 58, 59	May 13 10:15	May 13 11:45	^{60}Co, ^{88}Y, ^{137}Cs	run 347-355
61, 62, 63	May 14 15:28	May 14 17:00	^{60}Co, ^{88}Y, ^{137}Cs	Efficiency

3.5.2 DALI2 calibrations

During the beamtime, DALI2 was calibrated by several standard sources once per day. The sources were placed at the end of the secondary target chamber, close to the forward wall of the DALI2 crystal. In this experiment, the energy of the aimed γ-ray was 3 MeV, which corresponds up to 6 MeV in the most forward detectors. Table 3.5 is the list of the γ-ray sources used for the caribration runs. The intensities are also written in the table, which are dated at May 1 in 2014. Because ^{88}Y emits the highest energy among the γ rays, 1836.1 keV, and another energy at 898.04 keV, measurements were done at least with this source everyday. Table 3.6 summarizes the γ-ray calibration runs for DALI2. Because the radiation background from proton and neutron might cause a gain shift in the NaI(Tl) scintillators, the calibration run took place everyday. The table shows also the correspondence between the calibration runs and the physics runs.

Chapter 4

Data analysis

In this chapter, the calibration for each detector and the data analysis are described. In the following sections 4.1, 4.2, and 4.3, the calibration of the respective beamline detectors, the reconstruction of the particle identification, and the analysis of the DALI2 and MINOS devices are explained. To examine the validity of the Doppler correction employing the TPC of MINOS, the γ-ray spectra for ^{80}Zn were obtained with several conditions as a test case in section 4.4. The results and discussion of the obtained cross sections and γ-ray transitions are described in the next chapter.

4.1 Calibration of the beamline detectors

To identify the incoming and outgoing particles before and after the secondary target by means of the $B\rho - \Delta E -$ TOF method, the calibration of the respective beamline devices is necessary.

4.1.1 PPAC calibration

(1) δ-ray rejection in the PPACs

The elimination of contaminant events originating from δ rays in PPACs is important [133]. Recoil electrons produced by heavy ions traversing material along the beam path hit a PPAC detector, however, the position is irrelevant to the track. It is known that the energy deposit of δ rays in the PPAC is not negligible and a δ-ray hit causes misidentification in the PPAC detector. To avoid such events, a gate on the sum of the delay times, T_{sum} as defined below, was applied

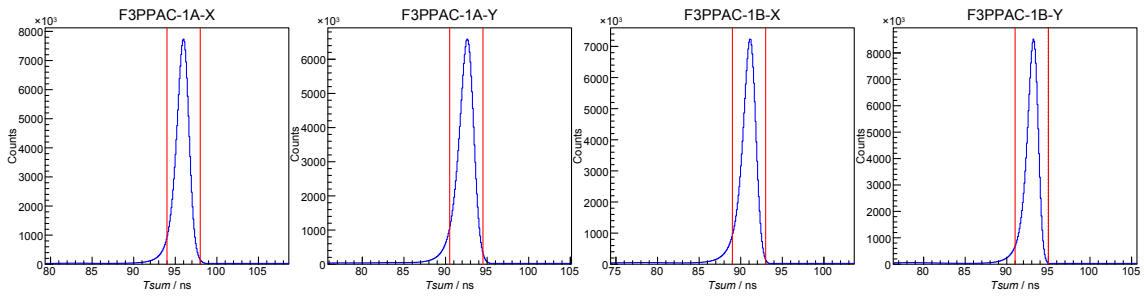

Fig. 4.1: Examples of T_{sum} of PPACs. The spectra of F3-1A and F3-1B PPACs with gates on T_{sum} are shown. The horizontal axes correspond to T_{sum} (ns) and the vertical axes are the number of counts.

Tab. 4.1: Measured PPAC efficiencies relative to the plastic detectors at F7 and F11. Values are given in %. The low value of the Y-position of the F5-2B PPAC might be caused by overlooking of the discriminator settings.

PPAC	1A (%)	1B (%)	2A (%)	2B (%)
F3X	88	89	93	91
F3Y	84	92	92	91
F5X	93	93	91	92
F5Y	92	93	89	4
F7X	90	91	92	88
F7Y	87	93	91	86
F8X	93	89	88	91
F8Y	92	92	89	51
F9X	94	89	93	88
F9Y	91	94	93	92
F11X	92	91	93	76
F11Y	82	91	91	85

for each PPAC:

$$T_{sum} \equiv T_{X1} + T_{X2}. \tag{4.1}$$

When only one particle hits the PPAC detector, T_{sum} will be a constant value, while T_{sum} becomes lower for a two- or multi-particle hit. To avoid multi-particle events including δ rays, the event selection with T_{sum} is important. Figure 4.1 shows examples of T_{sum} distributions of the F3-1A and F3-1B PPACs. Events satisfying the T_{sum} gate condition, which corresponds to the red lines, are accepted. The widths of the gates were set to around ±2 ns from the peak positions.

(2) PPAC efficiencies

Table 4.1 lists the efficiency for each PPAC detector in the ^{78}Ni settings after the evaluation of the T_{sum} gates. Here, the efficiency of the respective PPAC detector is defined as the ratio of counts in the PPAC relative to the counts of the plastic detectors at F7 and F11 under the assumption of the efficiencies that the plastic detectors are 100%. Because the Y information was not necessary to reconstruct the $B\rho$ or the momentum of the particle, only the efficiencies for the X direction were crucial for particle identification[a)]. Except for F11-2B, the efficiencies for the X direction were about 90% for each detector. As discussed in section 3.1.2, to determine the beam X-positon and X-angle (A), at least one each PPAC of both upstream (1A or 1B) and downstream (2A or 2B) detectors in each focal plane should have signal above threshold. If the efficiencies of the PPAACs are noted as ε_{1a}, ε_{1b}, ε_{2a}, andε_{2b}, the track reconstruction efficiency η is:

$$\eta = (1 - (1 - \varepsilon_{1a}) \times (1 - \varepsilon_{1b})) \times (1 - (1 - \varepsilon_{2a}) \times (1 - \varepsilon_{2b})).$$

For the case of each PPAC efficiency of $\varepsilon = 90\%$, the tracking efficiency in each focal plane, η, is calculated to be 98%, close to the ideal 100%. The F11 PPACs were not used in the particle identification, because the tracking efficiency for the F11 focus was slightly low.

[a)] While the values of Y-position and Y-angle were not used for the particle identification, the values in the F8 focal plane were used for the vertex reconstruction of the secondary reaction.

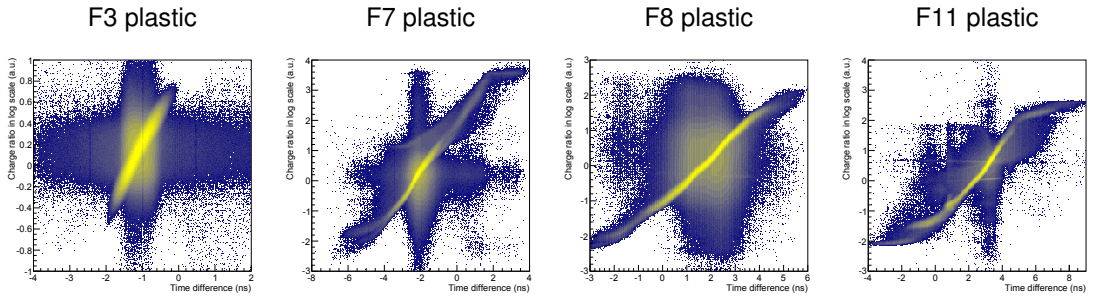

Fig. 4.2: Raw charge and timing values of the four plastic detectors. The relationship between the charge-ratios and time differences of F3, F7, F8, and F11, are shown from left to right panels. Horizontal axes ars the charge-ratios: $\log \frac{Q_L}{Q_R}$. Vertical axes are the time difference: $T_L - T_R$. Kinking structures are seen in F8 and F11 plastic which is caused by overrange events of the charge sensitive ADC (QDC). No event elimination was applied with the plastic detectors.

4.1.2 Plastic detectors: Charge ratio vs time difference

The plastic detectors, as described in section 3.1.1, were important to determine the time-of-flight of the particles. To measure the time accurately, there were two PMTs attached on the left and right sides of each plastic scintillator. As both the charge ratio, $\log \frac{Q_L}{Q_R}$, and the time difference, $T_L - T_R$, are known to be proportional to the X position of the particle hit in the plastic detector, the linear correlation between these values can be obtained to confirm the operation of the detectors [130]. Two dimensional plots of $\log \frac{Q_L}{Q_R}$ in the horizontal axis, and $T_L - T_R$ in the vertical axis of the respective plastic detectors F3, F7, F8, and F11 are presented in Fig. 4.2. The non linear structures seen in the F11 plastic are understood as overflow events in the charge-to-digital converter, QDC. Such overflow events are flagged in the 13^{th} bit of the output value of the V792 QDC [142]. While the charge values were not used for the particle identification in first order, these overrange events, occupying a few percent of the total events, were flagged, because the charge value was used in the second order correction of the walk-effect of the leading edge discriminators.

4.2 Particle identification

4.2.1 Procedures

Particle identification (PID) was performed based on the procedure explained in section 2.1.2, which is also detailed in Ref. [130]. The parameter which should be adjusted firstly is the time-offset of each plastic detector, which is important to reconstruct the time-of-flight. During the BigRIPS tuning of the experiment, which was mainly performed by the BigRIPS team, γ-ray transitions from several known isomers were measured to tag the incoming isotopes at F7 with a beam stopper and a HPGe γ-ray detector [129, 130]. The time offsets were adjusted by calibrating the measured mass-to-charge ratio, A/Q, with the isomer-tagged isotopes as references. The calibration coefficients of the ion chamber (MUSIC), which are necessary to deduce the atomic number, Z, were also adjusted to align the isomer-tagged isotopes to the correct Z value. The parameters for ZeroDegree were then adjusted using the PID of BigRIPS.

Figure 4.3 displays the PID plot of the radioactive beam accepted by the BigRIPS and ZeroDegree fragment separators. In this analysis, the $B\rho$ value was obtained with both F3-F5 and

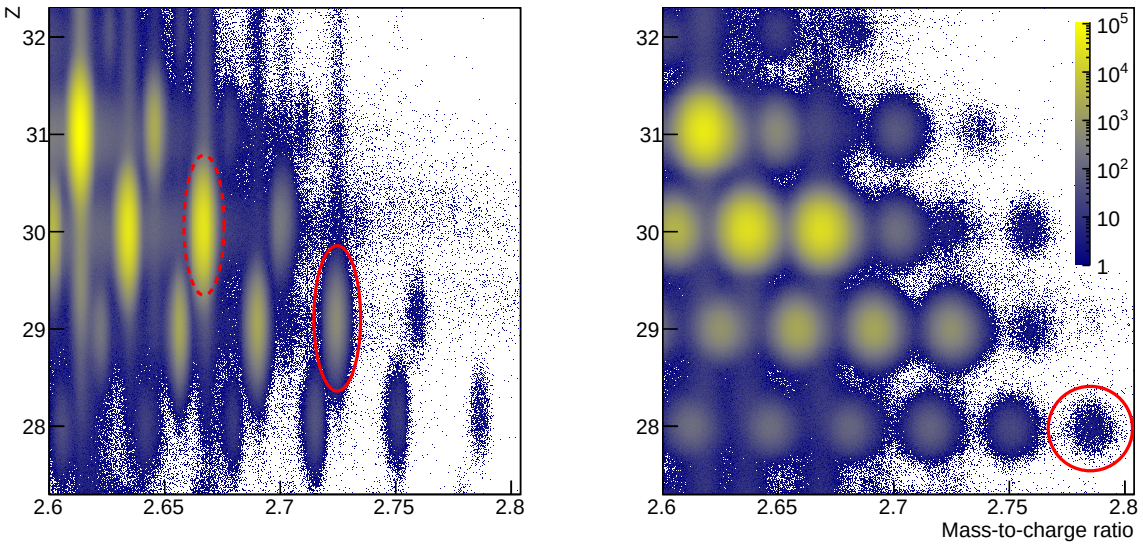

Fig. 4.3: Particle identification plot of the radioactive beam accepted by the BigRIPS and ZeroDegree fragment separators. In the left panel, the PID with BigRIPS is plotted, where events corresponding to ^{79}Cu and ^{80}Zn are enclosed by the red ellipse and red dashed ellipse, respectively. The PID plot of the ZeroDegree spectrometer, obtained by using the tracking information at F8 and F9, are shown in the right panel. A second order optical correction (explained in section 4.2.2) was applied to obtain a higher resolving power. Events corresponding to ^{78}Ni are enclosed by the red ellipse.

F5-F7 transfer matrixes to obtain higher resolution (see Ref. [130] for details) for the PID plot of BigRIPS. On the other hand, the $B\rho$ value of ZeroDegree was reconstructed only with a F8-F9 transfer matrix, which requires tracking information at F8X, F9X, and F9A and without the one of F11, because of the low tracking efficiency of the F11 PPACs (see section 4.1.1). This was crucial not to lose important events, as the significance can be seen in the number of counts for the same nuclei gated in the ZeroDegree PID. For example, the number of counts of ^{78}Ni in a certain measurement for an hour, run 355, were 48, 45, and 43 counts with the F8-F9, F9-F11, and F8-F9-F11 reconstructions, respectively. However, the $B\rho$ resolution in the ZeroDegree spectrometer is worse than the one in BigRIPS because of the smaller momentum dispersion and the lower time-of-flight resolution, which was determined by the shorter flight path of the ZeroDegree than the one of BigRIPS. Therefore, additional corrections to recover the degraded $B\rho$ resolution were essential. In the next section, the second order optical correction, which was applied to improve $B\rho$ resolution, is explained. Note that the PID plot of the ZeroDegree spectrometer utilizing both transfer matrixes, F8-F9 and F9-F11, which uses all the tracking information of F8, F9, and F11 are displayed in the appendix chapter, Fig. B.1. With this approach a much clearer separation than the one used in the actual analysis was achieved.

4.2.2 Optical correction

In this work, higher order optical corrections of the ion optical transfer matrix were applied to achieve better A/Q resolution for the ZeroDegree PID, while only first order ion optical transfer matrix elements were applied to the BigRIPS PID as introduced in section 2.1.2. Figure 4.4 shows the ZeroDegree particle identification plot before and after the second order optical corrections. As discussed in Eq. (2.3) and Eq. (2.6), the F8 to F9 reconstruction requires tracking information of F8X, F9X, and F9A for the ZeroDegree PID. Figure 4.4 shows an example of the optical corrections, in which left and right panels are shown without and with the correction up

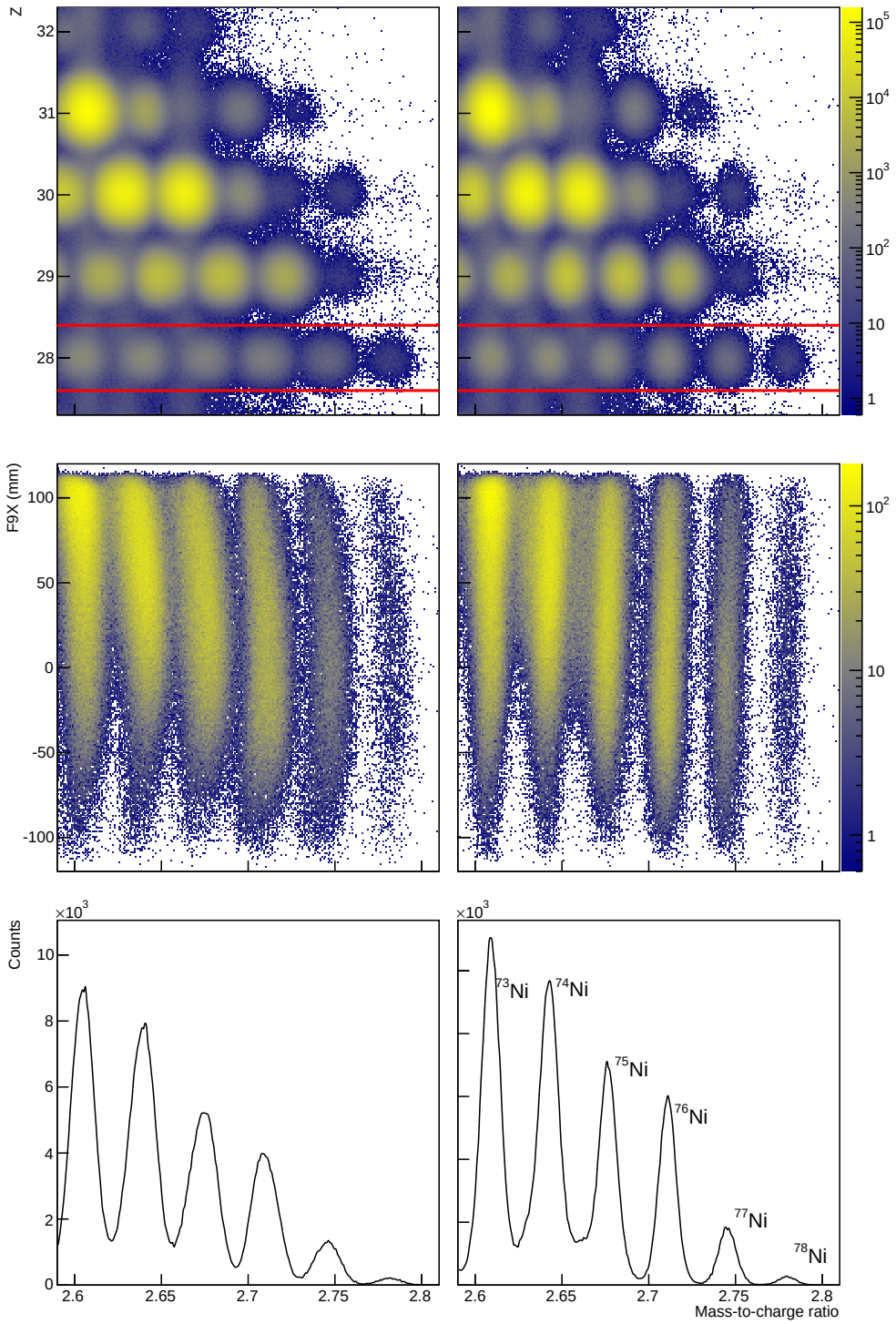

Fig. 4.4: Optical corrections for the ZeroDegree particle identification. Second order optical corrections were applied to improve the resolution of the mass-to-charge ratio, A/Q, of the PID plot obtained by using the tracking information at F8 and F9, as shown in the right panels. For a comparison, the PID plot with the 1st order reconstruction are shown in the left panels. The middle panels are the correlation between A/Q values and the F9X positions for the $Z = 28$ (Ni) condition, which is illustrated in the upper panels. The corrected and uncorrected A/Q distributions can be seen in the two bottom panels. The A/Q resolution of ^{78}Ni improved from 5.2σ to 6.3σ separations.

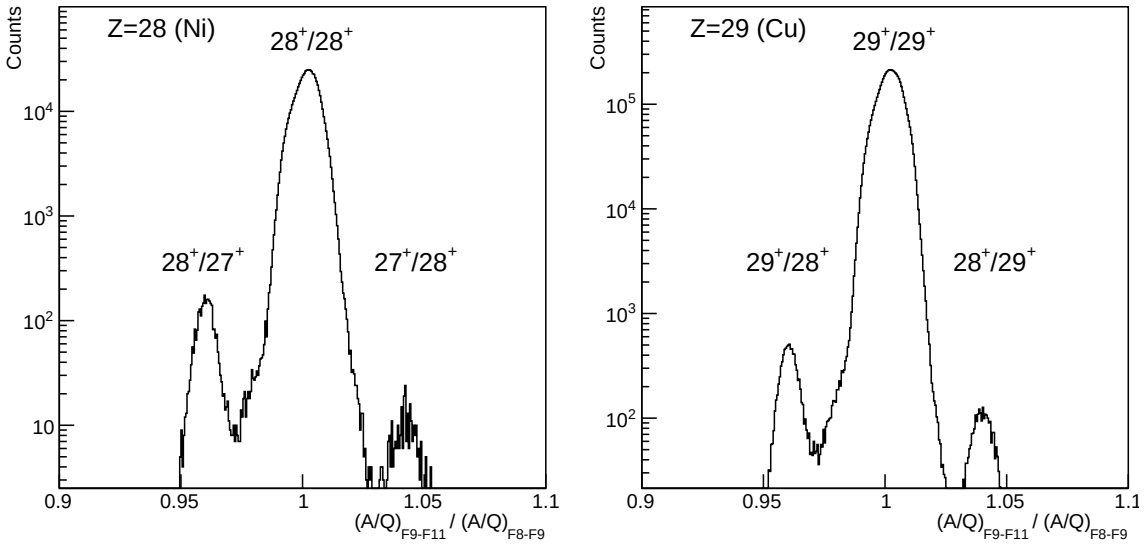

Fig. 4.5: Charge state contaminants in ZeroDegree. Ratios of A/Q values between the PIDs in F8-F9 and F9-F11 are displayed. The left figure shows the A/Q change for $Z = 28$ (Ni) isotopes, and the right one shows the one for $Z = 29$ (Cu) isotopes. For both distributions, a condition of $A/Q > 2.6$ was applied. When any reaction or charge state change occurs, the ratio of A/Q values is different from one. The left contaminant peak can be understood as a hydrogen-like state until F9, then fully stripped after F9, while the right peak is *vice versa*. Such A/Q changes are limited to less than 1% probability. Thus, no cut was applied in the analysis.

to second order. The middle panels are the A/Q trends for the $Z = 28$ (Ni) nuclei with respect to the F9X position shown on the vertical axes. Parabolic trends in all foci can be seen before the correction. The optical correction coefficients were obtained iteratively by checking each relationship among the positions, angles and the A/Q values to make the locus of ^{78}Ni as vertical as possible. As a result, the A/Q resolution of ^{78}Ni improved from 5.2σ to 6.3σ separations, defined as the ratio of the interval of the neighboring peaks divided by the peak width. The particle identification of F8-F9 reconstruction with second order optical corrections is used for the γ-ray spectroscopic analysis. On the other hand, for the cross section measurement (see section 5.1), the A/Q reconstruction with F8-F9-F11 was used because it allowed for a cleaner identification to eliminate cross contaminations of gates.

4.2.3 Charge state contaminants

Charge state contaminants in ZeroDegree were checked, as they can cause misidentification of particles. After passing through several detectors and a thick secondary target installed along the beamline, the remaining energy of the beam was only around 170 MeV/u at the exit of the target. Reaction residues at such low energies can easily pick up electrons from the target or detectors and thus not be in the fully stripped charge state anymore. For the ^{78}Ni case, a hydrogen-like ^{75}Ni^{27+} ($A/Q = 2.778$), which has a similar A/Q value to ^{78}Ni^{28+} ($A/Q = 2.786$), and it is difficult to distinguish them with the resolution of the spectrometer. To quantify the amount of the charge state contaminants, two measurements of the A/Q value from the F8-F9 and F9-F11 PIDs are compared and this confirmed that the charge state events are negligible (see Fig. 4.5). Along the beamline in the ZeroDegree spectrometer, the PPACs, filled with P10 gas and sealed with polyester films, installed at F9 were the only material, where charge state changes could occur. According to GLOBAL calculations [138, 143] implemented in the

Tab. 4.2: Numbers of isotopes in the beam. The PID gates with † marks were obtained using the down-scaled beam trigger, and others were recorded using the normal trigger, F7 × F11 × γ. The last four lines are the numbers of events with a condition on the vertex position reconstructed inside the MINOS target (see section 4.3.2). To obtain the real counts and rates, the down-scale factor and the DAQ live-time were taken into account.

Gate	Observed	Events (corrected)	Event rate (s^{-1})
BR(^{79}Cu)†	57,162	2.4×10^6	5.2
BR(^{80}Zn)†	3,149,940	1.3×10^8	290
ZD(^{78}Ni)†	179	7.6×10^3	1.6×10^{-2}
ZD(^{79}Cu)†	29,793	1.3×10^6	2.7
BR(^{79}Cu) ⊗ ZD(^{78}Ni)†	27	1.1×10^3	2.5×10^{-3}
BR(^{80}Zn) ⊗ ZD(^{78}Ni)†	21	8.9×10^2	1.9×10^{-3}
BR(^{79}Cu) ⊗ ZD(^{78}Ni) ⊗ γ	937	1.0×10^3	2.3×10^{-3}
BR(^{80}Zn) ⊗ ZD(^{78}Ni) ⊗ γ	815	8.9×10^2	2.0×10^{-3}
BR(^{79}Cu) ⊗ ZD(^{78}Ni) ⊗ γ ⊗ MINOS	811	8.9×10^2	2.0×10^{-3}
BR(^{80}Zn) ⊗ ZD(^{78}Ni) ⊗ γ ⊗ MINOS	636	7.0×10^2	1.6×10^{-3}
BR(^{79}Cu) ⊗ ZD(^{78}Ni) ⊗ $E_\gamma > 300$ keV	310	3.4×10^2	7.6×10^{-4}
BR(^{80}Zn) ⊗ ZD(^{78}Ni) ⊗ $E_\gamma > 300$ keV	222	2.4×10^2	5.4×10^{-4}

LISE++ toolkit, 99.7% of ^{78}Ni at an energy of 170 MeV/u remains fully stripped within the equilibrium charge states in carbon, which is the main component of polyester. When any reaction or charge state change occurs at F9, the A/Q value measured between F9 and F11 is different from the one between F8 and F9. Figure 4.5 shows the ratio of A/Q values between measured in F8-F9 and F9-F11 for $Z = 28$ (Ni) isotopes and $Z = 29$ (Cu) isotopes. It can be confirmed that the nuclei in most events do not change their charge states. As the charge state contaminant is negligibly small, no specific condition was applied to the chage state change in the later analysis.

4.2.4 Number of isotopes during the experiment

Table 4.2 lists the numbers of events in the beam with several gating conditions. The gates marked with † marks were obtained using the down-scaled beam trigger, and others were using the trigger F7 × F11 × γ. To obtain the real counts and rates, the down-scale factor[b)] and the DAQ live-time[c)] were taken into account. The number of events was obtained by fitting two dimensional Gaussian functions to PID plots shown in Fig. 4.3 and gated by an ellipse with 3.5σ for Z and A/Q axes for the γ-ray spectroscopy analysis as well as the counts in Tab. 4.2.

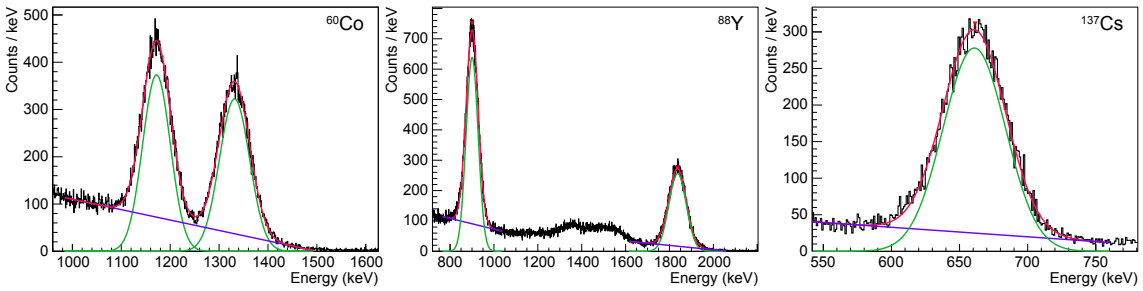

Fig. 4.6: Examples of the γ-ray spectra for three standard sources in the calibration runs of DALI2. Spectra (Detector ID:186) for the ^{60}Co, ^{88}Y, and ^{137}Cs souces are shown. All peaks are fitted with Gaussians (light green) and linear background functions (blue).

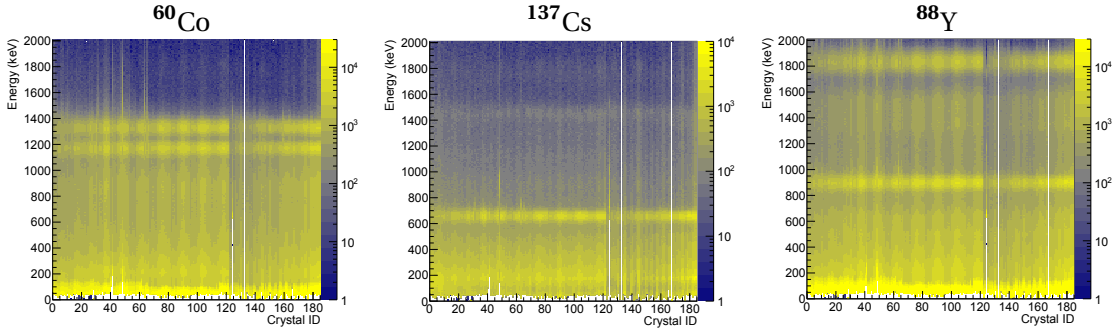

Fig. 4.7: Calibrated energy spectra of DALI2. Two dimensional plots, the calibrated energy versus the crystal ID, measured by three standard sources, ^{60}Co, ^{137}Cs, and ^{88}Y, are shown from the left to the right panels, respectively.

4.3 Calibration for the secondary reactions

4.3.1 DALI2

(1) Energy calibration with standard sources

The energy spectra of DALI2 obtained with γ-ray standard sources during the energy calibration runs were fitted by Gaussian functions and linear functions as background. As summarized in section 3.5.2, three standard γ-ray sources, ^{60}Co, ^{88}Y, and ^{137}Cs were placed around the exit of the target chamber for the measurements. The examples of the spectra and the fits for these sources are shown in Fig. 4.6. While the spectrum of ^{60}Co was fitted with two Gaussian functions on top of a common linear background, the two γ-ray peaks of ^{88}Y were fitted separately as their energies are well separated. Figure 4.7 shows the summarized spectra in two dimensional plots, the calibrated energy versus the crystal ID, for the three source measurements. The separation between two neighboring peaks of ^{60}Co can be seen. All examples show the spectra taken just after the beam time, which are runs 57, 58, and 59 (see Tab. 3.6).

The energy calibration was performed for each crystal with a linear function, $E = a \cdot \mathrm{Ch} + b$, for each crystal using all measured peak positions in ADC channels, Ch, taken from the centroid of the fitted Gaussian. An example of the energy calibration of DALI2 and the distribution of the discrepancy of the calibrated energy from the γ-ray energy is shown in Fig. 4.8.

(2) Linearity of the calibration

The γ-ray transitions of interest were up to around 3 MeV in the ejectile rest frame, which corresponds to 6 MeV in the laboratory frame for the forward-angle detectors. It was therefore important to ensure the linearity of the response of the DALI detectors up to high γ-ray energies. The calibration residuals in Fig. 4.8 show roughly a 5 keV uncertainty in the region up to 2 MeV. Another test was performed with the 2615-keV γ-ray from natural radiation from the β-decay of ^{208}Tl to ^{208}Pb, shown in Fig. 4.9. This spectrum was obtained from the calibration run with a ^{60}Co source immediately after the beam experiment. From the fitting with Gaussian and exponential functions, the peak position was deduced at 2600(2) keV. The discrepancy with the known energy, 2615 keV, amounts to 0.6%, which is larger than that of standard sources shown in the bottom right of Fig. 4.8. It is important to note that the signal-to-noise ratio of the peak is not as good as the peaks obtained using the standard γ-ray sources because there are many sources of background in the spectrum. Also, the peak position of the 2615-keV γ rays can be shifted for another reason that the response of the detectors is rather position dependent; in this case the 2615-keV γ rays shine from the back into the crystal, while the γ rays of interest are from the front. Thus, the discrepancy of 0.6% was estimated as the upper limit of the systematic error from the linearity of the γ-ray spectrometer.

(3) Energy resolution

An evaluation of the resolution of the DALI2 array as function of energy is necessary to create simulated γ-ray response functions in the GEANT4 Monte-Carlo simulation framework [139–141]. Figure 4.10 shows the measured energy resolution of the individual NaI(Tl) crystals of DALI2 with three standard γ-ray sources. The energy resolution, ΔE, for each NaI(Tl) crystal

[b] As summarized in Tab. 3.3, the setting of the DSF was changed from 1/20 to 1/40 during the beamtime. The averaged value is DSF = 38.6 as calculated in Eq. (5.32) discussed in section 5.5.

[c] The live-time was 90.8% as the ratio of the numbers of the gated and ungated trigger counts listed in Tab. 3.2.

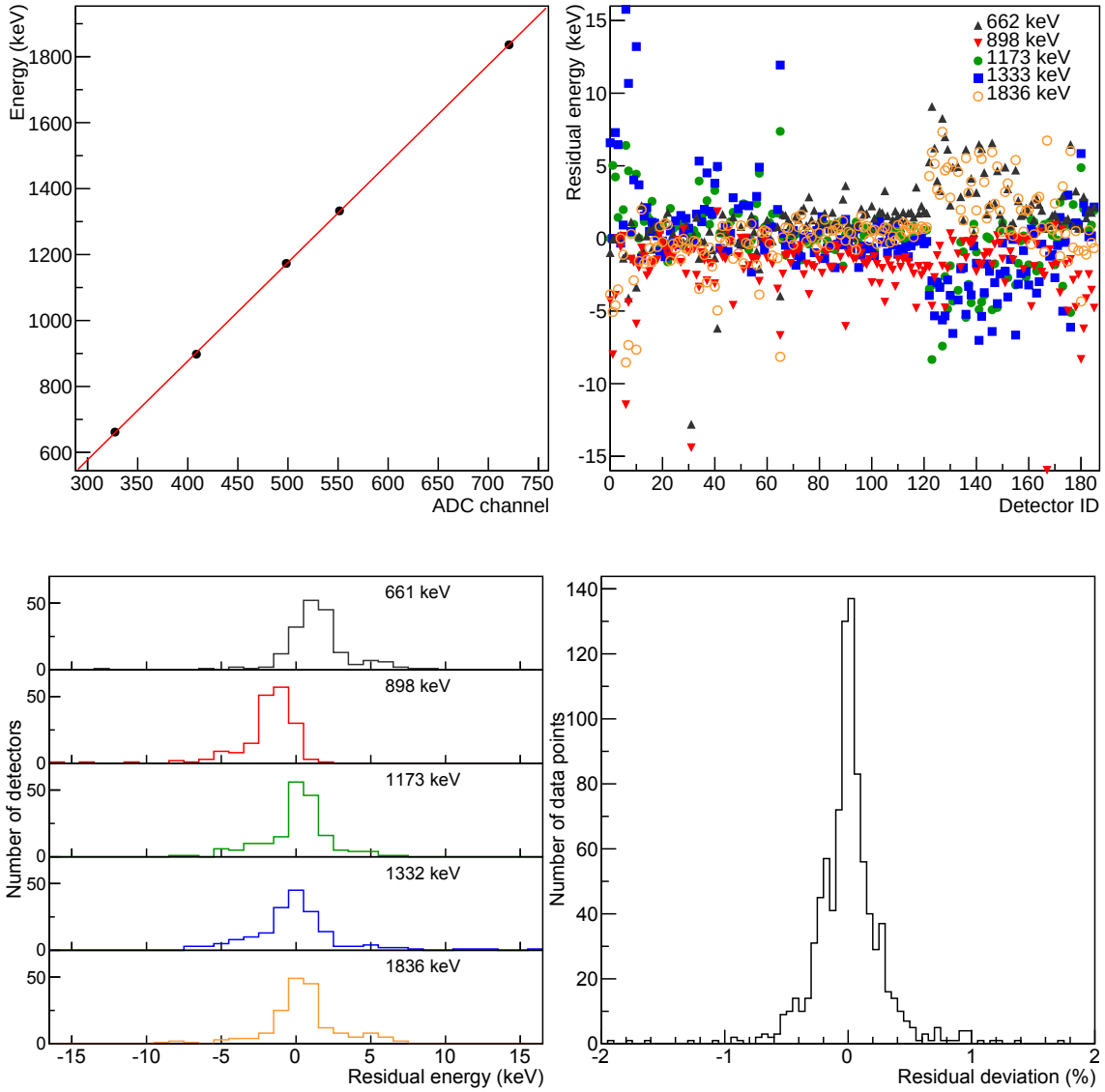

Fig. 4.8: Energy calibration of DALI2 and the distribution of residuals. Each scintillator of DALI2 was calibrated by a linear function as illustrated in the top left panel. The distribution of the energy residual after the calibration as plotted in the top right panel (distribution for each detector ID) and bottom left panel (histogram for respective peak energies) shows most of the detectors have energy residual withins a few keV. The relative residual deviation, the residual devided by the peak energy in %, is shown in the bottom right panel.

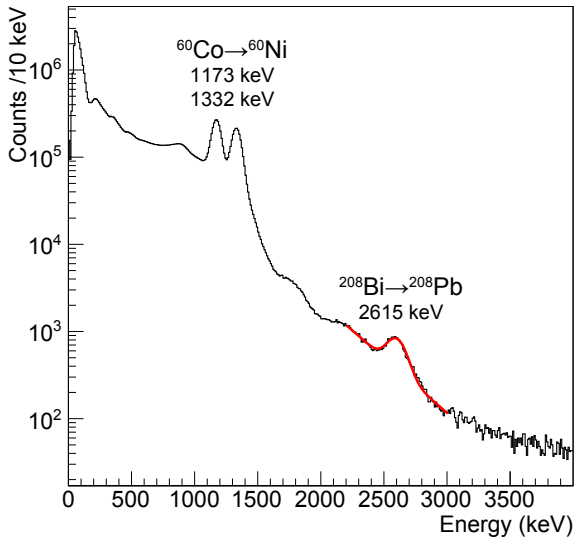

Fig. 4.9: DALI2 spectrum of a high energy transition from natural background. A spectrum of calibration measurement with ^{60}Co was used to check the linearity of the detector at high energy. The 2615 keV transition by β-decay of ^{208}Tl to ^{208}Pb is fitted with Gaussian and exponential function.

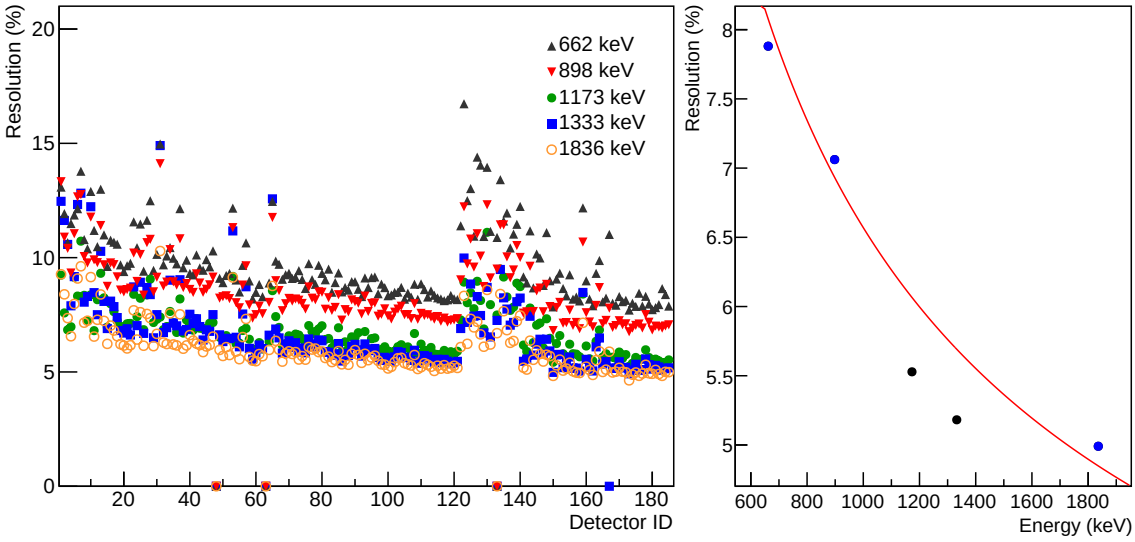

Fig. 4.10: Measured energy resolutions of the NaI(Tl) crystals of DALI2. In the left panel, the energy resolution for each NaI(Tl) crystal ID is shown in FWHM. Note that four bad crystals, ID: 48, 63, 132, and 167 were removed from the analysis and other crystals with bad resolution were put far from the target: in the outer ring of the wall layer (starting from ID 122) or at backward layers (low ID numbers). The measured resolution of each crystal was fitted by a $\Delta E \propto 1/\sqrt{E}$ function, as displayed in the right panel. The two data points of ^{60}Co, which are plotted with black dots, were not used in the fit due to the ambiguity of the background estimation of the spectra can cause an underestimation of the energy resolution. See text for the discussion.

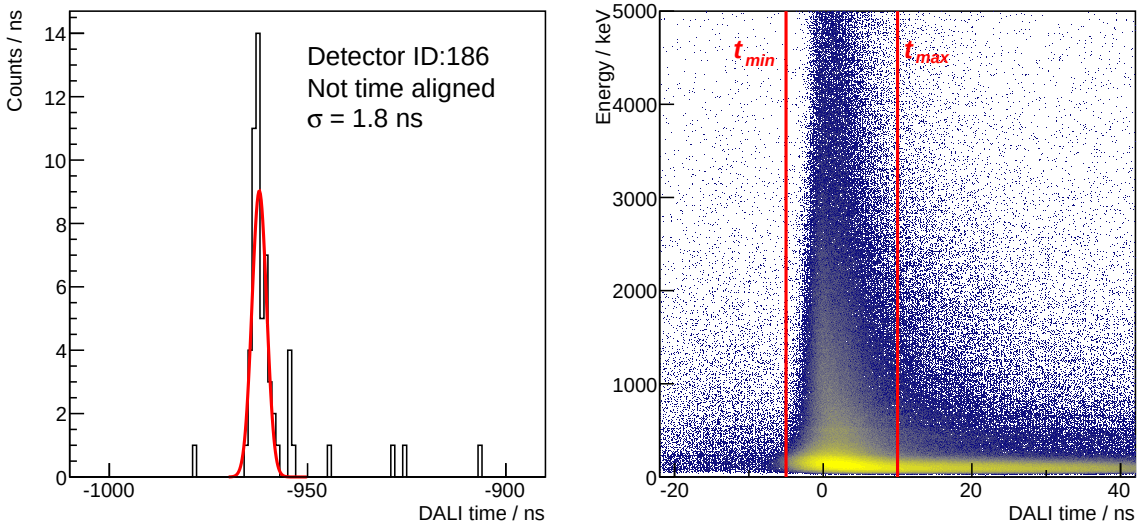

Fig. 4.11: Example of the time response of a NaI(Tl) detector with prompt γ rays. In the left panel, the raw structure of the time response of the forward detector, ID:186, with conditions of single γ-ray observation in the entire detector array and measured energy of larger than 500 keV is shown. The time distribution of each NaI(Tl) scintillator was fitted with a Gaussian function to align the peak position. The time structure versus observed energy is displayed in the right panel. To reduce background events from random coincidences, only the events between -5 ns and 10 ns, as illustrated with the red lines, were used in the analysis.

ID is shown in FWHM (Full Width Half Maximum). Note that four crystals with bad resolution, or sometimes having double peaks, ID: 48, 63, 132 and 167, were removed from the analysis, while other crystals with relatively bad resolutions were put far from the target position. From this measurement, the energy resolution of a NaI(Tl) crystal as a function of the γ-ray energy can be determined as:

$$\Delta E \propto \frac{1}{\sqrt{E}}.$$

By this relation, parameters for the Monte-Carlo simulation were determined for each crystal individually. The values measured with the ^{60}Co souce shown with black points in Fig. 4.10 were not used in the fit as these energy resolutions might have been underestimated. This underestimation might be caused by the assumption of the linear background for the fit shown in Fig. 4.6, while the actual background structure could be rather concave up. Also, the peaks of ^{60}Co are close to each other compared to their resolution to obtain proper values.

(4) Time alignment

To reject random background events, time conditions for the crystals were important. Figure 4.11 is an example of the time distribution of the NaI(Tl) detector signal relative to the timing of the nearest plastic detector at F8. Each scintillator was fitted with a Gaussian to obtain the timing offset. To avoid the tail structure caused by scattered γ rays and the walk-effect from low energy γ rays, events with only one crystal in the whole DALI2 array above threshold and with a γ-ray energy higher than 500 keV in the laboratory frame were used.

The time structure versus energy of DALI2 is shown in the right panel of Fig. 4.11. For lower energy events, delayed events can be seen, which are due to the γ rays scattered by Compton effect and the walk-effects of the discriminator. The time resolution of the entire array was

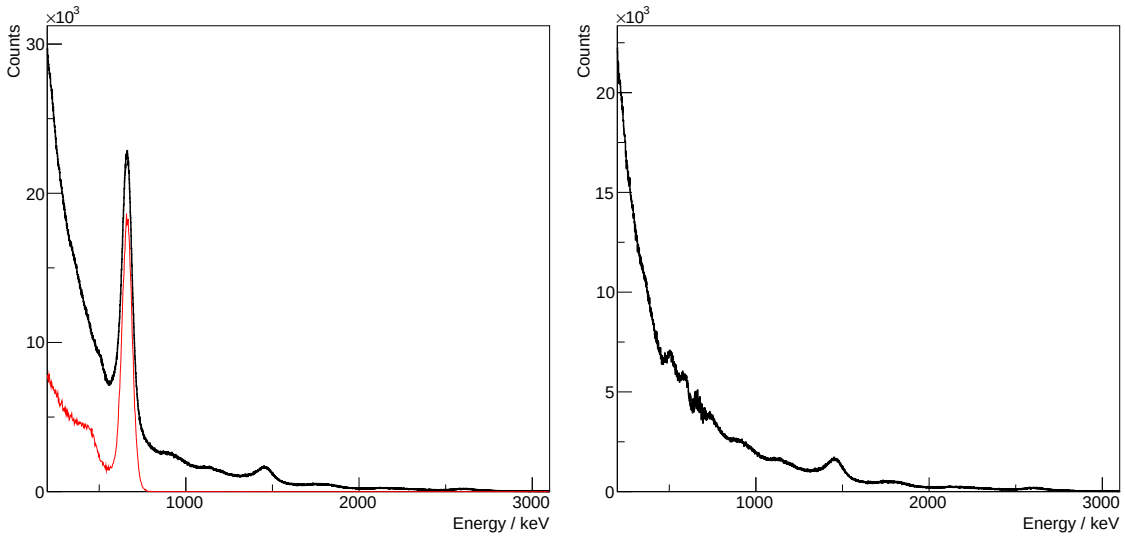

Fig. 4.12: Validation of the response function of DALI2. The reliability of the GEANT4 based DALI2 response was tested with the efficiency-calibration measurement. In the left panel, the spectrum of the ^{137}Cs source measurement (black curve) are drawn with a simulated response function at 662 keV peak (red curve). The γ-ray spectrum was subtracted with the simulated function as the residual distribution shown in the right panel.

deduced as 1.8 ns(σ) for energies above 500 keV. To reduce the background from random coincidence events, only the events between -5 ns and 10 ns were used in the further analysis.

(5) Validation of the GEANT4 simulation

The GEANT4 [139, 140] based simulation of the response function of the DALI2 γ-ray spectrometer [141] was used to deduce the number of the emitted γ rays from the nuclei of interest. To test the reliability of the GEANT4-based DALI2 response functions, a calibration measurement was performed with a ^{137}Cs standard source after the beam experiments to compare the spectrum with the results of the simulation. In order to conduct the detector efficiency measurement reducing the effect of the dependencies of the position of the γ-ray emission, the source was placed at the end of the liquid hydrogen target in the target chamber. For this calibration measurement, the exit window of the target chamber was cut to put the standard source inside the chamber. The measurement with the ^{137}Cs source was performed for T = 1832.0 seconds and the activity of the source was $I(^{137}\mathrm{Cs}) = 7.5(4) \times 10^3$ Bq, as listed in Tab. 3.5. The number of β decays occurring during the measurement amounts to $N_\beta = 1.37(7) \times 10^7$. In the spectrum shown in the left panel of Fig. 4.12, the γ-ray transitions of ^{137}Cs at 661.66 keV, the natural radiation of ^{40}K at 1460.8 keV, and several small peaks originating from natural radioactivity and activated material during the beam time. Unfortunately, the background measurement was not performed at that time, therefore, unresolved background structures were approximated by a double-exponential curve.

For the further discussion, it is also necessary to consider the branching ratio to the state at 661.66 keV after the β-decay of ^{137}Cs, R = 94.7%, and the livetime of the DAQ, λ = 49.25%. By considering them, the simulated response function was scaled with the expected number of γ rays, N_{sim}, calculated as:

$$N_{\mathrm{sim}} = N_\beta \times R \times \lambda = 6.4(3) \times 10^6. \tag{4.2}$$

Note that, to deduce the response function of DALI2, 10^6 γ rays were simulated, which is sufficient statistics compared to other uncertainties. Here, the validity for the intensity of response functions was evaluated by comparing with the measured spectrum. While the left panel of Fig. 4.12 shows the result of the simulated response function of γ rays at 661.66 keV drawn with a red curve, the right panel shows the residual γ-ray histogram subtracted with the simulated function. It can be seen in the latter spectrum that the peak structure from ^{137}Cs disappeared within statistical fluctuations and only the background structure can be seen. While the while the residual histogram shows the validity of the simulation within a few percent of ambiguity, the uncertainty of the intensity of the γ-ray source used for the calibration measurement, also contribute to the systematic error for the efficiency. Thus, 5%, was taken as the error for the further analysis of this work.

(6) Average interaction point

The angle between emitted γ-ray and beam is necessary to reconstruct the Doppler shifted γ rays. This angle is obtained by assuming the direction from the vertex position in MINOS to the position information of the DALI2 crystals with the highest energy released with respect to a straight line along the beam axis (z) for the reaction product. While the actual position of the γ-ray hit in the NaI(Tl) crystal could not be obtained, the average of simulated first interaction points by the GEANT4 package with a γ-ray energy of 2.7 MeV were assumed as the first interaction point for the Doppler reconstruction in each crystal. Only the first interaction point was taken into account for scattered gamma-rays.

(7) Add-back analysis

Due to Compton scattering, the energy of a single γ ray might be distributed over several crystals. By summing the energy deposits of one event within a certain time window and within a certain spherical distance from the crystal with the highest energy detected, these events can be recovered. The routine of the add-back analysis is described in the following. Firstly, the crystal with the highest energy deposited in the laboratory frame was assumed as the initial hit of the sequence of the Compton scattering, and its position information was used for the Doppler reconstruction. Subsequently, energy depositions of any crystal within a certain distance, set to 15 cm in this study because 2-MeV γ rays will interact further within this length about 90% of the time (see [144] for example), were summed up as a single γ-ray hit and were converted into the energy in the center-of-mass system. The add-back analysis was repeated until all the remaining crystals were processed.

4.3.2 MINOS

(1) TPC drift time calibration

The drift velocity of the electrons in the TPC was monitored on an run-by-run basis, as it depends on the pressure and impurities of the gas. The distributions of the trigger timing of the electrodes for all the events and the events with two tracks reconstructed are displayed in the left panel of Fig. 4.13 with blue and red curves, respectively. It can be seen that real events are distributed between 1 to 8 μs, indicated with vertical dash-dotted lines. As this distribution was seen also in a similar work [117], the structure with a maximum around 4 μs can be understood by the tracks of protons, which are penetrating the TPC in the forward direction in the laboratory frame. Considering the geometry with a 10-cm thick target, protons are expected to

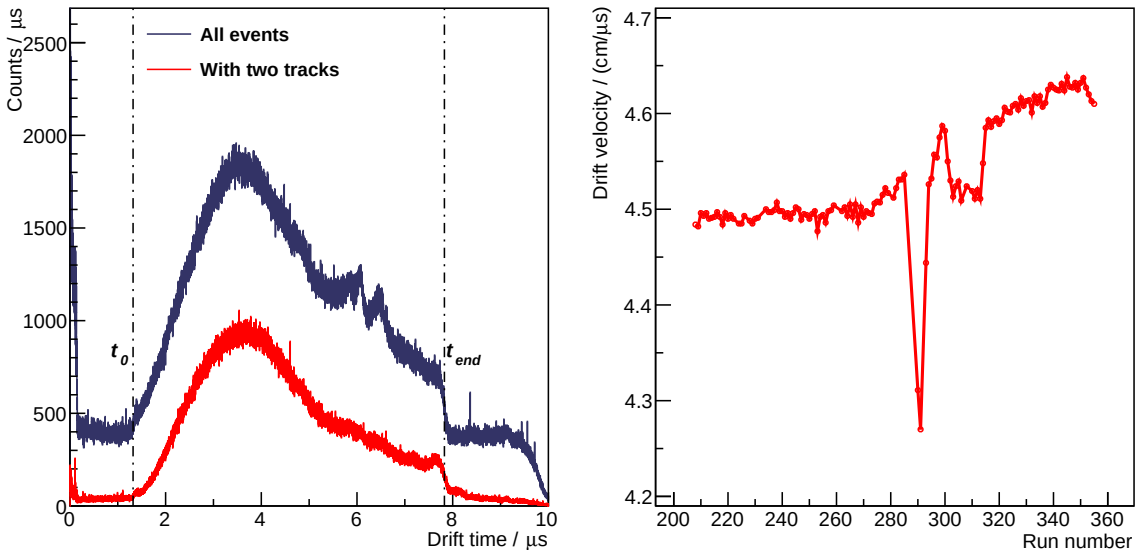

Fig. 4.13: Distribution of the drift time and time-evolution of the drift velocity of MINOS. The left panel shows examples of the distribution of the drift time of a physics run for about an hour with all the events (blue curve) and the events with two-tracks reconstructed (red curve). In order to reduce background contaminants and to select the events with proton tracks, events with less than 10 triggered pads were rejected. The two vertical dot-dash lines indicate the start- and the end-times, t_0 and t_{end}, respectively. See text for descriptions to deduce these values. The right panel shows the evolution of the drift velocity as a function of the run number of the physics measurement. The gas bottle of the TPC was replaced with a new one after run 284. The drop of the drift velocity, as seen in the graph, was caused by the gas flow mistakenly set to a less than the default value.

penetrate mostly the forward one third of the 30-cm chamber length. The abrupt decrease at 0 μs and 10 μs can be assumed as the artifical cut in the time-window of the front-end digitizers. The constant background around 1 μs and 8 to 9 μs seen in the distribution without any track condition, which were well suppressed with the condition of two track reconstructions, can be considered as uncorrelated trigger events.

The earliest timing, noted as t_0, and the latest one, t_{end} correspond to the position of the edge of the chamber on the electrode side and the other end of the chamber, respectively. While the position of t_0 remained constant during the entire run, the t_{end} depended on the drift velocity, v_{e^-}. The drift velocity was deduced from the length of the TPC, L_{TPC};

$$v_{e^-} = \frac{L_{TPC}}{t_{end} - t_0}. \tag{4.3}$$

As seen in the left figure of Fig. 4.13, the distribution showed a sudden drop at t_{end} position. It was fitted run-by-run with a Fermi-Dirac distribution, with three parameters p_0, p_1, and p_2, in addtion to t_{end} as:

$$f(\tau) = \frac{p_0}{\exp\{(\tau - t_{end})/p_1\}} + p_2. \tag{4.4}$$

The offset t_0 was determined with the summed distribution of all runs because of two reasons; the drop at t_0 was much smaller than t_{end}, and the position of t_0 did not change with v_{e^-}.

The time-evolution of the drift velocity, v_{e^-}, is illustrated in the right panel of Fig. 4.13. An abrupt drop of the velocity can be seen after run 284, when the gas bottle of the TPC was replaced with a new one. That is understood as the increase of the impurity of the gas, which

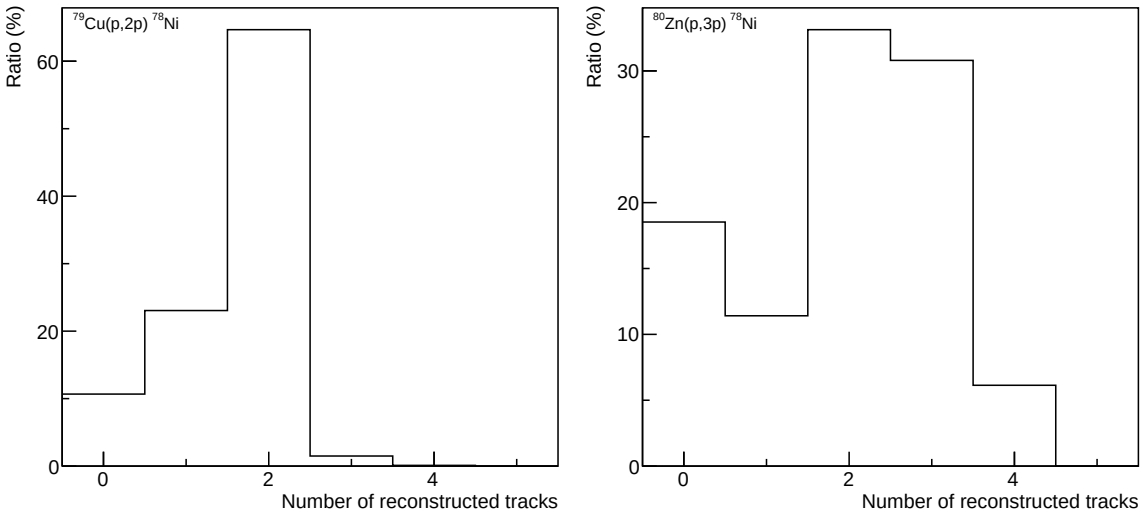

Fig. 4.14: Ratios of the number of reconstructed tracks of protons in MINOS. ^{79}Cu$(p,2p)^{78}$Ni and ^{80}Zn$(p,3p)^{78}$Ni reactions.

was caused by the gas flow rate set to lower values than the default. During that time, almost no track was reconstructed with the TPC.

Here, the z position of the proton track was reconstructed from the trigger timing of each electrode pad of the TPC as

$$z_{e^-} = v_{e^-} \cdot (t_{pad} - t_0). \tag{4.5}$$

(2) Vertex reconstruction

The vertex reconstruction system of MINOS was utilized to reduce the Doppler broadening effect of γ rays caused by the emission angle and β uncertainties. As illustrated in Fig. 3.3 and described in section 3.2, MINOS had a cylindrical TPC chamber surrounding the liquid hydrogen chamber and a DSSSD at the entrance of the liquid hydrogen chamber. Figure 4.14 shows the ratios of observed numbers of tracks for ^{79}Cu$(p,2p)^{78}$Ni and ^{80}Zn$(p,3p)^{78}$Ni reactions. When two or more tracks were reconstructed in the TPC chamber in one event, the vertex was evaluated using these tracks. When only one track was reconstructed, the beam track, which could be reconstructed using DSSSD and PPAC at F8, was used to obtain the interaction vertex. Since the efficiency of the DSSSD was not 100%, its position information was used whenever possible. Otherwise the beam track was extrapolated from the F8-PPAC position and angle. Figure 4.15 displays the comparison of the vertex reconstruction with two tracks in the TPC versus one in the TPC and a beam track. There are clear correlations in the figures, which suggest the vertex reconstruction with beam tracking works properly. Though it is difficult to obtain the position resolution from the distribution of the vertices of the thick target, it can be roughly estimated by the sharpness of the edge on both sides of the target (at $z = 0, 100$). Furthermore, the vertex resolution with one track in MINOS and the beam track without the DSSSD is worse than with the DSSSD. That is because the PPAC was located 1 m downstream from the MINOS chamber, while the DSSSD was next to the entrance of the target. Thus, the uncertainty in the beam angle determined without the DSSSD resulted in a larger uncertainty for the vertex. It can be seen in Fig. 4.15, that the distribution in the right panel, which used only the PPAC for the beam track, is more scattered. Figure 4.16 displays the distribution of reconstructed vertices. The length of the target, from 0 to 100 mm in z direction, is visible in the XZ-plane, while the focused beam

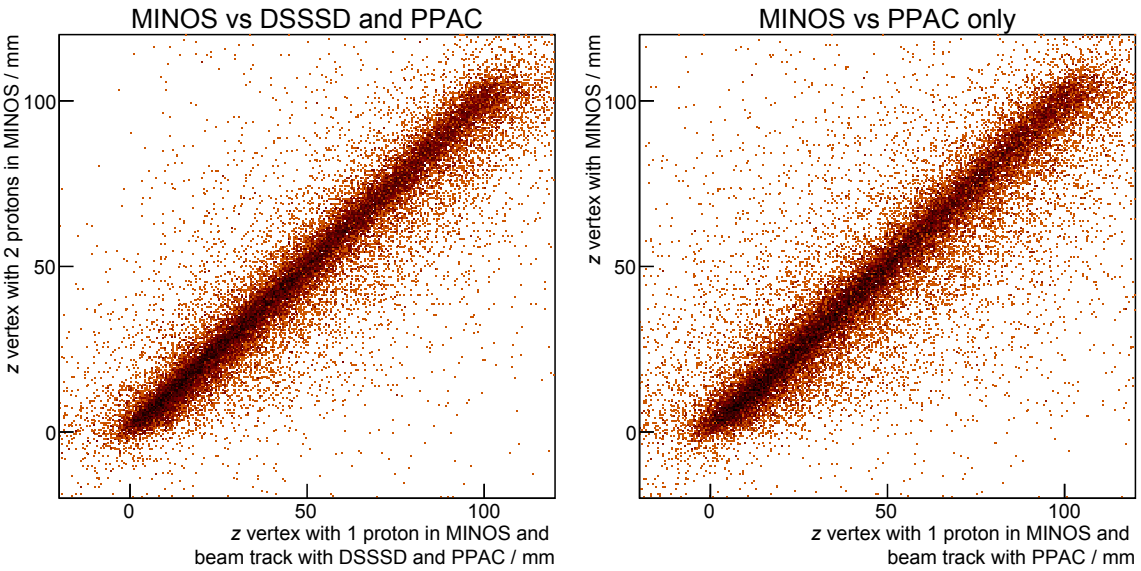

Fig. 4.15: Validation of the vertex reconstruction with beam tracking. The two vertex reconstruction methods, by a beam track and one proton track in the TPC (horizontal), or by two proton tracks (vertical) are compared. The horizontal axis in the left figure is obtained using a combination of the PPAC and the DSSSD positions, while the one in the right figure is obtained from only the PPAC tracking. It can be seen that the vertex obtained using MINOS alone is better than the one using the beam track.

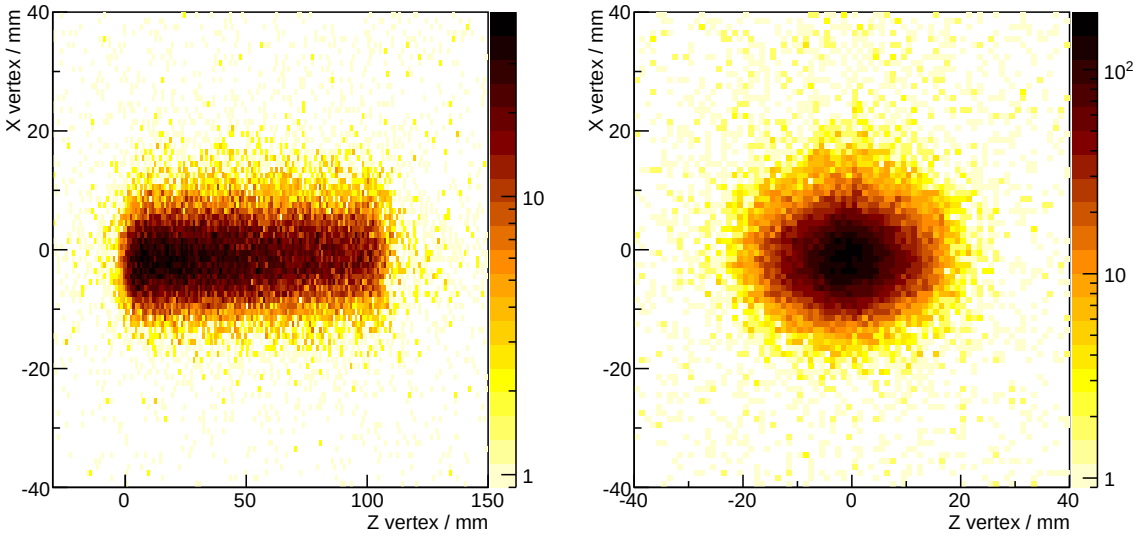

Fig. 4.16: Target shape obtained from the vertex reconstruction. Left and right panels show the distributions of reconstructed vertex positions in the XZ- and XY-planes, respectively. To obtain a clear target image, events with two reconstructed proton tracks were used.

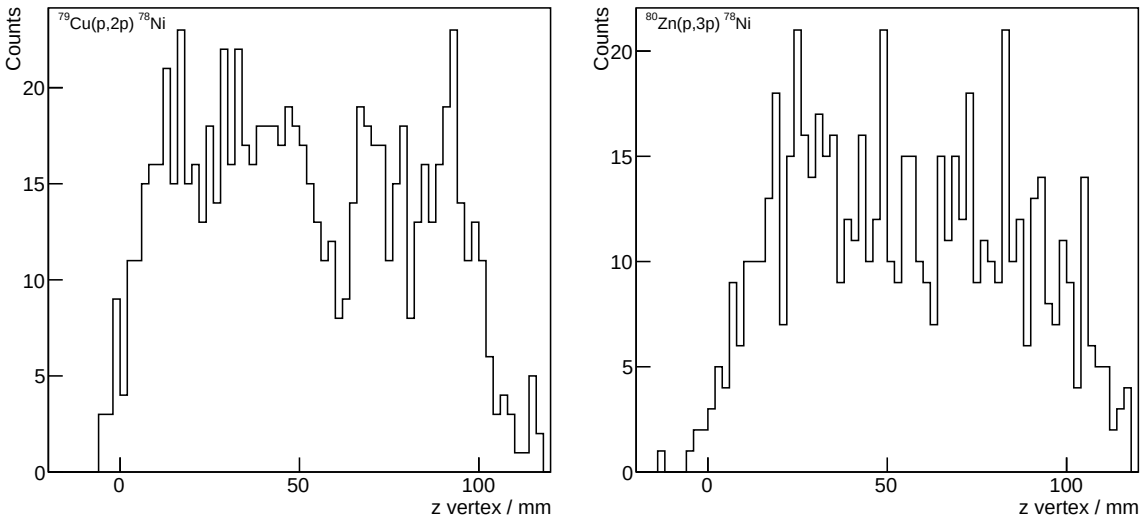

Fig. 4.17: Distribution of reconstructed vertices of each reaction channel. The reconstructed reaction vertices for ^{79}Cu$(p,2p)^{78}$Ni (left) and ^{80}Zn$(p,3p)^{78}$Ni (right) reactions.

size can be seen from the distribution of XY-plane. Though it is difficult to obtain a value for the position resolution from this data, they are consistent with the measured 5 mm resolution (FWHM) from a test measurement of the TPC performed with thin solid targets [123, 124].

(3) Target thickness

Once the drift velocity of the TPC is calibrated, the stability of the target length can be monitored using the distribution of the reconstructed vertex positions. As examples, the z distributions of the ^{80}Zn$(p,3p)^{78}$Ni and ^{79}Cu$(p,2p)^{78}$Ni reactions are shown in Fig. 4.17. While the distribution of the $(p,2p)$ reaction shows clear edges of the target shape, the one of the $(p,3p)$ channel is more blurred, which might be caused by the reaction mechanism and the acceptance of ZeroDegree, but the is no concrete explanation. This phenomenon can also be seen later in Eq. (4.8) of the vertex reconstruction efficiency of the $(p,3p)$ reaction, which is worse than that of the $(p,2p)$ channel. The target thickness was deduced by fitting the z distribution of all two-track events with Fermi functions, and was determined to be 102(1) mm by taking the average.

(4) Vertex reconstruction efficiency

To determine the final state exclusive cross sections, it is necessary to deduce the vertex reconstruction efficiency of the MINOS system. As only the events within a certain range of the target, $z = (-5, 115)$ (mm), were used in the later analysis, the definition of the efficiency is simply written as:

$$\varepsilon_{\text{vertex}} = \frac{N(\text{BR} \otimes \text{ZD} \otimes \text{MINOS})}{N(\text{BR} \otimes \text{ZD})} = \frac{N_{in}}{N_{pid}}. \tag{4.6}$$

N_{in} is defined as the number of the events for which the vertex position is reconstructed within the range. This is larger than the size of the target because of the vertex distribution for the $(p,3p)$ reaction is blurred in the downstream direction of MINOS. Using the numbers of events with proper vertex position for ^{80}Zn$(p,3p)^{78}$Ni and ^{79}Cu$(p,2p)^{78}$Ni reaction channels displayed

in Fig. 4.17 summarized in Tab. 4.2, the efficiency values for both reaction channels were deduced as:

$$\varepsilon_{p2p} = \frac{811}{937} \approx 87(4)\%, \tag{4.7}$$

$$\varepsilon_{p3p} = \frac{639}{815} \approx 78(4)\%. \tag{4.8}$$

These values are slightly lower than the measured values in similar works [84, 116], but are still consistent with the design value, 80% [123, 124]. Also, as mentioned above, the vertex reconstruction efficiency of the $(p,3p)$ reaction is worse than that of the $(p,2p)$ channel.

(5) Beam velocity β in the target

As discussed above, the elimination of the uncertainty of the velocity of the ejectile at the emission point of γ-ray is important in order to minimize the Doppler broadening. The velocity distribution after the target can be obtained from the time-of-flight measurement in the ZeroDegree spectrometer shown in the left panel of Fig. 4.18. As this velocity was averaged along the flight path of the ZeroDegree spectrometer, it was needed to be corrected for energy loss in the detectors of the spectrometer. Thus, an offset to the measured velocity deduced from the time-of-flight through the spectrometer, taking into account the energy loss along the spectrometer, which was checked with the LISE++ software [138], was applied to deduce the correct velocity at the end of the target, β_{out}. The velocity at the reaction vertex, β_{vertex}, depends on to the depth, z, of the reaction point in the thick liquid hydrogen target, and was deduced from the energy loss calculated with the ATIMA code [145], which is implemented into the LISE++ software. The internal division adopted to deduce β_{vertex} was expressed as:

$$\beta_{vertex} = \beta_{in} - z \times \frac{\beta_{in} - \beta_{out}}{L_{target}}, \tag{4.9}$$

where β_{in} is the calculated velocity at the entrance of the target with the energy loss of ^{78}Ni. Here, β_{in} of the $(p,2p)$ and $(p,3p)$ channels were 0.615 and 0.618, respectively. The distribution of the velocity at the reaction point is shown in the right of Figure 4.18. Note that the range of the horizontal axis is much wider than the left one.

It is also important to test the accuracy of the velocity at the incident point, β_{vertex}, with the linear interpolation of Eq. (4.9) as the energy loss per distance, $-\frac{dE}{dx}$, is not constatnt, but depends on the energy. The calculated remaining kinetic energy and β_{vertex} at a certain depth in the liquid hydrogen target, assuming a ^{78}Ni particle with 250 MeV/u at the entrance of the target, is illustrated in Fig. 4.19. In the bottom panels, the differences in energy and velocity between the values calculated by the ATIMA code [145] and the one from linear interpolations are displayed. While the relative difference of the velocity β_{vertex} was 0.6% at the maximum, the uncertainty of the reconstructed β value can be considered as the avarage of the discrepancy, 0.3%. This uncertainty of β can also be propagated, as Eq. (2.12), to the systematic error of the Doppler energy reconstruction for the γ rays. Though the equation has a dependence on the angle between the γ-ray emission and the beam direction, the average uncertainty of the reconstruction can be considered to be about 0.2%. Considering that the uncertainty of the γ-ray energy reconstruction by the DALI2 detector, 0.6% at the maximum, as in section 4.3.1, is larger than the one derived from the β uncertainty, the total systematic uncertainty of the γ-ray energy reconstruction may be possible to assume as 0.6%.

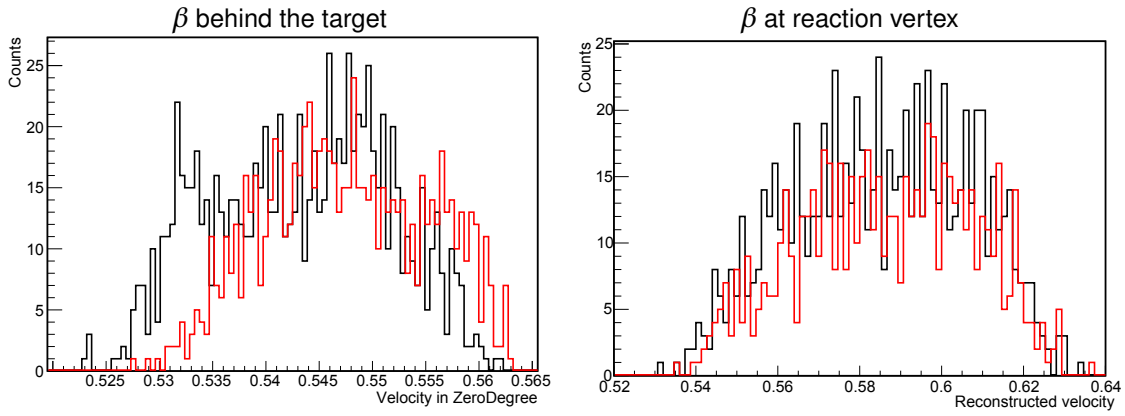

Fig. 4.18: Velocity distribution in the ZeroDegree spectrometer and in the target for both reaction channels, ^{79}Cu$(p,2p)^{78}$Ni (black) and ^{80}Zn$(p,3p)^{78}$Ni (red). The left figure shows the one in ZeroDegree deduced by the time-of-flight measurement, and the right figure shows the reconstructed one at the vertex position.

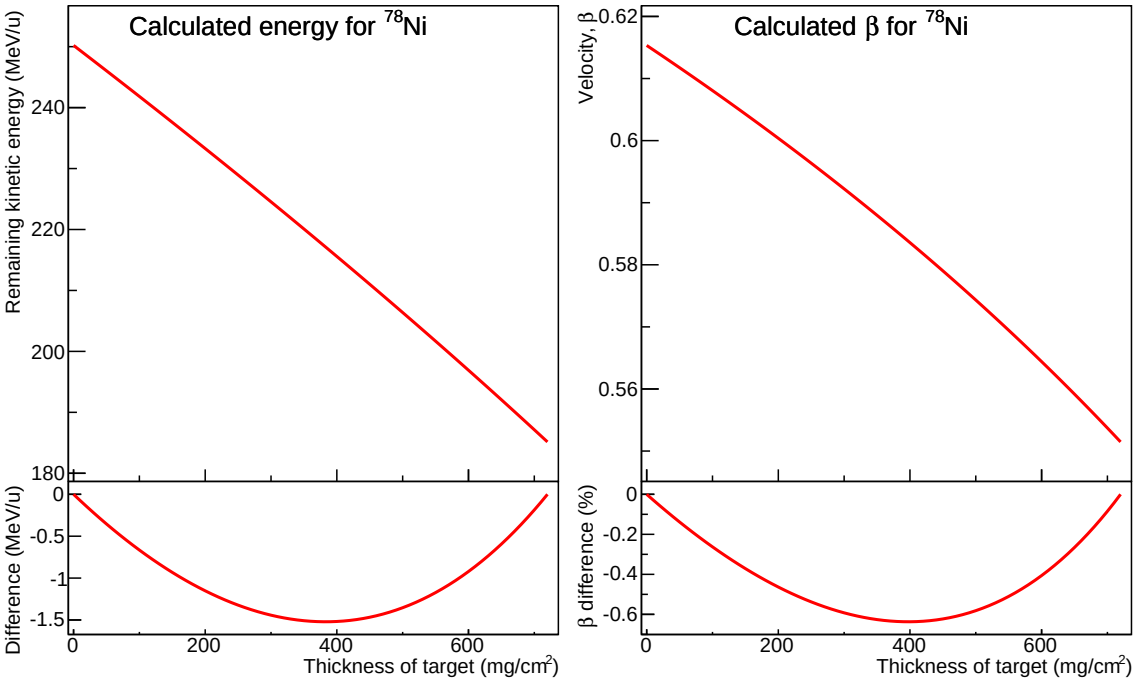

Fig. 4.19: Accuracy of interpolation of the energy loss in the secondary target. The velocity, β, at the reaction point in the liquid hydrogen target was interpolated linearly as Eq. (4.9). The top left panel shows the remaining kinetic energy of a ^{78}Ni particle with 250 MeV/u after passing through a certain amount of liquid hydrogen target, calculated by ATIMA code [145]. In the bottom left panel, the energy difference between the linear interpolation and the value calculated according to the material thickness is shown. Same comparison was performed for the reconstructed velocity, β, as shown in the right panels.

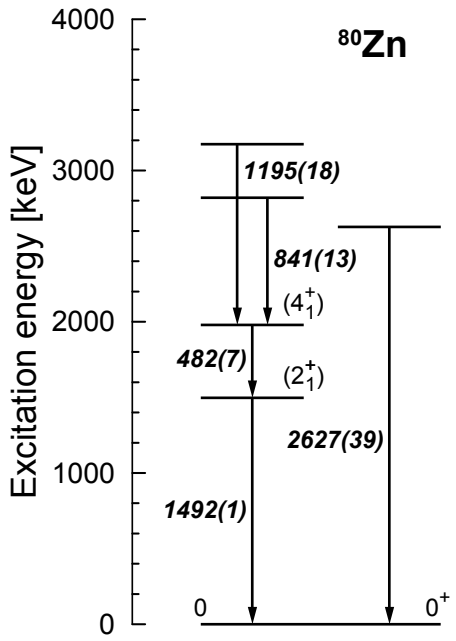

Fig. 4.20: Reported levels of ^{80}Zn. Performed γ-ray spectroscopy experiments [82, 91, 101] reports the energy levels of ^{80}Zn as summarized here.

4.4 Test case of γ-ray reconstruction: ^{80}Zn

To confirm the validity of the procedure of the analysis to obtain the γ-ray energy of transitions of interest, as test cases the ^{81}Ga$(p,2p)^{80}$Zn and ^{82}Ge$(p,3p)^{80}$Zn reactions were analyzed. The numbers of events of these nuclei were much higher than for ^{78}Ni, and also the excited states have been studied in previous experimental works [82, 91, 101]. The known level scheme of ^{80}Zn is shown in Fig. 4.20.

4.4.1 Doppler reconstructed γ-ray spectra

(1) Doppler reconstruction and add-back analysis

Firstly, Doppler reconstruction was performed to validate the determination of the vertex and β. The γ-ray spectra with and without Doppler reconstruction are displayed in Fig. 4.21. While the red spectrum, obtained after the Doppler reconstruction with the MINOS vertices, indicates several peaks in good agreement with Fig. 4.20, the other spectrum shows only a peak at 511 keV, due to electron-positron annihilation. Besides, the performance of the Doppler correction, the vertex reconstruction of MINOS and the add-back analysis were also examined in Fig. 4.22. It can be seen that the resolution of each peak was improved by employing the vertex reconstruction, except the transitions at 482 and 1492 keV, for which the energy resolution was deteriorated by increased uncertainty of the decay position by an effect of the known lifetime of the $(4^+) \rightarrow 2^+$ transition of 136^{+92}_{-67} ps [82].

(2) Lifetime effects

In case of excited states having a lifetime of a few hundred ps, the average γ-ray emission point shifts by a few centimeters downwards from the reconstructed vertices, which corresponds to

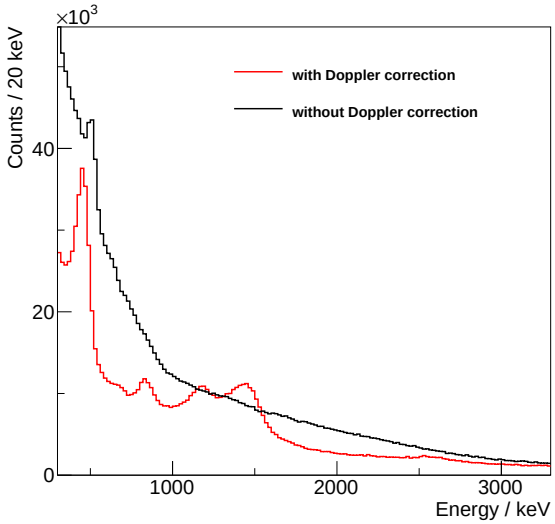

Fig. 4.21: Examination of Doppler reconstructions. Here, the γ-ray spectra of the ^{81}Ga$(p,2p)^{80}$Zn channel, with and without the reconstruction, are drawn with red and black histograms, respectively. The low-lying peak in the latter spectrum, which reflects the γ-ray energy in the lab frame, is the one at 511 keV from electron-positron annihilation.

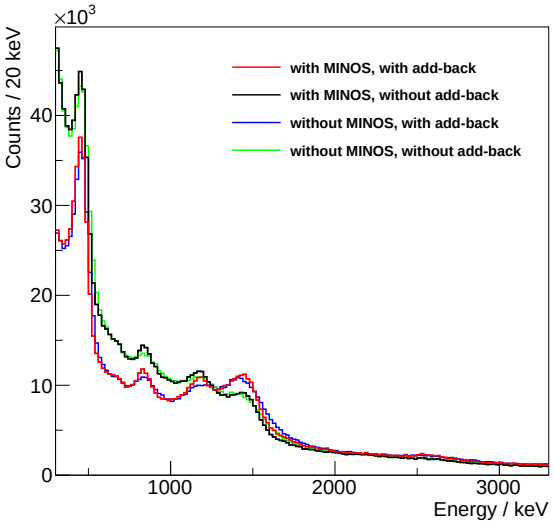

Fig. 4.22: Performance of the vertex reconstruction with MINOS and the add-back analysis. The improvement of the resolutions and the peak-to-total ratios especially for higher energy transitions, except the transitions at 482 and 1492 keV, which is known as being influenced by an effect of a lifetime of the (4^+) state, could be confirmed.

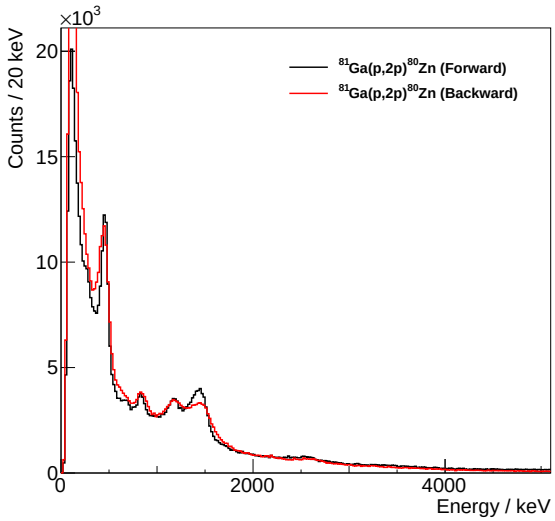

Fig. 4.23: Comparison of the energy spectra of forward and backward γ-ray detectors. The peak positions of the γ-ray transitions at 482 and 1492 keV of the ^{81}Ga$(p,2p)^{80}$Zn channel are different between the spectra of the forward (black curve) and backward (red curve) detectors in the beam direction. As discussed in the text, this can be explained by a lifetime effect of the excited state.

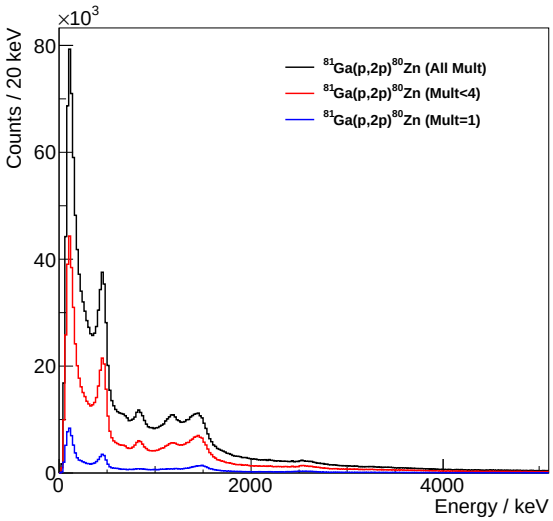

Fig. 4.24: The γ-ray spectra for the ^{81}Ga$(p,2p)^{80}$Zn channel for different detected γ-ray multiplicities. By restricting the condition on the γ-ray multiplicity, M_γ, from no condition (black curve) to $M_\gamma < 4$ (red curve), and $M_\gamma = 1$ (blue curve), it can be seen that the γ-ray transitions from the higher lying states, 841 and 1195 keV, tend to be suppressed more than the other ones.

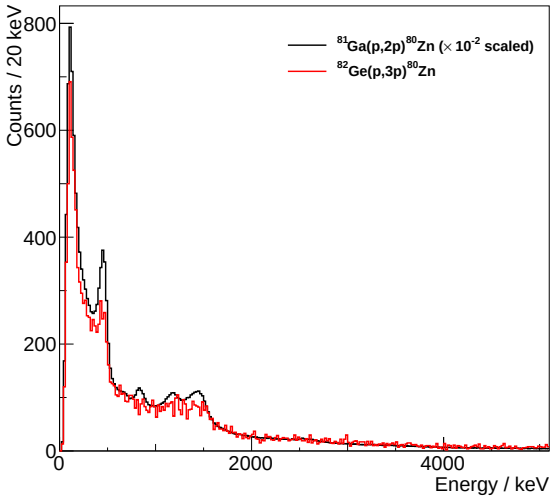

Fig. 4.25: γ-ray spectra of the ^{82}Ge$(p,3p)^{80}$Zn channel. The spectrum drawn with the red curve is compared with the one of the ^{81}Ga$(p,2p)^{80}$Zn channel (black curve), scaled by 1/100, as the number of events of the $(p,3p)$ channel was small. The 482- and 1492-keV peaks are observed in both histograms.

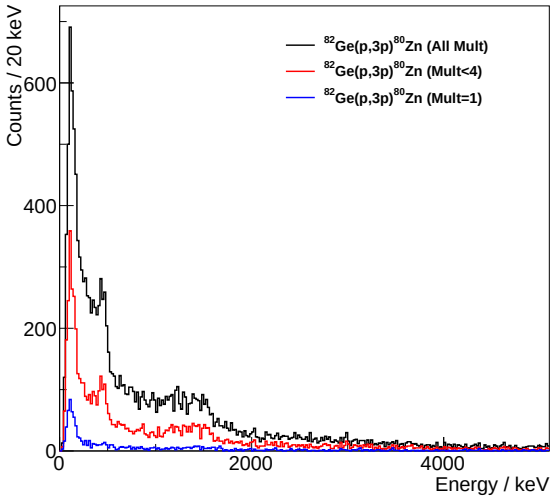

Fig. 4.26: γ-ray spectra for the ^{81}Ga$(p,2p)^{80}$Zn channel for different γ-ray multiplicities. The same analysis as presented in Fig. 4.24 was performed for the $(p,3p)$ histogram. Histograms gated on all multiplicities, $M_\gamma < 4$, and $M_\gamma = 1$ are drawn with black, red, and blue curves, respectively.

the point of the reaction. Thus, the reconstructed velocity and position of the ejectile do not represent the place of the γ-ray emission. As a consequence, a shift of the peak energy in the γ-ray spectrum is observed. The lifetime effect is visible in the spectrum of the ^{81}Ga$(p,2p)^{80}$Zn reaction shown in Fig. 4.23. This figure shows the Doppler corrected γ-ray energy spectra separately for forward and backward detectors of DALI2, drawn with red and black curves, respectively. While the 841-, 1195-, and 2627-keV peaks located at the same energy in both spectra, the 482- and 1492-keV ones exhibit different peak positions.

(3) γ-ray multiplicity gates

By restricting the condition on the detected γ-ray multiplicity for one reaction, M_γ, relative intensities of the γ-ray transitions from high-lying states, as well as such events of γ rays scattered by Compton effect, are generally suppressed. Figure 4.24 shows the γ-ray energy spectra for the ^{81}Ga$(p,2p)^{80}$Zn reaction with different detected γ-ray multiplicity conditions. It can be seen that the relative intensity of the 841- and 1195-keV transitions are reduced with strict multiplicity conditions. These two γ-ray transitions originate from states at 2815 and 3169 keV as shown in Fig. 4.20.

(4) The ^{82}Ge$(p,3p)^{80}$Zn two-proton-removal channel

In order to make sure that the Doppler correction was performed properly for the $(p,3p)$ reaction channel, the γ-ray spectra of the ^{82}Ge$(p,3p)^{80}$Zn channel were analyzed with the same procedure as for the $(p,2p)$ channel. Figure 4.25 compares the histograms of both reaction channels. Though number of the events for the $(p,3p)$ channel was small, it can be observed that the 482- and 1492-keV peaks were properly Doppler reconstructed. Furthermore, the γ-ray spectra with different conditions on the γ-ray multiplicity, M_γ, is shown in Fig. 4.26. It indicates that the peaks at 482 and 1492 keV were reduced compared to background for the small

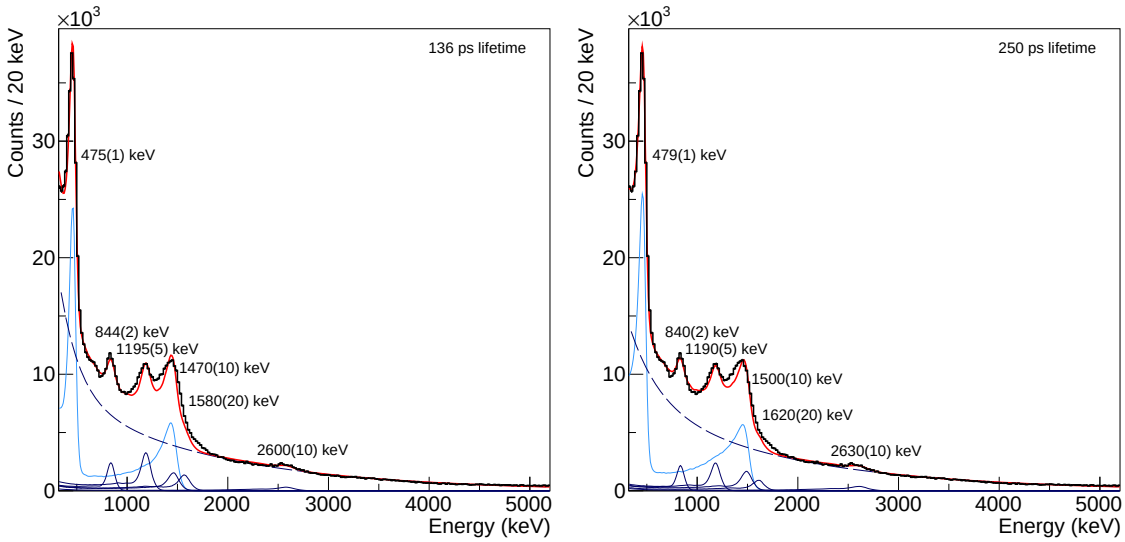

Fig. 4.27: Examples of γ-ray energy fitting considering the lifetime of the excited 4^+ state. The energy spectrum in coincidence with the ^{81}Ga$(p,2p)^{80}$Zn reaction was fitted with simulated response functions with the previously reported 841-, 1195-, 1492-, and 2627-keV transitions (blue curves) and the $(4^+) \rightarrow 2^+$ and its following $2^+ \rightarrow 0^+$ transitions assuming 136- (left panel) and 250-ps (right panel) lifetimes (light-blue curves). To fill the discrepancy between the γ-ray spectrum and the sum of the simulated spectra (red curves), another transition around 1600 keV was tentatively added. A double-exponential function drawn with blue dashed line was included for background. Detailed discussions are described in the main text.

M_γ condition. This is different from the one for the $(p,2p)$ channel shown in Fig. 4.24. Though this discussion is outside the scope of this thesis, it may be interpreted as this reaction channel populated mostly the high-lying states of ^{80}Zn than that for the $(p,2p)$ channel, resulting no storong population of the first and second excited states in the low γ-ray multiplicity events.

4.4.2 Determinating the energy of excited states of ^{80}Zn

To investigate the validity of the Doppler correction and the simulated response functions, the reconstructed γ-ray spectrum in prompt coincidence with the ^{81}Ga$(p,2p)^{80}$Zn reaction was analyzed. The peak positions and relative intensities were fit with the simulated response functions and the results are compared with the literature values [82,91,101] shown in Fig. 4.20. The principle to deduce the energy of peaks is the same as for the excited states of ^{78}Ni, described in section 5.2.1. The detailed results of the energy determination are discussed in the appendix chapter A. As the (4^+) state has a lifetime of 136^{+92}_{-67} ps, the following $2^+ \rightarrow 0^+$ transition is also affected by this [82]. Even though this analysis was aimed to test the validity of the γ-ray energy reconstruction, the spectrum of the ^{81}Ga$(p,2p)^{80}$Zn channel itself had a difficulty to reproduce the all the reported transitions with a coarse fittings since there are several unknown γ-ray transitions making discrepancy between the simulated curve and the spectrum. Especially, the 2600-keV transition had a difficulty to be fit with proper energy since its peak height was not high enough to be differentiated from the background. If it is the case of a sophisticated and careful analysis, the background shape might be better to be derermined from other reaction channels to reduce the uncertainty of the parameters, however, in this brief analysis no parameter of the background structure was fixed. Thus, the 2600-keV peak energy could not be reproduced well in the first attempt of fit with only the reported five transitions. This was understood

as the discrepancy on the higher energy side of 1492-keV transition, around 1600 keV, made estimation of the background shape deteriorated, resulting in the fit of the 2600-keV transition mistakenly. To solve this problem, a fitting, including another peak at 1600 keV tentatively, was performed. Figure 4.27 shows two versions of the γ-ray spectrum assuming lifetimes of 136 ps and 250 ps for the (4^+) state. For all other states, including the $2^+ \rightarrow 0^+$ transition estimated as the direct population from the $(p,2p)$ reaction, with prompt decay of a 0-ps lifetime have been assumed. It should be noted that there might be additional states and transitions populated in this experiment, which may be the main reason affecting the energy values of 1600- and 2600-keV transitions shifted between the fittings of two lifetimes estimated. Though the 2600-keV transition varies by 30 keV, in general, the other transition energies obtained in this work are in good agreement with previous studies [82, 91, 101], validating the method of the analysis.

From the next chapter, the obtained γ-ray spectra of ^{78}Ni are discussed.

Chapter 5

Results

There are two main results described in this work: The reaction cross sections and the excited levels of ^{78}Ni. In section 5.1, the systematic trend of the inclusive cross sections around ^{78}Ni are shown. The the γ-ray spectroscopy results are described, starting from section 5.2 with the Doppler reconstructed γ-ray energy spectra of the ^{79}Cu$(p,2p)^{78}$Ni and ^{80}Zn$(p,3p)^{78}$Ni channels. The level scheme of ^{78}Ni was obtained as following steps:

1. The transition energies were obtained from maximum likelihood fits (section 5.2),
2. Hypothesis tests were used to deduce the significance levels of the peaks (section 5.3),
3. γ-γ coincidence analysis was applied to build the level scheme (section 5.4).

Finally, the exclusive cross sections were obtained combining the results of the analysis in section 5.5.

5.1 Inclusive cross sections

The inclusive cross section is defined as the reaction cross section of each reaction channel summed over all bound final states. It is deduced from the ratio of the number of incoming and outgoing particles after correcting for the transmission efficiency, which is determined by the angular and momentum acceptance of the beam line. Firstly, the beam transmission efficiency was deduced from the dedicated measurement, as detailed in section 5.1.1. Then, the cross sections were analyzed for several reaction channels in the vicinity of ^{78}Ni, as described in section 5.1.2. From the systematic trend of the cross sections, the inclusive cross section to produce ^{78}Ni nuclei was found to be smaller than the neighboring nuclei. These results are presented in section 5.1.3.

5.1.1 Beam transmission in ZeroDegree spectrometer

The beam transmission efficiency of the ZeroDegree spectrometer is affected by the momentum acceptance of the spectrometer and the angular spread caused by the thick liquid hydrogen target. It was deduced from the ratio of the number of particles in BigRIPS and ZeroDegree spectrometers. For this analysis, to avoid any bias from the trigger selection, events triggered by the F7 plastic scintillator were used (see Tab. 3.1). As shown in Tab. 3.3, dedicated transmission measurement runs were taken without liquid hydrogen in the target system (empty target run), run 147, and with target filled, run 148. For both measurements, ^{79}Cu was centered in

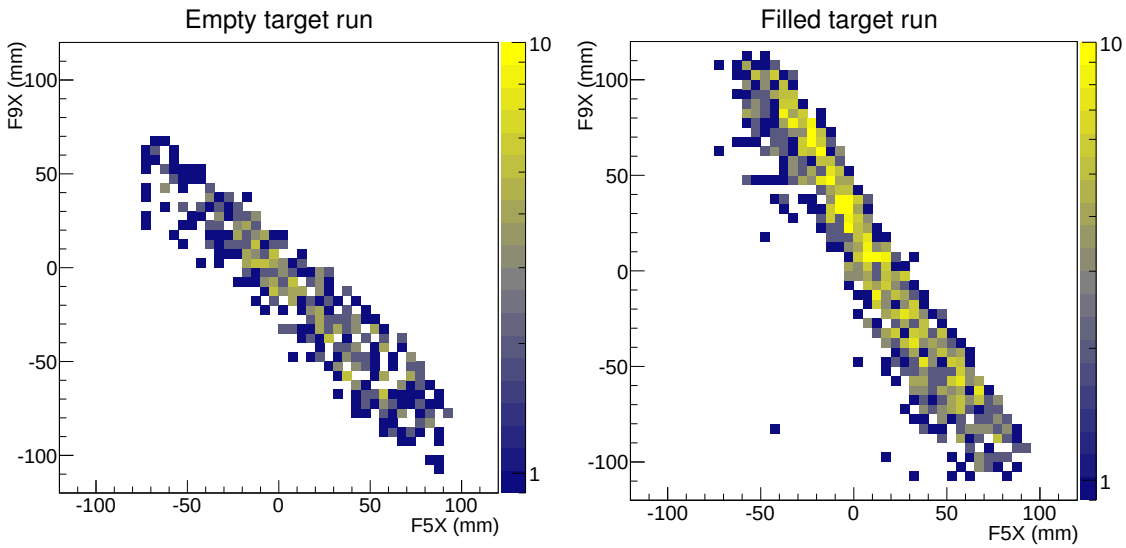

Fig. 5.1: Correlation of the beam position in the dispersive foci in the BigRIPS (F5X) and ZeroDegree (F9X) spectrometers gated on ^{79}Cu. As both dispersive foci have been set to be depended on the momentum of the particle, the correction of the respective positions can be seen for the empty target run (left panel) and the filled target run (right panel). The vertical axis is F5X and the horizontal axis is F9X. While both measurements show a similar negative correlation between F5X and F9X, the difference in the coefficient of the correlation is obviously seen. This can be understood as due to the energy loss in the target changed the momentum distribution wider.

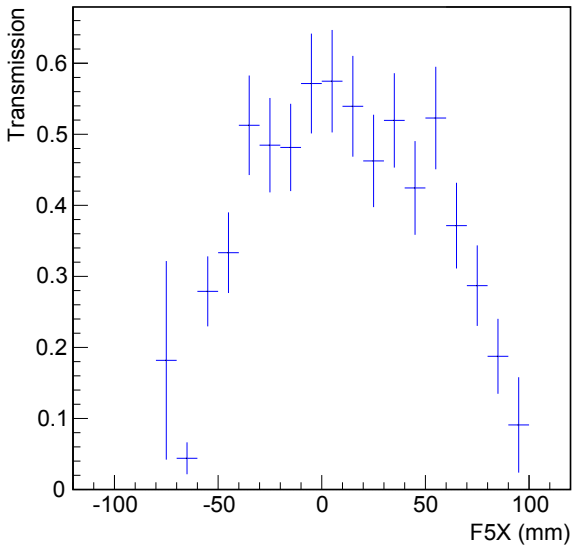

Fig. 5.2: Beam transmission for ^{79}Cu as a function of F5X. Because of the limitation of the number of events obtained during the dedicated transmission measurement, run 148, the error bars are relatively large. See text for the detailed discussions.

both the BigRIPS and ZeroDegree spectrometers. To check the transmission, the relationship of the positions at dispersive foci, F5 (BigRIPS) and F9 (ZeroDegree), which dependend on the momentum of the particle, are compared in Fig. 5.1. In this analysis, F3-F5-F7 reconstruction and F8-F9-F11 reconstruction were used for BigRIPS and ZeroDegree PID gated with 3.5σ area of the ^{79}Cu isotope. In order to deduce the inclusive cross sections, the both the transmission efficiency of the beam particle after the secondary target, going through the ZeroDegree spectrometer, ε_{trans}, as well as the efficiency of the particle identification with the beamline detectors, ε_{pid}, are necessary to be considered. The "effective transmission efficiency", τ, defined as the product of them:

$$\tau = \varepsilon_{pid} \times \varepsilon_{trans} = \frac{N(\mathrm{F9})}{N(\mathrm{F5})}, \tag{5.1}$$

was utilized in this analysis. As in the equation, it is also described as the ratio of the number of identified particles at F5 and F9. For the empty and filled target runs, efficiency values of τ_e = 73.5% and τ_f = 43% of were deduced, respectively. While the main factor for the empty run, τ_e, is caused by the integrated momentum and angular acceptance of the ZeroDegree spectrometer, the low value of τ_f is assumed to be caused by angular straggling in the thick liquid hydrogen target and reaction loss in the target. To investigate the behavior of the transmission in detail, the beam transmission for ^{79}Cu beam of the filled target run is shown in Fig. 5.2 as a function of the X position at F5. Because of the limitation of the number of events obtained during the dedicated transmission measurement, the error bars are relatively large, however, it is enough to discuss the characteristics of the transmission efficiency. The central part of the momentum distribution, which corresponds to F5X = 0, has the highest transmission with a constant value about 50% for ±50 mm region, while the efficiency in the outside of F5X = ±50 mm is rapidly decreasing. This phenomenon can be understood by the momentum straggling in the thick liquid hydrogen target and the limited angular and momentum acceptance of the ZeroDegree spectrometer.

Instead of the analysis above, there are several alternative methods to avoid such statistical uncertainty in Fig. 5.2, such as: Using isotopes with more events and analyzing the physics runs which have more events than the ones dedicated for the transmission measurement. However, they also have their own difficulties. For the former option, less exotic isotones instead of the ^{79}Cu beam, such as ^{80}Zn or ^{81}Ga, which have more count rate, could be utilized to obtain higher statistics. In this case, it is necessary to notice the energy losses in the thick target are different, and make modifications to the momentum distribution in the ZeroDegree spectrometer. The latter option, which was applied in a similar work [105], has the advantage of having more particles in the beam. However, it is important to notice that the beam transmission efficiency in the ZeroDegree spectrometer is not necessarily to be the same as the case of the dedicated transmission run because the magnetic rigidity $B\rho$ in the ZeroDegree spectrometer was set for one proton knock out reactions. Therefore, only the central part of the beam of momentum distribution can be used. Eventually, this method limits the usable range for the analysis of the inclusive cross section. Note that the inclusive cross section for the the ^{80}Zn$(p,2p)^{79}$Cu reaction deduced from the both analyses, results in consistent values with the same order of error bar [104, 105]. However, this method could not applied to the ^{79}Cu$(p,2p)^{78}$Ni reaction because of the large systematic uncertainties of the beam transmission in the ZeroDegree spectrometer.

5.1.2 Inclusive cross section analysis

To study the inclusive cross sections for several reaction channels systematically, the principle of the analysis is explained in this section. The definition of inclusive cross section σ_{incl} is

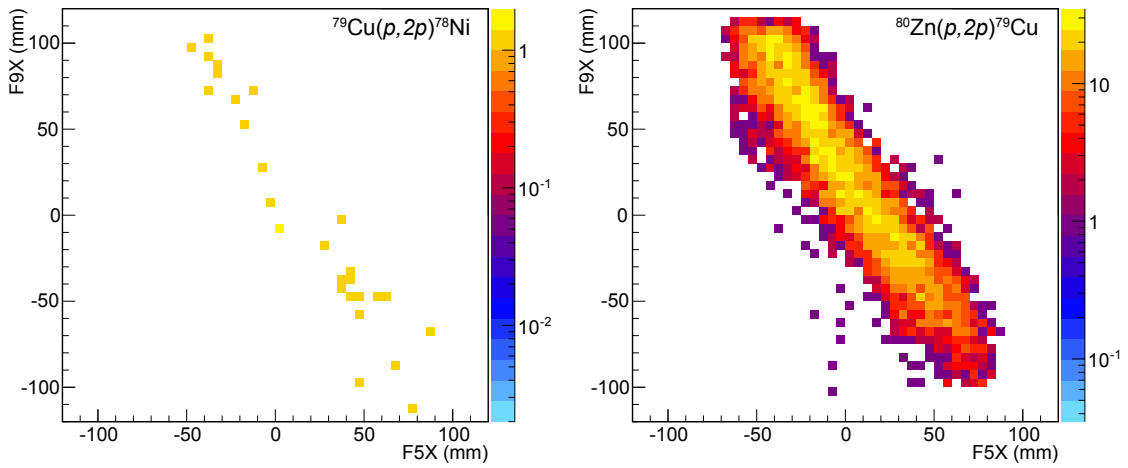

Fig. 5.3: Correlation between F5X and F9X for $(p,2p)$ reactions of ^{80}Zn and ^{79}Cu secondary beams. Both structures have similar trends as Fig. 5.1.

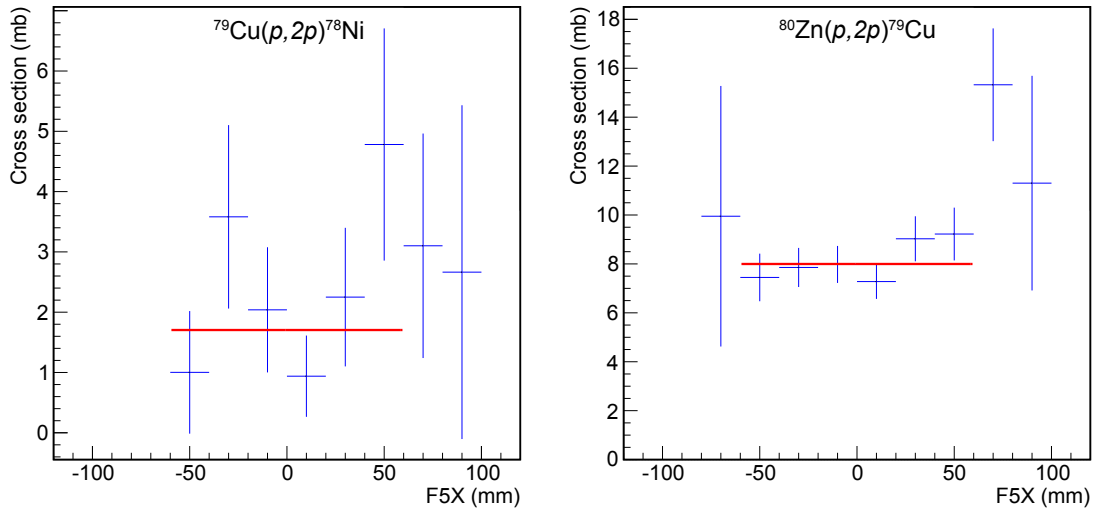

Fig. 5.4: Inclusive cross sections for $(p,2p)$ reactions of ^{80}Zn and ^{79}Cu secondary beams. To check the universality of the inclusive cross sections with the momentum of the secondary particles, the cross sections are calculated with respect to F5X with Eq. (5.2). The average between F5X= $(-60,60)$ mm for each reaction obtained as the inclusive cross sections are 1.7(4) mb and 8.0(3) mb.

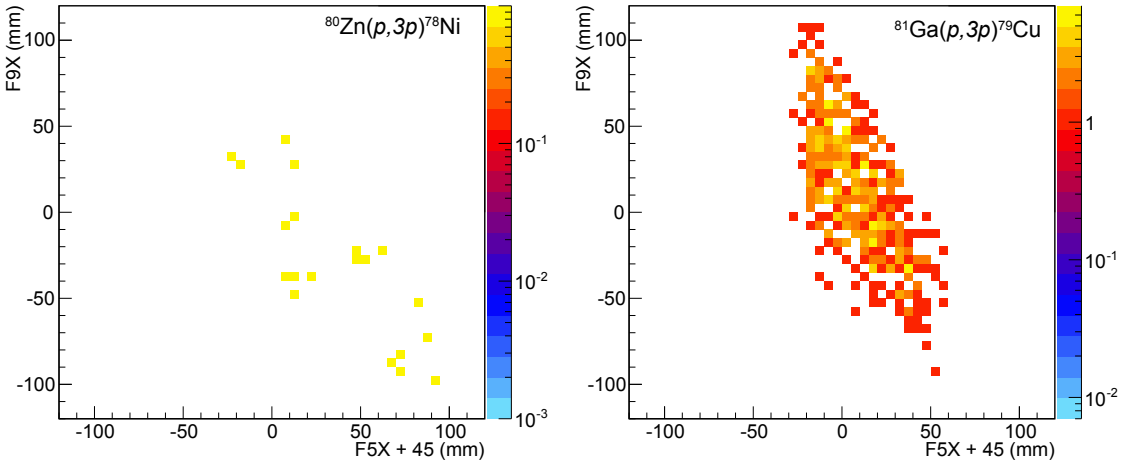

Fig. 5.5: Correlation between F5X and F9X for $(p,3p)$ reactions of ^{80}Ga and ^{80}Zn secondary beams. Because the changes of A/Q after the reaction are much different from $(p,2p)$ reactions, the centroid of the beam is shifted from the beam passing through the center of ZeroDegree. To align with the $(p,2p)$ channels and the transmission measurement run, the horizontal axis is shifted by 45 mm, *i.e.*, F9X in vertical axis vs F5X + 45 mm in the horizontal axis.

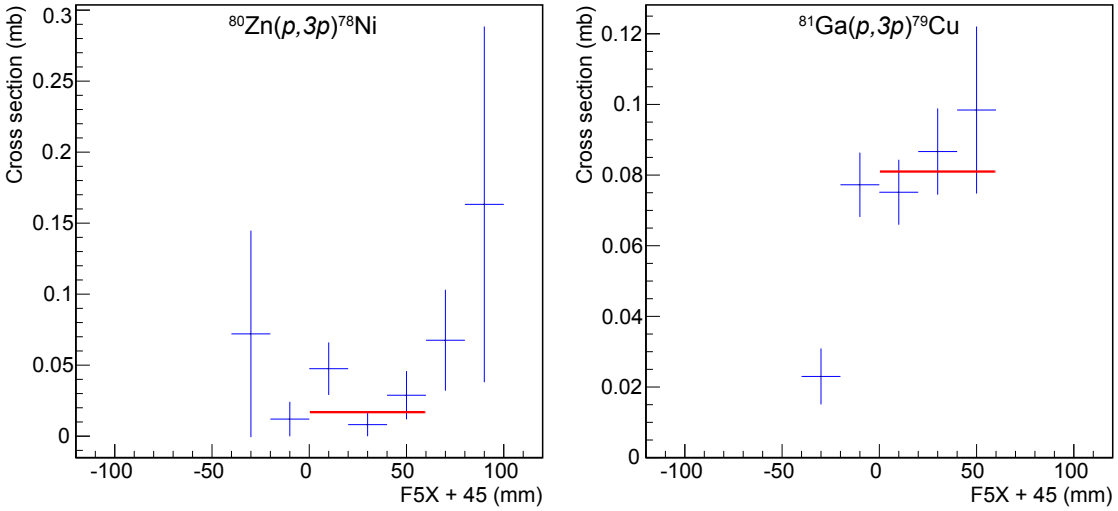

Fig. 5.6: Inclusive cross sections for $(p,3p)$ reactions of ^{80}Ga and ^{80}Zn secondary beams. As the slit condition was set F5X=-65 mm at the beginning of the measurement, the data points below -20 mm in this plot were not used in the analysis to exclude ambiguity of the numbers of incoming beam. The same analysis as Fig. 5.4 is applied to ^{80}Zn$(p,3p)^{78}$Ni and ^{81}Ga$(p,3p)^{79}$Cu reactions.

described as below with the number of particles gated in BigRIPS, N_{BR}, and ZeroDegree, N_{ZD}, beam transmission, τ, defined in Eq. (5.1), and the number density of target hydrogen per unit area, n_{dc}:

$$\sigma_{incl} = \frac{N_{ZD}}{N_{BR} \cdot \tau \cdot n_{dc}}. \tag{5.2}$$

Here, n_{dc} is defined as:

$$n_{dc} \equiv \frac{\rho_{LH_2} \cdot L_{LH_2} \cdot N_A}{M_H} = 4.32 \times 10^{23} \mathrm{cm}^{-2}. \tag{5.3}$$

As discussed in section 5.1.1, the beam transmission τ depended on the X-position at F9, which is in first order correlated with the momentum of the particle, and was limited by the acceptance of the ZeroDegree spectrometer. Thus, it was important to check the center of the beam X-distribution at the F9 focus. The correlation between F5X and F9X for each reaction channel is to be compared with the one of the transmission measurement. The cases of the ^{79}Cu$(p,2p)^{78}$Ni and ^{80}Zn$(p,2p)^{79}$Cu reactions are shown in Figure 5.3. Both structures have similar trends as Fig. 5.1. Note that the horizontal slit width at F5 was reduced from F5X = $(-75,120)$, until run 246, to F5X = $(-65,120)$, from run 247, as listed in Tab. 3.4[a)].

To confirm the performance of this analysis, the events were divided into several bins as a function of F5X position, and the respective inclusive cross sections were calculated individually to see the momentum dependence of the transmission efficiency on F5X, as shown in Fig. 5.2, were properly taken into account. Equation (5.2) was changed to describe the cross section as function of the F5X position, x, as:

$$\sigma_{incl}(x) = \frac{N_{ZD}(x)}{N_{BR}(x) \cdot \tau(x) \cdot n_{dc}}. \tag{5.4}$$

The calculated cross sections for ^{79}Cu$(p,2p)^{78}$Ni and ^{80}Zn$(p,2p)^{79}$Cu reaction channels as a function of F5X are shown in Fig. 5.4. The deduced values were constant within the error bars, which shows that the position dependence of the transmission efficiency of the ZeroDegree spectrometer was properly taken into account. The average values between F5X= $(-60,60)$ mm for these reactions were obtained to 1.7(4) mb and 8.0(3) mb as the inclusive cross sections for the respective channels.

The same analysis was applied to ^{80}Zn$(p,3p)^{78}$Ni and ^{81}Ga$(p,3p)^{79}$Cu reactions. As the change of A/Q after the $(p,3p)$ reaction was much different from $(p,2p)$ reactions, the centroid of the beam in BigRIPS will not correspond to the centroid of the beam in the ZeroDegree spectrometer. To treat such cases properly, the coordinate in Eq. (5.4) should be justified from the previous analysis, aligning with the $(p,2p)$ channels and the transmission measurement run. A coordinate transformation, $x \rightarrow x' = x + \Delta$, was applied to the distribution of the numbers of particles of gated on BigRIPS, $N_{BR}(x)$, and gated on BigRIPS and ZeroDegree, $N_{ZD}(x)$, as described below:

$$\sigma_{incl}(x+\Delta) = \frac{N_{ZD}(x+\Delta)}{N_{BR}(x+\Delta) \cdot \tau(x) \cdot n_{dc}}. \tag{5.5}$$

Though the momentum $B\rho$ is described with a first order approximation of Eq. (2.2) as:

$$B\rho \propto \frac{A}{Q}\beta, \tag{5.6}$$

[a)] The direction of the coordinate in the analysis framework ANAROOT [137] is opposite from the normal BigRIPS/ZeroDegree coordinate.

Tab. 5.1: List of measured inclusive cross sections for the $(p,2p)$ and $(p,3p)$ reactions.

Reaction	Cross section σ_{incl} (mb)	F5X offset Δ (mm)
^{78}Cu$(p,2p)^{77}$Ni	2.7(3)	0
^{79}Cu$(p,2p)^{78}$Ni	1.7(4)	0
^{79}Zn$(p,2p)^{78}$Cu	6.6(3)	0
^{80}Zn$(p,2p)^{79}$Cu	7.9(3)	0
^{81}Zn$(p,2p)^{80}$Cu	1.3(4)	0
^{80}Ga$(p,2p)^{79}$Zn	6.2(4)	0
^{81}Ga$(p,2p)^{80}$Zn	5.2(3)	0
^{82}Ge$(p,2p)^{81}$Ga	7.1(9)	0
^{79}Zn$(p,3p)^{77}$Ni	0.031(8)	45
^{80}Zn$(p,3p)^{78}$Ni	0.017(7)	45
^{80}Ga$(p,3p)^{78}$Cu	0.059(14)	45
^{81}Ga$(p,3p)^{79}$Cu	0.081(7)	45
^{82}Ga$(p,3p)^{80}$Cu	0.034(23)	45

it was difficult to deduce Δ by simply multiplying the dispersion coefficient of the ZeroDegree spectrometer because the energy loss in the target depends on the mass (A) and charge (Q) of the particle. Therefore, the offset values, Δ, were determined by adjusting the F9X to F5X correlation to be similar to Fig. 5.5. In this $(p,3p)$case, the F5X was shifted by 45 mm, *i.e.*, F9X in vertical axis vs F5X + 45 mm in the horizontal axis, as shown in Fig. 5.5. The distribution of the inclusive cross sections with respect to the corrected F5X position is shown in Fig. 5.6. To exclude ambiguity of the numbers of incoming beams as the slit condition was set F5X=-65 mm at the beginning of the measurement and changed to F5X=-75 mm later, the data points below -20 mm in this plot were not used in the analysis. Within this range F5X= $(=20,60)$ mm, it can be confirmed that the correction works properly since the inclusive cross sections had a rather constant tendency with respect to the F5X position. This result also supports the systematic error is negligibly small compare to the statistical errors. Note that the specifically low value at F5X= -30 mm in the ^{81}Ga$(p,3p)^{79}$Cu channel might be induced from contaminant events in the BigRIPS PID.

5.1.3 Systematics of inclusive cross sections

The same analysis as Eq. (5.5) was applied to several other reaction channels. Table 5.1 lists measured inclusive cross sections σ_{incl} and statistical errors of one standard deviation. Note that, as discussed above, the systematic error for this analyais can be thought as negligibly small compare to the statistical errors. Figure 5.7 illustrates the systematic trends along three isotonic chains ($N = 49-51$) for the $(p,2p)$ and $(p,3p)$ channels. Obviously, the cross sections to produce nickel isotopes are systematically smaller than other isotopes. For example, the cross sections for $(p,2p)$ reactions in the ZeroDegree spectrometer along $N = 49$ and 50 chains decrease suddenly from ≈ 6 mb to 1.7(4) mb for ^{78}Ni. A similar phenomenon is seen for $(p,3p)$ reactions dropping from ≈ 60 μb to 16(6) μb for ^{78}Ni. This sudden decrease, which may be due to the large shell gap at $Z = 28$, which causes the population at higher excited states above the neutron separation energy, will be discussed with the recently developed reaction theory in section 6.2.

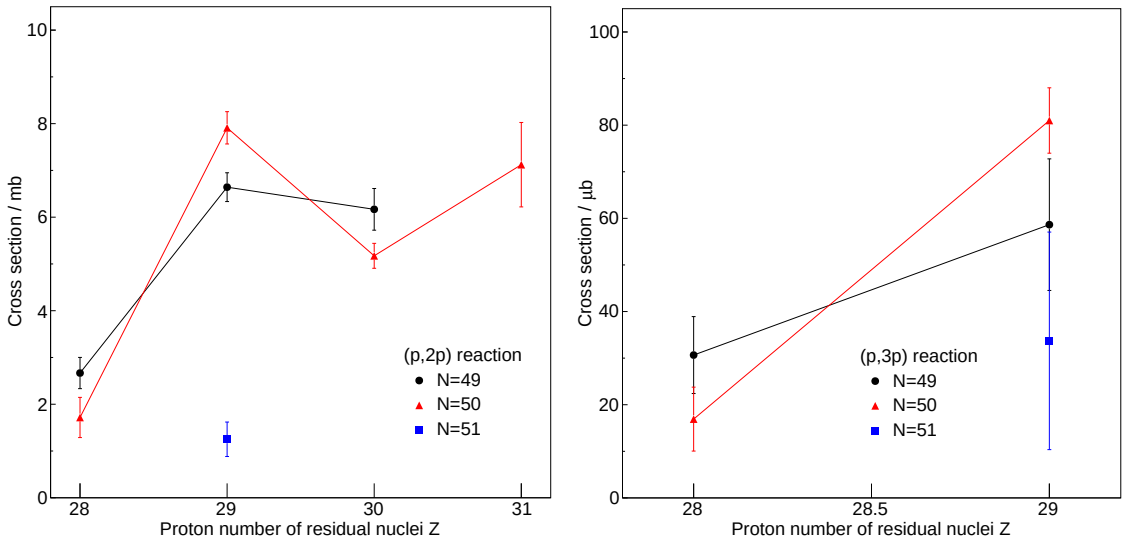

Fig. 5.7: Systematic trend of the obtained inclusive cross sections around ^{78}Ni. The $(p,2p)$ and $(p,3p)$ reactions along N = 49-51 isotones are illustrated in the left and right panels, respectively. Sudden decreases in cross sections for nickel isotopes can be seen. The drop in the cross section for N = 51 isotones may be explained by the decreased neutron separation energy, and thus available final states for the reaction products may be limited.

5.2 Determination of the γ-ray transitions from excited states

The energy spectra were obtained by Doppler correction of the measured γ-ray energy using the vertex position and the reconstructed velocity, as introduced in section 4.3.2. Because the energy of the γ-ray of interest was expected to be as high as 3 MeV, the add-back analysis, as detailed in section 4.3.1, was applied with a 15-cm add-back distance. In this section, energies of the γ-ray transitions are derived in accordance with the statistical treatment for the energy determination explained in section 5.2.1. By utilizing the statistical methods, specific results for the $(p,2p)$ and $(p,3p)$reactions are discussed. It may be assumed as a naive picture that the $(p,2p)$ reaction favors population of the single-particle states, while the $(p,3p)$ reaction, which involves two protons in the projectile nucleus at the same time, generates various states, including some collective states. Thus, the analysis of the $(p,2p)$ channel was firstly investigated in section 5.2.2, and then the $(p,3p)$ channel is discussed in section 5.2.3, as the spectrum of the $(p,2p)$ channel was supposed to be simpler than the one of the $(p,3p)$ channel. In section 5.2.4 the discrepancy of the energies observed between two channels are discussed.

5.2.1 Energy determination with maximum likelihood

(1) Fit with simulated response functions

The γ-ray spectrum can be described with several peaks and two exponentials. The latter represent the background at low and high energy. The peaks with energies $\mathbf{E} = (E_1, \cdots, E_i, \cdots, E_N)$ are described with response functions $f_{E_i}(\varepsilon)$. Then, the function $F_{\mathbf{E}}(\varepsilon)$:

$$F_{\mathbf{E}}(\varepsilon) = \sum_{i=1}^{N} C_i \cdot f_{E_i}(\varepsilon) + Ae^{-\alpha\varepsilon} + Be^{-\beta\varepsilon}, \tag{5.7}$$

describes the full spectrum. Here, the C_i are the intensity of each peak. There are several possible origins of the background events in the spectra, such as unresolved γ-ray transitions and

energy deposition of recoil protons or other particles in the scintillator, thus it was assumed as a double-exponential function with four parameters: A, B, α, β. To determine each peak energy E_i in such a multi-peak spectrum, multivariate probability density functions (PDFs) were used.

(2) Maximum likelihood with binned histograms

Principles Firstly, the response functions of the γ-ray detector with several γ-ray energies were simulated to obtain the probability by fitting the given spectrum with possible combinations of the peak energies of $\mathbf{E} = (E_1, \cdots, E_i, \cdots, E_N)$. The spectrum was binned with 10 keV width to allow the determination of the energy with a precision of $\approx$ 10 keV. Because the count of each bin is expected to be small to use normal chi-square fittings, the maximum binned likelihood method with the assumption that each bin count follows a Poisson distribution is taken. The given spectrum is fitted by Eq. (5.7) with the variables A, B, α, β and C_i. Note that the spectrum below 300 keV was not used in the fitting, because the energy thresholds of the CFDs for NaI(Tl) crystals were set around 150 keV in the laboratory frame, which is equivalent to 300 keV in the center-of-mass frame for the most backward angle. The fittings are processed by the Minuit framework implemented in the ROOT software package [136, 146].

The likelihood of the Poisson distribution $L_p(\mathbf{E})$ and the Gaussian (or normal) distribution $L_g(\mathbf{E})$ for each combination of $\mathbf{E} = (E_1, \cdots, E_i, \cdots, E_N)$ obtained after fitting the given binned-spectrum (histogram) $M(\varepsilon)$ with the number n of bins are formulated as:

$$L_p(\mathbf{E}) = \prod_{j=1}^{n} \exp\left(-F_{\mathbf{E}}(\varepsilon_j)\right) \cdot \frac{\left(F_{\mathbf{E}}(\varepsilon_j)\right)^{M(\varepsilon_j)}}{M(\varepsilon_j)!}, \tag{5.8}$$

$$L_g(\mathbf{E}) = \prod_{j=1}^{n} \frac{1}{\sqrt{2\pi}\cdot\sigma_j} \exp\left(-\frac{1}{2}\frac{\left(F_{\mathbf{E}}(\varepsilon_j) - M(\varepsilon_j)\right)^2}{\sigma_j^2}\right). \tag{5.9}$$

Here, the denominator of $L_g(\mathbf{E})$, σ_j^2, is the error of each bin; if the error follows the Gaussian distribution as an asymptotic limit of the Poisson distribution, $\sigma_j^2 = F_{\mathbf{E}}(\varepsilon_j)$. Note that when the statistics of each bin $M(\varepsilon)$ are large enough, L_p approaches asymptotically to L_g, as shown with Stirling's approximation below:

$$\log L_p(\mathbf{E}) = \sum_{j=1}^{n} \left\{-F_{\mathbf{E}}(\varepsilon_j) + M(\varepsilon_j)\log(F_{\mathbf{E}}(\varepsilon_j)) - \log(M(\varepsilon_j)!)\right\} \tag{5.10}$$

$$\simeq \sum_{j=1}^{n} \left\{-\left(F_{\mathbf{E}}(\varepsilon_j) - M(\varepsilon_j)\right) - \log\left(\sqrt{2\pi M(\varepsilon_j)}\right)\right\} + M(\varepsilon_j)\log\left(1 + \frac{F_{\mathbf{E}}(\varepsilon_j) - M(\varepsilon_j)}{M(\varepsilon_j)}\right) \tag{5.11}$$

$$\simeq \sum_{j=1}^{n} \left\{-\left(F_{\mathbf{E}}(\varepsilon_j) - M(\varepsilon_j)\right) - \log\left(\sqrt{2\pi M(\varepsilon_j)}\right)\right\} + M(\varepsilon_j)\left(\frac{F_{\mathbf{E}}(\varepsilon_j) - M(\varepsilon_j)}{M(\varepsilon_j)} - \frac{1}{2}\cdot\frac{\left(F_{\mathbf{E}}(\varepsilon_j) - M(\varepsilon_j)\right)^2}{\left(M(\varepsilon_j)\right)^2}\right) \tag{5.12}$$

$$= \sum_{j=1}^{n} \left\{\frac{\left(F_{\mathbf{E}}(\varepsilon_j) - M(\varepsilon_j)\right)^2}{2M(\varepsilon_j)} - \log\left(\sqrt{2\pi M(\varepsilon_j)}\right)\right\} \tag{5.13}$$

$$= \log L_g(\mathbf{E}). \tag{5.14}$$

Likelihood ratio and χ^2 value The common feature between the maximum likelihood and the least χ^2 is that both values are used to determine the most appropriate fitting for a certain probability distribution. In practice, the likelihood ratio λ is used for the fitting procedure for the maximum likelihood method as standardization:

$$\lambda(\mathbf{E}) = \frac{L(\mathbf{E})}{L_0}. \tag{5.15}$$

The value of L_0 is the likelihood when the fitting function $F_{\mathbf{E}}(\varepsilon_j)$ is exactly the same as $M(\varepsilon_j)$. More generally, the log-likelihood ratio,

$$\log\lambda = \log\frac{L(\mathbf{E})}{L_0} = \log L(\mathbf{E}) - \log L_0, \tag{5.16}$$

is commonly used for the fitting algorithms because it is equivalent to Pearson's χ^2 for the Gaussian distribution:

$$-2\log\frac{L_g(\mathbf{E})}{L_0} = -2\sum_{j=1}^{n}\left\{\frac{\left(F_{\mathbf{E}}(\varepsilon_j) - M(\varepsilon_j)\right)^2}{2M(\varepsilon_j)} - \log\left(\sqrt{2\pi M(\varepsilon_j)}\right)\right\} + 2\sum_{j=1}^{n} -\log\left(\sqrt{2\pi M(\varepsilon_j)}\right) \tag{5.17}$$

$$= -2\sum_{j=1}^{n}\frac{\left(F_{\mathbf{E}}(\varepsilon_j) - M(\varepsilon_j)\right)^2}{2M(\varepsilon_j)} \tag{5.18}$$

$$= \sum_{j=1}^{n}\frac{\left(F_{\mathbf{E}}(\varepsilon_j) - M(\varepsilon_j)\right)^2}{\sigma_j^2} = \chi_g^2. \tag{5.19}$$

The error of one standard-deviation is defined as the interval of the maximum log-likelihood ratio decreased by 0.5 as well as increased by 1.0 for the least χ^2.

Note that the log-likelihood ratio for the Poisson distribution is calculated as [63, 147]:

$$-2\log\frac{L_p(\mathbf{E})}{L_0} = 2\sum_{j=1}^{n}\left\{F_{\mathbf{E}}(\varepsilon_j) - M(\varepsilon_j) + M(\varepsilon_j)\log\frac{M(\varepsilon_j)}{F_{\mathbf{E}}(\varepsilon_j)}\right\}. \tag{5.20}$$

Multivariate probability density function (PDF) to determine the peak energies In general, the likelihood $L(\mathbf{E}|M)$ is defined as the event probability of the measured data set within the assumption of the set of parameters, $p(M|\mathbf{E})$, with a certain set of parameters $\mathbf{E}$ for the measured data set M.

$$p(M|\mathbf{E}) = L_p(\mathbf{E}|M). \tag{5.21}$$

Because the peaks are thought to be independent of each other, the summed PDF for the i-th peak $P_i(E_i)$ can be described with the sum of the probabilities $p(M,\mathbf{E})$ with a constant coefficient for standardization κ as:

$$P_i(E_i) = \kappa\sum_{E_1}\cdots\sum_{E_{i-1}}\sum_{E_{i+1}}\cdots\sum_{E_N} p(M|\mathbf{E}). \tag{5.22}$$

Then, the obtained PDF $P_i(E_i)$ is fitted by a normal distribution to deduce the centroid and 1-σ error of the peak energy. This PDF method had been applied to a similar work to the one discussed in this thesis. Note that in Ref. [85], the obtained statistics were sufficient to allow for the usage of normal distributions.

(3) Practical procedure of the energy determination

The analysis described above was done with a combination of GEANT4 [139–141], the ROOT software package [136, 146], and the R language [148].

Simulation and maximum likelihood fittings The response functions of the γ-ray detector with several γ-ray energies were simulated [141] for 5 to 10 keV intervals. Then, each possible combination of the peaks of $\mathbf{E} = (E_1, \cdots, E_i, \cdots, E_N)$ was fitted with a double-exponential background to obtain the log-likelihood ratio. During the fitting procedure in the ROOT software, the maximum likelihood was obtained by minimizing the log-likelihood ratio, $-\log\lambda$ (see the definition in Eq. (5.16)). When the histogram of the spectrum $F_{\mathbf{E}}(\varepsilon_j)$ is assigned as `TH1F *h`, the value (in this case, `amin`) can be extracted by a script after using the likelihood fitting ("L" option) as:

```
Double_t likelihood(TH1F *h){ // The histogram of interest
   Double_t amin, edm, errdef;
   Int_t nvpar, nparx;
   TVirtualFitter *fitter = TVirtualFitter::Fitter(h);
   fitter->GetStats(amin, edm, errdef, nvpar, nparx);
   return amin; // Return the log-likelihood ratio
}
```

Likelihood ratio and projecting to PDF of each peak Every calculated likelihood ratio was summed following Eq. (5.22) with the R language [148]. The summed PDF of each spectrum was plotted with respect to the energy of the peak, and the position of the peak and the area of 68% probability were determined. While the distribution might not follow any specific distribution, a normal distribution was assumed to deduce the γ-ray energy and its uncertainty from the PDF distribution.

5.2.2 γ-ray spectra of ^{79}Cu$(p,2p)^{78}$Ni channel

The γ-ray spectrum of the $(p,2p)$ reaction was assumed to be simpler than that of the $(p,3p)$ channel, since it was expected to populate only single-particle states. Thus, the γ-ray spectrum of ^{79}Cu$(p,2p)^{78}$Ni was analyzed prior to ^{80}Zn$(p,3p)^{78}$Ni channel.

(1) Energy spectra with different γ-ray multiplicities

The Doppler corrected γ-ray energy spectra of the ^{79}Cu$(p,2p)^{78}$Ni reaction are shown in Fig. 5.8 with several gating conditions of detected γ-ray multiplicity, m, which is defined as the number of the γ-ray hits after the add-back analysis with 15-cm add-back distance. In the case the add-back analysis is appried properly, m should be equal to or less than the number of the emitted γ rays from the nucleus. However, in the real case, it can be more because of Compton-scattered γ rays, which are not added back to a full energy peak event. In other words, constraining the condition of m to small values helps obtaining clear γ-ray peaks, avoiding the Compton-scattered events, while the m condition should not be too strict, as it also reduces the statistics. Therefore, it is important to find the optimum conditions for m to acquire the best signal-to-noise ratios, which are related to the significance levels. The evolution of the heights of peaks with a function of m gating can be seen in the respective spectra displayed in Fig. 5.8. Peak structures, located at around 600, 1100, 1500, and 2600 keV, can be clearly confirmed, besides a bump structure around 2000 keV. The 2600-keV peak is particularly visible in the

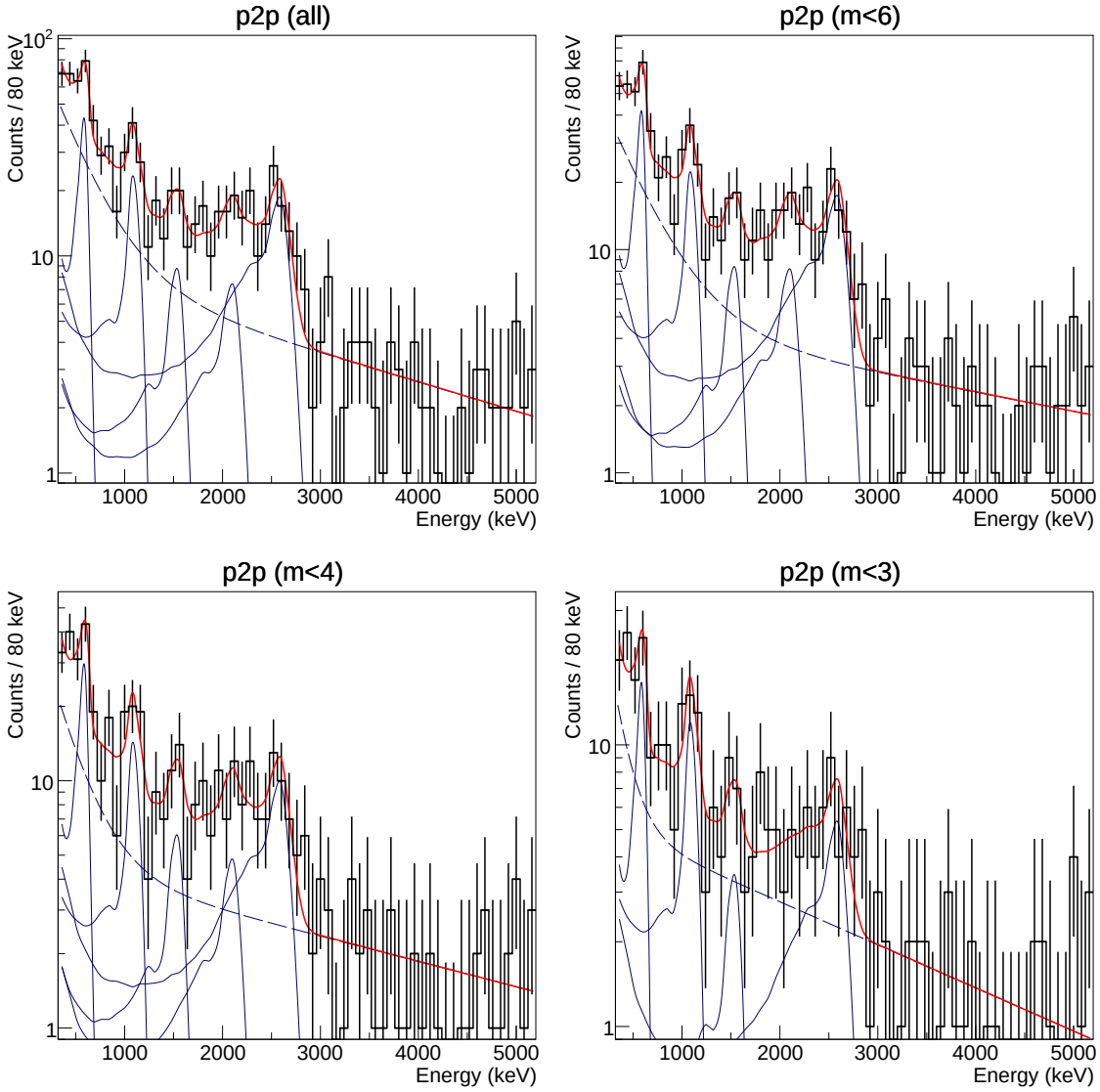

Fig. 5.8: Doppler corrected γ-ray spectra following the ^{79}Cu$(p,2p)^{78}$Ni reaction. 80 keV binning is adopted for the illustrations with several gatings of γ-ray multiplicity, m. The red curve is the fitting curve with maximum likelihood, while the blue line and blue dashed line are the each response function and the double-exponential background, respectively. Note that the histograms with linear scales are displayed in appendix Fig. B.2.

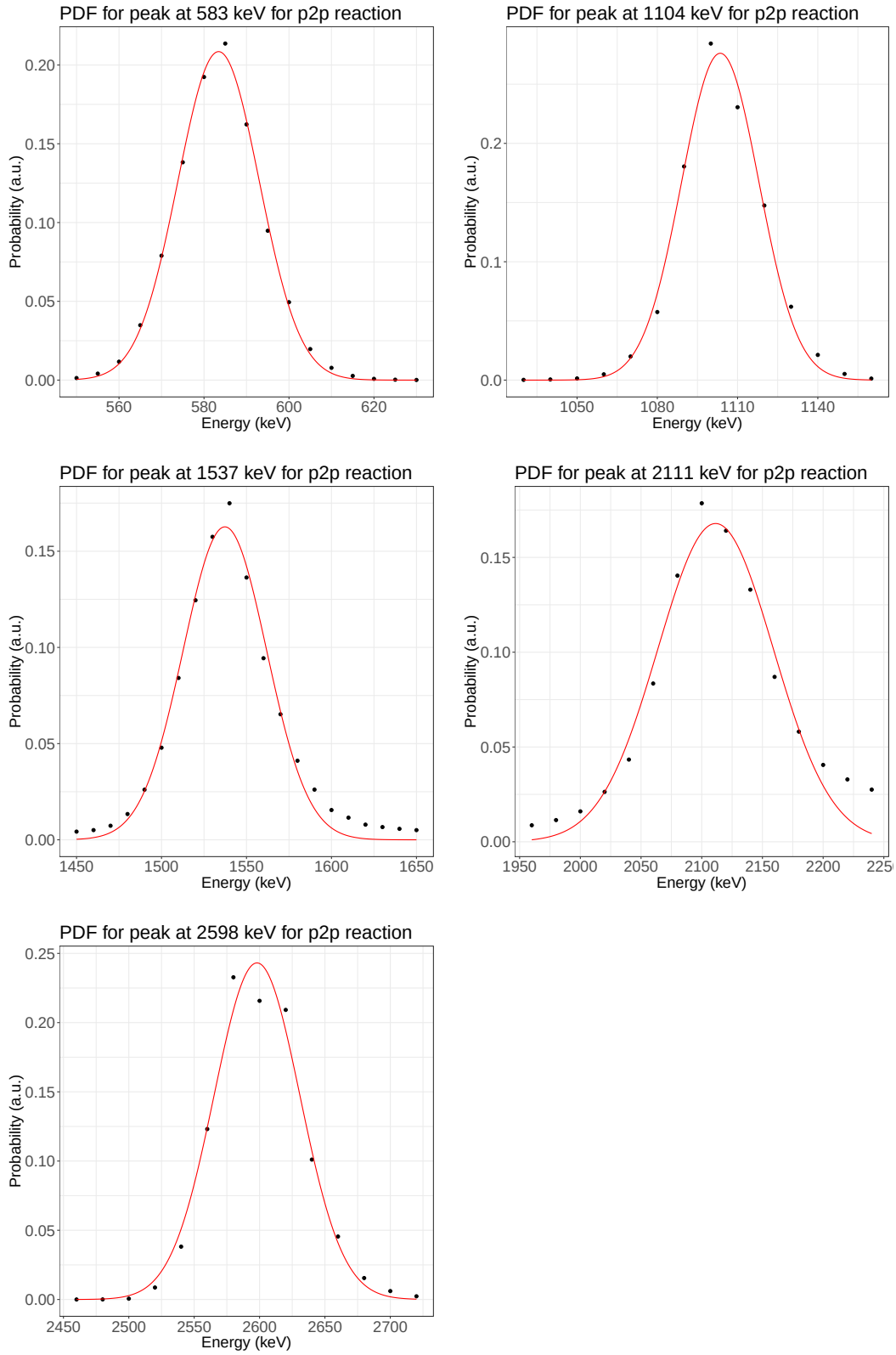

Fig. 5.9: Determination of each γ-ray energy in the $(p,2p)$ reaction with probability density functions. The probabilities as a function of the energy (black dots) are fitted with a normal distribution (red curve). For this analysis, any conditions for the γ-ray multiplicity m were not applied.

$m < 3$ spectrum, though the lower energy γ-ray peak should be distinct for such condition in general, as the detection efficiency for the lower energy was high. This may be an indication of the 2600-keV peak is a transition from the first excited state to the ground state. Here, the spectrum was fitted with the five simulated response functions to obtain their energies. The determination of each energy is introduced in the next section.

(2) Energy determination with PDF analysis

The energies of the five peak-candidates found in the γ-ray spectrum of the $(p,2p)$ channel were determined by the probability density functions as discussed in section 5.2.1. The combinations of the energy of peaks, $\mathbf{E} = (E_1, \cdots, E_i, \cdots, E_N)$, were selected as following:

- 550 to 630 keV with 5 keV interval
- 1030 to 1160 keV with 10 keV interval
- 1450 to 1650 keV with 10 keV interval
- 1960 to 2240 keV with 20 keV interval
- 2460 to 2720 keV with 20 keV interval

The distribution of the standardized PDF for each peak, which was calculated with Eq. (5.22), is drawn in Fig. 5.9. The PDF was assumed to approximately obey a normal distribution, to deduce the position of the peak and the area of 68% probability, which is the definition of 1-σ.

The centroid and the one-sigma range, which correspond to the statistical error of the peak energy, for these peaks are summarized in the second column of Tab. 5.2. The simulated curves of the five response functions, after the determination of the energies, and a double-exponential background are drawn in Fig. 5.8 on top of the obtained Doppler corrected γ-ray spectra. Note that the 2600 keV is the strongest γ-ray transition after the correction of the detection efficiency. Thus, it is tentatively assigned as the one from first excited state to the ground state. The relative intensity of each transition is also described in Tab. 5.2. The significance of each peak is discussed later in section 5.3.

5.2.3 γ-ray spectra of ^{80}Zn$(p,3p)^{78}$Ni channel

(1) Energy spectra with different multiplicities

Figure 5.10 shows the Doppler corrected γ-ray spectra of the $(p,3p)$ reaction channel with different multiplicity gatings, $m < 6$ and $m < 3$. Since the ^{80}Zn$(p,3p)^{78}$Ni channel has less number of events, and may have populated more states than the ^{79}Cu$(p,2p)^{78}$Ni channel, the γ-ray transitions were analyzed based on the obtained information from the $(p,2p)$ channel. Compare to the one obtained for the $(p,2p)$ channel, a clear manifestation of a γ-ray transition above 2600 keV can be seen that there were obviously some events at 2900 keV separated from the background levels, which can be seen around the 3000 keV region. This energy was higher than the one seen in the $(p,2p)$ reaction channel around 2600 keV. In the spectrum with lower multiplicity gating $m < 3$, excess events around 2900 keV become more visible. As well as the discussion for the 2600-keV peak in the $(p,2p)$ channel, this implies that the transition may be a decay to the ground state directly. On the other hand, the strength of the transition of 2600 keV, which was the strongest one in the $(p,2p)$ channel, was not as large as the one of 2900 keV, in particular for the $m < 3$ gating. The reason might be understood by the different mechanisms of the reactions. With in a naive discussion, while the $(p,3p)$ reaction might populate states at higher energy as two protons are involved in the reaction resulting in many γ-ray transitions, as well as higher spin states, the one at 2900 keV might be an exception as it was clear with low

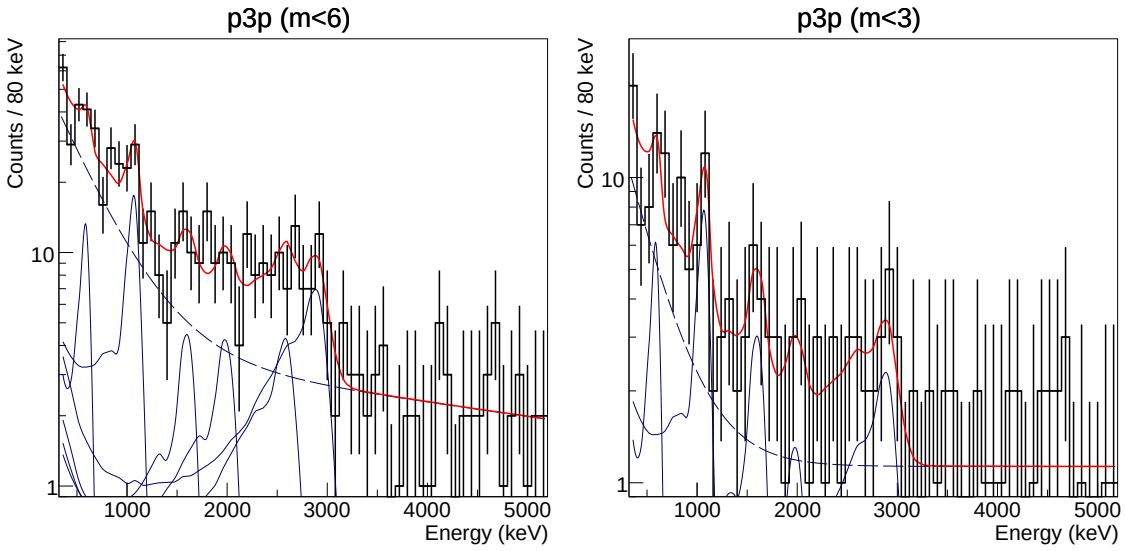

Fig. 5.10: γ-ray spectra after the ^{80}Zn$(p,3p)^{78}$Ni reaction. 80 keV binning is adopted for the illustrations of two gating conditions for the γ-ray multiplicity: $m < 6$ and $m < 3$. The red curve is the fitting curve with maximum likelihood, while the blue line and blue dashed line are the response functions and the double-exponential background, respectively. Note that the histograms with a linear scale are displayed in appendix Fig. B.3.

γ-ray multiplicity m gatings. This state will be further discussed in the next chapter as a possibility of a deformed state. Besides that, there were peak structures visible in the lower-energy region around 600 keV and 1100 keV.

(2) First attampt: Energy determination with PDF analysis with six peak candidates

As a first attempt, the Doppler corrected γ-ray spectrum was fitted with six simulated response functions, 2900 keV transition in addition to the five ones found in the $(p,2p)$ channel, even though three transitions at 1540, 2110 and 2600 keV were not visible. The energies of the six peak-candidates in the $(p,3p)$ channel were analyzed with the combination of the energy of peaks, $\mathbf{E} = (E_1, \cdots, E_i, \cdots, E_N)$, as following:

- 530 to 630 keV with 10 keV interval
- 1000 to 1140 keV with 20 keV interval
- 1440 to 1840 keV with 40 keV interval
- 1840 to 2160 keV with 40 keV interval
- 2400 to 3040 keV with 40 keV interval
- 2760 to 3040 keV with 40 keV interval

Note that the intervals of the fit energy were sparse from the one of the previous analysis in the $(p,2p)$ channel to reduce time of the computing, and also to make it possible to survey wider range of energy especially for the peaks of which the position cannot be recognized well by eye. Distributions of the standardized PDF for respective peaks are drawn in Fig. 5.11. As it can be seen from the shape of the energy spectrum, the PDF distributions of two peak candidates around 1600 and 2700 keV were rather scattered with large uncertainties, more than 200 keV, which inferred the non-existense of the peak in the $(p,3p)$ channel. Thus, another fitting excluding them was performed.

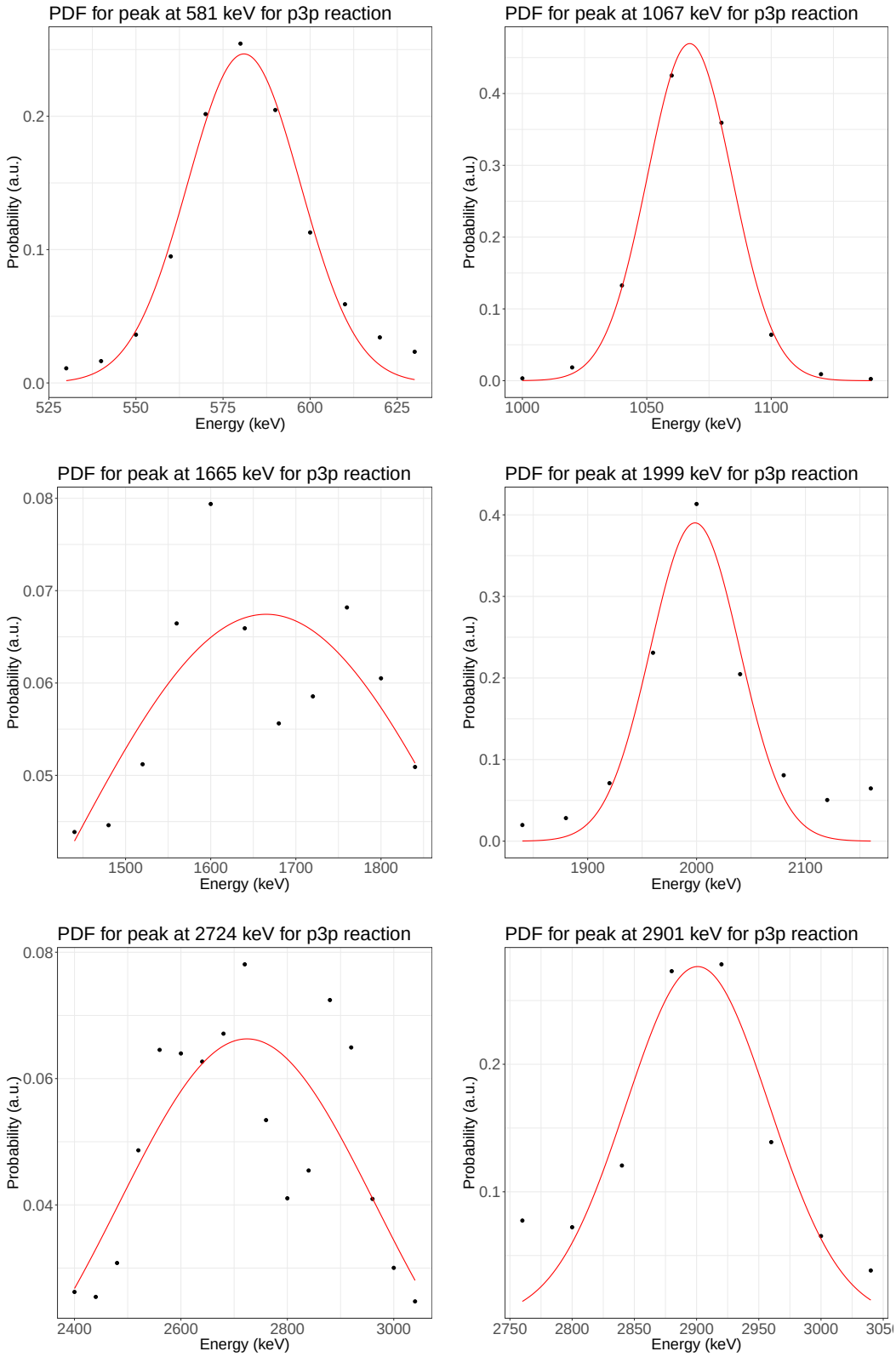

Fig. 5.11: Probability density functions with six peaks in the $(p,3p)$ reaction. The probabilities as a function of the energy (black dots) are fitted with a normal distribution (red curve). For this analysis, any conditions for the γ-ray multiplicity m were not applied.

(3) Second attampt: Energy determination with PDF analysis with four peak candidates

As the γ-ray transitions, which was observed in the $(p,2p)$ reaction channel at 1540 keV and 2600 keV could not be determined in the $(p,3p)$ channel, a fitting without the peak at 1600 keV and fixing the energy at 2600 keV for the other peak was examined as Fig. 5.12. Because the peak at 2600 keV, which was the strongest transition in the $(p,2p)$ channel, is thought to be possible to affect the determination of the energy at 2910 keV in the $(p,3p)$ spectrum, the peak at 2600 keV was kept fixed for the response function in Fig. 5.10 and later analysis. This is a similar approach with the case tested for the excited states of ^{80}Zn in section 4.4, for determining the peak position at high energy. In that case, the existence of a new tentative transition at 1600 keV was important to make the background estimation properly, though the intensity of the peak itself was small.

- 530 to 630 keV with 10 keV interval
- 1000 to 1140 keV with 20 keV interval
- 1840 to 2160 keV with 40 keV interval
- 2760 to 3040 keV with 40 keV interval
- And, peak with fixed energy at 2600 keV

As a consequence, obtained energies of the other four peaks are the same as in the previous fitting in Fig. 5.11, within the difference of one-tenths of the statistical uncertainties of the determined energy values. Such robustness of the peak energy can be understood as an indication that the parameters of them are rather independent among the peaks. The energy value and relative intensity of each transition to the most intense transition in this reaction channel, 2910 keV, are listed in Tab. 5.2.

5.2.4 Different γ-ray energy assignments between the $(p,2p)$ and $(p,3p)$ channels

As summarized in Tab. 5.2, some of the peaks have discrepancies in the energy between the different reactions. While the 583(10)-keV transition in the $(p,2p)$ channel is in good agreement with 581(16)-keV one in the $(p,3p)$ channel, with only 2 keV difference, the 1103(14)-keV transition in the $(p,2p)$ channel differs more than one standard deviation from the 1067(17)-keV transition in the $(p,3p)$ channel. Thus, the peaks around 1100 keV observed in the respective reaction channels might originate from different γ-ray transitions. This will also be discussed in the later analysis of γ-ray intensity relationships with other γ-ray transitions in each channel.

5.3 Significance levels

5.3.1 Principles of significance levels from the likelihood-ratio test

To obtain a quantitative criterion of the existence of the peak, the p-test, where two hypotheses without and with an assumption are compared, was commonly utilized. The former hypothesis of which the peak in question does not exist in this case, is called a null hypothesis H_0, while the one with the existence of the peak is called an alternative hypothesis H_1. If the probability of the establishment of the null hypothesis H_0 is small enough to get rejected, the alternative hypothesis H_1 is selected.

According to Wilks' theorem [149], the log-likelihood ratio of two hypotheses asymptotically follows the χ^2_d distribution with the degree of freedom d equal to the difference of the

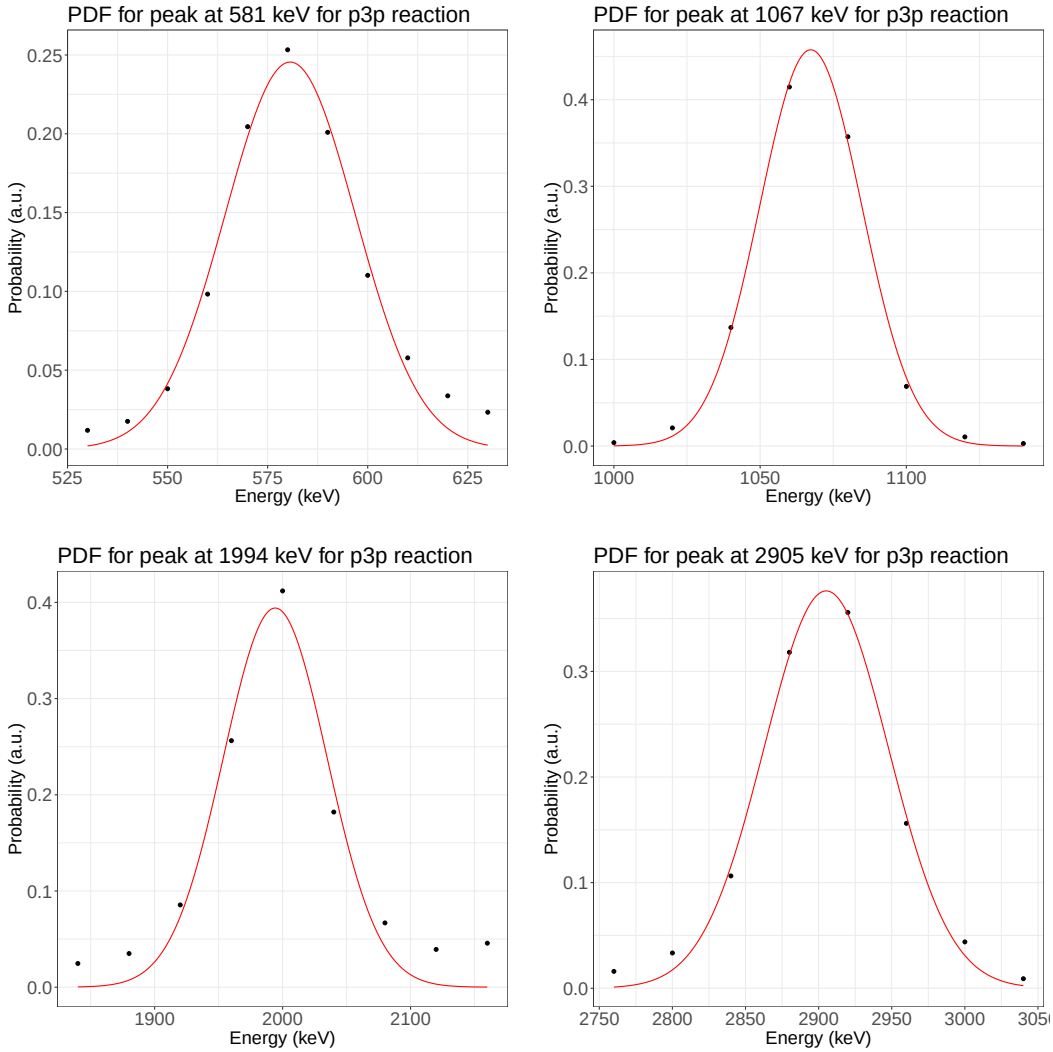

Fig. 5.12: Probability density functions with fixing two ambiguous peaks in the $(p,3p)$ reaction. The probabilities as a function of the energy (black dots) are fitted with a normal distribution (red curve). For this analysis, any conditions for the γ-ray multiplicity m were not applied.

ones in H_0 and H_1. In the case of this peak fitting, the equation for the i-th peak is written as:

$$\Lambda_i = \frac{L(\mathbf{E}|M)}{L_{-i}(\mathbf{E}|M)}, \qquad \text{where} \quad L(\mathbf{E}|M) : H_1, \quad L_{-i}(\mathbf{E}|M) : H_0. \tag{5.23}$$

$$-2\log\Lambda_i = 2\log L_{-i}(\mathbf{E}|M) - 2\log L(\mathbf{E}|M) \simeq \chi^2_{d=1}(x_i). \tag{5.24}$$

In this equation, the p-value of the null hypothesis p_0 is the right-hand side cumulative distribution function of $\chi^2_{d=1}$:

$$p_0 = \int_{x_i}^{\infty} \chi^2_{d=1}(x)\,dx. \tag{5.25}$$

In a normal statistical terminology, when the p-value is less than a pre-defined significance level α, the null hypothesis H_0 is rejected. In nuclear and particle physics, the n-σ confidence is mostly used instead of the p-value because it is easy to recognize [150]. In order to convert the p-value into the confidence level, the cumulative distribution function of the normal distribution $\Phi(x)$ is used:

$$\Phi(x) = \frac{1}{\sqrt{2\pi}} \int_{-\infty}^{x} e^{-\frac{t^2}{2}}\,dt. \tag{5.26}$$

The confidence level n is calculated by the inverse function Φ^{-1},

$$n = \Phi^{-1}\left(1 - p_0\right). \tag{5.27}$$

In particle physics, it is a *de facto* standard that the 5-σ confidence is required to claim a new observation/discovery and the 3-σ confidence is an indication. These criteria are adopted in this work.

5.3.2 Significance levels of the peaks and the candidates of 2^+ states

Here, the existence of each candidate for the γ-ray transition was checked quantitatively as described in the previous section. The significance level (S. L.) for the existence of each peak was deduced from the p-value of the likelihood ratio between the null hypothesis and the alternative hypothesis. They are listed as a function of the gates of the γ-ray multiplicity, m, in Tab. 5.2. Maximum values of S. Ls. within the m conditions are adopted to determine the existence of the peaks. The evolutions of the numbers of the γ rays and the S. Ls. for every transitions as a function of the γ-ray multiplicity, m, are illustrated in Fig. 5.13.

Evaluation of the uncertainty of the significance levels Prior to specific discussions about the existence of the observed γ-ray transitions, the reliability of the deduced S. Ls. is checked. By looking carefully the global trend of the S. Ls. in the charts of Fig. 5.13, it can be noticed all the graphs saturating at some point by loosening the conditions of the γ-ray multiplicity, m, and fluctuate within 0.5σ at the most. Though the S. L. is the only indicator of the probability of the existence, the reliability of itself is confirmed.

[i] Captions for Tab. 5.2: The significance level is tested with the obtained energy of 2910 keV from the analysis of the $(p,3p)$ channel. See text for the discussions.

[ii] Captions for Tab. 5.2: The energy value of 2600 keV, instead of 2710 keV, was used for the relative intensities I_{rel} and the significance levels. See text for the details.

Tab. 5.2: Observed γ-ray transition energies, relative intensities, and significance levels for the $(p,2p)$ and the $(p,3p)$ reaction channels. De-excitation energies E_γ with statistical errors (1 standard deviation) determined by maximizing likelihoods in PDF (see section 5.2) and the relative intensity I_{rel} to the most intensive transition for each reaction channel, 2600 keV and 2900 keV respectively, are listed. Here, the errors of energy and intensity are statistical only. In addition, the systematic error of energy determination is assumed as 0.6%, while the systematic error for the γ-ray intensity is supposed to be suppressed as for the case of the relative intensity. Significance levels (S. Ls.) of the existence of each peak (see section 5.3) as a function of the upper limit of the γ-ray multiplicity m are also listed. The largest values of S. Ls. within the m conditions are underlined.

Reaction	E_γ (keV)	I_{rel} (%)	S. L. (σ) with constraining the γ-ray multiplicity, m								
			All	≤ 8	≤ 7	≤ 6	≤ 5	≤ 4	≤ 3	≤ 2	$= 1$
$(p,2p)$	583(10)	49(11)	4.9	4.9	4.9	5.0	5.3	**5.7**	4.6	3.4	2.9
	1103(14)	49(12)	4.2	4.0	4.0	4.1	**4.3**	3.7	3.5	3.4	2.8
	1540(25)	28(11)	2.6	2.7	2.8	2.7	2.6	**2.9**	2.4	1.5	-0.2
	2110(48)	33(13)	2.5	2.5	2.8	2.8	**2.9**	2.6	1.9	-1.4	0.0
	2600(33)	100(15)	7.6	7.5	7.4	**7.6**	7.5	7.5	5.3	4.0	2.2
	2910(43)[i)]	—	1.4	1.3	**1.6**	1.4	1.2	1.2	1.5	1.1	1.3
$(p,3p)$	581(16)	46(20)	**2.3**	1.2	2.2	1.1	1.6	0.4	1.7	0.7	1.8
	1067(17)	82(27)	3.4	2.7	**3.5**	2.9	3.5	2.9	2.8	2.3	3.3
	1670(240)	19(24)	0.2	-0.2	0.4	0.1	**0.7**	0.5	0.2	0.0	0.2
	2000(40)	65(26)	**2.5**	2.2	2.5	2.3	2.4	2.1	1.5	1.3	1.3
	(2600)[ii)]	48(30)	1.3	1.3	1.5	1.5	1.4	**1.6**	1.2	1.3	1.4
	2910(43)	100(30)	3.7	3.4	3.4	3.1	3.5	3.2	**3.7**	3.5	3.6

The (p,2p) channel It is affirmed that the most intensive transition in the (p,2p) channel at 2600 keV scored the highest significance level, 7.6σ, with a $m \leq 6$ condition. The only peak other than the 2600-keV peak having the significance level larger than 5σ is the one at 583 keV with 5.7σ, while the ones at 1103, 1540 and 2110 keV marked about 3-4σ. In addition to the five proposed γ-ray transitions, the possibility of existence of the 2910 keV transition, which was observed in the (p,3p) channel but not in the (p,2p) channel, was tested. As shown in the table, the significance of this peak is only 1.6σ. Therefore, it is not included in any further analysis of the (p,2p) channel.

The (p,3p) channel As already noticed in the section 5.2.3, the most intense transition in the (p,2p) channel, 2600 keV, was not observed in the (p,3p) channel. The energy value of 2600 keV, instead of 2700(200) keV deduced by the PDF analysis, was used for the analysis of this channel, even though the significance of the 2600-keV transition itself was low. The peaks at 1067 keV and 2910 keV have the significance levels more than 3σ, while the ones at 581 keV and 2000 keV were between 2-3σ, of which the existence may not be indicated. Note that the γ-ray multiplicity condition, which gives the maximum significance for the 2910-keV transition, is $m \leq 4$. Though the significance level was not as large as 5σ, it was tentatively assigned as the transition directly feeding the ground state, because the intensity of the 2600-keV peak was much smaller than that of 2910 keV, even though it existed in the (p,3p) reaction.

5.4 Construction of the level scheme from γ-γ coincidence analysis

5.4.1 Strategy of γ-γ coincidence analysis

(1) Principle

By collecting events gated with at least one γ-ray observed within a certain range of energy, relationships between the γ-ray transition and others decaying in a cascade from higher lying states can be investigated. The γ-γ coincidence analysis was applied to the four most intense peaks among the (p,2p) and (p,3p) channels. In general, the energy gate was set to cover the region of a peak to be investigated to obtain the coincidence γ rays with the peak event. However, there was no way to select only the real γ rays within the coincidence gate, but background hits, such as Compton scattering events from transitions with different energy, cannot be avoided. Therefore, it is common to assume a background structure to subtract from the γ-ray spectrum. Such a background-subtracted spectrum can be derived by obtaining the differential between the coincidence spectrum and the off-gated one, which is a coincidence spectrum with background events by gating with certain ranges of the outside of the objective range. However, this treatment of the background subtraction was not implemented for this work because of the number of events was too small to discuss the γ-γ coincidence quantitatively. Furthermore, it was difficult to estimate the background structures because the structures of Compton scatterings and the peaks overlap in the γ-ray spectrum. Alternatively, to prevent such effects from the contaminants from Compton hits, the high energy γ-ray transitions were gated first, as no higher lying states to create Compton backgrounds within the energy gate of interest.

(2) Procedure of the γ-γ coincidence analysis

In the case of more than one γ-ray hit within the gated range, it is important to treat such events properly to avoid overestimating the number of γ-ray peaks within the range. Assuming that the number of unresolved γ-ray peaks within the energy range in one event is defined as n,

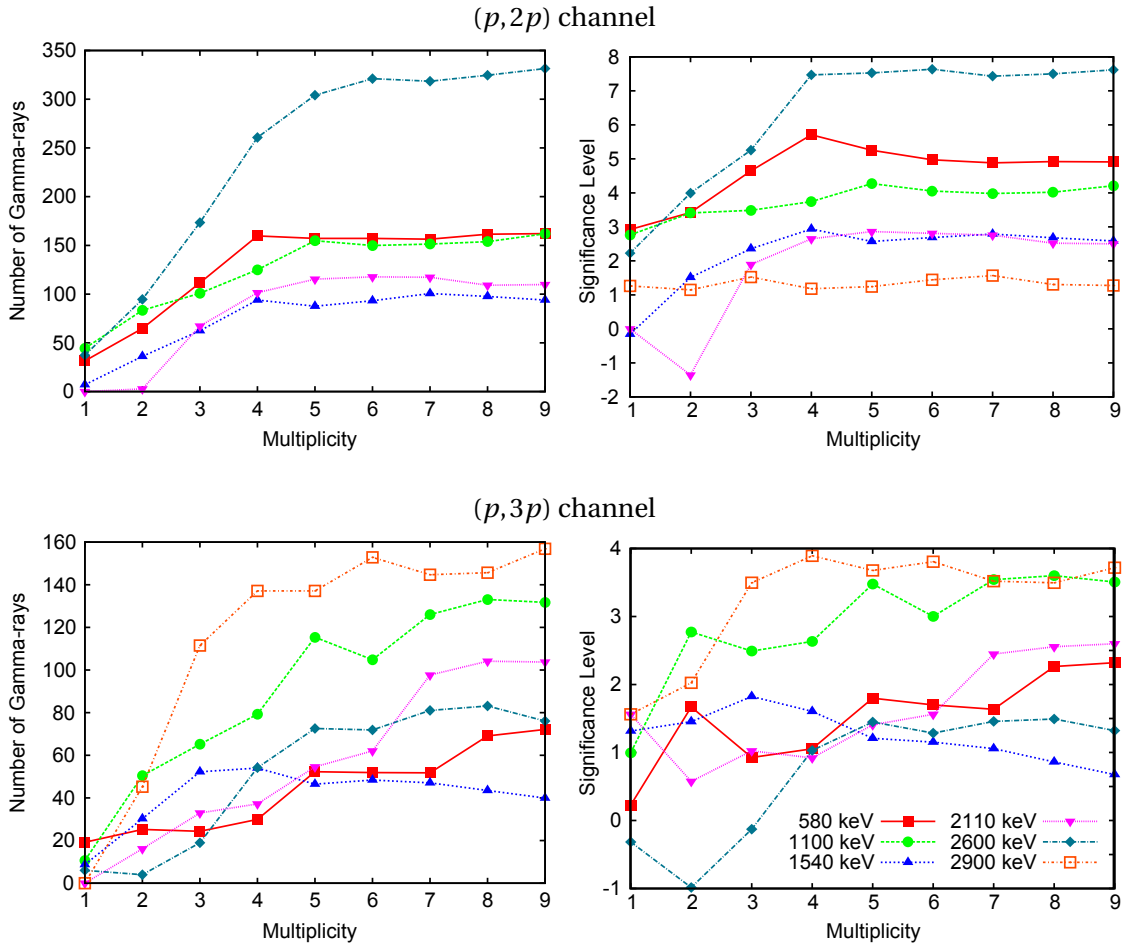

Fig. 5.13: Evolution of the number of γ rays (left panels) and the significance level of each transition as a function of the gates of the γ-ray multiplicity, m (right panels). The numbers on the horizontal axes, X, are the upper limit of the gating conditions, described as $m \leq X$. The points at $X = 9$ are the values with no gating condition of the γ-ray multiplicity. While the evoltions for the $(p,2p)$ channel are displayed in the top panels, the ones for the $(p,3p)$ channel are displayed in the bottom panels. The legend of the lines is placed in the bottom right figure.

the optimum γ-γ spectrum is generalized as a gated spectrum with $n-1$ peaks in the energy range of the gate. For the simplest case of $n = 1$, the γ-γ coincidence spectrum should be a spectrum without the peak in the gate, while for the $n > 1$ case, an "unresolved peak" with the γ-ray intensity of $n-1$ peaks should be appearing in the coincidence spectrum. Thus, the contribution of one of the peaks in the gate may be eliminated in the analysis. In this analysis, such events from multiple γ-ray hit within a gate were analyzed as the following way with the detected number of γ-ray hit within the gated range, N_{hit}. If there is only one γ-ray within the gate, $N_{hit} = 1$, the energies of the γ rays except the one in the gate are filled in the coincidence histogram, while in the case of more than one γ ray, $N_{hit} > 1$, fill all the events as $(N_{hit}-1)/N_{hit}$ event in the histogram. An alternative way for the simplicity is to select one of the γ rays within the gate to be eliminated from the coincidence spectrum and fill the other(s) in the spectrum.

(3) Counting the number of the events after the fitting

Assume the experimental γ-ray spectrum is binned with B_{exp}(keV) and the response function of the detector simulated by Monte-Carlo based GEANT4 with N_{sim} events is prepared with the same binning. The response function for a certain peak $f_{E_i}(\varepsilon)$[b)] is fitted with the coefficient p as $pf_{E_i}(\varepsilon)$ to the spectrum. In this case, the total number of γ rays emitted from the nuclei of interest during the measurement is calculated as:

$$N_\gamma = p \cdot N_{sim}. \tag{5.28}$$

Note that N_γ will be utilized to calculate the relative intensities I_{rel} and exclusive cross sections. By integrating[c)], or summing up the number of the values of the bins of simulated response function, $pf_{E_i}(\varepsilon)$, within the energy range of the coincidence gate for the γ-γ analysis, $(\varepsilon_-,\ \varepsilon_+)$, the number of "efficiency-corrected" γ rays within the coincidence gate, N_{gg}, can be derived as:

$$N_{gg} = \sum_{\varepsilon_- < \varepsilon < \varepsilon_+} pf_{E_i}(\varepsilon). \tag{5.29}$$

If the number of the efficiency-corrected γ rays from the γ-ray peaks of the i'-th γ-ray peak in coincidence, and the one of the γ-ray peak within the gate of interest, i-th, are defined as $N_{\gamma_i'}$ and N_{γ_i}, the coefficient, p', to deduce the expected response function of the i'-th peak in the gated coincidence spectrum can be derived by as follows by combining the two equations Eq. (5.28) and Eq. (5.29). There are two cases in the formulation, with the magnitude relation, $I_{ratio} = N_{\gamma_i'}/N_{\gamma_i}$. In the case of $N_{\gamma_i'} < N_{\gamma_i}$,

$$p' f_{E_{i'}}(\varepsilon') = \frac{N_{\gamma_i'}}{N_{\gamma_i}} \times \frac{N_{gg}}{N_{sim}} f_{E_{i'}}(\varepsilon') = \left(\frac{pN_{\gamma_i'}}{N_{\gamma_i} N_{sim}} \sum_{\varepsilon_- < \varepsilon < \varepsilon_+} f_{E_i}(\varepsilon) \right) \times f_{E_{i'}}(\varepsilon'), \tag{5.30}$$

[b)] The definition is same as the one in Eq. (5.7). This function corresponds to the one for the i-th peak at the energy of E_i.

[c)] In case of "integrating" the response function with software tools, such as root, it is important to be careful about the the binning of the experimental spectrum since such programs, such as `TF1::Integral()`, will simply calculate the area of the response function, while the number of events per the unit of energy in the binned γ-ray spectrum is described as $pf_{E_i}(\varepsilon)/B_{exp}$. Thus, the value should be divided by the width of the binning of the histogram as: $N_{gg} = \int_{\varepsilon_-}^{\varepsilon_+} d\varepsilon \frac{pf_{E_i}(\varepsilon)}{B_{exp}}$.

while, the other case of $N_{\gamma'_i} \geq N_{\gamma_i}$,

$$p' f_{E_{i'}}(\varepsilon') = \frac{N_{gg}}{N_{sim}} f_{E_{i'}}(\varepsilon') = \left(\frac{p}{N_{sim}} \sum_{\varepsilon_- < \varepsilon < \varepsilon_+} f_{E_i}(\varepsilon) \right) \times f_{E_{i'}}(\varepsilon'). \tag{5.31}$$

The latter case is assuming the case the gated γ-ray transition is followed by other γ-ray transitions. This response function with the expected intensity in the γ-γ spectrum can be used a rough indicator of the coincidence.

Note that the discussions above were performed with an assumption as background events, such as Compton scattered γ-ray hit from the higher energy γ-ray transitions, are not existing. In the realistic case, the expected response function can easily underestimate the γ-γ coincidence spectrum because no background subtraction was performed in these γ-γ coincidence analysis. In other words, if the experimental γ-γ spectrum is below the expected response functions, two γ-ray transitions were not in coincidence.

5.4.2 Obtained results from γ-γ analysis

As Compton background is limited to originated from the higher energy region for any gated transition, the γ-ray transition with the highest energy was gated first, then, lower-energy peaks were investigated to check the consistency with the analysis. The γ-γ coincidence spectra are shown in Fig. 5.14, where the energy of the gates are set as:

- 550 keV to 650 keV for the 580 keV peak
- 1000 keV to 1200 keV for the 1100 keV peak
- 2450 keV to 2750 keV for the 2600 keV peak

for the $(p,2p)$ channel, and

- 2750 keV to 3100 keV for the 2910 keV peak

for the $(p,3p)$ channel.

As defined in Eq. (5.30) and Eq. (5.31), the expected response functions with the expected intensity can be drawn in the coincidence spectra. Here, intensity ratios, $I_{ratio} = N_{\gamma'_i} / N_{\gamma_i}$, of the peaks were calculated based on the assignments obtained in the previous analysis, as listed in Tab. 5.2. The γ-γ coincidence spectra with several gating conditions on the obtained spectra are discussed in the following section.

(1) γ-γ coincidence analysis of the $(p,2p)$ channel

2600-keV peak As shown in the γ-ray spectra in Fig. 5.8, the peak at 2600 keV is much higher than the estimated background function. Thus, background events induced by Compton scattering hits from unrecognized higher lying transitions were assumed to be suppressed in the γ-γ coincidence spectrum. The coincidence spectrum in the bottom left panel of Fig. 5.14 shows all the lower-energy transitions having peak-like structures with a reduced background as expected, while it can also be recognized the estimated response functions are smaller than the obtained spectrum. As another possibility in addition to the inclusion of the background events, the underestimation of I_{rel} values of the peaks at 583, 1540, and 2110 keV in the γ-ray fit performed in section 5.2.2 can be considered. Though in this work, five γ-ray transitions were estimated in the $(p,2p)$ channel, there may be additional unresolved transitions undiscovered. Since the estimation of the background curve is found to be strongly connected with the inclusion of the γ-ray transitions in the fit, as already noticed in section 4.4, it can be reduced if other

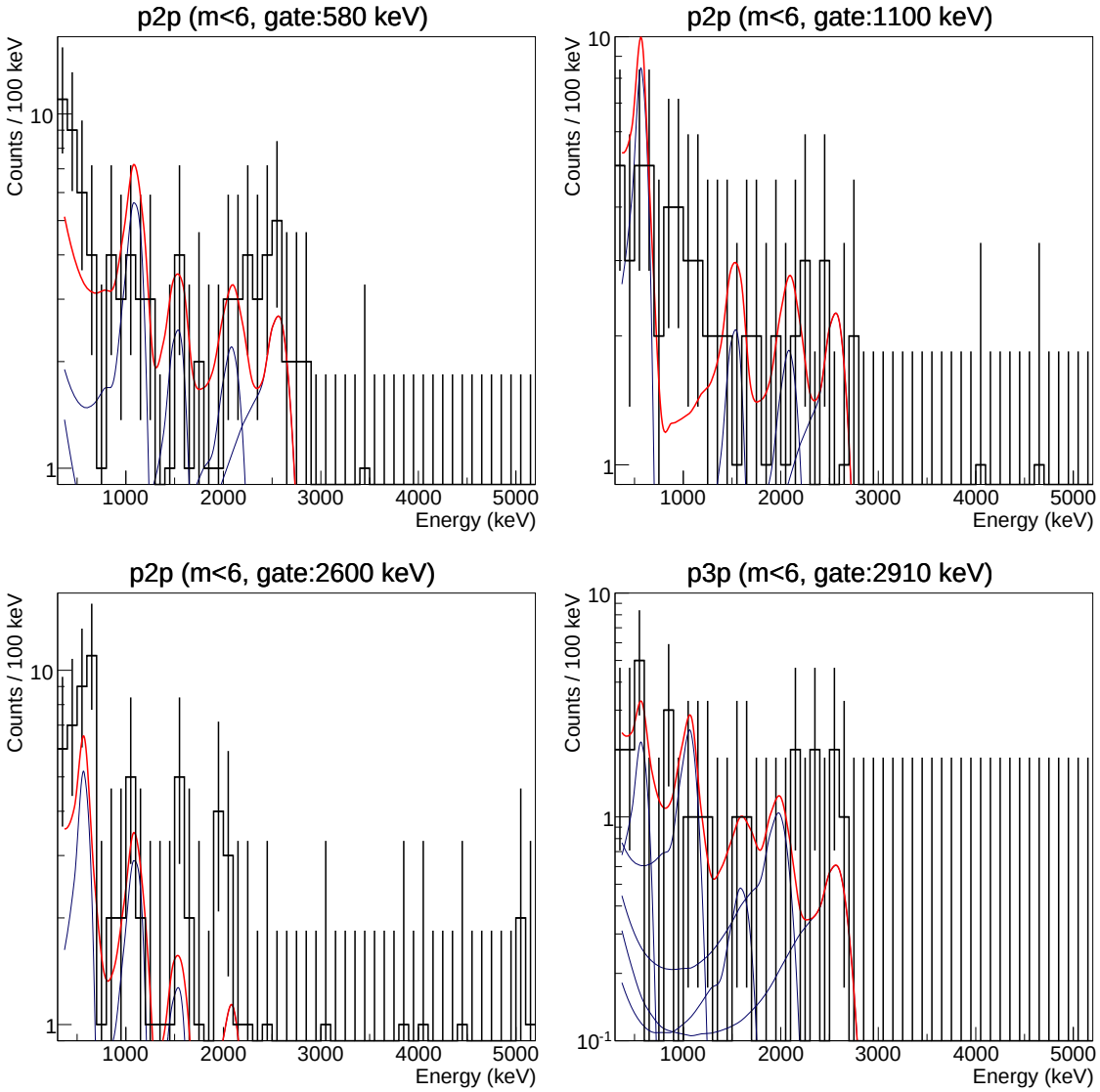

Fig. 5.14: γ-γ coincidence spectra with the expected response functions. The coefficients of the blue and the red curves are calculated based on the number of events within each coincidence gate. See text for detail discussions.

peaks taken into account, resulting in solving the possible underestimation of the intensity of the currently proposed five γ-ray transitions. In either case, all the four γ-ray transitions are reasonable to consider in coincidence with the 2600-keV transition. By taking into account the relationships of the γ-ray intensity, I_{rel}, the 2600-keV transition can be assumed as the γ-ray transition from the excited state at 2600 keV, feeding directly to the ground state.

580-keV peak The peak at 580 keV is the γ-ray transition with the second largest significance level and intensity in the $(p,2p)$ channel. However, the situation for the γ-γ coincidence analysis was different from the 2600-keV case. As seen in the Fig. 5.8, the peak structure of the 580 keV transition is located on the top of a double-exponential background, which is basically a contribution from unrecognized γ-ray transitions, and the Compton scattered events of higher lying states. Therefore, the γ-γ coincidence spectrum was expected to contain background events. The gated spectrum shown at the top left panel of Fig. 5.14 has more events especially in the region below 700 keV, while this was relatively suppressed in the case of the gated spectrum with the 2600-keV transition. As explained in the previous section, the expected response function only assume the recognized γ-ray transitions, the missing strength cannot be reproduced. Therefore, it may be possible to guess no coincidence with the 1100-keV transition, while it may have coincidences with the 2000-keV and 2600-keV transitions. Note that the underestimation of the expected response function of the peak at 2600 keV might be because of the Compton scattered γ-ray hits of the high-lying transitions such as the one at 1100 keV within the coincidence gate contributing to increase the number of counts around 2600 keV in the coincidence spectrum.

1100-keV peak The γ-γ spectrum gated with 1100 keV is also shown in the top right panel of Fig. 5.14. As it can be anticipated to have background events mainly from Compton scatterings of unrecognized higher lying transitions similar to the 580-keV case, the structure seen in the figure around 1000 keV might be the peak at 1100 keV itself caused by the coincidence with the Compton hit of the higher lying transitions, but the possibility of the existence of a double-peak at around 1100 keV cannot be excluded. On the other hand, it can be seen that the number of events at 580 keV does not explain the expected response functions. Thus, the 1100-keV transition might not be in coincidence with 580-keV one, unless the γ-ray transition at 1100 keV does not consist of several peaks with some of weak transition being in coincidence with the 580-keV transition. That is a consistent conclusion with the previous paragraph.

(2) γ-γ coincidence analysis of the $(p,3p)$ channel

2910-keV peak As summarized in Tab. 5.2, the γ-ray transition at 2910 keV was the most intense in the $(p,3p)$ channel. Therefore the 2910-keV transition is assumed as the transition feeding directly to the ground state. As a consequence, the γ-ray transitions at 2910 keV and 2600 keV were assumed to be independent. Though the coincidence spectrum of the high-lying γ-ray transition at 2910 keV was analyzed as shown in the bottom right panel of Fig. 5.14, there was a limitation of the number of events to deduce any conclusion with large error bars. No strong conclusion was obtained from this analysis.

5.4.3 Constructing the level scheme

The level scheme of the excited states of ^{78}Ni was constructed by ensuring the consistency of the consequences of the analysis of the γ-ray spectra. As summarized in Tab. 5.2, the most in-

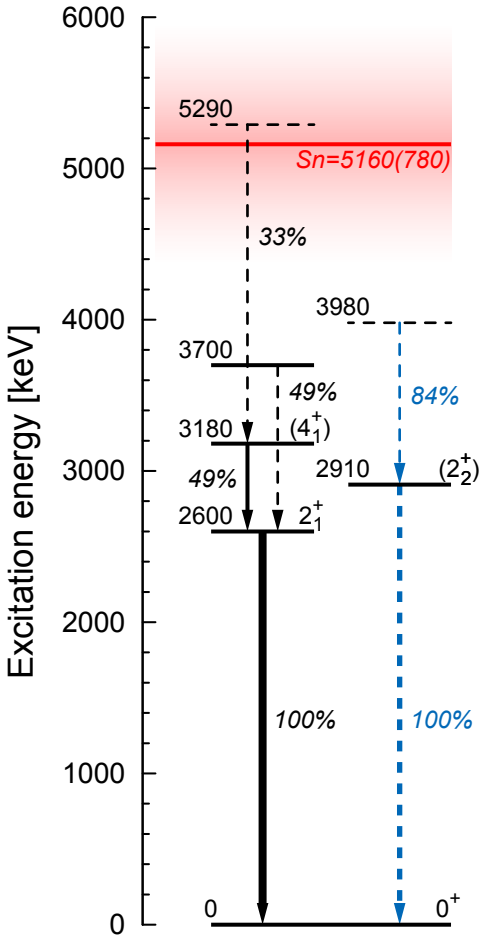

Fig. 5.15: Proposed level schemes of ^{78}Ni. Levels of the excited states are tentatively assigned from the obtained clues. See text for detail discussions. The arrows represent the γ-ray transitions with their relative intensities to the intensity of the transition to the ground state. The black arrows are mostly observed in the $(p,2p)$ channel, while the blue arrows are from the $(p,3p)$ channel. The solid and dashed lines represent the γ-ray transition with significance level $> 5\sigma$ and others, respectively. The extrapolated neutron separation energy, S_n [61], and its error is also indicated with a red line and a red shade.

tense transition was the one at 2600 keV in the $(p,2p)$ channel and at 2910 keV in the $(p,3p)$ channel. It is reasonable to assume both transitions feed the ground state directly. Especially the γ-ray transition at 2600 keV is regarded as the de-excitation to the ground state from the first excited state with spin and parity of 2_1^+, based on the systematics of even-even nuclei in the vicinity. Futhermore, the γ-γ coincidence analysis inferred that all low-lying transitions are coincident with the 2600-keV transition. Therefore, they were thought as the γ-ray transitions feeding the 2_1^+ state at 2600 keV. Although both the 580-keV and the 1100-keV transitions had almost half of the γ-ray intensity of the 2600-keV transition, $I_{rel} = 49\%$ for each, they were estimated as not coincident transitions since respective peaks were not observed in their γ-γ coincidence spectra. Thus, these transitions were considered as independent transitions feeding the 2600-keV state. As a result, other transitions at 1540 keV and 2110 keV, were assumed as not feeding directly to the 2600-keV state because the sum of the γ-ray intensity of the 580-keV and the 1100-keV transitions are already 98(16)% of the one of the $2^+ \rightarrow 0^+$ transition. Figure 5.15 shows the tentative assignment of the levels and the placement of the transitions with black line and arrows. The 2110-keV transition was tentatively placed on the top of the 3180(= 2600 + 580)-keV state as the indication of the coincidence was seen in the γ-γ spectrum gated with the 580-keV γ-ray, while the placement of the 1540-keV transition could not determined from the result of this work since no strong indication in the γ-γ coincidence spectra could obtained. Though the information about this transition is not sufficient, it might be possible to assume to place the transition on the top of the 3700(= 2600 + 1100)-keV state rather than the top of the 5290(= 2600 + 580 + 2110)-keV state as the neutron separation energy of ^{78}Ni is evaluated at S_n = 5160(780) keV [61]. However, it is not placed in the level scheme because direct feeding of the 2_1^+ state or the 3180-keV state could not be ruled out. In addition to the placement of the excited levels, the level at 3180(= 2600 + 580)-keV was tentatively assigned as a candidate of the 4_1^+ state.

Even though the $(p,3p)$ reaction was expected to populate various states, because of the combinations of two removed proton-holes, which impedes resolving the peaks in the γ-ray spectrum, the indication of the 2910-keV transition was seen rather clearly, especially with a low γ-ray multiplicity condition, m. Therefore, it can be considered as a candidate of the 2_2^+ state feeding directly to the ground state. Considering the significance levels in Tab. 5.2, the γ-ray transition with more than 3σ was the 1067-keV one in the $(p,3p)$ channel with 3.6σ. The 1067-keV transition was suspected as different to the one at 1103 keV in the $(p,2p)$ channel because of the much larger γ-ray intensity than that of the 2600-keV transition, and the difference of the energy compared to the uncertainty. Under the assumption that the 1070-keV transition in the $(p,3p)$ channel is different from the 1100-keV transition, the 3980(= 2910 + 1070)-keV state was tentatively assigned, feeding the 2910-keV state. Figure 5.15 illustrates these transitions of the $(p,3p)$ channel with blue arrows.

As an additional note, from the graphs in Fig. 5.13, convergence of the S. Ls. of the $(p,2p)$ channel had been achieved between $m \leq$ 4-6, while the convergence of the $(p,3p)$ channel took place at the lower multiplicity, especially for the 2910-keV transition. That implies the γ-ray transitions in the $(p,2p)$ channel might have been accompanied with several γ rays at the same time in cascade from the highly lying states, while this might not happen for the 2910-keV one in the $(p,3p)$ channel. It is consistent with the discussions of the γ-γ coincidence analysis.

5.5 Cross sections to excited states of ^{78}Ni

The exclusive cross sections populating the states of ^{78}Ni, constructed as Fig. 5.15, were calculated from the number of the de-excitation γ rays emitted from reacted ^{78}Ni particles, $N(\gamma)$,

and the number of the incoming particles to the reaction target. From these results, discussions are performed by employing a reaction theory to investigate the property of the states of ^{78}Ni in section 6.2.

As discussed in section 5.1, the inclusive cross sections of the corresponding reaction channels, σ_{incl}, were deduced from the ratio of the number of particles of the incoming particles identified as a certain isotope by the BigRIPS spectrometer, N(BR), and the outgoing particles identified as an isotope of interest by the ZeroDegree spectrometer in addition to the gatings of the incoming beam, N(BR $\otimes$ ZD). Because the trigger settings of the data acquisition system were configured for the combination of the coincidence trigger of the beam and the γ-ray detection (F7 $\times$ F11 $\times$ γ), and the down-scaled beam trigger (DS(F7)), as detailed in section 3.3.2, the number of the incoming beam should be converted from the number of the events in the γ-ray coincidence trigger to deduce the exclusive cross sections. Thus, the down-scaled factor (DSF), defined as the ratio between the measurement of γ rays and the inclusive cross section measurement, of the numbers of the incoming particles was necessary to be deduced. In this work, the former was obtained with the coincidence trigger from run 210 to 222 and 224 to 355 and the latter was with the down-scaled trigger from run 224 to 355. It could be calculated from the counts in the scaler module detailed in section 3.3.3 and Tab. 3.2 with the equation below:

$$\begin{aligned} DSF &= \frac{\text{Number of counts at F7 (Run 210 - 222 and 224 - 355)}}{\text{Number of counts of DS(F7) (Run 224 - 355)}}, \\ &= \frac{2.68\times10^{9}}{6.94\times10^{7}} = 38.6. \end{aligned} \tag{5.32}$$

Here, the formula to obtain the inclusive cross section, σ_{incl}, as Eq. (5.2) are rewritten with the relationship below,

$$\begin{cases} N_{ZD} &= N\left(\text{DS(F7)} \otimes \text{BR}\left(^{79}\text{Cu}\right) \otimes \text{ZD}\left(^{78}\text{Ni}\right)\right), \\ N_{BR} &= N\left(\text{DS(F7)} \otimes \text{BR}\left(^{79}\text{Cu}\right)\right), \\ \kappa &= 1/(\tau \cdot n_{dc}). \end{cases}$$

N_{ZD} is the number of particles gated with ^{79}Cu in the BigRIPS spectrometer and ^{78}Ni in the ZeroDegree spectrometer in DS(F7) trigger, N_{BR} is without applying the gating condition in the ZeroDegree spectrometer, and κ is a coefficient to produce the cross section. The equation is now formulated as:

$$\sigma_{incl} = \kappa \cdot \frac{N\left(\text{DS(F7)} \otimes \text{BR}\left(^{79}\text{Cu}\right) \otimes \text{ZD}\left(^{78}\text{Ni}\right)\right)}{N\left(\text{DS(F7)} \otimes \text{BR}\left(^{79}\text{Cu}\right)\right)}, \tag{5.33}$$

In a similar fashion, the exclusive cross section σ_{excl} for a certain γ-ray can be described as:

$$\sigma_{excl} = \kappa \cdot \frac{N\left(\gamma \otimes \text{BR}\left(^{79}\text{Cu}\right) \otimes \text{ZD}\left(^{78}\text{Ni}\right)\right)}{N\left(\text{BR}\left(^{79}\text{Cu}\right)\right)}. \tag{5.34}$$

The numerator is the number of γ rays, estimated by the fit of the simulated response functions of the γ-ray detector, DALI2, with a certain particle gating, after the correction of the values of the efficiency of the vertex reconstruction using MINOS, as Eq. (4.7) and Eq. (4.8). By employing Eq. (5.32) and Eq. (5.33), the equation can be converted into the following:

$$\begin{aligned} \sigma_{excl} &= \kappa \cdot \frac{N\left(\gamma \otimes \text{BR}\left(^{79}\text{Cu}\right) \otimes \text{ZD}\left(^{78}\text{Ni}\right)\right)}{DSF \times N\left(\text{DS(F7)} \otimes \text{BR}\left(^{79}\text{Cu}\right)\right)} \\ &= \frac{\sigma_{incl}}{DSF} \cdot \frac{N\left(\gamma \otimes \text{BR}\left(^{79}\text{Cu}\right) \otimes \text{ZD}\left(^{78}\text{Ni}\right)\right)}{N\left(\text{DS(F7)} \otimes \text{BR}\left(^{79}\text{Cu}\right) \otimes \text{ZD}\left(^{78}\text{Ni}\right)\right)}. \end{aligned} \tag{5.35}$$

Tab. 5.3: Summary of the exclusive and the inclusive cross sections. These values have been corrected with the efficiency values of DALI2 and MINOS. The errors in parentheses of energy and cross section are statistical only. The systematic errors of the energy of levels and the exclusive cross sections are 0.6% and 5%, respectively. The systematic error of the inclusive cross section, σ_{incl}, is assumed to be negligible since its statistical uncertainties are large. In addition, the exclusive cross section for the $(p,2p)$ reaction can be changed by roughly 0.2 mb due to the ambiguity of its placement of the 1540-keV transition.

Energy (keV)	State	σ_{p2p} (mb)	σ_{p3p} (μb)
0	0^+_1	≤1.07(28)	≤10.2(41)
2600(33)	2^+_1	≤0.01(23)	≤0.1(17)
3180(35)		0.10(14)	−0.8(17)
3700(36)		0.31(11)	—
5290(59)		0.21(10)	2.6(14)
2910(43)	(2^+_2)	—	0.6(25)
3980(46)		—	3.3(16)
Inclusive		1.70(42)	16.1(60)

The exclusive cross sections for both reaction channels are summarized in Tab. 5.3. They were deduced based on the level scheme proposed in Fig. 5.15, as well as the numbers of γ rays as summarized in Tab. 5.2. Here, the systematic errors of the energy of levels and the exclusive cross sections, which is basically same as the uncertainty of the γ-ray detection efficiency, are 0.6% and 5%, respectively, while the systematic error of the inclusive cross section, σ_{incl}, is assumed to be smaller than its statistical uncertainties. Note that the exclusive cross section for the $(p,2p)$ reaction can be changed by roughly 0.2 mb due to the ambiguity of the placement of the 1540-keV transition.

The physics interpretation is addressed in the following chapter.

Chapter 6

Discussion

In this chapter, the observed excited states of ^{78}Ni are discussed in comparison with several state-of-the-art theoretical predictions. Firstly, the energy of the excited states of ^{78}Ni is compared with several theoretical approaches to deduce structural information of such extremely neutron-rich nuclei in section 6.1. The trends of first 2^+ and 4^+ states as function of the proton and neutron number confirm the doubly magic nature of ^{78}Ni. Furthemore, other high-lying states are discussed to understand a possible emergence of shape coexistence in this region of the nuclear chart. Subsequently, the exclusive cross sections of ^{78}Ni are discussed in section 6.2. The origin of its particularly small cross section, which is a few times less than nuclei in the vicinity, is discussed by employing recently developed reaction theory in addition to the predictions above. The summary and conclusion of these discussions are presented in the next chapter.

6.1 Excited states of ^{78}Ni

The exicitation energies of ^{78}Ni obtained in this work are discussed in this section. Firstly, in section 6.1.1, the first 2^+ and 4^+ states along the isotopic and isotonic chains of ^{78}Ni are discussed. As there have been several theoretical calculation conducted to investigate the nuclear structure around ^{78}Ni, the predicted energy levels of the calculations were compared along the nickel isotopic chain. Not only the first 2^+ and 4^+ states but also other states have been observed in this work, thus the interpretation of the states, especially the origin of the second 2^+ state, is further discussed in section 6.1.2.

6.1.1 Isotopic and isotonic trends of first 2^+ and 4^+ states

The excitation energy, E_x, of first 2^+ and 4^+ states assigned in this work, tentatively, and their ratio,

$$R_{4/2} = \frac{E_4}{E_2},$$

are plotted in the graphs along the isotopic and isotonic chains of ^{78}Ni, shown in Fig. 6.1 and Fig. 6.2, respectively. The former figure shows systematic trends along the nickel ($Z = 28$) isotopic chain, and the latter figure illustrates the trends along the $N = 50$ isotonic chain. The red stars indicate the acquired values of ^{78}Ni in this work. Both sudden increase of $E(2^+)$ and sudden drop of $R_{4/2}$ can be seen at both $N = 50$ and $Z = 28$. Note that the excitation energy of $E(2^+) = 2.600(33)$ MeV is almost the same as the 2.700(1) MeV for the other doubly magic nickel

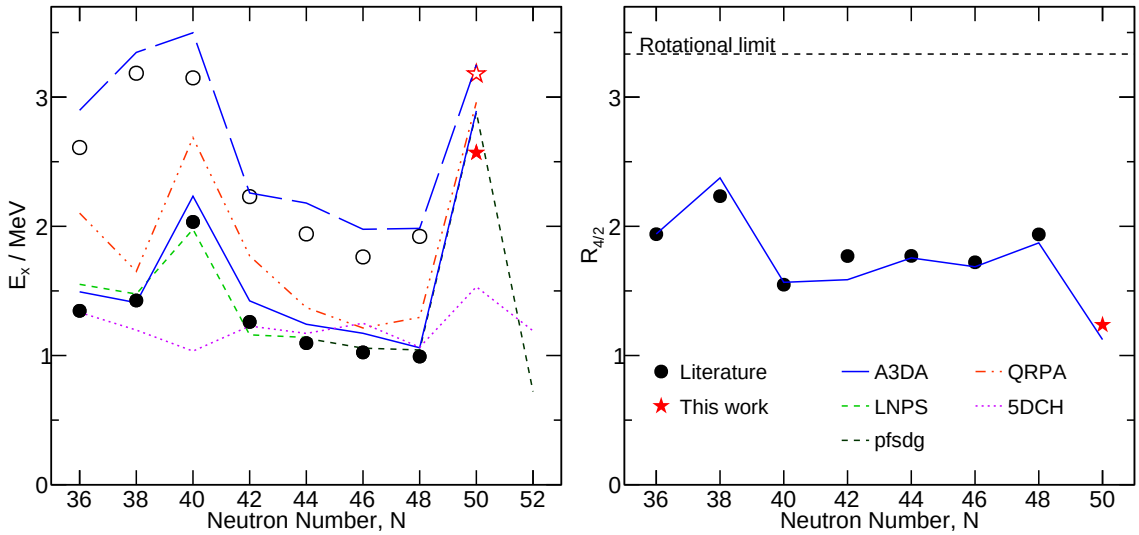

Fig. 6.1: Systematic trend and theoretical predictions of excitation energies along the $Z = 28$ isotopic chain. The observed excitation energies, E_x, of the first 2^+ (filled circle and filled star) and 4^+ (open circle and open star) states, and their ratios, $R_{4/2}$, are illustrated in the left and right panels, respectively. As comparison, five recently published theoretical predictions are also drawn with the respective colors as the legend in the right panel. A Monte-Carlo shell model (MCSM) calculation with the A3DA-m based Hamiltonian [114, 115] predicts not only the energies of 2^+ states (blue line) but also 4^+ states (blue dashed line) and their ratio $R_{4/2}$ in right panel. Two large-scale shell model calculations with the LNPS interaction [111] up to $N = 44$ and with the PFSDG-U interaction [34] above $N = 44$ are shown with green dashed lines. Two of mean-field based approaches with the quasi-particle random-phase approximation (QRPA) and five-dimension collective Hamiltonian (5DCH) formalisms [120] are also illustrated with red dot-dash and dotted lines. See text for a detailed discussion.

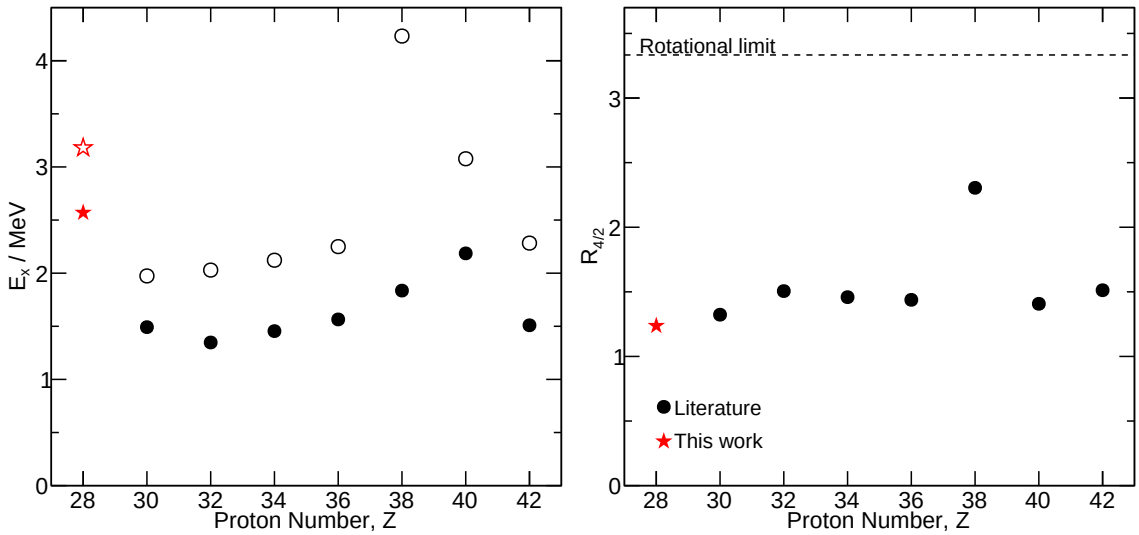

Fig. 6.2: Systematic trend of excitation energies along the $N = 50$ isotonic chain. As for Fig. 6.1, the observed excitation energies, E_x, of the first 2^+ and 4^+ states, and their ratios, $R_{4/2}$, are illustrated in the left and right panels, respectively. The sudden jump for the 4^+ energy at $Z = 38$ (^{88}Sr) might be due to lack of the experimental study of the identification of the first 4^+ state, which can be expected around 2.5 MeV.

isotope, ^{56}Ni, which has 28 protons and 28 neutrons. This fact supports the shell closure nature of the ground state of ^{78}Ni. Furthermore, the low value of the ratio

$$R_{4/2}\left(^{78}\mathrm{Ni}\right) = 3.180/2.600 = 1.22(2), \tag{6.1}$$

also confirms the doubly magic nature of ^{78}Ni, which is as small as stable doubly magic nuclei: ^{16}O ($R_{4/2} = 1.50$), ^{40}Ca (1.35), ^{48}Ca (1.18), ^{208}Pb (1.06). It is even smaller than for ^{56}Ni (1.46).

Figure 6.1 also illustrates the systematic trends of 2^+ and 4^+ excitation energies, and their $R_{4/2}$ ratios of the experimental results. Besides, several theoretical predictions by means of two types of large-scale shell model calculations, a Monte-Carlo shell model (MCSM) calculation with the A3DA-m interaction [114, 115] and a large-scale shell model calculation with two different model spaces named as LNPS [111] and PFSDG-U [34]; and two of beyond mean-field based approachs with the quasi-particle random-phase approximation (QRPA) and five-dimension collective Hamiltonian (5DCH) formalisms [120] are also drawn in Fig. 6.1. All calculation results, except the 5DCH formalism, are in good agreements with the acquired values of this work. To discuss the result further, the details of the individual theoretical calculations are discussed in the following.

A3DA-m The Monte-Carlo shell model calculation with the A3DA-m interaction employs the largest model space among the three shell model calculations, full pf shells, $0g_{9/2}$ and $1d_{5/2}$ orbits in proton and neutron shells, namely 6 orbits above the ^{40}Ca core ($Z = N = 20$). The energies of 2^+ and 4^+ states and their ratio $R_{4/2}$ are in good agreement with observations for the entire isotopic chain. However, this calculation is anticipated to have difficulties with the predictions of higher-lying states because of the limitation of the model space for neutrons. Though the predicted $E(2_1^+)$ and $E(4_1^+)$ for ^{80}Zn reproduced the experimental results [82] better than the one with the previous JUN45 interaction with the $1p_{1/2}$, $1p_{3/2}$, $0f_{5/2}$ and $0g_{9/2}$ orbits [151], discrepancies with the experimental results for higher lying states have been noticed. Similar inconsistencies have been recognized in the excited states of ^{79}Cu [104, 105]. Though the energy trend of the first excited 2^+ states was reproduced well in this calculation, the validity of the calculated energy for other states of ^{78}Ni is necessary to be checked, which is discussed in the next section.

LNPS and PFSDG-U The shell model calculation with the LNPS interaction successfully reproduced the excitation energies of $^{54-62}$Ni isotopes utilizing a model space of pf orbits for protons, and $1p_{1/2}$, $1p_{3/2}$, $0f_{5/2}$, $0g_{9/2}$, and $1d_{5/2}$ orbits for neutrons, respectively. The model space is composed of 20 protons and 28 neutrons above the ^{48}Ca core. Since all the neutron-orbitals except $1d_{5/2}$ are filled in the ^{78}Ni case in the calculation, which is the same situation as with the A3DA-m interaction, it has difficulties to predict excited states in such neutron-rich nickel isotopes. Thus, another calculation based on a different model space consisting of a wider neutron model space, PFSDG-U, has been developed. It accepts the full pf shell for protons, which is the same proton space as LNPS interaction, and the full sdg shell for neutrons on a ^{60}Ca core. In other words, this model space consists of the $3\hbar\omega$ harmonic oscillator (HO) shell for protons and $4\hbar\omega$ HO shell for neutrons. Since the LNPS interaction predicted the level-schemes of lighter neutron-rich nuclei, such as ^{66}Cr and ^{70,72}Fe, well [116, 117], the monopole interaction common with PFSDG-U was not changed from LNPS calculation, while the new parts have been adjusted from experimental data of the measurement of the mass and the excited states from nickel to zirconium isotopes. As shown in Fig. 6.1, the 2^+ energies of the nickel isotopes, $^{62-78}$Ni, were calculated in agreement with the experimental results. Though

Tab. 6.1: Average numbers of particle-hole (p-h) excitations across the proton- and neutron-shell gaps. The unit of the excitation energy, E_x, of each state is MeV. Note that the *ab initio* calculation with IM-SRG did not produce any collective state.

	PFSDG-U			MSCM			IM-SRG		
	E_x	$n^{\pi}_{p\text{-}h}$	$n^{\nu}_{p\text{-}h}$	E_x	$n^{\pi}_{p\text{-}h}$	$n^{\nu}_{p\text{-}h}$	E_x	$n^{\pi}_{p\text{-}h}$	$n^{\nu}_{p\text{-}h}$
0^+_{sp}	0.00	0.56	0.38	0.00	0.39	0.65	0.00	0.67	0.39
2^+_{sp}	3.15	1.47	1.55	2.57	0.91	1.67	3.25	0.85	1.34
4^+_{sp}	3.66	1.14	1.40	3.26	0.69	1.44	3.63	—	—
0^+_c	2.65	2.35	2.70	2.61	2.54	2.72	—	—	—
2^+_c	2.88	2.22	2.51	2.88	2.54	2.72	—	—	—
4^+_c	3.44	2.49	2.72	3.43	2.52	2.73	—	—	—

the discussion of the full level-scheme is detailed in the next section, it should be noted that the predicted nature of the 2^+_1 state is not a single-particle nature as MCSM pointed out, rather a collective behavior, in spite of the ground state with a spherical character, while the spherical excited states lie a few hundreds keV higher than the deformed ones, such as $E(2^+_2) = 3.15$ MeV and $E(4^+_2) = 3.66$ MeV.

QRPA and 5DCH The predicted energy values along nickel isotopic chain with two types of the beyond static mean-field approximation with finite-range two-body effective interaction, the Gogny D1S force [152, 153], are also illustrated in Fig. 6.1. It can be recognized that the 5DCH formalism estimates the excitation energies of ^{68,78}Ni lower than the observed values. This tendency is understood as this calculation has been deduced from triaxial constrained Hartree-Fock-Bogolyubov (HFB) solutions, and reproduces low-energy collective excitations, which are mainly the rotational and vibrational excitations, in open shell-nuclei. However, it is known to fail to describe 2^+ states in symmetric and rigid systems, such as doubly closed nuclei, since the calculation excludes spherical configuration, resulting in different and unreal predictions. On the other hand, the QRPA calculation, which was developed by a RPA formalism [154], conducts a better estimation of the excitation energies. Axial symmetric deformation was treated with this formalism, while the RPA one imposes spherical symmetry. As a consequence, QRPA succeeded to calculate the ground and excited states in even-even nuclei rather well along entire isotopic chains. However, it does not include the rotational degrees of freedom, thus excitation energies of some isotopes, such as ^{64,68,70}Ni, were overestimated. Some modifications to couple the advantages of both calculations are needed in order to achieve better predicting power. The calculated higher-lying levels of respective formalisms are examined in the next section.

6.1.2 Predicted level-schemes of ^{78}Ni

State-of-the-art theoretical calculations have tried to examine the excited levels of ^{78}Ni to extract their intrinsic properties. Figure 6.3 shows the experimental and theoretical level-schemes including unpublished results, which are also summarized in the article submitted [88]. In the following paragraphs, theoretical descriptions and interpretations about the excited states of ^{78}Ni with individual calculations: The large scale shell model, beyond mean-field, and first-principle (*ab initio*) calculations.

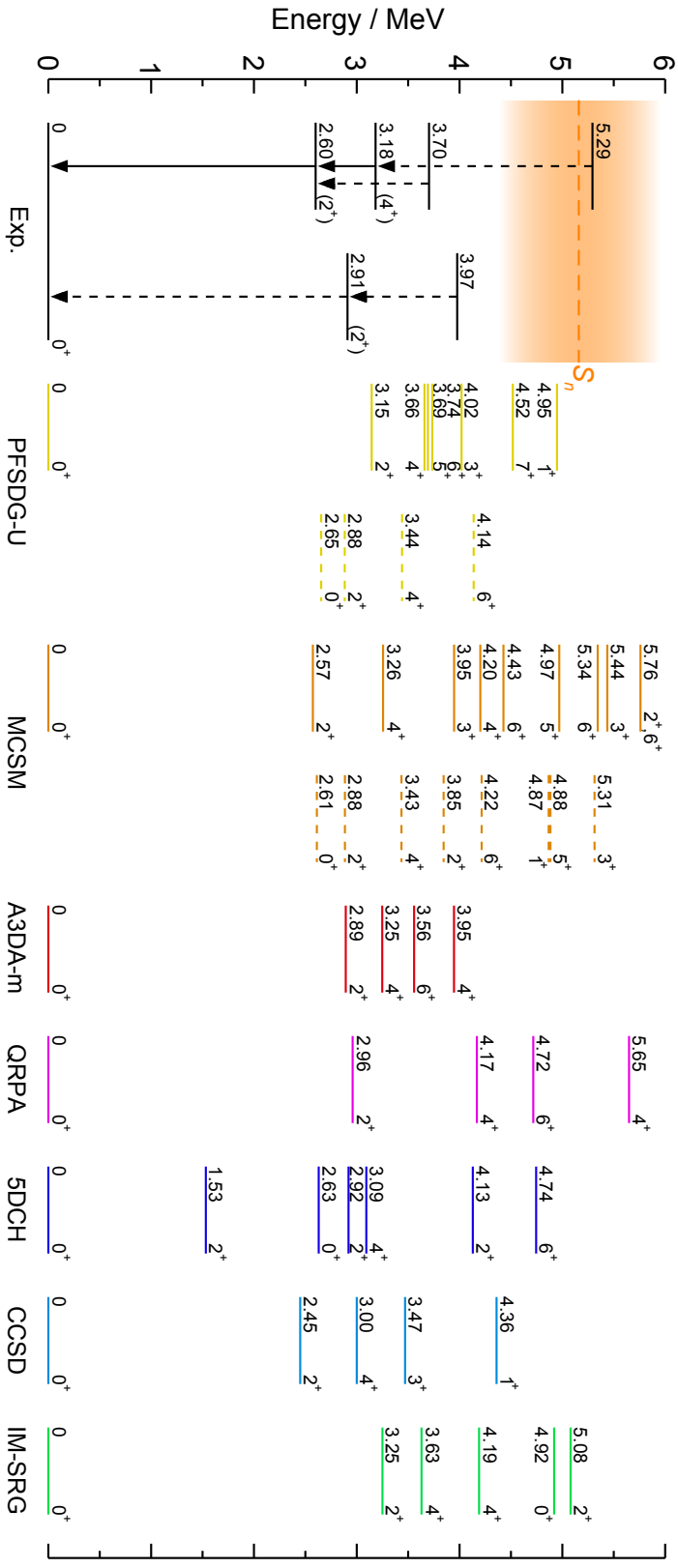

Fig. 6.3: Level schemes of state-of-the-art theoretical predictions. The experimental levels are compared with representative theoretical calculations. See section 6.1.2 for detailed discussions regarding to individual predictions.

(1) Shell model calculations — PFSDG-U, MCSM, and A3DA-m

In this section, three large scale shell model calculations, PFSDG-U, A3DA-m, and MCSM, have been performed for the excited states of ^{78}Ni. While it is important to compare the placement of the excited states in the level scheme, shown in Fig. 6.3, with the experimental results, it is also important to discuss the characteristics of the respective states, especially deformation. The average numbers of the particle-hole (p-h) excitations across the shell gaps of $Z = 28$ and $N = 50$ can be utilized as indicators for shell closure and deformation. By comparing the average numbers of particles in the respective orbitals, the number of p-h excitations is deduced. In contrast to the case of spherical states, many particle-hole (p-h) excitations, such as $2p$-$2h$ and $4p$-$4h$, are involved in deformed states. In this way, spherical and deformed states can be differentiated. The deformed states are thought as collective, consisting of more than $2p$-$2h$ excitations for both protons and neutrons, while the spherical states are expected as rather single-particle $1p$-$1h$ excitations. Table 6.1 lists the expected numbers of particle-hole (p-h) excitations across $Z = 28$ ($n^{\pi}_{p\text{-}h}$) and $N = 50$ ($n^{\nu}_{p\text{-}h}$) gaps of the 0^+, 2^+, and 4^+ states in the respective calculations. The individual calculations are discussed in the following paragraphs.

PFSDG-U The PFSDG-U calculation [34, 118], introduced in the previous section, is the first theoretical prediction which raised the possibility of shape coexistence in ^{78}Ni. The predicted energy levels are illustrated with yellow lines in Fig. 6.3 with solid lines representing the spherical levels including the ground state, and with dashed lines representing the deformed states consisting of a rotational excitation band starting from the 0^+_2 state in these calculations. Besides their averaged number of p-h excitations are summarized in Tab. 6.1. The existence of such deformed states in addition to the spherical ground state implies shape coexistence.

A3DA-m The A3DA-m calculation [114, 115], also introduced in the previous section, has difficulties to calculate highly excited states of ^{78}Ni due to the limitation of the model space with only one neutron valence orbital $1d_{5/2}$ taken into the calculation. The calculated levels, limited to only even-spin states below 4 MeV drawn for their visibility, are drawn with red lines in Fig. 6.3. It proposes the ground and excitated states of ^{78}Ni as spherical with firmly doubly-closed shell, however, shape coexistence characteristics are not produced. These different outcomes may be understood as the limited size of the neutron model space in contrast to the case of PFSDG-U with the full sdg shell for neutrons.

MCSM To overcome the limitation of the model space, a new shell model calculation was developed, dedicated for this work, with a very large model space, pf and sdg shells for both protons and neutrons, by extending the A3DA-m interaction [119]. In total, 60 states were computed, and some of the predicted levels are drawn in the figure with orange lines under the following conditions: spherical states (full lines) with spectroscopic factor of one-proton knockout channel larger than 0.1, plus possible intermediate states from high-lying states, 2^+_1 and 3^+_1; and deformed states (dashed lines) below 4 MeV, and other yrast states. As the specific name of this new calculation has not been determined yet, it is termed as "MCSM" in this thesis. While the A3DA-m calculation estimates the ground and excitated states of ^{78}Ni as spherical with firmly doubly-closed shell, this MCSM calculation indicates a shape coexistence as previously predicted in the PFSDG-U calculation. It might be also important to be noted that the ordering of the spherical and deformed levels is reversed between the PFSDG-U and MCSM calculations. While the energies of 2^+_1 states in both calculations are calculated around 2.6 MeV,

a deformed state in the PFSDG-U calculation and a spherical state in the MCSM calculation are predicted.

2_1^+ and (4_1^+) states As discussed in the previous chapter, the experimentally observed 2_1^+ and (4_1^+) states were mainly populated in the $(p,2p)$ channel. It might be possible to think that the states with $1p$-$1h$ excitation are preferred over the collective states with $2p$-$2h$ excitations in the one-proton knockout reaction. The calculated energy values of the spherical states, 2_{sp}^+ and 4_{sp}^+, by these three shell model predictions, as drawn in Fig. 6.3, range from 2.6 to 3.2 MeV, and from 3.3 to 3.7 MeV, respectively, while the observed energy were $E_{exp}(2_1^+) = 2.60(3)$ MeV and $E_{exp}(4_1^+) = 3.18(4)$ MeV. It is also possible to assume these states are deformed as the energy of the first excited 2_1^+ and 4^+ states in the PFSDG-U calculation, which are calculated as deformed states at 2.88 MeV and 3.44 MeV, are closer to the experimental values than these of 2_{sp}^+ and 4_{sp}^+. However, this might be incorrect, as the ground state of ^{79}Cu is assumed as spherical with $J^\pi = 5/2^-$ [104] and the cross sections to populate such deformed states accompanying many p-h excitations should be small for the $(p,2p)$ reaction.

2_2^+ state The state at 2.91(4) MeV assigned as 2_2^+, which was observed in the $(p,3p)$ channel solely, may be assumed as a collective 2_c^+ state at almost 2.9 MeV proposed in the PFSDG-U and MCSM calculations. Though a $0_c^+ = 0_2^+$ state is calculated in the calculations, the transition $2_c^+ \rightarrow 0_{gs}^+$ is preferred to $2_c^+ \rightarrow 0_2^+$ since the energy difference between these transitions is large enough to overcome the difference of the transition probabilities, $B(E2)$, calculated in both shell model calculations, PFSDG-U and MCSM.

Higher lying states It is difficult to interpret higher lying states indicated in the experiment above the (4^+) state at 3.18(4) MeV, as a high level density is predicted in the various models above the (4^+) level. Meanwhile, the reason of no direct, or only very little, population to the 2_1^+ state in the $(p,2p)$ reaction channel will be discussed further in section 6.2 combining with the recently developed reaction theory and spectroscopic factors obtained in these shell model calculations.

(2) Mean-field calculations

The predicted levels of the beyond mean-field calculations, QRPA [120, 121] and 5DCH [155, 156], are also illustrated in Fig. 6.3 with pink and blue lines, respectively. Though QRPA calculates excited states at high energy up to 16 MeV, only the states below 6 MeV are shown. As already mentioned in the previous section, due to the formulation of the QRPA calculation, no collective states could be obtained. On the other hand, the 5DCH is known to fail reproducing the characteristics of the nuclei with closed shell, and underestimating the excitation energy of their states. Better agreement of the excitation energy with $E_{exp}(2_1^+) = 2.60(3)$ MeV was obtained with QRPA at $E_{QRPA}(2_1^+) = 2.96$ MeV for ^{78}Ni. In addition to the trend of the energy along $Z = 28$ isotopes in QRPA, the incompatibility of 5DCH can be seen. This better agreement with QRPA may fortify the nature of shell closure of the ground state of ^{78}Ni. It is also important to consider possible reasons for the discrepancies of the energy values of the higher lying states of ^{78}Ni, which were basically overestimated in the QRPA calculation. As remarked in Ref. [120], the deviations might be due to the constraints of the formalism, which does not include any coupling between the rotational and vibrational degrees of freedom. A similar feature can be seen in Fig. 6.1 as the overestimation of the excitation energies of ^{68}Ni, though there is a good

agreement of transition probability $B(E2)$ between the experimental value and the QRPA calculations. A new formalism with more predicting power as an extension of QRPA formalism including the rotation degree of freedom might be needed.

(3) First-principle approaches

Up to now, several attempts with first-principle (*ab initio*) approaches have been developed to depict nuclear systems based on microscopic interactions of nucleons in the nuclei. The nuclear interactions were provided by chiral effective field theory (EFT) [37–39], which originates from quantum chromodynamics (QCD). Basically, the formalism estimates the nuclei consisting of nucleons interacting with the nucleon-nucleon (NN) force. Besides, the importance of the inclusion of three-nucleon forces ($3NF$) has been also recognized recently [26, 42, 43, 157]. In general, this first-principle approach is difficult due to the requirement of huge computational powers to handle such quantum many body systems. However, several theoretical frameworks have been developed to calculate efficiently assuming an appropriate core in the nuclei.

The nickel isotopes are at the frontier for these calculations. Here, the excitation energies of recently developed *ab initio* computational descriptions, based on coupled-cluster singles-doublets(-triplets) (CCSD(T)) [47], and in-medium similarity renormalization group (IM-SRG) [122] formalisms, are illustrated with light-blue and green lines in Fig. 6.3, respectively. While the CCSD(T) method approximates the system consisting of closed-shell and its $1p$-$1h$, $2p$-$2h$, and perturbatively included $3p$-$3h$ excitations. However, it can only calculate in the vicinity of closed nuclei. The IM-SRG formalism, which utilizes a normal-ordered two-body approximations, can calculate also open nuclei and deduce the absolute energy of their states [44–46]. For these calculations, the NN and $3N$ interactions were deduced by the chiral EFT interaction named as "1.8/2.0(EM)", which reproduces the energy in calcium isotopes most successfully, determined with momentum cutoffs of $\lambda = 1.8$ fm^{-1} for NN, and $\Lambda_{3NF} = 2.0$ fm^{-1} for $3NF$ parts. There is another formulation, many-body perturbation theory (MBPT), which reproduces the excited-state properties of calcium isotopes successfully [26, 43]. However, no calculation of the excitation energy of ^{78}Ni with this formulation is available yet as it suffers from the difficulty of the convergence in such perturbative way. Hereafter, individual *ab initio* calculations are detailed.

CCSD(T) The CCSD(T) is the first *ab initio* calculation applied to the ^{78}Ni case [47]. In order to see the convergence of the results, the model space of harmonic oscillator shells was varied from $N = 10$ to $N = 14$ with five empirical interactions with different parametrizations. Among these interactions, only the softest and most successful chiral EFT interaction, "1.8/2.0(EM)", achieved convergence as a function of the size of the model space. To confirm the validity of the calculation, the ground state property was firstly investigated. The neutron separation energy for ^{78}Ni was calculated to be $S_n \approx 4.5$ MeV, which is in good agreement with the AME (Atomic Mass Evaluation) 2016 [61] ($S_n = 5.16(78)$ MeV). The excited states calculated in this framework inferred the excited 2^+_1 and 4^+_1 states of ^{78}Ni are not states with a pure $1p$-$1h$ excitation, but rather containing $2p$-$2h$ and $3p$-$3h$ excitations, and possibly some amount of $4p$-$4h$ contributions. Thus, the uncertainty of the excitation energy was estimated at 300 keV, taking account of the ambiguity of many particle-hole excitations. The calculated excitation energies, shown in Fig. 6.3 with light-blue lines, were $E(2^+_1) = 2.45$ MeV and $E(4^+_1) = 3.00$ MeV, which is in agreement with the experimental levels. Howerver, the 2^+_2 state observed in the experiment could not be reproduced in this calculation. This might be because the state, which is expected

to be a collective state, requires many p-h excitations above $3p$-$3h$. It was pointed out in the paper [47] that the spin and parity of the ground state of ^{79}Ni was estimated as $J^\pi = 1/2^+$ state with an almost degenerating $5/2^+$ state, which is consistent with the consequences of both shell model calculations in Refs. [34, 119]. Because of the high excitation energy and the calculated neutron separation energy, the natue of shell closure was deduced as persistent in this calculation.

IM-SRG The IM-SRG approach is a non-perturbative method by employing the continuous unitary transformations, and has advantages to derive absolute energies of the core and matrix elements, which can be input parameters to shell model calculations. Similar to the CCSD(T) calculation, the chiral interaction of "1.8/2.0(EM)" provided the best results for binding energies, charge radii, and $E(2_1^+)$ of lighter nuclei among several chiral interactions, with only an exception of overestimating the 2^+ energy of closed-shell nuclei [46]. The probable cause of such an inaccuracy of the excitation energy of closed-nuclei is argued in Ref. [46] that the lack of inclusion of multi particle-hole excitations in this framework, especially the $3p$-$3h$ excitation, which was perturbatively included in CCSD(T) calculations and is known to take an important role to reproduce the excitation energy [47]. The excited states of ^{78}Ni were calculated recently [122], using a ^{60}Ca core, which is the same model space as the PFSDG-U shell model calculation [34]. As drawn in Fig. 6.3, the excitation energies, $E(2_1^+)$ = 3.25 MeV and $E(4_1^+)$ = 3.63 MeV, are estimated a few hundred keV higher than the observed energy levels, though the employed chiral interaction of "1.8/2.0(EM)" was the same as the one used for CCSD(T) calculation. This overestimation compared to the CCSD(T) result may be explained as the lack of proper treatments for multi particle-hole excitations in the IM-SRG calculation. Indeed, the coupled cluster calculation with only the $1p$-$1h$ and $2p$-$2h$ excitations, estimates the energy as $E(2_1^+)$ = 3.5 MeV [47], which is in good agreement with the result of the IM-SRG calculation. Besides, the average number of the proton and neutron p-h excitations are also calculated and listed in Tab. 6.1. It can be seen that the average numbers of excitations for protons and neutrons in the 2_1^+ states are similar to the spherical states of the two shell model calculations using the phenomenological interactions.

6.2 Reaction theory

The reaction cross section is one of the beneficial observables to obtain structural information of the final state nuclei [158]. As discussed in section 5.1, the inclusive cross sections for producing ^{78}Ni in both $(p,2p)$ and $(p,3p)$ reactions were about factor four smaller than in neighboring nuclei. In this section, this anomaly is considered employing a recently developed reaction theory, distorted wave impulse approximation (DWIA). Firstly, the current understanding and arguments of the nuclear reaction cross sections are introduced in section 6.2.1, then the DWIA calculation [159] is briefly explained in section 6.2.2. The result of this work is discussed in section 6.2.3 by comparison with the calculated values based on the DWIA result and the spectroscopic factors from PFSDG-U, MCSM, and IM-SRG.

6.2.1 Reduction factors

To visualize the predictability of theoretical calculations, a "reduction factor", defined as a ratio of measured and calculated cross sections as shown below, is often used:

$$R_s \equiv \frac{\sigma_{\rm exp}}{\sigma_{\rm th}}. \tag{6.2}$$

The theoretical cross section can be formulated from a spectroscopic factor, C^2S, and single-particle cross section, $\sigma_{\rm sp}$, with the spin, j, of the removed nucleon and the final state, α, as:

$$\sigma_{\rm th}(j,\alpha) = C^2S(j,\alpha)\cdot\sigma_{\rm sp}(j,S(\alpha)), \tag{6.3}$$

with the effective separation energy, $S(\alpha)$, described with the proton (neutron) separation energy, S_p (S_n), and excitation energy of the final state, E_α, as:

$$S(\alpha) = S_p\ (S_n) + E_\alpha. \tag{6.4}$$

Besides, the spectroscopic factor, C^2S, is defined as the overlap of the initial and final state wave functions:

$$C^2S(j,\alpha) = \frac{\left|\langle\Psi_{A+1}|a_j^\dagger|\Psi_A(\alpha)\rangle\right|^2}{2j+1}. \tag{6.5}$$

Note that a correction factor for transforming the harmonic oscillator basis to the center-of-mass system, $(A/(A-1))^N$, is multiplied to the right-hand side of Eq. (6.3), in case of applying Glauber's eikonal and sudden model. However, this is not the case for other approximations, such as the DWIA calculation applied in this work.

Generally, the reduction factor R_s in Eq. (6.2) is interpreted as a quantity of our knowledge about the nuclei, in other words, an indicator of the missing nucleon-nucleon (NN) correlations from the nuclear structure calculation, such as the shell model, mean-field, or *ab initio* calculations. It has been empirically known that the R_s is around 60-70% for stable isotopes from several measurements with $(e,e'N)$ reactions. Thus, this quenching was considered as rather universal in the entire nuclear chart. However, more experimental results of nucleon removal reactions from unstable nuclei with about 70-230 MeV/nucleon indicated the reduction factor has a strong dependence on the difference of the nucleon separation energies, $\Delta S = S_p - S_n$ for proton removal, and $\Delta S = S_n - S_p$ for neutron removal [160–162]. For these experiments, ^{9}Be and ^{12}C targets were employed, and the sudden and eikonal approximation was applied for the analysis of the one-proton or one-neutron removal cross sections. After these empirical findings, further studies on the reaction mechanism have been carried out with nucleon transfer reactions, such as (p,d), $(d,{}^3\mathrm{He})$, and (d,t) reactions [163, 164]. The theoretical cross sections for nucleon pickup reactions were calculated with the adiabatic distorted wave approximation (ADWA) and the coupled reaction channel (CRC) calculations, and no such asymmetry of the reduction factor R_s was observed. More recently, quasi-free proton knockout, $(p,2p)$, reactions with a hydrogen target were performed with ^{14,16,18,22,24}O beams systematically [165], and resulted in no dependency with ΔS within the error bars. For this case, the distorted wave impulse approximation (DWIA) formalism [159] was utilized as the reaction mechanism. The DWIA calculation with microscopic optical potential was also exploited in this work for the analysis of the ^{79}Cu$(p,2p)^{78}$Ni reaction channel, while the $(p,3p)$ channel could not be discussed as there is no available theory for multi-nucleon knockout reactions.

6.2.2 DWIA calculation

The DWIA calculation was conducted by K. Ogata [166] at RCNP, Osaka University, to deduce the single-particle cross sections feeding the excited states, $\sigma_{\rm sp}$. The same calculation was performed for the ^{80}Zn$(p,2p)^{79}$Cu channel [104, 105], which was obtained during the same measurement as this work. To obtain the theoretical cross sections, several conditions listed below were assumed:

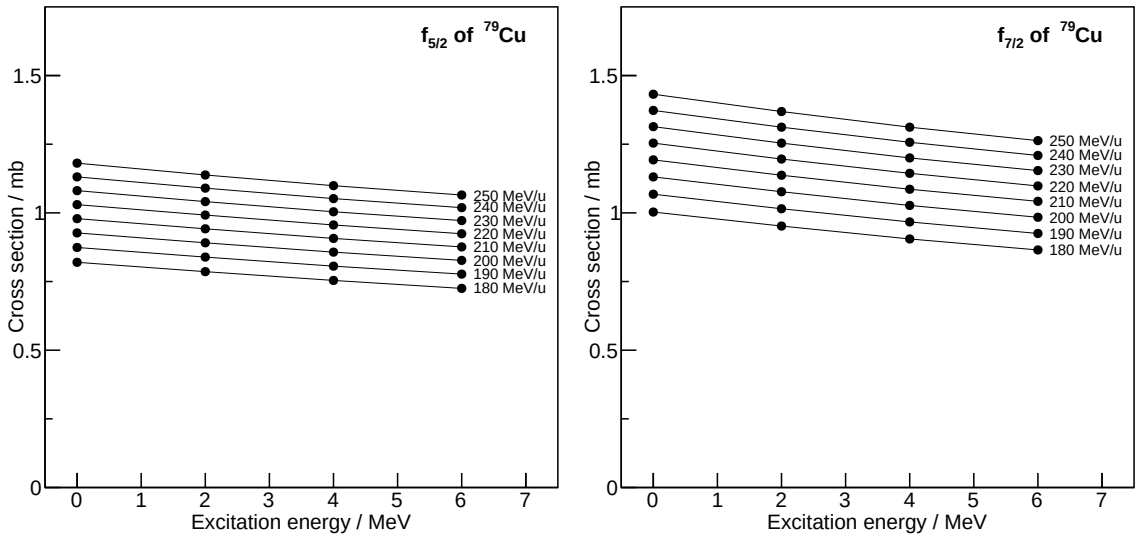

Fig. 6.4: Theoretical predictions of inclusive cross sections. Calculated single-particle cross sections for proton-induced proton knockout process from respective orbitals, $f_{5/2}$ (left) and $f_{7/2}$ (right), of ^{79}Cu with DWIA formalism with respect to each incident energy of beam from 180 MeV/u to 250 MeV/u.

- Density distribution of initial and final nuclei, ^{79}Cu and ^{78}Ni, were derived from Bohr-Mottelson's single-particle model to reproduce proper proton and neutron separation energy, S_p and S_n, by adjusting the central forces.
- The separation energy was adjusted for the recently published atomic mass evaluation and mass excess of ^{79}Cu [61, 62].
- The distorting optical potential was prepared from microscopic folding model with the nuclear density obtained by folding the Melbourne g-matrix interaction [167, 168] with the nuclear density distribution evaluated by Bohr-Mottelson's single-particle model.
- Effective density-dependent NN interaction of Ref. [169] was utilized.
- Integrate the triple differential cross section (TDX) for the entire solid angle to obtain the single-particle cross section, $\sigma_{\rm sp}$.

In addition, the integrated TDX of outgoing protons labeled 1 and 2 is divided by 2 to avoid the double count for two outgoing protons, which cannot be distinguished in the experiment:

$$\sigma_{\rm sp} = \frac{1}{2}\iiint dE_1 d\Omega_1 d\Omega_2 \frac{d^3\sigma}{dE_1 d\Omega_1 d\Omega_2}. \tag{6.6}$$

Here, the calculated single-particle cross sections, $\sigma_{\rm sp}$, for the $(p,2p)$ knockout process from $f_{5/2}$ and $f_{7/2}$ orbits of ^{79}Cu with respect to each incident energy of beam from 180 MeV/u to 250 MeV/u are shown in Fig. 6.4. The cross section depends on the incident energy. Because a 10-cm thick liquid hydrogen target was employed in this experiment, the kinetic energy of the beam at the reaction could slow down from 250 MeV/u at the entrance to 180 MeV/u at the exit. Thus, the geometrical average of these cross sections was calculated to deduce the theoretical single-particle cross section.

6.2.3 Predicted exclusive cross sections

Experimental results Figure 6.5 shows the evolution of the experimental and theoretical exclusive cross sections as a function of excitation energy of ^{78}Ni. The experimentally obtained

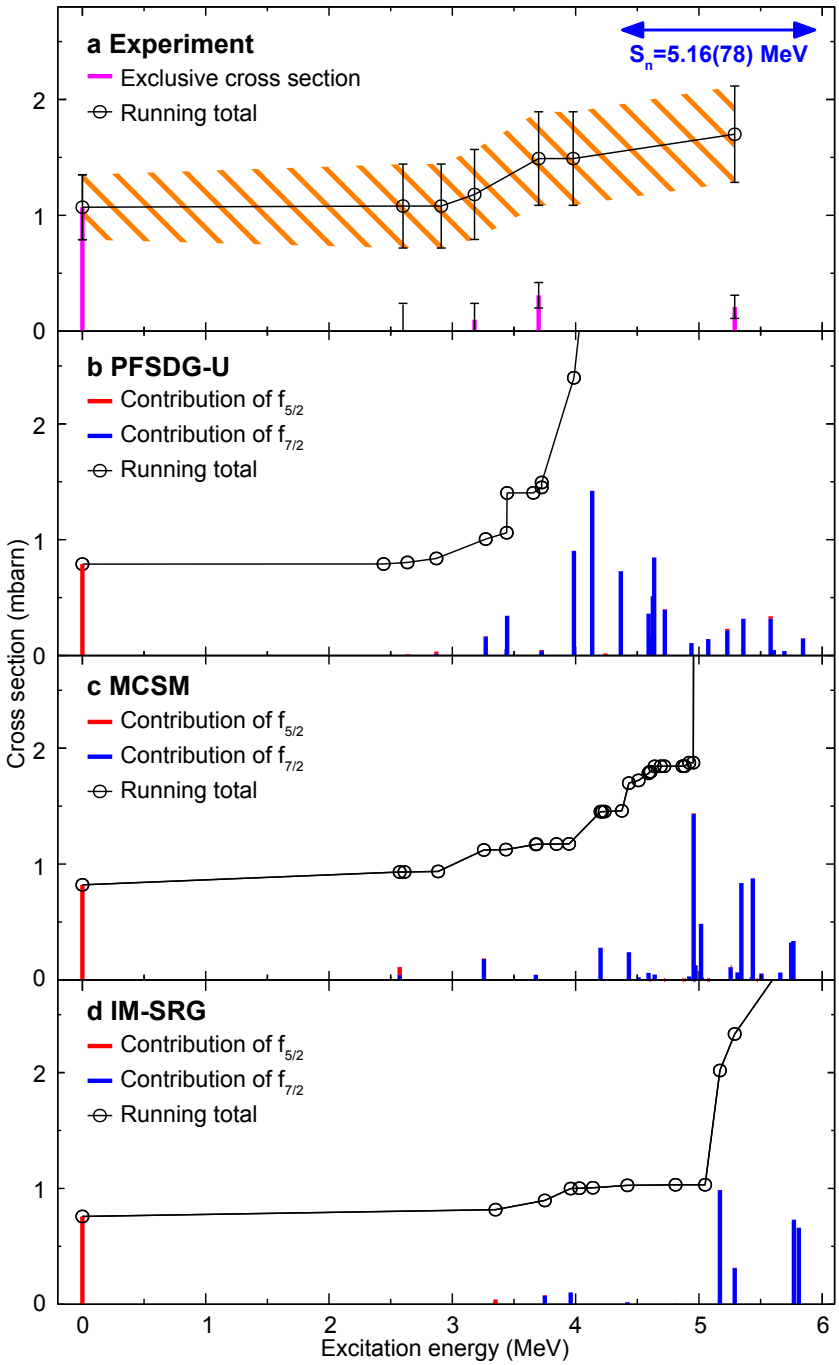

Fig. 6.5: Evolution of the experimental and theoretical cross sections as a function of excitation energy for the ^{79}Cu$(p,2p)^{78}$Ni reaction. Panel **a** shows the obtained experimental cross sections with magenta bars representing exclusive cross sections and their running total. The orange dashed area illustrates the error bars of the experimental uncertainty. The evaluated neutron separation energy (S_n = 5.16(78) MeV [61]) is also illustrated with a blue arrow. The calculated exclusive cross sections using PFSDG-U, MCSM, and IM-SRG, deduced by convolution spectroscopic factors with DWIA single-particle cross sections, are shown in panels **b**-**d**. Red and blue bars represent the amount of the contributions from the protons in the $f_{5/2}$ and $f_{7/2}$ orbitals of ^{79}Cu for the $(p,2p)$ reaction. The evolution of the running sum of the cross sections is shown with black lines. This figure is also included in the submitted paper of this work [88].

exclusive cross sections can also be found in Tab. 5.3. More than a half of the intensity contributes to generate the ground state, and other strengths exist above 3 MeV. Note that the sum of the exclusive cross sections is equivalent as the inclusive cross section σ_{incl} = 1.7(4) mb.

Contributions of $f_{5/2}$ and $f_{7/2}$ PFSDG-U and MCSM produced the spectroscopic factors for each excited state of ^{78}Ni from $f_{5/2}$ and $f_{7/2}$ orbits of the ground state of ^{79}Cu. By taking products of the spectroscopic factors $C^2S(j,\alpha)$ with single-particle cross sections $\sigma_{\rm sp}(j,S(\alpha))$ as denoted in Eq. (6.3), the expected exclusive cross section can be calculated. The theoretical exclusive cross sections are shown with red and blue bars, of which color represents the contribution of the orbital of the struck proton in ^{79}Cu, $f_{5/2}$ and $f_{7/2}$, respectively. The knockout reaction of the $f_{5/2}$ proton contributes mainly to the ground state, while the $f_{7/2}$ part produces excited states. This result agrees with an intuitive sense of the ground state of ^{79}Cu. In the case the valence proton in the $f_{5/2}$ orbital is taken away, no p-h excitations across Z = 28 can be populated, and the ground state, 0^+_{gs}, of ^{78}Ni, may be favored. On the other hand, in the case of the tightly bound proton in the $f_{7/2}$ orbital below Z = 28 gap reacting, several excited states at a few MeV excitation energy with discrete levels from $J^\pi = 1^+$ to 6^+ are expected, as the shell gap between $f_{5/2}$ and $f_{7/2}$ is assumed to be large. Note that the calculated cross sections of other proton states bound deeply, such as $p_{3/2}$ and $p_{1/2}$, were negligiblly small.

No population of 2^+_1 and deformed states in the $(p,2p)$ channel As indicated experimentally in section 5.5, there was no direct, or only very little, population from the $(p,2p)$ reaction to the 2^+_1 and 2^+_2 state at 2600 keV and 2900 keV, and another deformed state, tentatively assigned at 3980 keV. Following the discussion in section 6.1, the 2^+_1 state at 2600 keV is assumed as a spherical state 2^+_{sp}, while the 2900-keV state is considered as deformed state with multi p-h excitations, which may also happen in the tentatively assigned 3980-keV state. Though the $(p,2p)$ reaction is expected to prefer to populate spherical states since the ground state of ^{79}Cu is also thought to be spherical, there seems to be no, or only very little, population of the 2^+_1 state. The reason might be explained as that the 2^+_{sp} state contains rather large neutron excitations across the N = 50 gap, around 1.5 p-h excitations as listed in Tab. 6.1, which cannot be populated directly from the $(p,2p)$ reaction from the ground state of ^{79}Cu with about 0.4 p-h excitations. Similar argument can be applied to the deformed states, as 2^+_c and 4^+_{sp}, in which many p-h excitations occur. As shown in Fig. 6.5, the tendencies of no feeding to the 2^+_1 state and deformed states can be seen in the theoretical calculations.

Low inclusive cross section and neutron separation energy Though the distributions of the calculated strength for the theoretical calculations shown in Fig. 6.5 are not the same, it might be possible to discuss their similarities. The strength from $f_{7/2}$ knockout does not appear in the energy region below 4-5 MeV, depending on the calculations, while large strength suddenly appear near the neutron separation energy threshold. It can be noticed that the running totals of the exclusive cross sections for these calculations just below these thresholds are 1-2 mb, while the values above them rapidly increase. Considering the neutron separation energy of ^{78}Ni is evaluated at S_n = 5.16(78) MeV [61], it is possible to assume such high lying states are not bound, as they are predicted at similar energy of the neutron separation energy, S_n. At the same time, it might be worth to notice that the running sums below the threshold are close to the experimentally obtained inclusive cross section, σ_{incl} = 1.7(4) mb. Thus, it might also be possible to estimate that the reason of such low inclusive cross sections to produce ^{78}Ni, compared to the ones for the nuclei in the vicinity, as discussed in section 5.1.3, is due to the

large strength after the $(p,2p)$ reaction are for unbound states of ^{78}Ni, which may decay into ^{77}Ni consequently. This fact may be able to validate the accuracy of the atomic mass evaluation, S_n = 5.16(78) MeV, as the estimated energy of the threshold ranging 4-5 MeV for the three calculations, are in agreement with the S_n value of ^{78}Ni within the uncertainty.

Chapter 7

Conclusion and Future Outlook

In this work, excited states of the neutron-rich doubly magic isotope, ^{78}Ni, were investigated by means of in-beam γ-ray spectroscopy for the first time, taking advantage of the combination of the detector devices, MINOS and DALI2, at the world's highest secondary beam intensity accelerator facility, RIBF at RIKEN, Japan. ^{79}Cu and ^{80}Zn beams were produced at the BigRIPS spectrometer by in-flight fission of an ^{238}U primary beam with an energy of 345 MeV/u accelerated by a cyclotron complex. After the particle identification process, the secondary beams bombarded a 10-cm thick liquid hydrogen target system for inducing proton knockout reactions with a vertex reconstructing apparatus, MINOS. Subsequently, the reaction residues and their de-excitation γ rays were analyzed individually by a particle spectrometer, ZeroDegree, and a γ-ray detection array, DALI2.

The ^{79}Cu$(p,2p)^{78}$Ni and ^{80}Zn$(p,3p)^{78}$Ni reaction channels were analyzed separately. From the γ-ray spectra, several transition candidates were observed. To resolve these transitions, the spectra were fitted by the response functions of the γ-ray detector, simulated by a Monte-Carlo based simulation package, GEANT4, by maximizing the likelihood with a multivariable probability density function. Six candidates of γ-ray peaks, five in the $(p,2p)$ reaction channel and one additionally in the $(p,3p)$ channel, were examined by significance levels calculated from a likelihood ratio test. Furthermore, a γ-γ coincidence analysis was performed. By summarizing the experimental facts of the intensity relationships, significance levels, and the γ-γ correlations, the following conclusions were achieved:

- The most intense γ-ray transitions of 2600(33) keV and 2910(43) keV for the $(p,2p)$ and the $(p,3p)$ channel, respectively, were confirmed with 7.6σ and 3.9σ significance levels.
- They were understood as the transitions from the first and second 2^+ states decaying directly to the ground state.
- According to the γ-γ coincidence analysis, the four other γ-ray transitions confirmed in the $(p,2p)$ channel do not decay directly to the ground state but passed through the 2^+_1 state.
- Additional γ-γ coincidence analysis, the intensity relationships, and the evaluated neutron separation energy S_n = 5160(780) keV indicated that there are at least three bound excited states at 3180(55) keV, 3700(36) keV, and 5290(59) keV.
- The states at 2910(43) keV and 3980(46) keV, which were recognized only in the $(p,3p)$ channel, might have strong connection with the two-proton knockout reaction.

The obtained experimental level scheme described above was compared with several state-of-the-art theoretical predictions, large-scale shell model, mean-field, and *ab initio* calculations. While the first 2^+ state was reproduced well among these calculations, the second 2^+

state was explained only by two large-scale shell model calculations with large model spaces for neutrons, full sdg shell above the $N = 50$ gap. Both shell model predictions indicate the 2^+_2 state is an "intruder" state with more than $2p$-$2h$ excitations for both proton and neutron configurations. While the ground and excited states observed in the $(p,2p)$ reaction are expected to be of spherical shape, the "intruder" states are supposed to be deformed states establishing rotational excitations. Thus, a shape coexistence feature is emerging. In addition, the shell closure of both proton and neutron is predicted to be quenched for more neutron-rich isotopes and isotones. Namely, ^{78}Ni is expected to be a nuclei at an anchor point against deformation.

Even though the "intruder" states were not reproduced by other calculations, this hypothesis is partially supported. The mean-field calculations agreed with the spherical feature of the ground state, but also suggested that the excited states cannot be depicted as a simple vibrational excitation but rather explained well with an assumption of a mixture with both vibrational and rotational degrees of freedom. Likewise, the *ab initio* computational results inferred that contributions from the $2p$-$2h$, $3p$-$3h$ and even more p-h excitations take important roles in the excited states. These explanations of the missing strengths underlined the possible shape coexistence and shell-quenching phenomena towards nuclei far from the stability line.

The reaction cross sections to produce ^{78}Ni from ^{79}Cu and ^{80}Zn turned out to be significantly lower than in neighboring nuclei. A possible explanation is that the excitation energy of the final state after the knockout reactions is higher than the neutron separation energy, owing to a large shell gap at $Z = 28$ between $f_{5/2}$ and $f_{7/2}$ orbitals. In a naive picture of the nuclear reaction, while the final states after removing the proton in $f_{5/2}$ is preferred to be the ground state of ^{78}Ni, the knockout reaction from the $f_{7/2}$ orbit can be assumed to be several states with high excitation energy. To figure out the origin of such a low cross section in the $(p,2p)$ reaction, an advanced theoretical framework for calculating a quasi-free one nucleon knockout reaction was applied in combination with the spectroscopic factors of shell model calculations. The theoretical results were in good agreement with the experimental cross sections: The ground and spherical excited states were favored, while the deformed states were not populated. Additionally, as it was expected, most of the cross sections after the reaction were found to feed states above the neutron separation energy threshold, which eventually evaporates one or more neutrons.

In this work, the predictive power of the $(p,2p)$ reaction mechanism was demonstrated quantitatively. However, there is no tool yet to explain the $(p,3p)$ reactions, especially the reason why the deformed states were mainly populated despite the ground state of ^{80}Zn is assumed to be spherical by several observations and calculations. Explanations of this "selectivity" were attempted by means of two nucleon amplitudes (TNAs), which represent overlaps of the wave functions of the initial and final states of the reaction as defined below, by a recent shell model calculation [119]:

$$\mathrm{TNA}: C(j_1, j_2, J) = \frac{\langle \Psi_{A+2} | A^\dagger(j_1, j_2) | \Psi_A \rangle}{\sqrt{2J_{A+2}+1}}. \tag{7.1}$$

Here, the $A^\dagger$ is a transfer operator, which is proportional to the two-neucleon annihilation operator, $a^\dagger_{j_1} a^\dagger_{j_2}$. Remarkably, the TNA values revealed that the spherical states have larger values than for the deformed states even in the two-proton knockout reaction, in which the $2p$-$2h$ "intruder" configuration can be naively considered as favored. This surprising fact is necessary to be investigated in further theoretical developments in both calculations of shell model and reaction mechanism.

As a conclusion of the experimental observations and theoretical interpretations, ^{78}Ni was confirmed as doubly magic, while emergence of shape coexistence was proposed. This finding

casts a question on the shell closure of proton $Z = 28$ and neutron $N = 50$ gaps in the heavier isotopes and lighter isotones than ^{78}Ni, where the ground states are expected to be deformed due to reduced spin-orbit splitting of the gaps, as reported by the recent shell model calculations. In other words, ^{78}Ni is located at the starting point of shell quenching. Low inclusive cross sections of both $(p,2p)$ and $(p,3p)$ reactions indicated that most of the final states after the knockout reaction is high above the nucleon separation energy. From these results, new experiments to explore this unique feature are needed to be examined, such as:

- Improve the detection efficiency and/or the Compton suppressing ability of the γ-ray spectrometer, which is especially important for the γ-γ coincidence analysis; a new detector based on a new type of scintillator, or γ-ray tracking array with HPGe semiconductor detector would be necessary.
- Invariant mass spectroscopy with neutrons is needed to probe the mechanism of the one- or two-proton knockout reactions.
- To determine the existence of 0^+_2 state, some experiment to observe the $E0$ transition of $0^+_2 \rightarrow 0^+_1$, such as conversion electron spectroscopy, should be considered.
- Coulomb excitation to the first and second 2^+ states, or life-time measurement from the excited states are also important to be conducted to obtain the reduced transition probabilities: $B(E2 : 2^+_x \rightarrow 0^+_{gs})$.
- Further studies of the isotopic ($Z = 28$) and isotonic ($N = 50$) chains, especially the excited states of ^{80}Ni and ^{76}Fe are necessary to conclude the shell-quenching scheme proposed by the shell model calculations.

This study concludes the persistence of the shell closure for ^{78}Ni, and indicated the shell-quenching and shape coexistence at the same time. An emergence of new phenomena in such "exotic" nuclei located far from the stability line pins down an anchor point to constrain our picture of the nuclear shell structure, and ensures the necessity of the development of our knowledge on the interactions of nucleons in a nuclear system, especially with very unbalanced proton-neutron ratio. From the experimental point of view, a more detailed and wider survey for the entire nuclear chart to see such anomalous characters would be meaningful. Besides, further theoretical developments, such as mean-field and *ab initio* calculations, to universally understand the nuclear chart are desired.

Acknowledgements

I would like to express my sincere gratitude to all the persons concerned, without whom this work could not be completed.

First of all, I would like to appreciate my supervisor Prof. H. Sakurai for excellent tuition for more than 7 years from when I was a senior student. Without his support I could not get this valuable chance to study the physics of the nuclear structure with the world-leading accelerator facility. I could also have opportunity to acquire the experience of the detectors which he provided me a chance to work on the scintillator based detector during my Master program, that made me not hesitating to work on the complicated detector system in this experiment. I have been stimulated by his broad knowledge of the nuclear physics, which illuminates my stuck ideas whenever I come to ask his advice. There is no doubt that I have had an invaluable period as a graduate student because of him.

I really want to convey special thanks for the contributions of the spokespersons of the experimental campaign, Dr. P. Doornenbal and Dr. A. Obertelli. It was fortunate for me to collaborate with them as a PhD student. Even though it was the first time for me to analyze data from the RIBF experiment, they are patiently teaching me anything about the knowledge and technique of how to perform the in-beam γ-ray spectroscopy experiment and the analysis of the obtained data.

My work could not be performed without the core members of the SEASTAR experiments. I would like to say thank you to the local members and the MINOS core members, Dr. G. Authelet, Dr. H. Baba, Dr. D. Calvet, Dr. F. Château, Dr. A. Corsi, Dr. A. Delbart, Dr. J.-M. Gheller, Dr. A. Gillibert, Dr. T. Isobe, Dr. V. Lapoux, Dr. M. Matsushita, Mr. S. Momiyama, Dr. T. Motobayashi, Dr. M. Niikura, Dr. H. Otsu, Dr. C. Péron, Dr. A. Peyaud, Dr. E.C. Pollacco, Dr. J.-Y. Roussé, Dr. C. Santamaria, Dr. Y. Shiga, Dr. S. Takeuchi, Dr. T. Uesaka, Dr. H. Wang, and Dr. K. Yoneda, for the contribution to the preparations of the experiments including the installation of the MINOS system at the first physics experiment.

Besides, I would like to thank to all the collaborators for participating in the experiment, Dr. F. Browne, Dr. L.X. Chung, Dr. Zs. Dombradi, Dr. S. Franchoo, Dr. F. Giacoppo, Dr. A. Gottardo, Dr. K. Hadynska-Klek, Dr. Z. Korkulu, Mr. S. Koyama, Dr. Y. Kubota, Dr. J. Lee, Dr. M. Lettmann, Dr. C. Louchart, Dr. R. Lozeva, Mr. K. Matsui, Mr. T. Miyazaki, Dr. S. Nishimura, Dr. L. Olivier, Dr. S. Otam, Dr. Z. Patel, Dr. E. Sahin, Dr. C. Shand, Dr. P.A. Söderström, Dr. I. Stefan, Dr. D. Steppenbeck, Dr. T. Sumikama, Dr. D. Suzuki, Dr. Zs. Vajta, Dr. V. Werner, Dr. J. Wu, and Dr. Z.Y. Xu, for their worthy effort and the enjoyable time during and the after the experiment.

I would like to respect and thank for the helps from the theorists Dr. J. Holt, Dr. J. Menendez, Dr. F. Nowacki, Dr. K. Ogata, Dr. T. Otsuka, Dr. S. Péru, Dr. A. Poves, Dr. A. Schwenk, Dr. J. Simonis, Dr. S.R. Stroberg, and Dr. Y. Tsunoda. for making large number of the discussions even it took for a long time to obtain the final results. Thanks to the fruitful interactions with them, I could get various perspectives on the nuclear physics.

I appreciate all the colleagues of NEX group at the University of Tokyo, Prof. H. Sakurai,

Prof. R.S. Hayano, Prof. K. Wimmer, Prof. K. Yako, Dr. M. Niikura, Dr. T. Suzuki, Dr. M. Hori, Dr. M. Sato, Dr. N. Kobayashi, Dr. H.X. Shi, Mr. Y. Fujiwara, Dr. T. Hashimoto, Dr. T. Kobayashi, Dr. Z.Y. Xu, Dr. K. Todoroki, Dr. T. Nishi, Dr. Y. Tanaka, Mr. K. Okochi, Mr. K. Matsui, Dr. Y. Murakami, Mr. H. Yamada, Mr. S. Momiyama, Mr. T. Miyazaki, Mr. Y. Watanabe, Mr. S. Koyama, Mr. T. Saito, Mr. S. Nagamine, Mr. T. Ando, Mr. T. Aoki, Mr. T. Koiwai, and Mr. N. Yoshida for welcoming me to join the group even though I do not collaborate with them directly, and for sharing their knowledge and fun time with me all the time, which were quite important for my study life at the university.

I would like to acknowledge all the members working, or used to work, for the in-beam γ-ray spectroscopy at the RIBF facility, in particular, Dr. F. Browne, Dr. S. Chen, Dr. P. Doornenbal, Dr. I. Murrawy, Dr. M.L. Cortés, Ms. N. Paul, and Mr. W. Rodriguez, for working with me on the data obtained by MINOS system and the DALI2 γ-ray spectrometer. They are very eager to improve and obtain nice analysis which encouraged me very much.

I would like to express my gratitude to all my friends. And finally, sincere thanks to my parents for their considerations, encouragements, emotional support, and loves for years, which are the most essential to accomplish this big goal.

Appendix A

Analysis of excited states of ^{80}Zn

To confirm the procedure to deduce the γ-ray transition energies, applied for the analysis of ^{78}Ni, the γ-ray spectrum of the excited states of ^{80}Zn was also analyzed in section 4.4. The method is presented in section 5.2.1. In this chapter, the result of the γ-ray energy determination for ^{81}Ga$(p,2p)^{80}$Zn channel is described. As the excited states of ^{80}Zn have been studied well in previous experimental works [82, 91, 101], the five known γ-ray transitions are summarized in Fig. 4.20. The excited (4^+) state at 1974 keV is known to have a lifetime of 136^{+92}_{-67} ps decaying through the $(4^+) \rightarrow 2^+$ and $2^+ \rightarrow 0^+$ transitions to the ground state [82]. Thus the γ-ray peak of the $2^+ \rightarrow 0^+$ transition of 1492 keV in the spectrum may consist of two components: deteriorated one with the same lifetime effect and intensity as the $(4^+) \rightarrow 2^+$ transition, and another one without any lifetime. The former represents the (4^+) state decaying sequentially after the $(4^+) \rightarrow 2^+$ transition. While the latter is due to the direct population of the 2^+ state after the proton-removal reaction or feeding from other higher lying states.

The γ-ray spectrum shown in Fig. 4.27 has relatively wide peak structure around 1500 keV. To reproduce the γ-ray spectrum, GEANT4 simulations [139–141], with not only the reported lifetime of 136 ps, but also with a longer lifetime of 250 ps, to reproduce the width of the peak, were performed. Because the purpose of this analysis was to confirm the validity of the determination of the γ-ray transition energies by fitting the γ-ray spectrum of ^{80}Zn, confirming the robustness of the result with the reported energy values between the two different lifetimes of the excited state, is sufficient. In addition to the reported five γ-ray transitions as listed in Tab. A.1, another transition around 1600 keV was included in the fit to fill the discrepancy

Tab. A.1: Energy values of the excited states of ^{80}Zn. The literature values and the fit result with the assumption of 136- and 250-ps lifetime of the excited (4^+) state. The unit of energy is keV. The transition marked with † mark is not reported in previous works [82, 91, 101], but tentatively placed to fill the discrepancy with the simulated response function and the obtained γ-ray spectrum. The values in parenthesis are the uncertainties of the values.

Literature	136-ps lifetime	250-ps lifetime
482(7)	475(1)	479(1)
841(13)	844(3)	840(2)
1195(18)	1195(5)	1187(7)
1492(1)	1470(10)	1500(10)
—	1580(20)†	1620(20)†
2627(39)	2600(10)	2630(20)

with the simulated response function and the obtained γ-ray spectrum. The energy values and their statistical errors of the γ-ray transitions were determined by deducing the maximum likelihood with six-dimensional multivariate probability density functions (PDFs) as detailed in section 5.2.1. To handle the lifetime effect of the (4^+) state at 1974 keV, the γ-ray peaks of the 482- and 1492-keV transitions with a common lifetime and identical intensity were used in the fit. This simulated response function is illustrated with light-blue curve in Fig. 4.27. Besides, another response function for 1492-keV peak without assuming the lifetime effect to reproduce events without feeding through the $(4^+) \rightarrow 2^+$ transition was taken into account in the fitting, as well as the other γ-ray transitions with no lifetime effect. They are drawn with dark-blue curves in Fig. 4.27.

The obtained PDFs with 136- and 250-ps lifetimes are displayed in Fig. A.1 and Fig. A.2, respectively. As the analysis was carried out coarsely, the intervals of the energy values for the peaks were not dense enough to fit with Gaussian distribution. Thus, the energy value of the maximum likelihood in the distribution was taken as the one of each γ-ray transition. The uncertainty of the energy determination was assumed with the interval of the binning of the PDF analysis, as the width of the distribution was assumed no more than the binning. The deduced energy values are summarized in Tab. A.1.

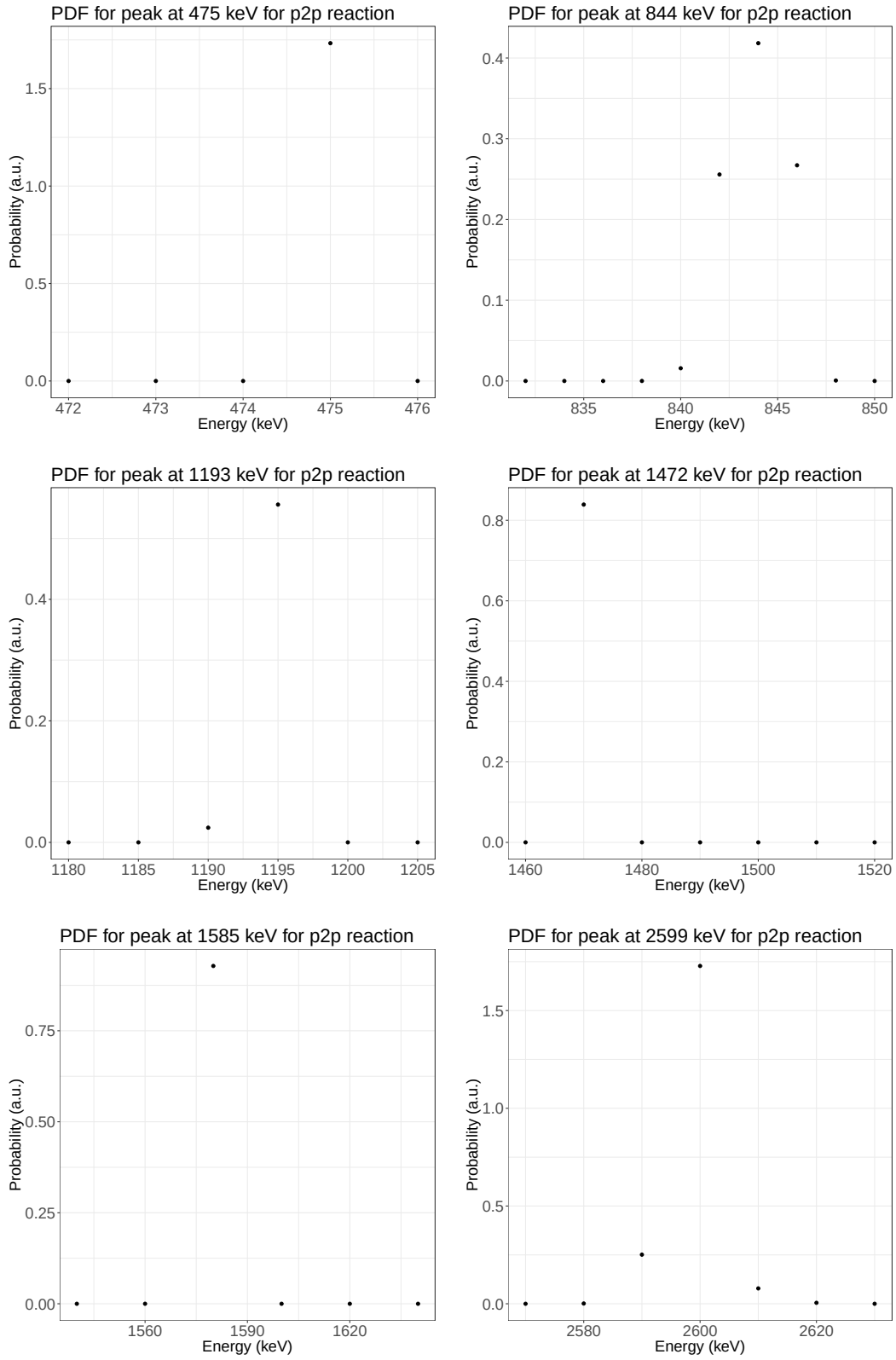

Fig. A.1: Probability density functions with six peaks of ^{81}Ga$(p,2p)^{80}$Zn reaction with assuming 136-ps lifetime of the (4^+) state.

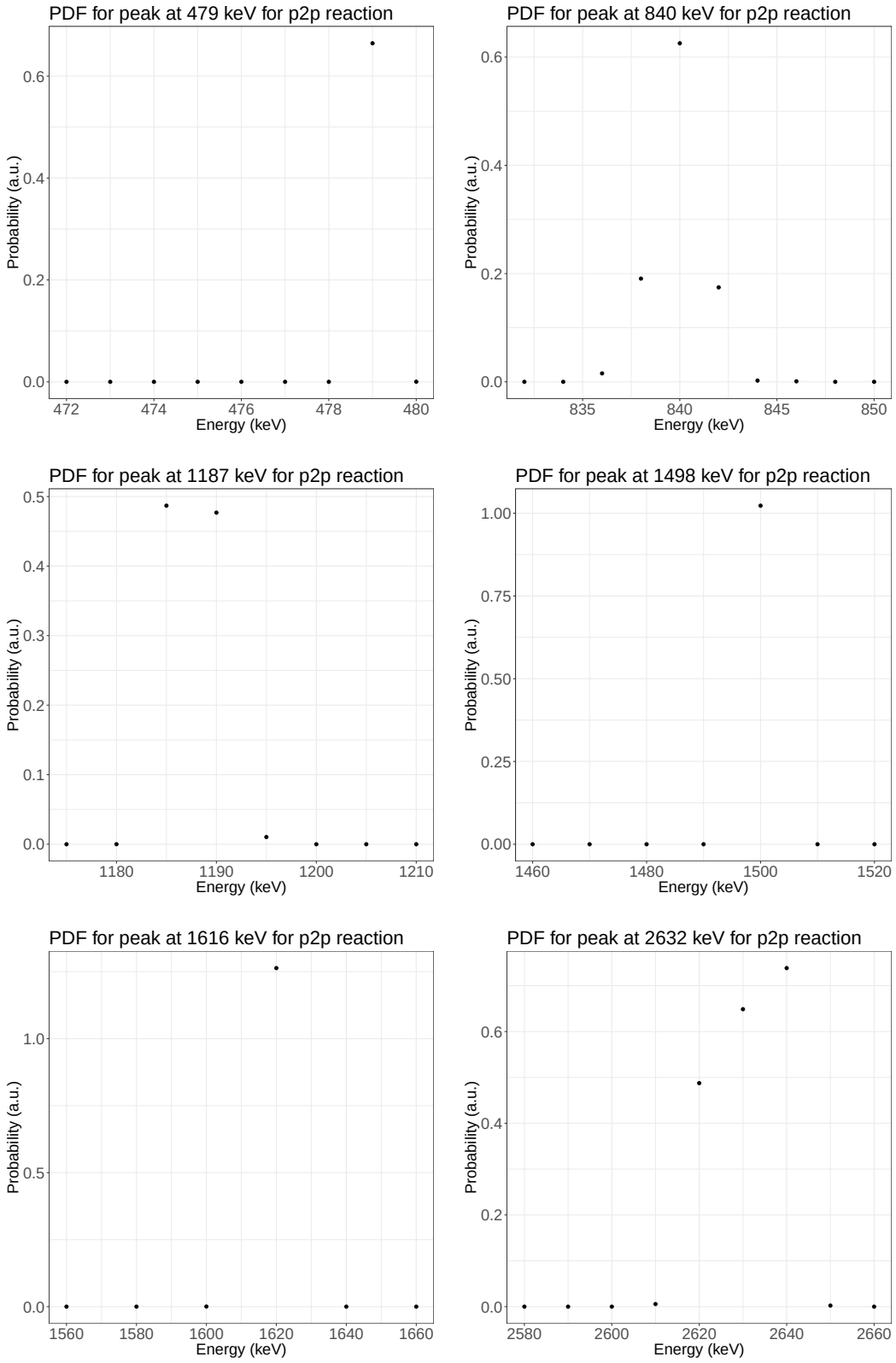

Fig. A.2: Probability density functions with six peaks of ^{81}Ga$(p,2p)^{80}$Zn reaction with assuming 250-ps lifetime of the (4^+) state.

Appendix B

Miscellaneous figures

Miscellaneous figures which are not displayed in the main text are shown in this chapter. The description of each figure is written in the respective caption.

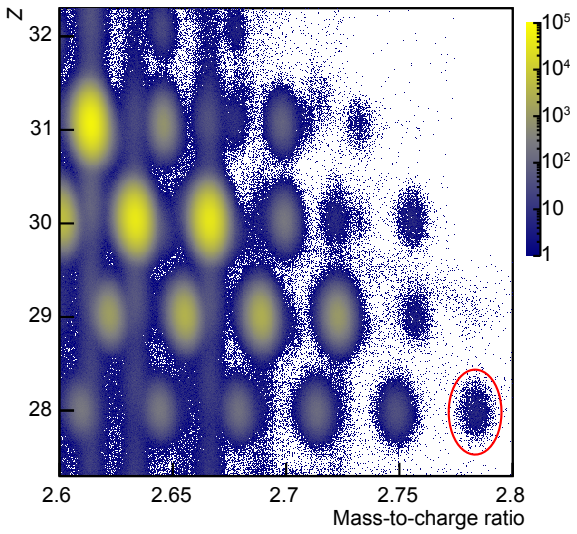

Fig. B.1: Particle identification plot of the radioactive beam by the ZeroDegree fragment separators with trajectories of all focal planes. The PID plot obtained with F8, F9, and F11 is plotted. It has better A/Q resolution but looses some events because of the efficiency of F11 PPACs. Thus, trajectory information of F11 was not used for the actual analysis. See section 4.2 and Fig. 4.3 for the detailed explanations.

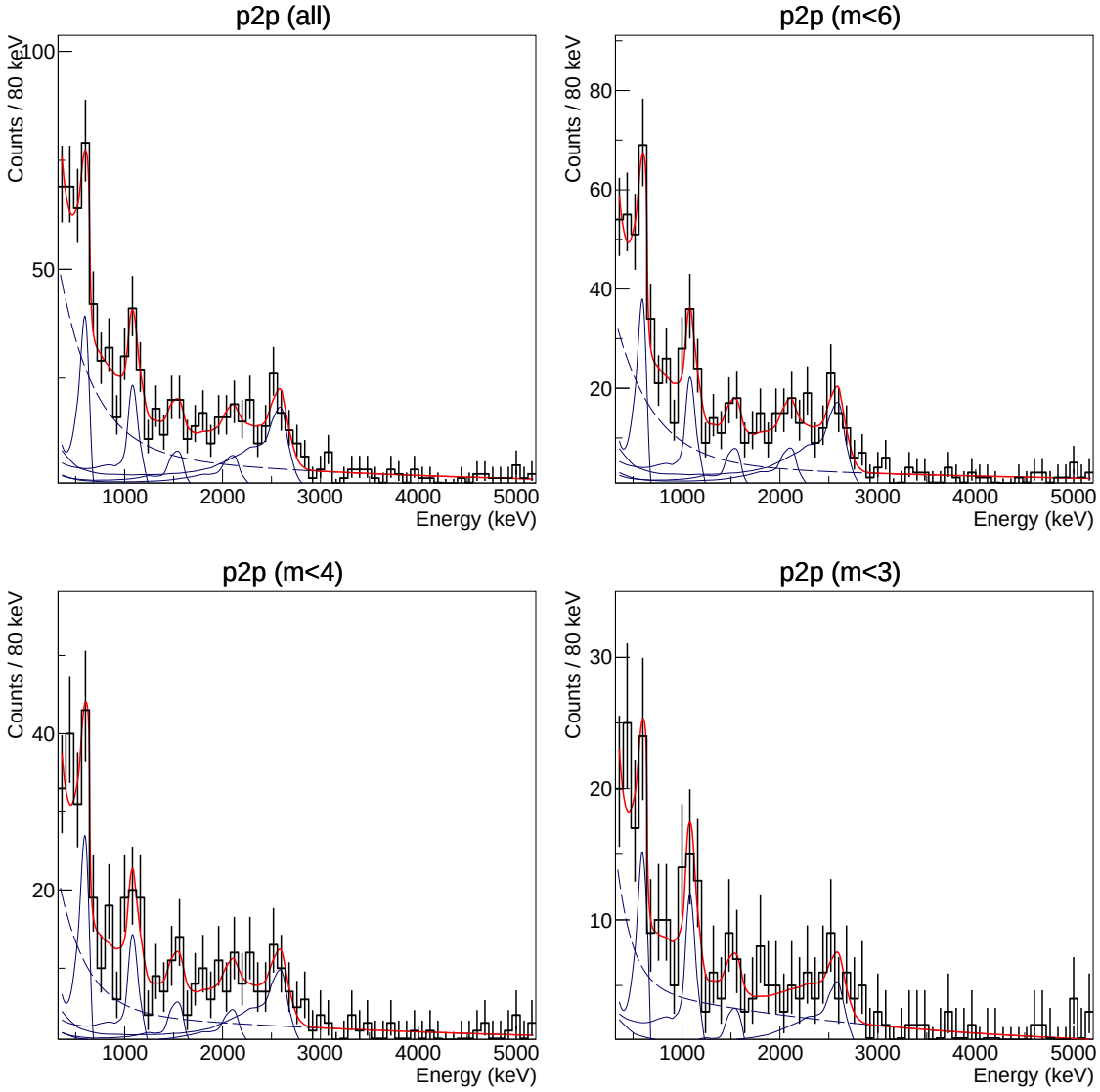

Fig. B.2: γ-ray spectra after the ^{79}Cu$(p,2p)^{78}$Ni reaction (Linear scale). Same data and fittings as Fig. 5.8 with linear plot. 80 keV binning is adopted for the illustrations with several gatings of γ-ray multiplicity, m. The red curve is the fitting curve with maximum likelihood, while the blue line and blue dashed line are the each response function and the double-exponential background, respectively.

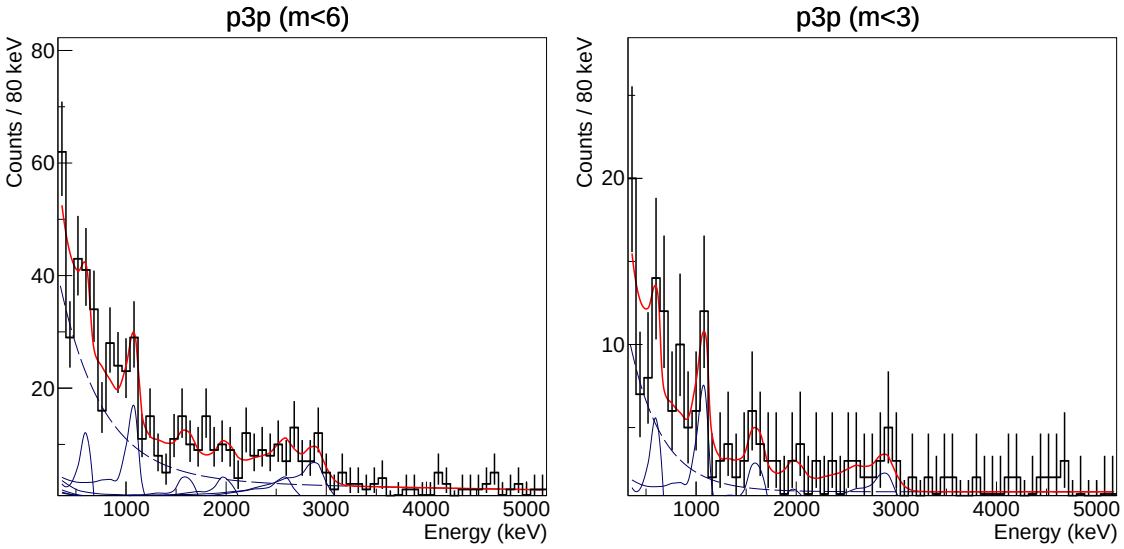

Fig. B.3: γ-ray spectra after the ^{80}Zn$(p,3p)^{78}$Ni reaction (Linear scale). Same data and fittings as Fig. 5.10 with linear scale. 80 keV binning is adopted for the illustrations of two gating conditions for the γ-ray multiplicity: $m < 6$ and $m < 3$. The red curve is the fitting curve with maximum likelihood, while the blue line and blue dashed line are the response functions and the double-exponential background, respectively.

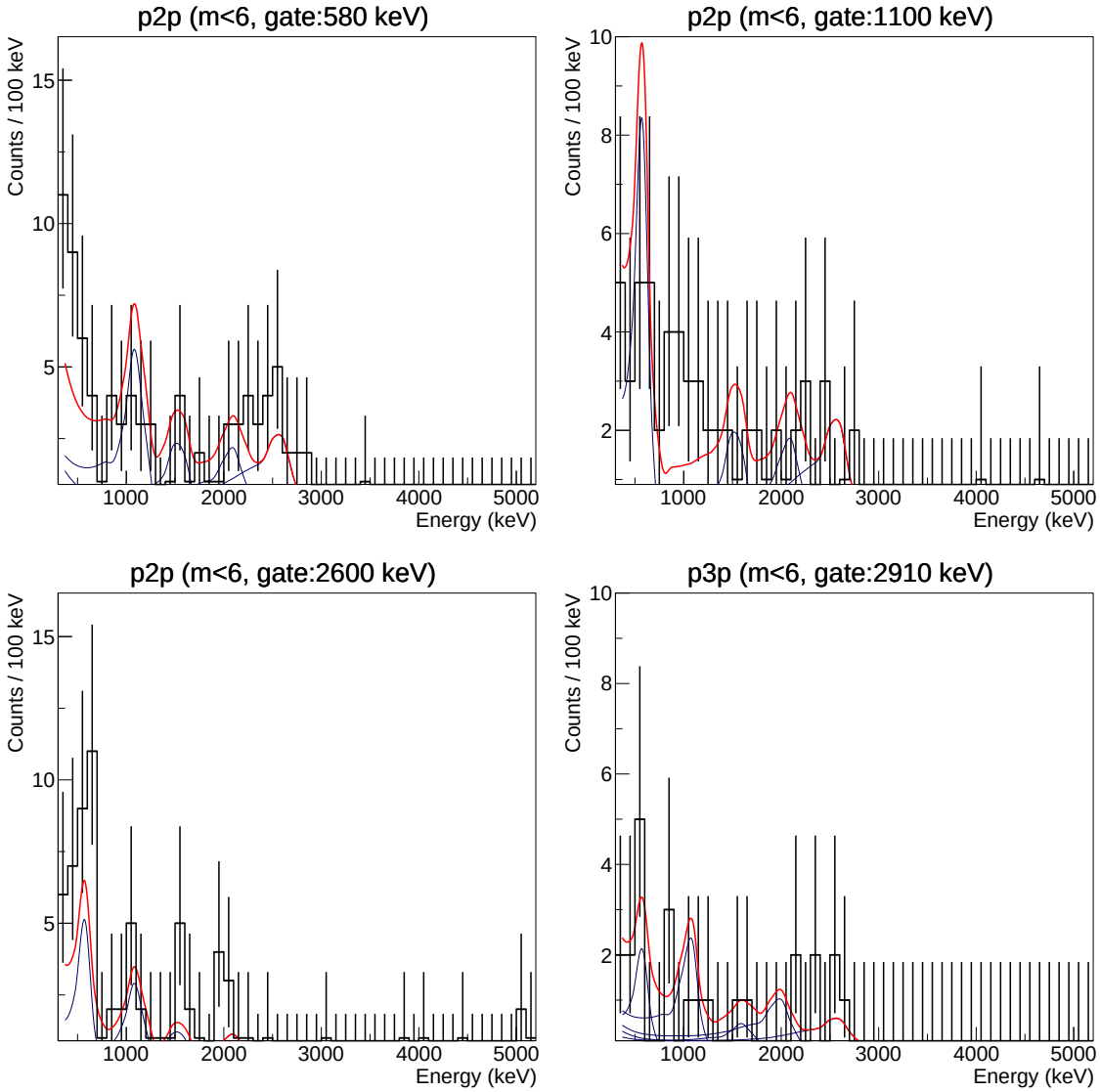

Fig. B.4: γ-γ coincidence spectra with expected response functions (Linear scale). The coefficients of the blue and the red curves are calculated from the number of events within each coincidence gate. See discussions in section 5.4.

Bibliography

[1] E. Rutherford, *The scattering of α and β particles by matter and the structure of the atom*, Philos. Mag. J. Sci. Ser. 6 **21**, 669 (1911).

[2] M.G. Mayer, *On Closed Shells in Nuclei. II*, Phys. Rev. **75**, 1969–1970 (1949).

[3] O. Haxel, J. Jensen, and H. Suess, *On the "Magic Numbers" in Nuclear Structure*, Phys. Rev. **75**, 1766–1766 (1949).

[4] W.D. Knight, K. Clemenger, W.A. De Heer, W.A. Saunders, M.Y. Chou, and M.L. Cohen, *Electronic shell structure and abundances of sodium clusters*, Phys. Rev. Lett. **52**, 2141–2143 (1984).

[5] I. Katakuse, T. Ichihara, Y. Fujita, T. Matsuo, T. Sakurai, and H. Matsuda, *Mass distributions of negative cluster ions of copper, silver, and gold*, Int. J. Mass Spectrom. Ion Proceses **74**, 33–41 (1986).

[6] *National Nuclear Data Center*, `http://www.nndc.bnl.gov/`.

[7] M.G. Mayer, *On closed shells in nuclei*, Phys. Rev. **74**, 235–239 (1948).

[8] D.H. Wilkinson, and D.E. Alburger, *Beta Decay of* ^{11}*Be*, Phys. Rev. **113**, 563–571 (1959).

[9] I. Talmi, and I. Unna, *Order of Levels in the Shell Model and Spin of* ^{11}*Be*, Phys. Rev. Lett. **4**, 469–470 (1960).

[10] C. Thibault, R. Klapisch, C. Rigaud, A.M. Poskanzer, R. Prieels, L. Lessard, and W. Reisdorf, *Direct measurement of the masses of* ^{11}Li *and* $^{26-32}$Na *with an on-line mass spectrometer*, Phys. Rev. C **12**, 644–657 (1975).

[11] G. Huber, F. Touchard, S. Büttgenbach, C. Thibault, R. Klapisch, H.T. Duong, S. Liberman, J. Pinard, J.L. Vialle, P. Juncar, and P. Jacquinot, *Spins, magnetic moments, and isotope shifts of Spins, magnetic moments, and isotope shifts of* $^{21-31}$Na *by high resolution laser spectroscopy of the atomic* D_1 *line*, Phys. Rev. C **18**, 2342–2354 (1978).

[12] C. Détraz, D. Guillemaud, G. Huber, R. Klapisch, M. Langevin, F. Naulin, C. Thibault, L.C. Carraz, and F. Touchard, *Beta decay of* $^{27-32}$*Na and their descendants*, Phys. Rev. C **19**, 164–176 (1979).

[13] D. Guillemaud-Mueller, C. Detraz, M. Langevin, F. Naulin, M. d Saint-Simon, C. Thibault, F. Touchard, and M. Epherre, *β-Decay schemes of very neutron-rich sodium isotopes and their descendants*, Nucl. Physics, Sect. A **426**, 37–76 (1984).

[14] T. Motobayashi, Y. Ikeda, K. Ieki, M. Inoue, N. Iwasa, T. Kikuchi, M. Kurokawa, S. Moriya, S. Ogawa, H. Murakami, S. Shimoura, Y. Yanagisawa, T. Nakamura, Y. Watanabe, M. Ishihara, T. Teranishi, H. Okuno, and R.F. Casten, *Large deformation of the very neutron-rich nucleus* ^{32}*Mg from intermediate-energy Coulomb excitation*, Phys. Lett. B **346**, 9–14 (1995).

[15] I. Tanihata, H. Hamagaki, O. Hashimoto, Y. Shida, N. Yoshikawa, K. Sugimoto, O. Yamakawa, T. Kobayashi, and N. Takahashi, *Measurements of Interaction Cross Sections and Nuclear Radii in the Light p-Shell Region*, Phys. Rev. Lett. **55**, 2676–2679 (1985).

[16] H. Simon, D. Aleksandrov, T. Aumann, L. Axelsson, T. Baumann, M.J. Borge, L.V. Chulkov, R. Collatz, J. Cub, W. Dostal, B. Eberlein, T.H. Elze, H. Emling, H. Geissel, A. Grünschloss, M. Hellström, J. Holeczek, R. Holzmann, B. Jonson, J.V. Kratz, G. Kraus, R. Kulessa, Y. Leifels, A. Leistenschneider, T. Leth, I. Mukha, G. Münzenberg, F. Nickel, T. Nilsson, G. Nyman, B. Petersen, M. Pfützner, A. Richter, K. Riisager, C. Scheidenberger, G. Schrieder, W. Schwab, M.H. Smedberg, J. Stroth, A. Surowiec, O. Tengblad, and M.V. Zhukov, *Direct experimental evidence for strong admixture of different parity States in* ^{11}*Li*, Phys. Rev. Lett. **83**, 496–499 (1999).

[17] A. Navin, D.W. Anthony, T. Aumann, T. Baumann, D. Bazin, Y. Blumenfeld, B. Brown, T. Glasmacher, P.G. Hansen, R.W. Ibbotson, P.A. Lofy, V. Maddalena, K. Miller, T. Nakamura, B.V. Pritychenko, B.M. Sherrill, E. Spears, M. Steiner, J.A. Tostevin, J. Yurkon, and A. Wagner, *Direct Evidence for the Breakdown of the* $N = 8$ *Shell Closure in* ^{12}*Be*, Phys. Rev. Lett. **85**, 266–269 (2000).

[18] H. Iwasaki, T. Motobayashi, H. Akiyoshi, Y. Ando, N. Fukuda, H. Fujiwara, Z. Fülöp, K. Hahn, Y. Higurashi, M. Hirai, I. Hisanaga, N. Iwasa, T. Kijima, A. Mengoni, T. Minemura, T. Nakamura, M. Notani, S. Ozawa, H. Sagawa, H. Sakurai, S. Shimoura, S. Takeuchi, T. Teranishi, Y. Yanagisawa, and M. Ishihara, *Low-lying intruder* 1^- *state in* ^{12}*Be and the melting of the* $N = 8$ *shell closure*, Phys. Lett. B **491**, 8–14 (2000).

[19] C.M. Campbell, N. Aoi, D. Bazin, M.D. Bowen, B. Brown, J.M. Cook, D.C. Dinca, A. Gade, T. Glasmacher, M. Horoi, S. Kanno, T. Motobayashi, W.F. Mueller, H. Sakurai, K. Starosta, H. Suzuki, S. Takeuchi, J.R. Terry, K. Yoneda, and H. Zwahlen, *Measurement of Excited States in* ^{40}Si *and Evidence for Weakening of the* $N = 28$ *Shell Gap*, Phys. Rev. Lett. **97**, 112501 (2006).

[20] T. Glasmacher, B.A. Brown, M.J. Chromik, P.D. Cottle, M. Fauerbach, R.W. Ibbotson, K.W. Kemper, D.J. Morrissey, H. Scheit, D.W. Sklenicka, and M. Steiner, *Collectivity in* ^{44}*S*, Phys. Lett. B **395**, 163–168 (1997).

[21] B. Bastin, S. Grévy, D. Sohler, O. Sorlin, Z. Dombrádi, N.L. Achouri, J.C. Angélique, F. Azaiez, D. Baiborodin, R. Borcea, C. Bourgeois, A. Buta, A. Bürger, R. Chapman, J.C. Dalouzy, Z. Dlouhy, A. Drouard, Z. Elekes, S. Franchoo, S. Iacob, B. Laurent, M. Lazar, X. Liang, E. Liénard, J. Mrazek, L. Nalpas, F. Negoita, N. Orr, Y. Penionzhkevich, Z. Podolyák, F. Pougheon, P. Roussel-Chomaz, M.G. Saint-Laurent, M. Stanoiu, I. Stefan, F. Nowacki, and A. Poves, *Collapse of the* $N = 28$ *Shell Closure in* ^{42}Si, Phys. Rev. Lett. **99**, 022503 (2007).

[22] S. Takeuchi, M. Matsushita, N. Aoi, P. Doornenbal, K. Li, T. Motobayashi, H. Scheit, D. Steppenbeck, H. Wang, H. Baba, D. Bazin, L. Càceres, H. Crawford, P. Fallon, R. Gern-

häuser, J. Gibelin, S. Go, S. Grévy, C. Hinke, C.R. Hoffman, R. Hughes, E. Ideguchi, D. Jenkins, N. Kobayashi, Y. Kondo, R. Krücken, T. Le Bleis, J. Lee, G. Lee, A. Matta, S. Michimasa, T. Nakamura, S. Ota, M. Petri, T. Sako, H. Sakurai, S. Shimoura, K. Steiger, K. Takahashi, M. Takechi, Y. Togano, R. Winkler, and K. Yoneda, *Well Developed Deformation in ^{42}Si*, Phys. Rev. Lett. **109**, 182501 (2012).

[23] H.L. Crawford, P. Fallon, A.O. Macchiavelli, R.M. Clark, B. Brown, J.A. Tostevin, D. Bazin, N. Aoi, P. Doornenbal, M. Matsushita, H. Scheit, D. Steppenbeck, S. Takeuchi, H. Baba, C.M. Campbell, M. Cromaz, E. Ideguchi, N. Kobayashi, Y. Kondo, G. Lee, I.Y. Lee, J. Lee, K. Li, S. Michimasa, T. Motobayashi, T. Nakamura, S. Ota, S. Paschalis, M. Petri, T. Sako, H. Sakurai, S. Shimoura, M. Takechi, Y. Togano, H. Wang, and K. Yoneda, *Shell and shape evolution at $N = 28$: The ^{40}Mg ground state*, Phys. Rev. C **89**, 041303 (2014).

[24] K. Tshoo, Y. Satou, H. Bhang, S. Choi, T. Nakamura, Y. Kondo, S. Deguchi, Y. Kawada, N. Kobayashi, Y. Nakayama, K.N. Tanaka, N. Tanaka, N. Aoi, M. Ishihara, T. Motobayashi, H. Otsu, H. Sakurai, S. Takeuchi, Y. Togano, K. Yoneda, Z.H. Li, F. Delaunay, J. Gibelin, F.M. Marqués, N.A. Orr, T. Honda, M. Matsushita, T. Kobayashi, Y. Miyashita, T. Sumikama, K. Yoshinaga, S. Shimoura, D. Sohler, T. Zheng, and Z.X. Cao, *$N = 16$ Spherical Shell Closure in ^{24}O*, Phys. Rev. Lett. **109**, 022501 (2012).

[25] A. Huck, G. Klotz, A. Knipper, C. Miehé, C. Richard-Serre, G. Walter, A. Poves, H.L. Ravn, and G. Marguier, *Beta decay of the new isotopes ^{52}K, ^{52}Ca, and ^{52}Sc; a test of the shell model far from stability*, Phys. Rev. C **31**, 2226–2237 (1985).

[26] F. Wienholtz, D. Beck, K. Blaum, C. Borgmann, M. Breitenfeldt, R.B. Cakirli, S. George, F. Herfurth, J.D. Holt, M. Kowalska, S. Kreim, D. Lunney, V. Manea, J. Menéndez, D. Neidherr, M. Rosenbusch, L. Schweikhard, A. Schwenk, J. Simonis, J. Stanja, R.N. Wolf, and K. Zuber, *Masses of exotic calcium isotopes pin down nuclear forces*, Nature **498**, 346–349 (2013).

[27] D. Steppenbeck, S. Takeuchi, N. Aoi, P. Doornenbal, M. Matsushita, H. Wang, H. Baba, N. Fukuda, S. Go, M. Honma, J. Lee, K. Matsui, S. Michimasa, T. Motobayashi, D. Nishimura, T. Otsuka, H. Sakurai, Y. Shiga, P.A. Söderström, T. Sumikama, H. Suzuki, R. Taniuchi, Y. Utsuno, J. Valiente-Dobón, and K. Yoneda, *Evidence for a new nuclear 'magic number' from the level structure of ^{54}Ca*, Nature **502**, 207–210 (2013).

[28] S. Michimasa, M. Kobayashi, Y. Kiyokawa, S. Ota, D.S. Ahn, H. Baba, G.P.A. Berg, M. Dozono, N. Fukuda, T. Furuno, E. Ideguchi, N. Inabe, T. Kawabata, S. Kawase, K. Kisamori, K. Kobayashi, T. Kubo, Y. Kubota, C.S. Lee, M. Matsushita, H. Miya, A. Mizukami, H. Nagakura, D. Nishimura, H. Oikawa, H. Sakai, Y. Shimizu, A. Stolz, H. Suzuki, M. Takaki, H. Takeda, S. Takeuchi, H. Tokieda, T. Uesaka, K. Yako, Y. Yamaguchi, Y. Yanagisawa, R. Yokoyama, K. Yoshida, and S. Shimoura, *Magic Nature of Neutrons in ^{54}Ca: First Mass Measurements of $^{55-57}$Ca*, Phys. Rev. Lett. **121**, 022506 (2018).

[29] E. Caurier, G. Martínez-Pinedo, F. Nowacki, A. Poves, and P.A. Zuker, *The shell model as a unified view of nuclear structure*, Rev. Mod. Phys. **77**, 427–488 (2005).

[30] O. Sorlin, and M.G. Porquet, *Nuclear magic numbers: New features far from stability*, Prog. Part. Nucl. Phys. **61**, 602–673 (2008).

[31] H. Morinaga, *Interpretation of some of the excited states of 4n self-conjugate nuclei*, Phys. Rev. **101**, 254–258 (1956).

[32] K. Heyde, and J.L. Wood, *Shape coexistence in atomic nuclei*, Rev. Mod. Phys. **83**, 1467–1521 (2011).

[33] J.L. Wood, and K. Heyde, *A focus on shape coexistence in nuclei*, J. Phys. G Nucl. Part. Phys. **43**, 020402 (2016).

[34] F. Nowacki, A. Poves, E. Caurier, and B. Bounthong, *Shape Coexistence in ^{78}Ni as the Portal to the Fifth Island of Inversion*, Phys. Rev. Lett. **117**, 272501 (2016).

[35] R.B. Wiringa, V.G.J. Stoks, and R. Schiavilla, *Accurate nucleon-nucleon potential with charge-independence breaking*, Phys. Rev. C **51**, 38–51 (1995).

[36] R. Machleidt, *High-precision, charge-dependent Bonn nucleon-nucleon potential*, Phys. Rev. C **63**, 024001 (2001).

[37] D.R. Entem, and R. Machleidt, *Accurate charge-dependent nucleon-nucleon potential at fourth order of chiral perturbation theory*, Phys. Rev. C **68**, 041001 (2003).

[38] R. Machleidt, and D.R. Entem, *Chiral effective field theory and nuclear forces*, Phys. Rep. **503**, 1–75 (2011).

[39] K. Hebeler, S.K. Bogner, R.J. Furnstahl, A. Nogga, and A. Schwenk, *Improved nuclear matter calculations from chiral low-momentum interactions*, Phys. Rev. C **83**, 3–7 (2011).

[40] K. Hebeler, J. Holt, J. Menéndez, and A. Schwenk, *Nuclear Forces and Their Impact on Neutron-Rich Nuclei and Neutron-Rich Matter*, Annu. Rev. Nucl. Part. Sci. **65**, 457–484 (2015).

[41] M. Hjorth-Jensen, T.T. Kuo, and E. Osnes, *Realistic effective interactions for nuclear systems*, Phys. Rep. **261**, 125–270 (1995).

[42] G. Hagen, M. Hjorth-Jensen, G.R. Jansen, R. Machleidt, and T. Papenbrock, *Evolution of Shell Structure in Neutron-Rich Calcium Isotopes*, Phys. Rev. Lett. **109**, 032502 (2012).

[43] J.D. Holt, J. Menéndez, J. Simonis, and A. Schwenk, *Three-nucleon forces and spectroscopy of neutron-rich calcium isotopes*, Phys. Rev. C **90**, 024312 (2014).

[44] S.K. Bogner, H. Hergert, J.D. Holt, A. Schwenk, S. Binder, A. Calci, J. Langhammer, and R. Roth, *Nonperturbative Shell-Model Interactions from the In-Medium Similarity Renormalization Group*, Phys. Rev. Lett. **113**, 142501 (2014).

[45] H. Hergert, S. Bogner, T. Morris, A. Schwenk, and K. Tsukiyama, *The In-Medium Similarity Renormalization Group: A novel ab initio method for nuclei*, Phys. Rep. **621**, 165–222 (2016).

[46] J. Simonis, S.R. Stroberg, K. Hebeler, J.D. Holt, and A. Schwenk, *Saturation with chiral interactions and consequences for finite nuclei*, Phys. Rev. C **96**, 014303 (2017).

[47] G. Hagen, G.R. Jansen, and T. Papenbrock, *Structure of ^{78}Ni from First-Principles Computations*, Phys. Rev. Lett. **117**, 172501 (2016).

[48] B. Brown, *The nuclear shell model towards the drip lines*, Prog. Part. Nucl. Phys. **47**, 517–599 (2001).

[49] H. Grawe, *Shell Model from a Practitioner's Point of View*, Lect. Notes Phys. **651**, 33–75 (2004).

[50] T. Otsuka, T. Suzuki, R. Fujimoto, H. Grawe, and Y. Akaishi, *Evolution of Nuclear Shells due to the Tensor Force*, Phys. Rev. Lett. **95**, 232502 (2005).

[51] T. Otsuka, T. Suzuki, M. Honma, Y. Utsuno, N. Tsunoda, K. Tsukiyama, and M. Hjorth-Jensen, *Novel Features of Nuclear Forces and Shell Evolution in Exotic Nuclei*, Phys. Rev. Lett. **104**, 012501 (2010).

[52] T. Otsuka, *Exotic nuclei and nuclear forces*, Phys. Scr. **T152**, 014007 (2013).

[53] T. Otsuka, T. Suzuki, J.D. Holt, A. Schwenk, and Y. Akaishi, *Three-Body Forces and the Limit of Oxygen Isotopes*, Phys. Rev. Lett. **105**, 032501 (2010).

[54] M. Bender, P.H. Heenen, and P.G. Reinhard, *Self-consistent mean-field models for nuclear structure*, Rev. Mod. Phys. **75**, 121–180 (2003).

[55] J.R. Stone, and P.G. Reinhard, *The Skyrme interaction in finite nuclei and nuclear matter*, Prog. Part. Nucl. Phys. **58**, 587–657 (2007).

[56] D. Vretenar, A.V. Afanasjev, G.A. Lalazissis, and P. Ring, *Relativistic Hartree-Bogoliubov theory: Static and dynamic aspects of exotic nuclear structure*, Phys. Rep. **409**, 101–259 (2005).

[57] J. Meng, H. Toki, S.G. Zhou, S.Q. Zhang, W.H. Long, and L.S. Geng, *Relativistic continuum Hartree Bogoliubov theory for ground-state properties of exotic nuclei*, Prog. Part. Nucl. Phys. **57**, 470–563 (2006).

[58] C.B. Hinke, M. Böhmer, P. Boutachkov, T. Faestermann, H. Geissel, J. Gerl, R. Gernhäuser, M. Górska, A. Gottardo, H. Grawe, J.L. Gręboszb, R. Krücken, N. Kurz, Z. Liu, L. Maier, F. Nowacki, S. Pietri, Z. Podolyák, K. Sieja, K. Steiger, K. Straub, H. Weick, H.J. Wollersheim, P.J. Woods, N. Al-Dahan, N. Alkhomashi, A. Ataç, A. Blazhev, N.F. Braun, I.T. Čeliković, T. Davinson, I. Dillmann, C. Domingo-Pardo, P.C. Doornenbal, G. d France, G.F. Farrelly, F. Farinon, N. Goel, T.C. Habermann, R. Hoischen, R. Janik, M. Karny, A. Kaşkaş, I.M. Kojouharov, T. Kröll, Y. Litvinov, S. Myalski, F. Nebel, S. Nishimura, C. Nociforo, J. Nyberg, a.R. Parikh, A. Procházka, P.H. Regan, C. Rigollet, H. Schaffner, C. Scheidenberger, S. Schwertel, P.a. Söderström, S.J. Steer, A. Stolz, and P. Strmeň, *Superallowed Gamow-Teller decay of the doubly magic nucleus* ^{100}*Sn*, Nature **486**, 341–345 (2012).

[59] O.B. Tarasov, D.S. Ahn, D. Bazin, N. Fukuda, A. Gade, M. Hausmann, N. Inabe, S. Ishikawa, N. Iwasa, K. Kawata, T. Komatsubara, T. Kubo, K. Kusaka, D.J. Morrissey, M. Ohtake, H. Otsu, M. Portillo, T. Sakakibara, H. Sakurai, H. Sato, B.M. Sherrill, Y. Shimizu, A. Stolz, T. Sumikama, H. Suzuki, H. Takeda, M. Thoennessen, H. Ueno, Y. Yanagisawa, and K. Yoshida, *Discovery of* ^{60}Ca *and Implications For the Stability of* ^{70}Ca, Phys. Rev. Lett. **121**, 022501 (2018).

[60] C. Engelmann, F. Ameil, P. Armbruster, M. Bernas, S. Czajkowski, P. Dessagne, C. Donzaud, H. Geissel, A. Heinz, Z. Janas, C. Kozhuharov, C. Miehé, G. Münzenberg, M. Pfützner, C. Röhl, W. Schwab, C. Stéphan, K. Sümmerer, L. Tassan-Got, and B. Voss, *Production and identification of heavy Ni isotopes: evidence for the doubly magic nucleus* $^{78}_{28}$*Ni*, Zeitschrift für Phys. A Hadron. Nucl. **352**, 351–352 (1995).

[61] M. Wang, G. Audi, F.G. Kondev, W. Huang, S. Naimi, and X. Xu, *The AME2016 atomic mass evaluation (II). Tables, graphs and references*, Chinese Phys. C **41**, 030003 (2017).

[62] A. Welker, N.A.S. Althubiti, D. Atanasov, K. Blaum, T.E. Cocolios, F. Herfurth, S. Kreim, D. Lunney, V. Manea, M. Mougeot, D. Neidherr, F. Nowacki, A. Poves, M. Rosenbusch, L. Schweikhard, F. Wienholtz, R.N. Wolf, and K. Zuber, *Binding Energy of ^{79}Cu: Probing the Structure of the Doubly Magic ^{78}Ni from Only One Proton Away*, Phys. Rev. Lett. **119**, 192502 (2017).

[63] C. Patrignani, and E. al., *Review of Particle Physics*, Chinese Phys. C **40**, 100001 (2016).

[64] Z.Y. Xu, S. Nishimura, G. Lorusso, F. Browne, P. Doornenbal, G. Gey, H.S. Jung, Z. Li, M. Niikura, P.a. Söderström, T. Sumikama, J. Taprogge, Z. Vajta, H. Watanabe, J. Wu, A. Yagi, K. Yoshinaga, H. Baba, S. Franchoo, T. Isobe, P.R. John, I. Kojouharov, S. Kubono, N. Kurz, I. Matea, K. Matsui, D. Mengoni, P. Morfouace, D.R. Napoli, F. Naqvi, H. Nishibata, A. Odahara, E. Sahin, H. Sakurai, H. Schaffner, I.G. Stefan, D. Suzuki, R. Taniuchi, and V. Werner, *β-Decay Half-Lives of ^{76,77}Co, ^{79,80}Ni , and ^{81}Cu: Experimental Indication of a Doubly Magic ^{78}Ni*, Phys. Rev. Lett. **113**, 032505 (2014).

[65] B.W. Sargent, and M. A., *The Maximum Energy of the β-Rays from Uranium X and other Bodies*, Proc. R. Soc. A Math. Phys. Eng. Sci. **139**, 659–673 (1933).

[66] E. Fermi, *Versuch einer Theorie der β-Strahlen. I*, Zeitschrift für Phys. A Hadron. Nucl. **88**, 161–177 (1934).

[67] P.T. Hosmer, H. Schatz, A. Aprahamian, O. Arndt, R.R.C. Clement, A. Estrade, K.L. Kratz, S.N. Liddick, P.F. Mantica, W.F. Mueller, F. Montes, a.C. Morton, M. Ouellette, E. Pellegrini, B. Pfeiffer, P. Reeder, P. Santi, M. Steiner, A. Stolz, B.E. Tomlin, W.B. Walters, and A. Wöhr, *Half-life of the doubly magic r-process nucleus ^{78}Ni*, Phys. Rev. Lett. **94**, 112501 (2005).

[68] M. Lipoglavšek, D. Seweryniak, C. Davids, C. Fahlander, M. Górska, R. Janssens, J. Nyberg, J. Uusitalo, W. Walters, I. Ahmad, J. Blomqvist, M. Carpenter, J.A. Cizewski, S. Fischer, H. Grawe, G. Hackman, M. Huhta, C. Lister, D. Nisius, G. Poli, P. Reiter, J. Ressler, J. Schwartz, and A. Sonzogni, *E2 polarization charge in Sn*, Phys. Lett. B **440**, 246–250 (1998).

[69] R. Julin, K. Helariutta, and M. Muikku, *Intruder states in very neutron-deficient Hg, Pb and Po nuclei*, J. Phys. G Nucl. Part. Phys. **27**, R109–R139 (2001).

[70] P.T. Greenlees, R.D. Herzberg, S. Ketelhut, P.A. Butler, P. Chowdhury, T. Grahn, C. Gray-Jones, G.D. Jones, P. Jones, R. Julin, S. Juutinen, T.L. Khoo, M. Leino, S. Moon, M. Nyman, J. Pakarinen, P. Rahkila, D. Rostron, J. Sarén, C. Scholey, J. Sorri, S.K. Tandel, J. Uusitalo, and M. Venhart, *High-K structure in ^{250}Fm and the deformed shell gaps at N=152 and Z=100*, Phys. Rev. C **78**, 021303 (2008).

[71] G.D. Dracoulis, G.J. Lane, F.G. Kondev, H. Watanabe, D. Seweryniak, S. Zhu, M.P. Carpenter, C.J. Chiara, R.V.F. Janssens, T. Lauritsen, C.J. Lister, E.A. McCutchan, and I. Stefanescu, *Lifetime of the $K^{\pi} = 8^{-}$ isomer in the neutron-rich nucleus ^{174}Er, and $N = 106$ $E1$ systematics*, Phys. Rev. C **79**, 061303 (2009).

[72] Z. Elekes, Z. Dombrádi, T. Aiba, N. Aoi, H. Baba, D. Bemmerer, B. Brown, T. Furumoto, Z. Fülöp, N. Iwasa, Á. Kiss, T. Kobayashi, Y. Kondo, T. Motobayashi, T. Nakabayashi,

T. Nannichi, Y. Sakuragi, H. Sakurai, D. Sohler, M. Takashina, S. Takeuchi, K. Tanaka, Y. Togano, K. Yamada, M. Yamaguchi, and K. Yoneda, *Persistent decoupling of valence neutrons toward the dripline: Study of ^{20}C by γ spectroscopy*, Phys. Rev. C **79**, 011302 (2009).

[73] P.A. Söderström, J. Nyberg, P.H. Regan, A. Algora, G. De Angelis, S.F. Ashley, S. Aydin, D. Bazzacco, R.J. Casperson, W.N. Catford, J. Cederkäll, R. Chapman, L. Corradi, C. Fahlander, E. Farnea, E. Fioretto, S.J. Freeman, A. Gadea, W. Gelletly, A. Gottardo, E. Grodner, C.Y. He, G.A. Jones, K. Keyes, M. Labiche, X. Liang, Z. Liu, S. Lunardi, N. Mărginean, P. Mason, R. Menegazzo, D. Mengoni, G. Montagnoli, D. Napoli, J. Ollier, S. Pietri, Z. Podolyák, G. Pollarolo, F. Recchia, E. Sahin, F. Scarlassara, R. Silvestri, J.F. Smith, K.M. Spohr, S.J. Steer, A.M. Stefanini, S. Szilner, N.J. Thompson, G.M. Tveten, C.A. Ur, J.J. Valiente-Dobón, V. Werner, S.J. Williams, F.R. Xu, and J.Y. Zhu, *Spectroscopy of neutron-rich $^{168,170}Dy$: Yrast band evolution close to the NpNn valence maximum*, Phys. Rev. C **81**, 166–170 (2010).

[74] M. Petri, P. Fallon, A.O. Macchiavelli, S. Paschalis, K. Starosta, T. Baugher, D. Bazin, L. Cartegni, R.M. Clark, H.L. Crawford, M. Cromaz, A. Dewald, A. Gade, G.F. Grinyer, S. Gros, M. Hackstein, H.B. Jeppesen, I.Y. Lee, S. McDaniel, D. Miller, M.M. Rajabali, A. Ratkiewicz, W. Rother, P. Voss, K.a. Walsh, D. Weisshaar, M. Wiedeking, and B. Brown, *Lifetime Measurement of the 2_1^+ State in ^{20}C*, Phys. Rev. Lett. **107**, 102501 (2011).

[75] J. Piot, B.J.P. Gall, O. Dorvaux, P.T. Greenlees, N. Rowley, L.L. Andersson, D.M. Cox, F. Dechery, T. Grahn, K. Hauschild, G. Henning, A. Herzan, R.D. Herzberg, F.P. Heßberger, U. Jakobsson, P. Jones, R. Julin, S. Juutinen, S. Ketelhut, T.L. Khoo, M. Leino, J. Ljungvall, A. Lopez-Martens, P. Nieminen, J. Pakarinen, P. Papadakis, E. Parr, P. Peura, P. Rahkila, S. Rinta-Antila, J. Rubert, P. Ruotsalainen, M. Sandzelius, J. Sarén, C. Scholey, D. Seweryniak, J. Sorri, B. Sulignano, and J. Uusitalo, *In-beam spectroscopy with intense ion beams: Evidence for a rotational structure in ^{246}Fm*, Phys. Rev. C **85**, 041301 (2012).

[76] A. Gottardo, J.J. Valiente-Dobón, G. Benzoni, R. Nicolini, A. Gadea, S. Lunardi, P. Boutachkov, A.M. Bruce, M. Górska, J. Grebosz, S. Pietri, Z. Podolyák, M. Pfützner, P.H. Regan, H. Weick, J. Alcántara Núñez, A. Algora, N. Al-Dahan, G. d Angelis, Y. Ayyad, N. Alkhomashi, P.R.P. Allegro, D. Bazzacco, J. Benlliure, M. Bowry, A. Bracco, M. Bunce, F. Camera, E. Casarejos, M.L. Cortes, F.C.L. Crespi, A. Corsi, A.M. Denis Bacelar, A.Y. Deo, C. Domingo-Pardo, M. Doncel, Z. Dombradi, T. Engert, K. Eppinger, G.F. Farrelly, F. Farinon, E. Farnea, H. Geissel, J. Gerl, N. Goel, E. Gregor, T. Habermann, R. Hoischen, R. Janik, S. Klupp, I. Kojouharov, N. Kurz, S.M. Lenzi, S. Leoni, S. Mandal, R. Menegazzo, D. Mengoni, B. Million, A.I. Morales, D.R. Napoli, F. Naqvi, C. Nociforo, A. Prochazka, W. Prokopowicz, F. Recchia, R.V. Ribas, M.W. Reed, D. Rudolph, E. Sahin, H. Schaffner, A. Sharma, B. Sitar, D. Siwal, K. Steiger, P. Strmen, T.P.D. Swan, I. Szarka, C.A. Ur, P.M. Walker, O. Wieland, H.J. Wollersheim, F. Nowacki, E. Maglione, and A.P. Zuker, *New Isomers in the Full Seniority Scheme of Neutron-Rich Lead Isotopes: The Role of Effective Three-Body Forces*, Phys. Rev. Lett. **109**, 162502 (2012).

[77] Z. Patel, P.A. Söderström, Z. Podolyák, P.H. Regan, P.M. Walker, H. Watanabe, E. Ideguchi, G.S. Simpson, H.L. Liu, S. Nishimura, Q. Wu, F.R. Xu, F. Browne, P. Doornenbal, G. Lorusso, S. Rice, L. Sinclair, T. Sumikama, J. Wu, Z.Y. Xu, N. Aoi, H. Baba, F.L. Bello Garrote, G. Benzoni, R. Daido, Y. Fang, N. Fukuda, G. Gey, S. Go, A. Gottardo, N. Inabe, T. Isobe, D. Kameda, K. Kobayashi, M. Kobayashi, T. Komatsubara, I. Kojouharov,

T. Kubo, N. Kurz, I. Kuti, Z. Li, M. Matsushita, S. Michimasa, C.B. Moon, H. Nishibata, I. Nishizuka, A. Odahara, E. Sahin, H. Sakurai, H. Schaffner, H. Suzuki, H. Takeda, M. Tanaka, J. Taprogge, Z. Vajta, A. Yagi, and R. Yokoyama, *Isomer decay spectroscopy of ^{164}Sm and ^{166}Gd: Midshell collectivity around N = 100*, Phys. Rev. Lett. **113**, 262502 (2014).

[78] P.A. Söderström, P.H. Regan, P.M. Walker, H. Watanabe, P. Doornenbal, Z. Korkulu, P. Lee, H.L. Liu, J.J. Liu, G. Lorusso, S. Nishimura, T. Sumikama, V.H. Phong, J. Wu, F.R. Xu, A. Yagi, G.X. Zhang, T. Alharbi, H. Baba, F. Browne, A.M. Bruce, R. Carroll, K.Y. Chae, Z. Dombradi, A. Estrade, N. Fukuda, C. Griffin, E. Ideguchi, N. Inabe, T. Isobe, H. Kanaoka, I. Kojouharov, F.G. Kondev, T. Kubo, S. Kubono, N. Kurz, I. Kuti, S. Lalkovski, G.J. Lane, C.S. Lee, E.J. Lee, G. Lotay, C.B. Moon, I. Nishizuka, C.R. Nita, A. Odahara, Z. Patel, Z. Podolyák, O.J. Roberts, H. Sakurai, H. Schaffner, C.M. Shand, H. Suzuki, H. Takeda, S. Terashima, Z. Vajta, J.J. Valiente-Dòbon, Z.Y. Xu, and S. Yoshida, *Heavy rotation-evolution of quadrupole collectivity centred at the neutron-rich doubly mid-shell nucleus ^{170}Dy*, Nucl. Struct. Dyn. Proc. **326**, 030010 (2015).

[79] W.F. Rogers, S. Garrett, A. Grovom, R.E. Anthony, A. Aulie, A. Barker, T. Baumann, J.J. Brett, J. Brown, G. Christian, P.A. DeYoung, J.E. Finck, N. Frank, A. Hamann, R.A. Haring-Kaye, J. Hinnefeld, A.R. Howe, N.T. Islam, M.D. Jones, A.N. Kuchera, J. Kwiatkowski, E.M. Lunderberg, B. Luther, D.A. Meyer, S. Mosby, A. Palmisano, R. Parkhurst, A. Peters, J. Smith, J. Snyder, A. Spyrou, S.L. Stephenson, M. Strongman, B. Sutherland, N.E. Taylor, and M. Thoennessen, *Unbound excited states of the N = 16 closed shell nucleus ^{24}O*, Phys. Rev. C **92**, 034316 (2015).

[80] B. Pritychenko, M. Birch, B. Singh, and M. Horoi, *Tables of E2 transition probabilities from the first 2^+ states in even-even nuclei*, At. Data Nucl. Data Tables **107**, 1–139 (2016).

[81] Y. Kondo, T. Nakamura, R. Tanaka, R. Minakata, S. Ogoshi, N.A. Orr, N.L. Achouri, T. Aumann, H. Baba, F. Delaunay, P. Doornenbal, N. Fukuda, J. Gibelin, J.W. Hwang, N. Inabe, T. Isobe, D. Kameda, D. Kanno, S. Kim, N. Kobayashi, T. Kobayashi, T. Kubo, S. Leblond, J. Lee, F.M. Marqués, T. Motobayashi, D. Murai, T. Murakami, K. Muto, T. Nakashima, N. Nakatsuka, A. Navin, S. Nishi, H. Otsu, H. Sato, Y. Satou, Y. Shimizu, H. Suzuki, K. Takahashi, H. Takeda, S. Takeuchi, Y. Togano, A.G. Tuff, M. Vandebrouck, and K. Yoneda, *Nucleus ^{26}O: A Barely Unbound System beyond the Drip Line*, Phys. Rev. Lett. **116**, 102503 (2016).

[82] Y. Shiga, K. Yoneda, D. Steppenbeck, N. Aoi, P. Doornenbal, J. Lee, H. Liu, M. Matsushita, S. Takeuchi, H. Wang, H. Baba, P. Bednarczyk, Z. Dombradi, Z. Fulop, S. Go, T. Hashimoto, M. Honma, E. Ideguchi, K. Ieki, K. Kobayashi, Y. Kondo, R. Minakata, T. Motobayashi, D. Nishimura, T. Otsuka, H. Otsu, H. Sakurai, N. Shimizu, D. Sohler, Y. Sun, A. Tamii, R. Tanaka, Z. Tian, Y. Tsunoda, Z. Vajta, T. Yamamoto, X. Yang, Z. Yang, Y. Ye, R. Yokoyama, and J. Zenihiro, *Investigating nuclear shell structure in the vicinity of ^{78}Ni: Low-lying excited states in the neutron-rich isotopes ^{80,82}Zn*, Phys. Rev. C **93**, 024320 (2016).

[83] H. Wang, N. Aoi, S. Takeuchi, M. Matsushita, T. Motobayashi, D. Steppenbeck, K. Yoneda, H. Baba, Z. Dombrádi, K. Kobayashi, Y. Kondo, J. Lee, H. Liu, R. Minakata, D. Nishimura, H. Otsu, H. Sakurai, D. Sohler, Y. Sun, Z. Tian, R. Tanaka, Z. Vajta, Z. Yang, T. Yamamoto, Y. Ye, and R. Yokoyama, *First spectroscopic information from even-even nuclei in the region "southeast" of ^{132}Sn: Neutron-excitation dominance of the 2_1^+ state in ^{132}Cd*, Phys. Rev. C **94**, 051301 (2016).

[84] S. Chen, P. Doornenbal, A. Obertelli, T.R. Rodríguez, G. Authelet, H. Baba, D. Calvet, F. Château, A. Corsi, A. Delbart, J.M. Gheller, A. Giganon, A. Gillibert, V. Lapoux, T. Motobayashi, M. Niikura, N. Paul, J.Y. Roussé, H. Sakurai, C. Santamaria, D. Steppenbeck, R. Taniuchi, T. Uesaka, T. Ando, T. Arici, A. Blazhev, F. Browne, A.M. Bruce, R. Caroll, L.X. Chung, M.L. Cortés, M. Dewald, B. Ding, F. Flavigny, S. Franchoo, M. Górska, A. Gottardo, A. Jungclaus, J. Lee, M. Lettmann, B.D. Linh, J. Liu, Z. Liu, C. Lizarazo, S. Momiyama, K. Moschner, S. Nagamine, N. Nakatsuka, C.R. Nita, C. Nobs, L. Olivier, R. Orlandi, Z. Patel, Z. Podolyak, M. Rudigier, T. Saito, C. Shand, P.A. Söderström, I. Stefan, V. Vaquero, V. Werner, K. Wimmer, and Z. Xu, *Low-lying structure and shape evolution in neutron-rich Se isotopes*, Phys. Rev. C **95**, 041302 (2017).

[85] N. Paul, A. Corsi, A. Obertelli, P. Doornenbal, G. Authelet, H. Baba, B. Bally, M. Bender, D. Calvet, F. Château, S. Chen, J.P. Delaroche, A. Delbart, J.M. Gheller, A. Giganon, A. Gillibert, M. Girod, P.H. Heenen, V. Lapoux, J. Libert, T. Motobayashi, M. Niikura, T. Otsuka, T.R. Rodríguez, J.Y. Roussé, H. Sakurai, C. Santamaria, N. Shimizu, D. Steppenbeck, R. Taniuchi, T. Togashi, Y. Tsunoda, T. Uesaka, T. Ando, T. Arici, A. Blazhev, F. Browne, A.M. Bruce, R. Carroll, L.X. Chung, M.L. Cortés, M. Dewald, B. Ding, F. Flavigny, S. Franchoo, M. Górska, A. Gottardo, A. Jungclaus, J. Lee, M. Lettmann, B.D. Linh, J. Liu, Z. Liu, C. Lizarazo, S. Momiyama, K. Moschner, S. Nagamine, N. Nakatsuka, C. Nita, C.R. Nobs, L. Olivier, Z. Patel, Z. Podolyák, M. Rudigier, T. Saito, C. Shand, P.A. Söderström, I. Stefan, R. Orlandi, V. Vaquero, V. Werner, K. Wimmer, and Z. Xu, *Are There Signatures of Harmonic Oscillator Shells Far from Stability? First Spectroscopy of* ^{110}*Zr*, Phys. Rev. Lett. **118**, 032501 (2017).

[86] R. Lică, G. Benzoni, T.R. Rodríguez, M.J. Borge, L.M. Fraile, H. Mach, A.I. Morales, M. Madurga, C.O. Sotty, V. Vedia, H. De Witte, J. Benito, R.N. Bernard, T. Berry, A. Bracco, F. Camera, S. Ceruti, V. Charviakova, N. Cieplicka-Oryńczak, C. Costache, F.C. Crespi, J. Creswell, G. Fernandez-Martínez, H. Fynbo, P.T. Greenlees, I. Homm, M. Huyse, J. Jolie, V. Karayonchev, U. Köster, J. Konki, T. Kröll, J. Kurcewicz, T. Kurtukian-Nieto, I. Lazarus, M.V. Lund, N. Mărginean, R. Mărginean, C. Mihai, R.E. Mihai, A. Negret, A. Orduz, Z. Patyk, S. Pascu, V. Pucknell, P. Rahkila, E. Rapisarda, J.M. Regis, L.M. Robledo, F. Rotaru, N. Saed-Samii, V. Sánchez-Tembleque, M. Stanoiu, O. Tengblad, M. Thuerauf, A. Turturica, P. Van Duppen, and N. Warr, *Evolution of deformation in neutron-rich Ba isotopes up to A=150*, Phys. Rev. C **97**, 024305 (2018).

[87] J. Erler, N. Birge, M. Kortelainen, W. Nazarewicz, E. Olsen, A.M. Perhac, and M. Stoitsov, *The limits of the nuclear landscape*, Nature **486**, 509–512 (2012).

[88] R. Taniuchi, C. Santamaria, P. Doornenbal, A. Obertelli, K. Yoneda, G. Authelet, H. Baba, D. Calvet, F. Château, A. Corsi, A. Delbart, J.M. Gheller, A. Gillibert, J. Holt, T. Isobe, V. Lapoux, M. Matsushita, J. Menéndez, S. Momiyama, T. Motobayashi, M. Niikura, F. Nowacki, K. Ogata, H. Otsu, T. Otsuka, C. Péron, S. Péru, A. Peyaud, E. Pollacco, A. Poves, J.Y. Roussé, H. Sakurai, A. Schwenk, Y. Shiga, J. Simonis, S. Stroberg, S. Takeuchi, Y. Tsunoda, T. Uesaka, H. Wang, F. Browne, L. Chung, Z. Dombradi, S. Franchoo, F. Giacoppo, A. Gottardo, K. Hadynska-Klek, Z. Korkulu, S. Koyama, Y. Kubota, J. Lee, M. Lettmann, C. Louchart, R. Lozeva, K. Matsui, T. Miyazaki, S. Nishimura, L. Olivier, S. Ota, Z. Patel, E. Sahin, C. Shand, P.A. Söderström, I. Stefan, D. Steppenbeck, T. Sumikama, D. Suzuki, Z. Vajta, V. Werner, J. Wu, and Z. Xu, ^{78}*Ni revealed as a doubly magic stronghold against nuclear deformation (submitted)*.

[89] O. Sorlin, S. Leenhardt, C. Donzaud, J. Duprat, F. Azaiez, F. Nowacki, H. Grawe, Z. Dombrádi, F. Amorini, A. Astier, D. Baiborodin, M. Belleguic, C. Borcea, C. Bourgeois, D.M. Cullen, Z. Dlouhy, E. Dragulescu, M. Górska, S. Grévy, D. Guillemaud-Mueller, G. Hagemann, B. Herskind, J. Kiener, R. Lemmon, M. Lewitowicz, S.M. Lukyanov, P. Mayet, F. de Oliveira Santos, D. Pantalica, Y.E. Penionzhkevich, F. Pougheon, A. Poves, N. Redon, M.G. Saint-Laurent, J.A. Scarpaci, G. Sletten, M. Stanoiu, O. Tarasov, and C. Theisen, $^{68}_{28}Ni_{40}$*: Magicity versus Superfluidity*, Phys. Rev. Lett. **88**, 092501 (2002).

[90] C. Guénaut, G. Audi, D. Beck, K. Blaum, G. Bollen, P. Delahaye, F. Herfurth, A. Kellerbauer, H.J. Kluge, J. Libert, D. Lunney, S. Schwarz, L. Schweikhard, and C. Yazidjian, *High-precision mass measurements of nickel, copper, and gallium isotopes and the purported shell closure at* $N = 40$, Phys. Rev. C **75**, 044303 (2007).

[91] J. Van De Walle, F. Aksouh, F. Ames, T. Behrens, V. Bildstein, A. Blazhev, J. Cederkäll, E. Clément, T.E. Cocolios, T. Davinson, P. Delahaye, J. Eberth, A. Ekström, D.V. Fedorov, V.N. Fedosseev, L.M. Fraile, S. Franchoo, R. Gernhauser, G. Georgiev, D. Habs, K. Heyde, G. Huber, M. Huyse, F. Ibrahim, O. Ivanov, J. Iwanicki, J. Jolie, O. Kester, U. Köster, T. Kröll, R. Krücken, M. Lauer, A.F. Lisetskiy, R. Lutter, B.A. Marsh, P. Mayet, O. Niedermaier, T. Nilsson, M. Pantea, O. Perru, R. Raabe, P. Reiter, M. Sawicka, H. Scheit, G. Schrieder, D. Schwalm, M.D. Seliverstov, T. Sieber, G. Sletten, N. Smirnova, M. Stanoiu, I. Stefanescu, J.C. Thomas, J.J. Valiente-Dobón, P. Van Duppen, D. Verney, D. Voulot, N. Warr, D. Weisshaar, F. Wenander, B.H. Wolf, and M. Zielińska, *Coulomb excitation of neutron-rich Zn isotopes: First observation of the* 2^+_1 *state in* ^{80}*Zn*, Phys. Rev. Lett. **99**, 142501 (2007).

[92] J. Rainwater, *Nuclear Energy Level Argument for a Spheroidal Nuclear Model*, Phys. Rev. **79**, 432–434 (1950).

[93] B. Mottelson, *Collective Motion in the Nucleus*, Rev. Mod. Phys. **29**, 186–190 (1957).

[94] J.M. Blatt, and V.F. Weisskopf, *Theoretical nuclear physics*, Wiley, (1952).

[95] E. Segrè, *Nuclei and particles : an introduction to nuclear and subnuclear physics*, W. A. Benjamin, (1977).

[96] V.F. Weisskopf, *Radiative Transition Probabilities in Nuclei*, Phys. Rev. **83**, 1073–1073 (1951).

[97] O. Perru, O. Sorlin, S. Franchoo, F. Azaiez, E. Bouchez, C. Bourgeois, A. Chatillon, J.M. Daugas, Z. Dlouhy, Z. Dombrádi, C. Donzaud, L. Gaudefroy, H. Grawe, S. Grévy, D. Guillemaud-Mueller, F. Hammache, F. Ibrahim, Y. Le Coz, S.M. Lukyanov, I. Matea, J. Mrazek, F. Nowacki, Y.E. Penionzhkevich, F. de Oliveira Santos, F. Pougheon, M.G. Saint-Laurent, G. Sletten, M. Stanoiu, C. Stodel, C. Theisen, and D. Verney, *Enhanced Core Polarization in* ^{70}Ni *and* ^{74}Zn, Phys. Rev. Lett. **96**, 232501 (2006).

[98] N. Aoi, S. Kanno, S. Takeuchi, H. Suzuki, D. Bazin, M.D. Bowen, C.M. Campbell, J.M. Cook, D.C. Dinca, A. Gade, T. Glasmacher, H. Iwasaki, T. Kubo, K. Kurita, T. Motobayashi, W.F. Mueller, T. Nakamura, H. Sakurai, M. Takashina, J.R. Terry, K. Yoneda, and H. Zwahlen, *Enhanced collectivity in* ^{74}*Ni*, Phys. Lett. Sect. B Nucl. Elem. Part. High-Energy Phys. **692**, 302–306 (2010).

[99] T. Marchi, G. d Angelis, J.J. Valiente-Dobón, V.M. Bader, T. Baugher, D. Bazin, J. Berryman, A. Bonaccorso, R. Clark, L. Coraggio, H.L. Crawford, M. Doncel, E. Farnea, A. Gade,

A. Gadea, A. Gargano, T. Glasmacher, A. Gottardo, F. Gramegna, N. Itaco, P.R. John, R. Kumar, S.M. Lenzi, S. Lunardi, S. McDaniel, C. Michelagnoli, D. Mengoni, V. Modamio, D.R. Napoli, B. Quintana, A. Ratkiewicz, F. Recchia, E. Sahin, R. Stroberg, D. Weisshaar, K. Wimmer, and R. Winkler, *Quadrupole transition strength in the ^{74}Ni nucleus and core polarization effects in the neutron-rich Ni isotopes*, Phys. Rev. Lett. **113**, 182501 (2014).

[100] K. Kolos, D. Miller, R. Grzywacz, H. Iwasaki, M. Al-Shudifat, D. Bazin, C.R. Bingham, T. Braunroth, G. Cerizza, A. Gade, A. Lemasson, S.N. Liddick, M. Madurga, C. Morse, M. Portillo, M.M. Rajabali, F. Recchia, L.L. Riedinger, P. Voss, W.B. Walters, D. Weisshaar, K. Whitmore, K. Wimmer, and J.A. Tostevin, *Direct Lifetime Measurements of the Excited States in* ^{72}Ni, Phys. Rev. Lett. **116**, 122502 (2016).

[101] M.L. Cortés, P. Doornenbal, M. Dupuis, S.M. Lenzi, F. Nowacki, A. Obertelli, S. Péru, N. Pietralla, V. Werner, K. Wimmer, G. Authelet, H. Baba, D. Calvet, F. Château, A. Corsi, A. Delbart, J.m. Gheller, A. Gillibert, T. Isobe, V. Lapoux, C. Louchart, M. Matsushita, S. Momiyama, T. Motobayashi, M. Niikura, H. Otsu, C. Péron, A. Peyaud, E.C. Pollacco, J.y. Roussé, H. Sakurai, C. Santamaria, M. Sasano, Y. Shiga, S. Takeuchi, R. Taniuchi, T. Uesaka, H. Wang, K. Yoneda, F. Browne, L.X. Chung, Z. Dombradi, S. Franchoo, F. Giacoppo, A. Gottardo, K. Hadynska-Klek, Z. Korkulu, S. Koyama, Y. Kubota, J. Lee, M. Lettmann, R. Lozeva, K. Matsui, T. Miyazaki, S. Nishimura, L. Olivier, S. Ota, Z. Patel, E. Sahin, C.M. Shand, P.A. Söderström, I. Stefan, D. Steppenbeck, T. Sumikama, D. Suzuki, Z. Vajta, J. Wu, and Z. Xu, *Inelastic scattering of neutron-rich Ni and Zn isotopes off a proton target*, Phys. Rev. C **97**, 044315 (2018).

[102] A. Gottardo, D. Verney, C. Delafosse, F. Ibrahim, B. Roussière, C. Sotty, S. Roccia, C. Andreoiu, C. Costache, M.C. Delattre, I. Deloncle, A. Etilé, S. Franchoo, C. Gaulard, J. Guillot, M. Lebois, M. MacCormick, N. Marginean, R. Marginean, I. Matea, C. Mihai, I. Mitu, L. Olivier, C. Portail, L. Qi, L. Stan, D. Testov, J. Wilson, and D.T. Yordanov, *First Evidence of Shape Coexistence in the ^{78}Ni Region: Intruder 0_2^+ State in ^{80}Ge*, Phys. Rev. Lett. **116**, 182501 (2016).

[103] X.F. Yang, C. Wraith, L. Xie, C. Babcock, J. Billowes, M.L. Bissell, K. Blaum, B. Cheal, K.T. Flanagan, R.F. Garcia Ruiz, W. Gins, C. Gorges, L.K. Grob, H. Heylen, S. Kaufmann, M. Kowalska, J. Kraemer, S. Malbrunot-Ettenauer, R. Neugart, G. Neyens, W. Nörtershäuser, J. Papuga, R. Sánchez, and D.T. Yordanov, *Isomer Shift and Magnetic Moment of the Long-Lived $1/2^+$ Isomer in $^{79}_{30}Zn_{49}$: Signature of Shape Coexistence near ^{78}Ni*, Phys. Rev. Lett. **116**, 182502 (2016).

[104] L. Olivier, S. Franchoo, M. Niikura, Z. Vajta, D. Sohler, P. Doornenbal, A. Obertelli, Y. Tsunoda, T. Otsuka, G. Authelet, H. Baba, D. Calvet, F. Château, A. Corsi, A. Delbart, J.M. Gheller, A. Gillibert, T. Isobe, V. Lapoux, M. Matsushita, S. Momiyama, T. Motobayashi, H. Otsu, C. Péron, A. Peyaud, E.C. Pollacco, J.Y. Roussé, H. Sakurai, C. Santamaria, M. Sasano, Y. Shiga, S. Takeuchi, R. Taniuchi, T. Uesaka, H. Wang, K. Yoneda, F. Browne, L.X. Chung, Z. Dombradi, F. Flavigny, F. Giacoppo, A. Gottardo, K. Hadyńska-Klęk, Z. Korkulu, S. Koyama, Y. Kubota, J. Lee, M. Lettmann, C. Louchart, R. Lozeva, K. Matsui, T. Miyazaki, S. Nishimura, K. Ogata, S. Ota, Z. Patel, E. Sahin, C. Shand, P.A. Söderström, I. Stefan, D. Steppenbeck, T. Sumikama, D. Suzuki, V. Werner, J. Wu, and Z. Xu, *Persistence of the $Z = 28$ Shell Gap Around ^{78}Ni: First Spectroscopy of ^{79}Cu*, Phys. Rev. Lett. **119**, 192501 (2017).

[105] L. Olivier, "*Nuclear structure in the vicinity of ^{78}Ni: in-beam gamma-ray spectroscopy of ^{79}Cu through proton knockout*", Ph.D. thesis, University Paris-Saclay (2017).

[106] K.T. Flanagan, P. Vingerhoets, M. Avgoulea, J. Billowes, M.L. Bissell, K. Blaum, B. Cheal, M. De Rydt, V.N. Fedosseev, D.H. Forest, C. Geppert, U. Köster, M. Kowalska, J. Krämer, K.L. Kratz, A. Krieger, E. Mané, B.A. Marsh, T. Materna, L. Mathieu, P.L. Molkanov, R. Neugart, G. Neyens, W. Nörtershäuser, M.D. Seliverstov, O. Serot, M. Schug, M.A. Sjoedin, J.R. Stone, N.J. Stone, H.H. Stroke, G. Tungate, D.T. Yordanov, and Y.M. Volkov, *Nuclear Spins and Magnetic Moments of ^{71,73,75}Cu: Inversion of $\pi 2p_{3/2}$ and $\pi 1f_{5/2}$ Levels in ^{75}Cu*, Phys. Rev. Lett. **103**, 142501 (2009).

[107] U. Köster, N.J. Stone, K.T. Flanagan, J.R. Stone, V.N. Fedosseev, K.L. Kratz, B.A. Marsh, T. Materna, L. Mathieu, P.L. Molkanov, M.D. Seliverstov, O. Serot, A.M. Sjödin, and Y.M. Volkov, *In-source laser spectroscopy of ^{75,77,78}Cu: Direct evidence for a change in the quasiparticle energy sequence in ^{75,77}Cu and an absence of longer-lived isomers in ^{78}Cu*, Phys. Rev. C **84**, 034320 (2011).

[108] C. Petrone, J.M. Daugas, G.S. Simpson, M. Stanoiu, C. Plaisir, T. Faul, C. Borcea, R. Borcea, L. Cáceres, S. Calinescu, R. Chevrier, L. Gaudefroy, G. Georgiev, G. Gey, O. Kamalou, F. Negoita, F. Rotaru, O. Sorlin, and J.C. Thomas, *Nearly degenerate isomeric states of* ^{75}Cu, Phys. Rev. C **94**, 024319 (2016).

[109] E. Sahin, F. Bello Garrote, Y. Tsunoda, T. Otsuka, G. d Angelis, A. Görgen, M. Niikura, S. Nishimura, Z. Xu, H. Baba, F. Browne, M.C. Delattre, P. Doornenbal, S. Franchoo, G. Gey, K. Hadyńska-KlÈl'k, T. Isobe, P. John, H. Jung, I. Kojouharov, T. Kubo, N. Kurz, Z. Li, G. Lorusso, I. Matea, K. Matsui, D. Mengoni, P. Morfouace, D. Napoli, F. Naqvi, H. Nishibata, A. Odahara, H. Sakurai, H. Schaffner, P.A. Söderström, D. Sohler, I. Stefan, T. Sumikama, D. Suzuki, R. Taniuchi, J. Taprogge, Z. Vajta, H. Watanabe, V. Werner, J. Wu, A. Yagi, M. Yalcinkaya, and K. Yoshinaga, *Shell Evolution towards* ^{78}Ni*: Low-Lying States in* ^{77}Cu, Phys. Rev. Lett. **118**, 242502 (2017).

[110] I. Hamamoto, *Neutron shell structure and deformation in neutron-drip-line nuclei*, Phys. Rev. C **85**, 064329 (2012).

[111] S.M. Lenzi, F. Nowacki, A. Poves, and K. Sieja, *Island of inversion around ^{64}Cr*, Phys. Rev. C **82**, 054301 (2010).

[112] K. Sieja, and F. Nowacki, *Three-body forces and persistence of spin-orbit shell gaps in medium-mass nuclei: Toward the doubly magic ^{78}Ni*, Phys. Rev. C **85**, 051301 (2012).

[113] N. Shimizu, T. Abe, Y. Tsunoda, Y. Utsuno, T. Yoshida, T. Mizusaki, M. Honma, and T. Otsuka, *New-generation Monte Carlo shell model for the K computer era*, Prog. Theor. Exp. Phys. **2012**, 01A205 (2012).

[114] Y. Tsunoda, T. Otsuka, N. Shimizu, M. Honma, and Y. Utsuno, *Novel shape evolution in exotic Ni isotopes and configuration-dependent shell structure*, Phys. Rev. C **89**, 031301 (2014).

[115] Y. Tsunoda, "*Structure of medium-mass nuclei studied by Monte Carlo Shell-Model calculations*", Ph.D. thesis, The university of Tokyo (2015).

[116] C. Santamaria, C. Louchart, A. Obertelli, V. Werner, P. Doornenbal, F. Nowacki, G. Authelet, H. Baba, D. Calvet, F. Château, A. Corsi, A. Delbart, J.M. Gheller, A. Gillibert, T. Isobe, V. Lapoux, M. Matsushita, S. Momiyama, T. Motobayashi, M. Niikura, H. Otsu, C. Péron, A. Peyaud, E.C. Pollacco, J.Y. Roussé, H. Sakurai, M. Sasano, Y. Shiga, S. Takeuchi, R. Taniuchi, T. Uesaka, H. Wang, K. Yoneda, F. Browne, L.X. Chung, Z. Dombradi, S. Franchoo, F. Giacoppo, A. Gottardo, K. Hadynska-Klek, Z. Korkulu, S. Koyama, Y. Kubota, J. Lee, M. Lettmann, R. Lozeva, K. Matsui, T. Miyazaki, S. Nishimura, L. Olivier, S. Ota, Z. Patel, N. Pietralla, E. Sahin, C. Shand, P.A. Söderström, I. Stefan, D. Steppenbeck, T. Sumikama, D. Suzuki, Z. Vajta, J. Wu, and Z. Xu, *Extension of the $N = 40$ Island of Inversion towards $N = 50$: Spectroscopy of ^{66}Cr, $^{70,72}Fe$*, Phys. Rev. Lett. **115**, 192501 (2015).

[117] C. Santamaria, "*Quest for new nuclear magic numbers with MINOS*", Ph.D. thesis, l'Université Paris Sud XI (2015).

[118] F. Nowacki, *Private communication.*

[119] Y. Tsunoda, and T. Otsuka, *Private communication.*

[120] S. Péru, and M. Martini, *Mean field based calculations with the Gogny force: Some theoretical tools to explore the nuclear structure*, Eur. Phys. J. A **50**, 88 (2014).

[121] S. Péru, *Private communication.*

[122] J. Menendez, A. Schwenk, and J.D. Holt, *Private communication.*

[123] A. Obertelli, A. Delbart, S. Anvar, L. Audirac, G. Authelet, H. Baba, B. Bruyneel, D. Calvet, F. Château, A. Corsi, P. Doornenbal, J.M. Gheller, A. Giganon, C. Lahonde-Hamdoun, D. Leboeuf, D. Loiseau, A. Mohamed, J.P. Mols, H. Otsu, C. Péron, A. Peyaud, E.C. Pollacco, G. Prono, J.Y. Rousse, C. Santamaria, and T. Uesaka, *MINOS: A vertex tracker coupled to a thick liquid-hydrogen target for in-beam spectroscopy of exotic nuclei*, Eur. Phys. J. A **50**, 8 (2014).

[124] C. Santamaria, A. Obertelli, S. Ota, M. Sasano, E. Takada, L. Audirac, H. Baba, D. Calvet, F. Château, A. Corsi, A. Delbart, P. Doornenbal, A. Giganon, A. Gillibert, Y. Kondo, Y. Kubota, C. Lahonde-Hamdoun, V. Lapoux, D. Leboeuf, C. Lee, H. Liu, M. Matsushita, T. Motobayashi, M. Niikura, M. Kurata-Nishimura, H. Otsu, A. Peyaud, E. Pollacco, G. Prono, H. Tokieda, T. Uesaka, and J. Zenihiro, *Tracking with the MINOS Time Projection Chamber*, Nucl. Instrum. Methods Phys. Res. A **905**, 138–148 (2018).

[125] S. Takeuchi, T. Motobayashi, Y. Togano, M. Matsushita, N. Aoi, K. Demichi, H. Hasegawa, and H. Murakami, *DALI2: A NaI(Tl) detector array for measurements of γ rays from fast nuclei*, Nucl. Instrum. Methods Phys. Res. A **763**, 596–603 (2014).

[126] P. Doornenbal, *In-beam gamma-ray spectroscopy at the RIBF*, Prog. Theor. Exp. Phys. **2012**, 3C004 (2012).

[127] H. Okuno, N. Fukunishi, and O. Kamigaito, *Progress of RIBF accelerators*, Prog. Theor. Exp. Phys. **2012**, 3C002 (2012).

[128] T. Kubo, D. Kameda, H. Suzuki, N. Fukuda, H. Takeda, Y. Yanagisawa, M. Ohtake, K. Kusaka, K. Yoshida, N. Inabe, T. Ohnishi, A. Yoshida, K. Tanaka, and Y. Mizoi, *BigRIPS separator and ZeroDegree spectrometer at RIKEN RI Beam Factory*, Prog. Theor. Exp. Phys. **2012**, 3C003 (2012).

[129] *BigRIPS technical information*, http://www.nishina.riken.jp/RIBF/BigRIPS/tecinfo.html.

[130] N. Fukuda, T. Kubo, T. Ohnishi, N. Inabe, H. Takeda, D. Kameda, and H. Suzuki, *Identification and separation of radioactive isotope beams by the BigRIPS separator at the RIKEN RI Beam Factory*, Nucl. Instrum. Methods Phys. Res. B **317**, 323–332 (2013).

[131] H. Baba, T. Ichihara, T. Ohnishi, S. Takeuchi, K. Yoshida, Y. Watanabe, S. Ota, and S. Shimoura, *New data acquisition system for the RIKEN Radioactive Isotope Beam Factory*, Nucl. Instrum. Methods Phys. Res. A **616**, 65–68 (2010).

[132] H. Baba, T. Ichihara, T. Isobe, C. Houarner, C. Maugeais, B. Raine, F. Saillant, G. Wittwer, N. Kurz, H. Schaffner, R. Gernhauser, S. Anvar, D. Calvet, F. Chateau, and E. Pollacco, *DAQ coupling in RIKEN RIBF*, 19th IEEE-NPSS Real Time Conf. **2014**, 1–5 (2014).

[133] H. Kumagai, T. Ohnishi, N. Fukuda, H. Takeda, D. Kameda, N. Inabe, K. Yoshida, and T. Kubo, *Development of Parallel Plate Avalanche Counter (PPAC) for BigRIPS fragment separator*, Nucl. Instrum. Methods Phys. Res. B **317**, 717–727 (2013).

[134] K. Kimura, T. Izumikawa, R. Koyama, T. Ohnishi, T. Ohtsubo, A. Ozawa, W. Shinozaki, T. Suzuki, M. Takahashi, I. Tanihata, T. Yamaguchi, and Y. Yamaguchi, *High-rate particle identification of high-energy heavy ions using a tilted electrode gas ionization chamber*, Nucl. Instrum. Methods Phys. Res. A **538**, 608–614 (2005).

[135] H. Kumagai, and T. Ohnishi, *Signal transport system with optical fiber for RIBF*, RIKEN Accel. Prog. Rep. **41**, 121–122 (2008).

[136] *ROOT web page*, http://root.cern.ch/.

[137] *ANAROOT web page*, http://ribf.riken.jp/RIBFDAQ/index.php?Tools%2FAnalysis%2FANAROOT.

[138] O.B. Tarasov, and D. Bazin, *LISE++: Radioactive beam production with in-flight separators*, Nucl. Instruments Methods Phys. Res. Sect. B Beam Interact. with Mater. Atoms **266**, 4657–4664 (2008).

[139] S. Agostinelli, J. Allison, K. Amako, J. Apostolakis, H. Araujo, P. Arce, M. Asai, D. Axen, S. Banerjee, G. Barrand, F. Behner, L. Bellagamba, J. Boudreau, L. Broglia, A. Brunengo, H. Burkhardt, S. Chauvie, J. Chuma, R. Chytracek, G. Cooperman, G. Cosmo, P. Degtyarenko, A. Dell'Acqua, G. Depaola, D. Dietrich, R. Enami, A. Feliciello, C. Ferguson, H. Fesefeldt, G. Folger, F. Foppiano, A. Forti, S. Garelli, S. Giani, R. Giannitrapani, D. Gibin, J.J. Gomez Cadenas, I. Gonzalez, G. Gracia Abril, G. Greeniaus, W. Greiner, V. Grichine, A. Grossheim, S. Guatelli, P. Gumplinger, R. Hamatsu, K. Hashimoto, H. Hasui, A. Heikkinen, A. Howard, V. Ivanchenko, A. Johnson, F.W. Jones, J. Kallenbach, N. Kanaya, M. Kawabata, Y. Kawabata, M. Kawaguti, S. Kelner, P. Kent, A. Kimura, T. Kodama, R. Kokoulin, M. Kossov, H. Kurashige, E. Lamanna, T. Lampen, V. Lara, V. Lefebure, F. Lei, M. Liendl, W. Lockman, F. Longo, S. Magni, M. Maire, E. Medernach, K. Minamimoto, P. Mora de Freitas, Y. Morita, K. Murakami, M. Nagamatu, R. Nartallo, P. Nieminen, T. Nishimura, K. Ohtsubo, M. Okamura, S. O'Neale, Y. Oohata, K. Paech, J. Perl, A. Pfeiffer, M.G. Pia, F. Ranjard, A. Rybin, S. Sadilov, E. d Salvo, G. Santin, T. Sasaki, N. Savvas, Y. Sawada, S. Scherer, S. Sei, V. Sirotenko, D. Smith, N. Starkov, H. Stoecker, J. Sulkimo, M. Takahata, S. Tanaka, E. Tcherniaev, E. Safai Tehrani, M. Tropeano, P. Truscott, H. Uno,

L. Urban, P. Urban, M. Verderi, A. Walkden, W. Wander, H. Weber, J.P. Wellisch, T. Wenaus, D.C. Williams, D. Wright, T. Yamada, H. Yoshida, and D. Zschiesche, *GEANT4 - A simulation toolkit*, Nucl. Instruments Methods Phys. Res. Sect. A Accel. Spectrometers, Detect. Assoc. Equip. **506**, 250–303 (2003).

[140] *Geant4 web page*, `http://geant4.cern.ch/`.

[141] P. Doornenbal. *DALI2 Geant4 simulation package*, `http://ribf.riken.jp/~pieter/shogun/`.

[142] *CAEN Electronic Instrumentation Web Page*, `http://www.caen.it/`.

[143] C. Scheidenberger, T. Stöhlker, W. Meyerhof, H. Geissel, P. Mokler, and B. Blank, *Charge states of relativistic heavy ions in matter*, Nucl. Instrum. Methods Phys. Res. B **142**, 441–462 (1998).

[144] Saint-Gobain Crystals. *Absorption Efficiency Calculator*, `https://www.crystals.saint-gobain.com/media-center/efficiency-calculator`.

[145] *ATIMA code*, `https://web-docs.gsi.de/~weick/atima/`.

[146] *ROOT User's Guide*, `https://root.cern.ch/guides/users-guide`.

[147] S. Baker, and R.D. Cousins, *Clarification of the use of CHI-square and likelihood functions in fits to histograms*, Nucl. Instruments Methods Phys. Res. **221**, 437–442 (1984).

[148] *R: A Language and Environment for Statistical Computing*, `https://www.r-project.org/`.

[149] S.S. Wilks, *The Large-Sample Distribution of the Likelihood Ratio for Testing Composite Hypotheses*, Ann. Math. Stat. **9**, 60–62 (1938).

[150] C.A. Pruneau, *Data analysis techniques for physical scientists*, Cambridge University Press, (2017).

[151] M. Honma, T. Otsuka, T. Mizusaki, and M. Hjorth-Jensen, *New effective interaction for f5pg9-shell nuclei*, Phys. Rev. C **80**, 064323 (2009).

[152] J. Dechargé, and D. Gogny, *Hartree-Fock-Bogolyubov calculations with the D*1 *effective interaction on spherical nuclei*, Phys. Rev. C **21**, 1568–1593 (1980).

[153] J.F. Berger, M. Girod, and D. Gogny, *Time-dependent quantum collective dynamics applied to nuclear fission*, Comput. Phys. Commun. **63**, 365–374 (1991).

[154] S. Péru, J.F. Berger, and P.F. Bortignon, *Giant resonances in exotic spherical nuclei within the RPA approach with the Gogny force*, Eur. Phys. J. A **26**, 25–32 (2005).

[155] J.P. Delaroche, M. Girod, J. Libert, H. Goutte, S. Hilaire, S. Péru, N. Pillet, and G.F. Bertsch, *Structure of even-even nuclei using a mapped collective Hamiltonian and the D1S Gogny interaction*, Phys. Rev. C **81**, 014303 (2010).

[156] J.P. Delaroche, M. Girod, J. Libert, H. Goutte, S. Hilaire, S. Péru, N. Pillet, and G. Bertsch. *HFB+5DCH tabulated results*, `http://www-phynu.cea.fr/science_en_ligne/carte_potentiels_microscopiques/tables/HFB-5DCH-table_eng.htm`.

[157] A.T. Gallant, J.C. Bale, T. Brunner, U. Chowdhury, S. Ettenauer, A. Lennarz, D. Robertson, V.V. Simon, A. Chaudhuri, J.D. Holt, A.A. Kwiatkowski, E. Mané, J. Menéndez, B.E. Schultz, M.C. Simon, C. Andreoiu, P. Delheij, M.R. Pearson, H. Savajols, A. Schwenk, and J. Dilling, *New Precision Mass Measurements of Neutron-Rich Calcium and Potassium Isotopes and Three-Nucleon Forces*, Phys. Rev. Lett. **109**, 032506 (2012).

[158] K. Wimmer, *Nucleon transfer reactions with radioactive beams*, J. Phys. G Nucl. Part. Phys. **45**, 033002 (2018).

[159] T. Wakasa, K. Ogata, and T. Noro, *Proton-induced knockout reactions with polarized and unpolarized beams*, Prog. Part. Nucl. Phys. **96**, 32–87 (2017).

[160] A. Gade, P. Adrich, D. Bazin, M.D. Bowen, B. Brown, C.M. Campbell, J.M. Cook, T. Glasmacher, P.G. Hansen, K. Hosier, S. McDaniel, D. McGlinchery, A. Obertelli, K. Siwek, L.A. Riley, J.A. Tostevin, and D. Weisshaar, *Reduction of spectroscopic strength: Weakly-bound and strongly-bound single-particle states studied using one-nucleon knockout reactions*, Phys. Rev. C **77**, 044306 (2008).

[161] J.A. Tostevin, and A. Gade, *Systematics of intermediate-energy single-nucleon removal cross sections*, Phys. Rev. C **90**, 057602 (2014).

[162] J. Lee, H. Liu, P. Doornenbal, M. Kimura, K. Minomo, K. Ogata, Y. Utsuno, N. Aoi, K. Li, M. Matsushita, H. Scheit, D. Steppenbeck, S. Takeuchi, H. Wang, H. Baba, E. Ideguchi, N. Kobayashi, Y. Kondo, S. Michimasa, T. Motobayashi, H. Sakurai, M. Takechi, and Y. Togano, *Asymmetry dependence of reduction factors from single-nucleon knockout of* ^{30}*Ne at 230 MeV/nucleon*, Prog. Theor. Exp. Phys. **2016**, 083D01 (2016).

[163] J. Lee, M.B. Tsang, D. Bazin, D. Coupland, V. Henzl, D. Henzlova, M. Kilburn, W.G. Lynch, A.M. Rogers, A. Sanetullaev, A. Signoracci, Z.Y. Sun, M. Youngs, K.Y. Chae, R.J. Charity, H.K. Cheung, M. Famiano, S. Hudan, P. O'Malley, W.A. Peters, K. Schmitt, D. Shapira, and L.G. Sobotka, *Neutron-Proton Asymmetry Dependence of Spectroscopic Factors in Ar Isotopes*, Phys. Rev. Lett. **104**, 112701 (2010).

[164] F. Flavigny, A. Gillibert, L. Nalpas, A. Obertelli, N. Keeley, C. Barbieri, D. Beaumel, S. Boissinot, G. Burgunder, A. Cipollone, A. Corsi, J. Gibelin, S. Giron, J. Guillot, F. Hammache, V. Lapoux, A. Matta, E.C. Pollacco, R. Raabe, M. Rejmund, N. d Séreville, A. Shrivastava, A. Signoracci, and Y. Utsuno, *Limited Asymmetry Dependence of Correlations from Single Nucleon Transfer*, Phys. Rev. Lett. **110**, 122503 (2013).

[165] S. Kawase, T. Uesaka, T.L. Tang, D. Beaumel, M. Dozono, T. Fukunaga, T. Fujii, N. Fukuda, A. Galindo-Uribarri, S. Hwang, N. Inabe, T. Kawabata, T. Kawahara, W. Kim, K. Kisamori, M. Kobayashi, T. Kubo, Y. Kubota, K. Kusaka, C. Lee, Y. Maeda, H. Matsubara, S. Michimasa, H. Miya, T. Noro, Y. Nozawa, A. Obertelli, K. Ogata, S. Ota, E. Padilla-Rodal, S. Sakaguchi, H. Sakai, M. Sasano, S. Shimoura, S. Stepanyan, H. Suzuki, T. Suzuki, M. Takaki, H. Takeda, A. Tamii, H. Tokieda, T. Wakasa, T. Wakui, K. Yako, J. Yasuda, Y. Yanagisawa, R. Yokoyama, K. Yoshida, K. Yoshida, and J. Zenihiro, *Exclusive quasi-free proton knockout from oxygen isotopes at intermediate energies*, Prog. Theor. Exp. Phys. **2018**, 021D01 (2018).

[166] K. Ogata, *Private communication.*

[167] K. Amos, P.J. Dortmans, H.V. v Geramb, S. Karataglidis, and J. Raynnal, *Nucleon-Nucleus Scattering: A Microscopic Nonrelativistic Approach*, Springer US, pages 276–536, (2002).

[168] K. Minomo, K. Ogata, M. Kohno, Y.R. Shimizu, and M. Yahiro, *Brieva-Rook localization of the microscopic nucleon-nucleus potential*, J. Phys. G Nucl. Part. Phys. **37**, 085011 (2010).

[169] M.A. Franey, and W.G. Love, *Nucleon-nucleon t-matrix interaction for scattering at intermediate energies*, Phys. Rev. C **31**, 488–498 (1985).